CONSTRAINING THE NEUTRON STAR EQUATION OF STATE WITH ASTROPHYSICAL OBSERVABLES

by

Carolyn A. Raithel

Copyright © Carolyn A. Raithel 2020

A Dissertation Submitted to the Faculty of the

DEPARTMENT OF ASTRONOMY

In Partial Fulfillment of the Requirements
For the Degree of

DOCTOR OF PHILOSOPHY
WITH A MAJOR IN ASTRONOMY AND ASTROPHYSICS

In the Graduate College

THE UNIVERSITY OF ARIZONA

2020

THE UNIVERSITY OF ARIZONA
GRADUATE COLLEGE

As members of the Dissertation Committee, we certify that we have read the dissertation prepared by: Carolyn Raithel
titled: Constraining the Neutron Star Equation of State with Astrophysical Observables

and recommend that it be accepted as fulfilling the dissertation requirement for the Degree of Doctor of Philosophy.

Date: May 13, 2020
Feryal Ozel

Date: May 13, 2020
Dimitrios Psaltis

David Sand
Date: May 13, 2020
David Sand

Date: May 13, 2020
Nathan Smith

Vasileios Paschalidis
Date: Sep 30, 2020
Vasileios Paschalidis

Final approval and acceptance of this dissertation is contingent upon the candidate's submission of the final copies of the dissertation to the Graduate College.

I hereby certify that I have read this dissertation prepared under my direction and recommend that it be accepted as fulfilling the dissertation requirement.

Date: May 13, 2020
Feryal Ozel
Department of Astronomy

ACKNOWLEDGEMENTS

Looking back over the last five years, this dissertation would not have been possible with the support of many people. First and foremost, I would like to thank my advisor, Feryal Özel, from whom I have learned so much – about not only the science I want to do, but about the type of scientist I want to be. I am grateful as well for the support and mentorship of Dimitrios Psaltis and Vasileios Paschalidis – I have so enjoyed working with and learning from you both. To Joel Weisberg, my undergraduate research advisor who first got me started on this journey and who has continued to support me throughout, thank you. I believe a scientist is shaped by the mentors she has early in her career, and I am grateful to have had so many excellent ones.

I am deeply thankful for my friends, near and far, who have supported me, encouraged me, and helped preserve my sanity over the last five years. To our astronomy crafting group Lia, Ekta, Samantha, and Allie; to my office mates David, Gabrielle, Tyler, Kaushik, and Michi; to Sarah, Marina, Tanner, Charlie, and Lina– thank you.

I will be forever grateful to my family for their continual support – especially my parents, Don and Kathy, who instilled in me a love for learning from a very young age and who have encouraged me ever since.

Finally, I would like to thank my husband, Nathan, who has been there from the start, when we were just two undergraduates studying pulsars in our first summer of research. You have encouraged me daily, made me laugh when I didn't think it was possible, helped me think through more than one statistical pathology, and been my rock through it all. Thank you.

DEDICATION

For my parents

TABLE OF CONTENTS

LIST OF FIGURES 9

LIST OF TABLES 12

ABSTRACT 13

CHAPTER 1 Introduction 15
- 1.1 Overview 15
- 1.2 Predicting neutron star observables from theoretical EOS 17
- 1.3 Observations of neutron star properties 18
  - 1.3.1 Masses 19
  - 1.3.2 Radii 22
  - 1.3.3 Moment of inertia 25
  - 1.3.4 Tidal deformability 26
- 1.4 Constraining the EOS from neutron star observables 28
- 1.5 Dynamical phenomena and the finite-temperature EOS 30
- 1.6 Outline of this work 31

CHAPTER 2 An Optimal Parametrization of the EOS 34
- 2.1 Optimizing the parametric EOS 35
- 2.2 From EOS to observables 37
- 2.3 Generating mock equations of state 39
  - 2.3.1 The mock EOS 41
  - 2.3.2 Determining the goodness of the parametric representation . . 44
  - 2.3.3 Results of parametrization of mock EOS 44
- 2.4 Adding phase transitions to the mock EOS 47
- 2.5 Application of the parametrization to physically-motivated EOS . . . 49
- 2.6 Conclusions 52

CHAPTER 3 Bayesian Inference of EOS Pressures 54
- 3.1 Bayesian inference of EOS pressures 55
  - 3.1.1 Priors on the pressures 56
  - 3.1.2 Regularizers 57
- 3.2 Testing the Bayesian inference with mock data 58
- 3.3 Biases due to marginalization 64
- 3.4 Conclusions 69

TABLE OF CONTENTS – *Continued*

CHAPTER 4 Model-Independent Mapping from a Moment of Inertia Measurement to the Neutron Star Radius 72
- 4.1 The moment of inertia in the double pulsar system 73
- 4.2 Neutron star moments of inertia for various EOS 74
- 4.3 Absolute bounds on the moment of inertia 77

CHAPTER 5 Gravitational Wave Events as a Direct Probe of the Neutron Star Radius 83
- 5.1 Gravitational waves and the EOS 84
- 5.2 Properties of GW170817 86
  - 5.2.1 Updated analysis of GW170817 87
- 5.3 Effective tidal deformability for GW170817 88
- 5.4 Effective tidal deformability in the Newtonian limit 90
- 5.5 Comparison to existing radius constraints 93
- 5.6 Bayesian inference of the radius 97
- 5.7 Black hole-neutron star mergers 100
- 5.8 Conclusions 100

CHAPTER 6 Connecting Gravitational Wave Events to Fundamental Nuclear Parameters 102
- 6.1 Motivations for studying the nuclear symmetry energy 102
- 6.2 Nuclear expansion of the equation of state 105
- 6.3 Polytropic approximation 107
- 6.4 Relating the tidal deformability to the symmetry energy 113
- 6.5 Constraints on higher-order nuclear parameters 119
- 6.6 Conclusions 122

CHAPTER 7 Optimized Statistical Approach for Comparing Multi-Messenger Neutron Star Data 124
- 7.1 Overview of multi-messenger data for neutron stars 124
- 7.2 Motivation and past work 127
- 7.3 Defining Bayesian priors 131
- 7.4 Transformation functions 134
  - 7.4.1 From the nuclear symmetry energy to the neutron star radius 135
  - 7.4.2 From tidal deformability to the neutron star radius 135
  - 7.4.3 Summary of transformations 136
- 7.5 Example application to gravitational wave data 138
- 7.6 Composite constraints on the neutron star radius 141
- 7.7 Conclusions 146

TABLE OF CONTENTS – *Continued*

CHAPTER 8 The Birth Mass Distribution of Neutron Stars and Black Holes 147
8.1 Previous studies of the compact object mass distribution 148
8.2 Pre-SN stellar evolution and explosion 152
8.3 Observations of remnant masses 156
8.4 Black hole mass distribution 159
8.4.1 Comparing the simulated and observed black hole mass distributions 164
8.5 Neutron star mass distribution 167
8.5.1 Comparing the simulated and observed pulsar mass distributions 171
8.6 Missing high-mass remnants 173
8.6.1 High-mass black holes 174
8.6.2 Missing high-mass neutron stars 177
8.6.3 Effect of binary evolution 178
8.7 Conclusions 179

CHAPTER 9 Finite-Temperature Extension for Cold Neutron Star EOS . . 181
9.1 Dynamical phenomena and the finite-temperature EOS 181
9.2 Overview of finite-temperature EOS 186
9.3 Generic model of a finite temperature EOS 191
9.4 Derivation of the cold symmetry energy in the Fermi Gas limit 194
9.5 Thermal contribution to the energy 200
9.5.1 M^*-approximation 204
9.5.2 Performance of the M^*-approximation of thermal effects at fixed Y_p 209
9.5.3 M^*-approximation for non-RMF models 212
9.6 Putting it all together 214
9.7 Complete model: Comparison of realistic EOS at arbitrary Y_p and T . 218
9.8 Conclusions 221

CHAPTER 10 Future Prospects 223
10.1 Upcoming new data 224
10.1.1 X-ray observations 224
10.1.2 Radio pulsar observations 225
10.1.3 Gravitational waves 227
10.2 New simulations of binary neutron star mergers 231
10.3 Conclusions 232

CHAPTER 11 Appendices 234
A Linear parametrization of the EOS 234

TABLE OF CONTENTS – *Continued*

B Relationship between the β-equilibrium proton fraction and the symmetry energy for n-p-e matter 237
C Calculation of the sound speed 239

REFERENCES 243

LIST OF FIGURES

1.1 Mass-radius relations for realistic EOS 18
1.2 Mass distribution of neutron stars and black holes. 20
1.3 Current sample of radius measurements 25

2.1 Piecewise polytrope schematic 36
2.2 Distribution of polytropic indices for realistic EOS 39
2.3 Grid of polytropic, mock EOS 42
2.4 Mass-radius curves for sample of mock EOS 43
2.5 Distribution of errors in radii and the maximum mass introduced by various parametrizations, for the mock EOS 45
2.6 Distribution of errors in the moment of inertia introduced by various parametrizations, for the mock EOS 46
2.7 Distribution of errors in radii and the maximum mass introduced by various parametrizations, for mock EOS with a first-order phase transition 48
2.8 Distribution of errors introduced by the optimal parametrization for 42 realistic EOS 50
2.9 Four realistic EOS and their mass-radius relations, for both the full EOS and our optimal parametrization of the EOS 51

3.1 Distribution of second derivatives in pressure for realistic EOS 58
3.2 EOS inference for example mass-radius data with various priors . . . 59
3.3 Individual mass-radius curves for inferred EOS 60
3.4 Correlations between the five inferred pressures 61
3.5 EOS inference from example mass-radius data with a Gaussian regularizer 65
3.6 Distribution of errors in inferred EOS for many example datasets . . 66
3.7 Bias introduced by two-dimensional histograms of mass-radius relations 67
3.8 Fidelity of recovered radii for inferred EOS 69

4.1 Moments of inertia and radii for realistic EOS 77
4.2 Stellar configurations for extremal moments of inertia 79
4.3 Universal mapping from moment of inertia to radius for various radii for one low-density EOS 80
4.4 Universal mapping from moment of inertia to radius for various radii for many realistic EOS 81

LIST OF FIGURES – *Continued*

5.1 Binary tidal deformability as a direct probe of the neutron star radius 89
5.2 Binary tidal deformability as a function of the primary component mass 90
5.3 Constraints on the radius from GW170817 94
5.4 Ensemble of EOS constraints from X-ray radius measurements and GW170817 95
5.5 EOS inference for sample tidal deformability data 99

6.1 Distribution of polytropic indices for nuclear-expansion EOS 111
6.2 Errors in approximating nuclear EOS with a single polytrope 112
6.3 Mass-radius curves, tidal apsidal constants, and tidal deformabilities for varying values of L_0 114
6.4 Binary tidal deformability as a function of the nuclear symmetry energy 115
6.5 Inferred constraints on L_0 from GW170817 117
6.6 Inferred constraints on $K_{\rm sym}$ and K_0 from GW170817 121

7.1 Example consistency check between two theoretical EOS and a collection of multi-messenger data 130
7.2 Transformations of priors between the tidal deformability, radius, and pressure 134
7.3 Constraints from GW170817 for different choices of priors 137
7.4 Constraints from GW190425 for different choices of priors 137
7.5 Summary constraints on the neutron star radius from X-rays, gravitational waves, and nuclear experimental data 142
7.6 Joint posterior distribution on the radius, for different combinations of experimental data 144

8.1 Remnant masses as a function of progenitor ZAMS mass 154
8.2 Fraction of remnant neutron stars as a function of progenitor ZAMS mass 156
8.3 Observed neutron star and black hole masses 157
8.4 Simulated implosion black hole masses as a function of progenitor mass 160
8.5 Simulated black hole mass distribution 165
8.6 Constraints on the stellar envelope ejection fraction 167
8.7 Simulated neutron star masses as a function of progenitor mass 167
8.8 Simulated baryonic mass distribution for neutron stars 171
8.9 Simulated gravitational mass distribution for neutron stars 172
8.10 Remnant masses at ultra-low metallicity 175

9.1 Cross-section of a phase diagram for dense matter 183

LIST OF FIGURES – *Continued*

9.2 Phase regimes where cold or thermal pressure dominates 189
9.3 Zero-temperature EOS model at fixed Y_p 199
9.4 Particle effective mass for pure neutron matter 207
9.5 Particle effective mass for symmetric nuclear matter 208
9.6 Thermal pressure for realistic EOS, hybrid EOS, and M^*-approximation 210
9.7 Dependence of the thermal pressure on M^* parameters 211
9.8 Error in the thermal pressure introduced by the M^*-approximation for RMF models 212
9.9 Error in the thermal pressure introduced by the M^*-approximation for non-RMF models 214
9.10 Complete model for the pressure at finite temperature and fixed Y_p . 219
9.11 Errors introduced by the complete model for the pressure 219

A1 Distribution of errors in radii and maximum mass introduced by a linear parametrization, for the mock EOS 236
A2 Distribution of errors in radii and maximum mass introduced by a linear parametrization, for 42 realistic EOS 237

LIST OF TABLES

5.1 $\widetilde{\Lambda}_{qN}$ expansion terms for the initial chirp mass ($\mathcal{M}_c = 1.188$) measured from GW170817. 93

6.1 Error in the polytropic approximation of a nuclear EOS for seven realistic EOS. 110

8.1 Fraction of outcomes that yield black holes in each branch of Fig. 8.4 for the five central engine models included in our analysis. 162
8.2 Fraction of outcomes that yield neutron stars in each branch of Fig. 8.7. 170
8.3 Gaussian Parameters for low-mass neutron star peak in Fig. 8.9 . . . 173

9.1 Symmetry energy parameters characterizing each EOS at $k_BT = 0.1$ MeV. 196
9.2 Parameters characterizing M^*, fit together at $k_BT = 1, 10$, and 47.9 Mev, for either pure neutron matter (PNM) or symmetric matter (SM). 206

10.1 Binary neutron star detection ranges for existing and upcoming detectors. 229

ABSTRACT

Neutron stars provide a unique probe of the dense-matter equation of state (EOS), which in turn governs many astrophysical transients of interest today, including gamma-ray bursts, kilonovae, core-collapse supernovae, and gravitational waves from neutron star mergers. While many theoretical predictions for the dense-matter EOS have been calculated and constrained by laboratory experiments at low densities, these methods do not constrain the EOS at the densities or compositions reached in neutron star interiors. Recently, the EOS community has been driven by a push to incorporate new observations of neutron star phenomena. In this dissertation, I develop a multi-pronged framework for using astrophysical observations of neutron stars to constrain the dense-matter EOS. To that end, I develop a Bayesian statistical inference scheme to map from neutron star observables to an optimally parametrized EOS. I also derive several new methods to directly compare diverse types of observations, including a model-independent mapping between the moment of inertia of a pulsar and the neutron star radius, as well as a one-to-one mapping between the radius and the tidal deformability measured from a neutron star merger. These relationships allow us to directly compare radii inferred from gravitational wave data (or from a future moment of inertia measurement) to X-ray observations of the neutron star radius. With this mapping, I use the tidal deformability from the first neutron star merger, GW170817, to place new constraints on the neutron star radius of $10.2 < R < 11.7$ km (68% confidence; for a flat prior in R), which are already competitive, though consistent with previous results from the X-ray community. Additionally, I develop a method for connecting gravitational wave data to the slope of the nuclear symmetry energy and I show that gravitational waves imply smaller values than have been found in Earth-based experiments. In the final chapters of my dissertation, I tie in dynamical phenomena to these constraints. Using

results from state-of-the-art supernovae simulations, I show that such simulations are starting to accurately recreate the observed compact object mass distribution and I use these results to identify the origins of various features in the observed mass distribution. Finally, I introduce a new microphysical framework for extending models of the cold EOS to arbitrary temperatures and compositions, which can be used to simulate neutron star mergers or core-collapse supernovae with robust physics.

CHAPTER 1

Introduction

1.1 Overview

During the explosions that mark the deaths of massive stars, standard stellar evolution processes produce the densest matter found anywhere in the Universe. While the outer layers of the star are cast off, the core collapses and is compressed by gravity to form a neutron star, whose central densities are 10^{14} times denser than found in matter on Earth. At these densities, the wave-functions of individual neutrons overlap and the final fate of the matter remains an open question. One of the long-standing goals of both modern nuclear and astrophysics is to better understand the equation of state (EOS) under these extreme conditions.

A wide variety of theoretical models for the dense-matter EOS have been proposed. The earliest models were for a simple, cold Fermi gas of degenerate neutrons (Oppenheimer and Volkoff, 1939), but these provide too little pressure to support the masses of astrophysically-observed neutron stars. More modern EOS include additional sources of pressure, generated by repulsive interactions between particles. However, the nature of these interactions, as well as the number of degrees of freedom involved, remains highly uncertain. The resulting suite of EOS range from models in which the matter is purely nucleonic at high densities (e.g., Baym et al. 1971; Friedman and Pandharipande 1981; Akmal et al. 1998; Douchin and Haensel 2001) to models predicting the emergence of more exotic phases of matter, such as pion condensates (e.g., Pandharipande and Smith 1975), kaon condensates (e.g., Kaplan and Nelson 1986), hyperons (e.g., Balberg and Gal 1997), or deconfined quark matter (e.g., Collins and Perry 1975). More recently, some studies have started to incorporate quark degrees of freedom using state-of-the-art results from perturbative QCD (e.g., Fraga et al. 2014).

Nuclear experiments offer some constraints for these various theoretical models. For example, the two-body potential can be constrained from nucleon-nucleon scattering data at energies below 350 MeV while the three-body force can be constrained using the properties of light nuclei (e.g., Akmal et al., 1998; Morales et al., 2002). These few-body potentials can then be used to bound the EOS at densities near the nuclear saturation density, $\rho_{\rm sat} = 2.7 \times 10^{14}$ g/cm^3 . Experimental constraints can also be expressed in terms of the nuclear symmetry energy, which characterizes the difference in energy between pure neutron matter and symmetric nuclear matter, which has equal numbers of protons and neutrons. The value of the nuclear symmetry energy at the nuclear saturation density, S_0, and its slope, L_0, have been constrained by fits to nuclear masses (e.g., Danielewicz, 2003); by measurements of the neutron skin thickness (Centelles et al., 2009; Horowitz et al., 2014), the giant dipole resonance (Trippa et al., 2008), and the electric dipole polarizability of ^{208}Pb (Tamii et al., 2011); and by observations of multifragmentation or isospin diffusion in heavy ion collisions (e.g., Tsang et al., 2004). For a recent review of these measurements, see Oertel et al. (2017).

However, these nuclear experiments typically probe densities at or below $\rho_{\rm sat}$; extrapolations to higher densities remain difficult (Lattimer, 2012). These experiments also tend to probe matter that is hot, relative to the Fermi energy, and fairly symmetric. This adds an additional two dimensions over which experimental results must be extrapolated to match the conditions found in neutron star interiors. Moreover, while the interactions between particles can be written in terms of few-body potentials up to $\sim \rho_{\rm sat}$ (Akmal et al., 1998; Morales et al., 2002; Gandolfi et al., 2012), the expansion of interactions into few-body terms starts to break down at higher densities, due in part to the overlap of the particle wave-functions (Özel and Freire, 2016). Without a well-defined framework for parameterizing particle interactions, even theoretical progress poses a challenge.

Thus, to constrain the neutron star EOS, the only practical way forward is to use observations of neutron stars themselves. All macroscopic properties of a neutron star – including its mass, radius, moment of inertia, and quadrupole moment, as measured through a tidal deformability – are determined by the EOS at densities above ρ_{sat}. Observations of these properties, therefore, provide a unique probe of the EOS in the ultra-dense limit, where terrestrial-based efforts break down. Throughout the course of this dissertation, I will develop a multi-pronged theoretical framework to connect such observations of neutron star phenomena to the dense-matter EOS.

1.2 Predicting neutron star observables from theoretical EOS

To understand how neutron star properties connect to the EOS, I will start with the forward-facing problem: for any star, the stellar propoerties can be calculated from the EOS using the stellar structure equations. However, because neutron stars are extremely compact objects, with typical compactness $GM/Rc^2 \simeq 0.2$ for a canonical 1.4 $M_\odot$ neutron star with a radius of 10 km, the classical stellar structure equations break down. A relativistic version of the stellar structure equations was first derived in a pair of contemporaneous papers by Tolman (1939) and Oppenheimer and Volkoff (1939), using a solution to Einstein's equation for a perfect fluid in static, spherically-symmetric equilibrium. The eponymous "TOV" equation relates the pressure, P, and energy density, ϵ, of a particular EOS to the stellar mass, M, enclosed by a given radius, r, according to

$$\frac{\partial P}{\partial r} = -\frac{G}{c^2} \frac{(\epsilon + P)\left(M + 4\pi r^3 \frac{P}{c^2}\right)}{r^2 (1 - \frac{2GM}{rc^2})}, \tag{1.1}$$

where the mass is given by

$$\frac{\partial M}{\partial r} = \frac{4\pi r^2 \epsilon}{c^2}. \tag{1.2}$$

Here and throughout this dissertation, G and c are the gravitational constant and speed of light, respectively. By numerically integrating the TOV equations outward from the center of the star, one can solve for the point at which the pressure becomes negligible and, hence, for the total mass and radius of a star with a given central density.

The TOV equations provide a one-to-one mapping of the microscopic properties of matter to macroscopic observables. For a given EOS, this translates into a specific

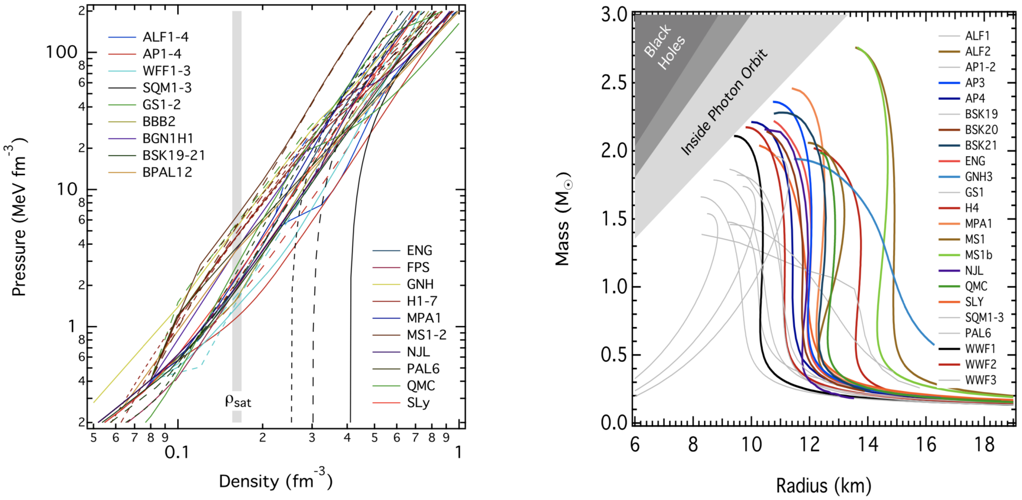

Figure 1.1 A large sample of proposed EOS (*left*) and their corresponding mass-radius relations (*right*). Figure reproduced with permission from Özel and Freire (2016).

prediction for the allowed combination of masses and radii that all neutron stars must obey. Figure 1.1 shows a sample of mass-radius curves for a wide range of proposed EOS. As shown in the right panel of this figure, modern EOS calculations predict that the radius of a 1.4 $M_{\odot}$ star is between ∼10 and 15 km and that the maximum mass of a neutron star is between 2 and nearly 2.8 $M_{\odot}$. By measuring these and other properties of neutron stars, it is thus possible test the predictions of individual EOS and, potentially, constrain families of models.

1.3 Observations of neutron star properties

There are a variety of neutron star properties that are observationally accessible for testing the predictions of the EOS, including not only neutron star masses and radii, but also higher order moments of the interior mass distribution such as the moment of inertia and the tidal deformability. In this section, I will describe how these measurements are made and will review recent results.

1.3.1 Masses

To date, more than 30 precision neutron star masses have been measured, by carefully tracking pulse arrival times from radio pulsars in binary systems. Fitting the pulse arrival times to an elliptical orbit allows for the determination of the five Keplerian parameters that characterize an orbit, from which we can determine the binary mass function

$$f = \frac{4\pi^2}{T_\odot}\frac{x_{\rm PSR}^3}{P_b^2} = \frac{(M_{\rm c}\sin i)^3}{M_{\rm T}^2}, \tag{1.3}$$

where $T_\odot \equiv GM_\odot/c^3$ is the mass of the sun in time units, P_b is the binary period, $x_{\rm PSR}$ is the projection of the pulsar's semi-major axis onto the observer's line of sight, i is the inclination of the orbit, and $M_{\rm c}$, $M_{\rm PSR}$ and $M_T \equiv M_{\rm c} + M_{\rm PSR}$ are the companion mass, pulsar mass, and total binary mass, respectively. In order to break the degeneracy in the mass function and solve for $M_{\rm PSR}$, we need a separate measure of the companion mass. This is typically accomplished in one of two ways for radio pulsars. If the companion is also a compact object – either a white dwarf or a second neutron star – and the orbit is sufficiently compact, then relativistic effects can be measured using a post-Keplerian (PK) framework and treating both objects as point masses. The measurement of a single PK parameter can be used to place bounds on $M_{\rm PSR}$, while the measurement of two PK parameters can tightly constrain the pulsar mass (e.g., Taylor and Weisberg, 1989; Damour and Taylor, 1992). Alternatively, if the radio pulsar has a white dwarf companion that is optically bright, then phase-resolved spectroscopy can be used to measure the projected orbital velocity of the white dwarf which, when combined with the orbital velocity of the pulsar, can be used to constrain the mass ratio. Doppler broadening in the spectrum of the white dwarf atmosphere can further be used to determine the local gravitational acceleration and, hence, the white dwarf mass. From the white dwarf mass and the mass ratio, one can trivially determine the mass of the pulsar (Thorsett and Chakrabarty, 1999, and references therein).

For a subset of neutron stars that are not radio pulsars, it is still possible to infer mass constraints if the neutron star resides within an X-ray binary system.

For accretion-powered pulsars in an eclipsing binary with a high-mass companion, X-ray observations of the neutron star, combined with optical observations of the stellar companion, can be used to solve for the binary parameters of the system, including the mass of the neutron star. For neutron stars in accreting low-mass X-ray binaries, it is possible to simultaneously constrain the neutron star mass and radius (see §1.3.2), though these mass measurements are less precise than those obtained from radio pulsar timing. For a recent review on neutron star masses measured with all of these methods, see Özel and Freire (2016).

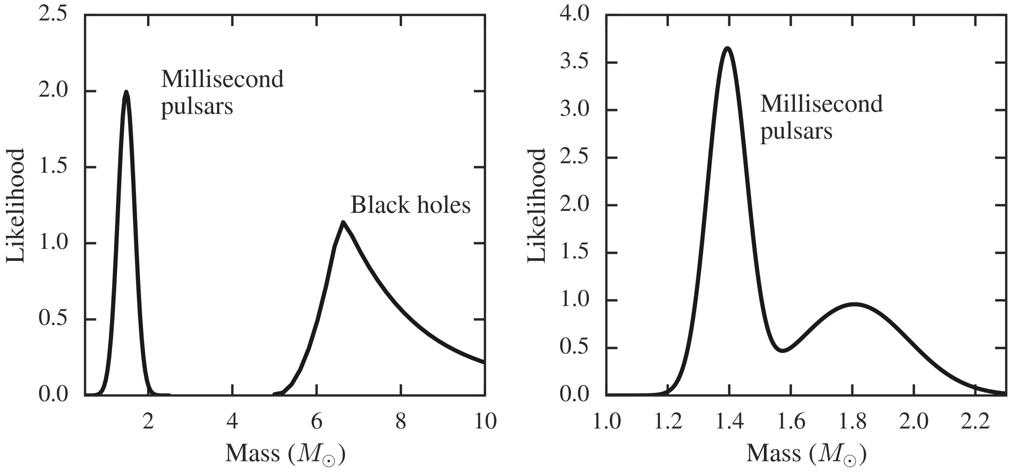

Figure 1.2 *Left:* Observed mass distribution of pulsars and black holes, including the apparent gap of compact objects with masses $\sim 2-5\ M_\odot$ (Özel et al., 2012). *Right:* Updated pulsar mass distribution, showing new evidence of bimodality (Antoniadis et al., 2016).

The masses measured with these three methods range from $\sim 1.1\ M_\odot$ (Rawls et al., 2011; Özel et al., 2012), to greater than 2 $M_\odot$ (Demorest et al., 2010; Antoniadis et al., 2013; Fonseca et al., 2016; Cromartie et al., 2020). The observed pulsar mass distribution is shown in the left panel Fig. 1.2, with the galactic black hole mass distribution shown for comparison (Özel et al., 2012). The right panel of Fig. 1.2 shows a more recent update for the pulsar mass distribution, which suggests that the population may in fact be bimodal (Antoniadis et al., 2016). While the lower end of this mass distribution offers interesting insight into how neutron stars form (e.g., Suwa et al., 2018), it is the highest mass neutron stars that allow for the most direct constraints on the EOS. Unlike in Newtonian stars, in neutron stars, the pressure does not simply oppose the gravity but also contributes to the overall mass-energy of the system and, hence, to the total gravity. This can be seen directly in the right-hand side of eq. (1.1) and leads to a unique prediction of general relativity: that there exists a maximum neutron star mass, $M_{\rm max}$, above which an object will collapse to a black hole. Current observations imply $M_{\rm max} \gtrsim 2\ M_{\odot}$, based on the measurement of two roughly 2 $M_{\odot}$ neutron stars, PSR J1614-2230 (Demorest et al., 2010; Fonseca et al., 2016) and PSR J0348+0432 (Antoniadis et al., 2013). When these pulsars were first discovered, their existence was used to rule out EOS families that did not provide enough pressure to support such a large $M_{\rm max}$, including models that allowed for meson condensates or hyperonic matter, both of which soften the overall EOS (Demorest et al., 2010). Several such EOS are shown as gray lines in Fig. 1.1. However, some of these softer EOS models have since been modified, so that they now provide sufficient pressure to be consistent with the existence of massive neutron stars (see, e.g., Bednarek et al. 2012 for an allowed hyperonic model). Recently, Cromartie et al. (2020) reported the detection of a new possible candidate for the most massive pulsar, whose mass is $M = 2.14^{+0.10}_{-0.09}\ M_{\odot}$. While the 1σ error bars for this measurement are still large, the system is a promising candidate for further EOS constraints.

The compact object mass distribution shown in Fig. 1.2 can also be used to test the predictions of state-of-the-art simulations of core-collapse supernovae. While much progress has been made in modeling the late stages of stellar evolution and the explosion mechanism of the core-collapse over the last decade, significant uncertainties remain. Many of these uncertainties result from the inherent complexity of the explosion mechanism. A core-collapse supernova successfully explodes only if the outgoing shock wave, which stalls due to neutrino losses and photo-dissociation, is revived. The long-favored, though still unproven, method for this revival is through neutrino energy transport. Although great progress is being made on this problem, the community has yet to reach a consensus on the details of the neutrino-driven explosion mechanism (Janka et al., 2016, and references therein). Additionally, observational evidence from Supernova 1987A (e.g., Arnett et al., 1989; Hillebrandt and Hoflich, 1989), other well-observed supernovae (e.g., Maeda et al., 2008), supernova remnants (e.g., Grefenstette et al., 2014; Milisavljevic and Fesen, 2015), and from neutron star natal kicks (e.g., Lai et al., 2001; Hobbs et al., 2005) suggest that successful explosions are significantly asymmetric and, therefore, require multi-dimensional simulations to study. While 3D simulations are now possible (see e.g., Hammer et al., 2010, for one of the first sets of results), such simulations are extremely computationally expensive, which limits the possible parameter space that can be explored.

An alternate way forward, then, is to use simplified, one-dimensional simulations that facilitate large parameter studies. For example, Sukhbold et al. (2016) surveyed the explosion outcomes for a large and fine grid of stellar models (from Woosley and Heger, 2007; Sukhbold and Woosley, 2014; Woosley and Heger, 2015), combined with a novel one-dimensional neutrino-driven explosion mechanism (Ugliano et al., 2012; Ertl et al., 2016). While simplified, this approach produces successful explosions across a wide range of progenitor masses and recreates many of the features of fully 3D models. Moreover, the simplifications of these 1D simulations have allowed for an unprecedented, large-scale study of supernova outcomes (Sukhbold et al., 2016), which makes it possible, for the first time, to directly confront state-of-the-art theoretical models with the growing sample of neutron star mass measurements. Additionally, the origin of various features shown in Fig. 1.2 – such as the bimodality of the neutron star mass distribution and the observed gap between the most massive neutron stars and the lightest black holes – can start to be understood by systematically comparing with the results from such simulations (see Chapter 8).

1.3.2 Radii

We can also test the predictions of individual EOS using measurements of the neutron star radius. Currently, the most stringent radius constraints come from the detection of thermal emission from the neutron star surface, either through spectroscopic or pulse timing measurements.

A spectroscopic radius measurement combines two key pieces of information: an effective temperature, T_{eff}, which can be modeled from the thermal spectrum of the stellar surface, and the thermal bolometric flux, F_{bol}. Combined with an independent measurement of the distance to the source, D, which can be found if the source is selected carefully, e.g. to be in a globular cluster with a known distance, then the observed radius is simply given by

$$R_{\mathrm{obs}} = \left(\frac{F_{\mathrm{bol}}}{\sigma_{\mathrm{B}} T_{\mathrm{eff}}^4} \right)^{1/2} D. \tag{1.4}$$

For a classical star, this would be the end of the story; but, for a neutron star, the surface emission is gravitationally lensed by its own self-gravity (Pechenick et al., 1983; Psaltis et al., 2000) and so the radius that is observed is larger than the true radius. Correlated constraints on the true radius, R, and the stellar mass, M, can be extracted by correcting for this self-lensing, according to

$$R_{\mathrm{obs}} = \left(1 - \frac{2GM}{Rc^2} \right)^{-1/2} R. \tag{1.5}$$

Spectroscopic radius measurements have been made primarily for two types of systems. In the first, a neutron star in an accreting low-mass X-ray binary (LMXB) is observed during quiescence, when the accretion temporarily slows or halts altogether. This allows for the stellar surface to be observed as the star re-radiates the heat it stored during the accretion phase, and hence for T_{eff} and F_{bol} to be directly measured (e.g., Guillot et al., 2013; Guillot and Rutledge, 2014; Heinke et al., 2014; Bogdanov et al., 2016). Alternatively, for some neutron stars in accreting LMXBs, enough material can accumulate that it undergoes a thermonuclear burst, which can spread across the surface of the star. van Paradijs (1978) first showed that the spectral properties of the cooling tails from such a burst could be used to measure R_{obs} using eq. (1.4), and thus correlated $M-R$ constraints using eq. (1.5) (van Paradijs, 1979). More stringent radius constraints can be measured for the subset of cases in which the thermonuclear burst is powerful enough to lift the photosphere away from the surface of the star. For these photospheric radius expansion (PRE) events, some of the degeneracy between the mass and radius can be broken by additionally measuring the Eddington flux, which corresponds to the flux at the moment the photosphere touches back down onto the surface of star, defined as

$$F_{\mathrm{Edd}} = \frac{GMc}{\kappa_{\mathrm{es}} D^2} \left(1 - \frac{2GM}{Rc^2}\right)^{1/2}, \tag{1.6}$$

where κ_{es} is the opacity to electron scattering. Combined observations of the cooling tail and the Eddington flux provide some of the most stringent radius constraints to date (e.g., Özel et al. 2009; Güver et al. 2010; Güver and Özel 2013).

The current sample of quiescent LMXB and PRE radius measurements are summarized in Fig. 1.3, reproduced with permission from Özel and Freire (2016). Under the assumption that all neutron stars have a common radius (as is predicted by the vertical mass-radius relations in Fig. 1.1) and that the observed scatter of measurements is simply experimental error, these data combine to yield a narrowly-constrained radius of $R = 10.3 \pm 0.5$ km (Özel et al., 2016). This common-radius assumption is reasonable for EOS that remain nucleonic to high densities. With a more general inference in which exotic EOS are also allowed, Özel and Freire (2016) find that the neutron star radius of a 1.5 $M_\odot$ star is constrained to the range $9.9 - 11.2$ km. (See also a similar analysis of LMXB data by Steiner et al. (2013), in which the radius of a $1.4 M_\odot$ star is constrained to the range $10.4 - 12.9$ km.)

Pulse profile modeling offers a complementary approach to these spectroscopic methods for constraining the neutron star radius. A subset of isolated pulsars show thermal emission in the soft X-rays, which is powered by return-current heating of the magnetic-field polar caps. This surface emission is gravitationally lensed by the neutron star spacetime, so that even when the hot-spot rotates out of our direct line of sight, part of the emission is still beamed towards us. By carefully modeling the observed pulse profiles – taking into account the effects of the temperature distribution, size, and location of the hot-spot, as well as the beaming pattern of the emitted radiation and the lensing effect of the neutron star's self-gravity – correlated constraints on the mass and radius can be inferred.

The Neutron Star Interior Composition ExploreR (NICER) is a NASA Mission of Opportunity that is currently timing a small number of rotation-powered X-ray

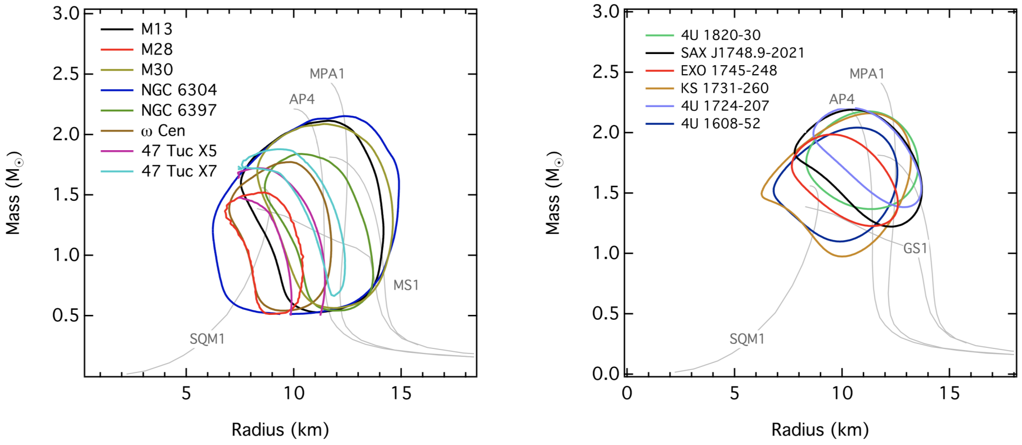

Figure 1.3 Summary of radius constraints measured from neutron stars in LMXBs during quiescence (left) or from PRE sources (right). All contours are shown at the 68% confidence-level. Figure reproduced with permission from Özel and Freire (2016).

pulsars, with the goal of measuring the neutron star radius from their pulse profiles (Gendreau et al., 2012). Recently, the NICER collaboration published the first radius measurement from one of their sources, PSR J0030+0451, which they find to be $R = 12.71^{+1.14}_{-1.19}$ km for a multi-component, phenomenological set of pulse-profile models (Bogdanov et al. 2019; Riley et al. 2019; see also Miller et al. 2019). While these constraints are still broad, they seem to favor larger radii than have previously been found. As more physical pulse-profile models are developed for interpreting these data, it will be interesting to see whether this discrepancy with the LMXB sources persists.

1.3.3 Moment of inertia

Higher-order moments of the neutron star mass distribution provide further constraints on the dense-matter EOS. While §1.2 focused on calculating masses and radii from an EOS, the TOV equations can be augmented to solve for the corresponding moments of inertia as well (see Chapter 4). Just as a particular EOS predicts a unique radius for a star of a given mass, so too does it predict a unique moment of inertia.

The first measurement of the neutron star moment of inertia is expected to be announced imminently, following the discovery and continued observations of the double pulsar system, PSR J0737−3039 (Lyne et al., 2004). This system makes such a measurement possible for two key reasons. First, PSR J0737−3039 is the only known double neutron star system in which both stars are visible as active radio pulsars. By carefully measuring the pulse arrival times from each pulsar, their orbits can be accurately and independently tracked, which provides unparalleled constraints on the mass ratio of the system. Additionally, the system is among the most relativistic binaries known, with an orbital period of 147 min and a small but non-zero eccentricity, which allows for the measurement of multiple PK parameters.

The most relevant PK parameter for this measurement is the advance of the periastron, $\dot{\omega}$, which depends on two competing effects: (1.) the post-Newtonian orbital dynamics, which are determined by the masses of the two pulsars and (2.) the coupling between the spin vector of the more rapidly-spinning star, Pulsar A, and the total orbital angular momentum of the system. The amount of the spin-orbit coupling, in turn, depends on the moment of inertia of Pulsar A. Thus, by modeling the post-Newtonian contribution and subtracting it from the total observed $\dot{\omega}$, one can, in principle, measure the moment of inertia of Pulsar A. This process requires accurate knowledge of the masses of each pulsar, which can be obtained with the measurement of at least two additional post-Keplerian parameters. Current timing simulations suggest that the masses can be best determined by combining the Shapiro delay "shape" parameter, s, and the decay of the binary orbital period, $\dot{P}_b$. With continued tracking of the system, $\dot{P}_b$ will be be sufficiently accurate to allow a 10% measurement of the moment of inertia within the next few years (Kramer and Wex, 2009).

1.3.4 Tidal deformability

Another probe of the neutron star interior mass distribution has recently emerged: through the observation of gravitational waves emitted during a binary neutron star merger. When two neutron stars orbit one another, the stars emit gravitational radiation, which causes the system to spiral inward and ultimately coalesce. Weisberg and Taylor (1981) provided the first indirect evidence for gravitational waves, by measuring the orbital decay of the double neutron star system, B1913+16, with radio pulsar timing (Weisberg and Taylor, 1981; Taylor and Weisberg, 1982; Weisberg and Huang, 2016). The direct detection of gravitational waves was the founding goal of the Laser Interferometer Gravitational wave Observatory (LIGO), which consists of two interferometers located in Hanford, Washington and Livingston, Louisiana. Following a first observing run from 2002 - 2010, the two observatories were upgraded to higher sensitivity and to probe lower gravitational wave frequencies. With these improvements, Advanced LIGO commenced O1 operations in 2015 and soon made the first direct detection of gravitational waves, from a binary black hole merger (Abbott et al., 2016d). In the subsequent O2 observing run, which started in 2017, the Italian gravitational wave observatory, Virgo, came online and joined the LIGO network.

Soon thereafter, on August 17, 2017, the LIGO-Virgo collaboration recorded the first detection of gravitational waves from a binary neutron star merger, with event GW170817. Following the binary coalescence by 1.7 seconds, a gamma-ray burst was observed independently by the Fermi Gamma-ray Burst Monitor and the International Gamma-Ray Astrophysics Laboratory, in the same direction as GW170817 (Abbott et al., 2017a). Roughly 11 hours later, a fading optical transient was discovered by the Swope Supernova Survey (SSS17a/AT2017gfo; Coulter et al., 2017), which was extensively followed up (Abbott et al., 2017d). Early observations of this source indicated a blue transient that faded over the initial 48 hours and reddened over the next $\sim$ 10 days. Altogether, these observations have confirmed neutron star mergers as the central engines powering at least some short-duration gamma-ray bursts, as has long been theorized (Eichler et al., 1989; Narayan et al., 1992; Berger, 2014). These observations have also confirmed that neutron star mergers can indeed produce a kilonova, powered by the radioactive decay of merger ejecta (Li and Paczyński, 1998; Metzger et al., 2010; Abbott et al., 2017d). With the coincident detection of gravitational and electromagnetic signals, GW170817 has ushered in a new era of multi-messenger astrophysics.

With current detector sensitivity, the main EOS information from a neutron star merger is encoded in the tidal deformability, which characterizes the quadrupolar response of an object to an external tidal field. The tidal deformability is another unique prediction of the EOS and, like the moment of inertia, it can be calculated using an augmented set of TOV equations (see Chapter 6). During an inspiral, as the two neutron stars become increasingly tidally deformed, the resulting asymmetry causes a phase shift in the emitted gravitational waves. Thus, by fitting the time-dependent phase of the observed gravitational signal, one can measure the tidal deformability and use it to constrain the EOS (Flanagan and Hinderer, 2008; Hinderer, 2008; Read et al., 2009b; Hinderer et al., 2010; Read et al., 2013; Lackey and Wade, 2015). Already, many studies have started to use the tidal deformability information from GW170817, and, in some cases, from the second likely binary neutron star merger (GW190425; The LIGO Scientific Collaboration et al., 2020), to place constraints on the predictions of theoretical EOS (e.g., Abbott et al. 2018; Landry and Essick 2019; Capano et al. 2020; The LIGO Scientific Collaboration et al. 2020; for a recent review, see Raithel 2019 and references therein).

1.4 Constraining the EOS from neutron star observables

Each of the measurements described in § 1.3 – on the maximum neutron star mass, stellar radius, moment of inertia, or tidal deformability – provides a test for the predictions of a particular EOS. However, this method of testing already-formulated EOS is inherently limited in scope: it remains possible, even likely, that the current sample of proposed EOS does not probe the full range of physical possibilities.

One alternate approach is to instead infer the functional form of the EOS directly from the observations. Formally, it is possible to invert the TOV equations to recover the EOS, given high-quality mass and radius observations that completely populate the mass-radius curve (Lindblom, 1992). However, even with roughly a dozen radius measurements, the current sample of data is sparse. Moreover, there is no known mechanism for producing neutron stars below $\sim 1M_{\odot}$ and none have ever been observed (see Fig. 1.2). As a result, performing an exact inversion remains observationally unrealistic.

A second approach is to infer a simplified functional form for the EOS, using a parametrization. This requires fewer observations and allows for the EOS to be recovered from a more limited range of data. Many parametrizations have been proposed, ranging from a spectral expansion of the enthalpy (Lindblom and Indik, 2012, 2014) to discrete segments that are piecewise polytropic or linear (Read et al., 2009a; Özel and Psaltis, 2009; Hebeler et al., 2010; Steiner et al., 2016). However, despite these various proposals, only limited systematic optimizations have been undertaken to determine the ideal number of segments and functional forms for a parametric EOS. Moreover, these early parametrization studies relied on a sample of existing theoretical EOS as benchmarks, which limits the diversity of EOS that can subsequently be inferred. They also only sought to reproduce the predicted radii to uncertainties that are rather large by today's standards, reflecting the data that were available at the time. Given the growing sample of mass and radius measurements, as well as the anticipated moment of inertia measurement from PSR J0737−3039, any useful parametrization must be able to recreate masses and radii to higher precision than ever before, while still maintaining a minimum set of parameters (see Chapter 2).

Once such a parametrization is found, the parameters can be determined using a Bayesian statistical inference scheme. Such methods have been previously developed in Steiner et al. (2010, 2016) and Özel et al. (2016) for a variety of mass and radius data from LMXB sources. However, amongst the existing inference schemes, important statistical considerations have yet to be explored. For example, it is not obvious what types of prior distributions should be used – or on which parameters the priors should be defined – and biases in currently-used methods of marginalization persist. These statistical issues can significantly influence the resulting EOS constraints, particularly when the data are sparse (as will be addressed in Chapter 3) or come from different types of experiments (as will be addressed in Chapter 7).

1.5 Dynamical phenomena and the finite-temperature EOS

All of the measurements discussed so far constrain the dense-matter EOS at zero-temperature and in β-equilibrium. These conditions are appropriate for old, static neutron stars that have had sufficient time to cool and equilibrate, following their formation during a core-collapse supernovae. However, during and soon after the core-collapse, the matter in a proto-neutron star can be quite hot – meaning that the average energy of the particles exceeds the local Fermi energy – and nearly symmetric. Similarly, although the neutron stars remain cold and in β-equilibrium during the early inspiral phase of a merger, at late times in the merger, shock heating can significantly raise the temperature of the system and the composition of the matter can evolve away from β-equilibrium, as the dynamical timescale becomes shorter than the neutrino-interaction timescale. Thus, when it comes to modeling the matter in a core-collapse supernova, in a cooling proto-neutron star, or in the late stages of a neutron star merger, the cold, β-equilibrium EOS no longer applies. Rather, these phenomena are governed by the finite-temperature EOS with non-equilibrium compositions.

This distinction is particularly important as we look to incorporate new observations of dynamical phenomena into our framework for constraining the EOS over the next decade. For example, one promising new probe of the EOS is anticipated with the future measurement of post-merger gravitational waves – which are expected to be emitted by a neutron star remnant of a binary merger, as the remnant relaxes down to an equilibrium configuration (e.g., Bauswein and Janka, 2012; Read et al., 2013; East et al., 2016; Rezzolla and Takami, 2016). (For a discussion of the detectability of the post-merger signal, see Chapter 10.) However, with temperatures far exceeding the Fermi energy and non-equilibrium compositions in the remnant, it is in fact the finite-temperature EOS that these post-merger gravitational waves probe. Thus, combining the EOS constraints derived from such a measurement with the EOS constraints derived from cold neutron stars will require a robust framework for disentangling the role of the underlying cold pressure, the thermal pressure, and the effect of the changing composition on the pressure for these dynamical phenomena.

Currently, there exist only a few theoretical models for the EOS at non-zero temperatures and non-equilibrium compositions. These models span a very limited range of the physical possibilities that may arise in neutron stars interiors, and many predict neutron star properties that are inconsistent with the latest observations (e.g., radii $\gtrsim$ 13 km). In order to probe a wider range of underlying physics or to study more observationally-consistent models, most modern merger simulations employ an ad-hoc approach that consists of a thermal correction term added to a parametrized cold EOS. The thermal correction is derived from an ideal-fluid treatment of the matter (e.g., Janka et al., 1993), which assumes that the matter is diffuse and non-interacting. While this ideal-fluid approximation was a useful first step towards considering the role of the thermal pressure, it neglects the effects of degeneracy, which can reduce the thermal pressure by up to four orders of magnitude at neutron star densities. By so drastically over-estimating the thermal pressure, the ideal-fluid approximation can introduce large errors into key observable features, such as the lifetime of the remnant object and the post-merger gravitational wave frequencies (Bauswein et al., 2010). Furthermore, this ad-hoc framework neglects the changing proton fraction inside the star altogether. An improved framework to address these issues will be the topic of Chapter 9.

1.6 Outline of this work

In this dissertation, I describe new contributions to the field of deriving EOS constraints from astrophysical observables, ranging from mass and radius measurements, to gravitational waves from binary neutron star mergers.

I will start with a statistical framework that I have developed for optimally inferring EOS constraints. In Chapter 2, I describe a new parametrization of the EOS that has been systematically optimized to recover a wide range of possible EOS behavior. In Chapter 3, I introduce a Bayesian statistical inference scheme to recover the pressures of this optimally-parametrized EOS. I also identify an important bias in currently-used inference techniques, resulting from a statistical subtlety in the marginalization of a multi-dimensional parameter-space and I demonstrate how to avoid such pitfalls.

I then introduce a set of new, EOS-independent mappings between higher-order moments of the mass distribution and the neutron star radius. In Chapter 4, I derive maximal bounds on the moment of inertia for a pulsar of a given mass, which can be used to map the anticipated measurement of the moment of inertia to the neutron star radius in a model-independent way. In Chapter 5, I report a new universal mapping between the binary tidal deformability, as measured from a gravitational wave event, and the neutron star radius. Both of these relationships provide a direct route for transforming a high-order moment of the mass distribution to a corresponding stellar radius. These transformations can thus facilitate novel comparisons between radii inferred from three very different types of observations: X-ray spectra (for the direct radius measurement), radio timing measurements (for the moment of inertia), and gravitational waves (for the tidal deformability). This will allow for an unprecedented check for systematic biases or modeling uncertainties in each of these independent measurements, and has already provided new constraints on the neutron star radius.

Motivated by the direct mapping from gravitational waves to the neutron star radius, and the long-known correlations between the neutron star radius and the nuclear symmetry energy (e.g., Lattimer and Prakash, 2001), Chapter 6 introduces a new method for constraining the nuclear symmetry energy from a neutron star merger event. I also report the resulting constraints on the slope of the symmetry energy, L_0, inferred from GW170817, which are in modest tension with what has been found in terrestrial nuclear experiments.

With the new wealth of multi-messenger constraints on the EOS, it is no longer obvious how to best compare experimental results that are measured in different domains. In Chapter 7, I discuss statistical biases that can arise when the domain of measurement differs from the domain of comparison and I introduce an optimized approach to robustly compare multi-messenger neutron star data.

In the final chapters of this dissertation, I transition to considering simulations of dynamical phenomena. In Chapter 8, I report on results from state-of-the-art supernova simulations from a collaborator, and I calculate the predicted mass functions of the remnant compact objects. I compare these simulated mass functions to the observed mass functions and find strong agreement, providing new evidence in favor of these simulations. Using these results, I also identify the origins of different features in the neutron star mass distribution. In Chapter 9, I introduce a new microphysical framework to calculate the EOS at finite temperatures and arbitrary compositions. This framework will allow for more robust and systematic studies of EOS effects in future simulations of binary neutron star merger simulations and core-collapse supernovae. Finally, in Chapter 10, I summarize the main conclusions from this dissertation and discuss the future prospects for constraining the EOS over the next decade.

Each chapter in this dissertation is based on the results of individual studies that I led, but that include valuable contributions from several co-authors and collaborators. At the start of each chapter, I include a citation and acknowledgment of the contributors to the work included in that chapter and, to acknowledge these joint efforts, I will switch to using “we” throughout.

CHAPTER 2

An Optimal Parametrization of the EOS†

We will start with the topic of an optimally parametrized EOS, motivated by the increasing number and precision of measurements of neutron star masses, radii, and, in the near future, moments of inertia. One way to facilitate the mapping of such observables to the EOS is through a parametrization of the latter. In this chapter, we present a generic method for optimizing the parametrization of any physically allowed EOS. In order to test our parametrization as generally as possible, we generate mock EOS that incorporate physically extreme behavior. We then apply our parametrization to these mock EOS and determine the differences in masses, radii, and moments of inertia between the parametrized and the full EOS. We optimize the number of segments included in the parametric EOS by requiring these differences to be smaller than the expected accuracy of observations. We find that sampling the EOS with five fiducial densities that are evenly spaced in the logarithm of density (i.e., using five polytropes) recreates the radii of the assumed EOS to within $\lesssim$0.5 km for the extreme cases and to within $\lesssim$0.12 km for 95% of a sample of 42 proposed EOS with a wide range of input physics. Such a parametrization is also able to reproduce the maximum mass to within $\lesssim 0.04 M_\odot$ and the moment of inertia to within $\lesssim$10% for 95% of the proposed EOS sample.

---

† A version of this chapter has been published previously as Raithel, Özel, and Psaltis (2016). *From Neutron Star Observables to the Equation of State. I. An Optimal Parametrization.* ApJ, 831, 44. We thank Gordon Baym for useful comments on that manuscript and we gratefully acknowledge support from NASA grant NNX16AC56G for this project.

2.1 Optimizing the parametric EOS

We parametrize the EOS in terms of n piecewise polytropes,[1] spaced between two densities, $\rho_{\min}$ and $\rho_{\max}$. We define the dividing density and pressure between each piecewise polytrope to be ρ_i and P_i, respectively. Each polytropic segment is then given by

$$P = K_i \rho^{\Gamma_i} \quad (\rho_{i-1} \leq \rho \leq \rho_i), \tag{2.1}$$

where the constant, K_i, is determined from the pressure and density at the previous fiducial point according to

$$K_i = \frac{P_{i-1}}{\rho_{i-1}^{\Gamma_i}} = \frac{P_i}{\rho_i^{\Gamma_i}} \tag{2.2}$$

and the polytropic index for the segment, Γ_i, is given by

$$\Gamma_i = \frac{\log_{10}(P_i/P_{i-1})}{\log_{10}(\rho_i/\rho_{i-1})}. \tag{2.3}$$

Figure 2.1 shows an example of piecewise polytropes over three density segments, with various values of their polytropic indices, Γ, to illustrate the behavior of eqs. (2.1)-(2.3). Our primary goal in optimizing the parametrization is to reduce the errors in the prediction of observables (i.e., mass, radius, and moment of inertia) below a threshold that is comparable to the uncertainties in present or upcoming observations, while keeping the number of polytropic segments to a minimum. For the optimization process, we produce extreme, albeit physically allowed EOS between $1-8\ \rho_{\rm sat}$ to test how well our parametrizations reproduce observables with various numbers of polytropic segments included. Once our parametrization is optimized, we then apply it to more reasonable, physically motivated EOS to test its ability to recreate those as well.

In addition to the number of polytropes to include in the parametrization, there are two other variables that we have to optimize: the density at which the parametrization should start and the spacing of the polytropic segments. For the question of where to start the parametrization, we explored starting at $\rho_0 = 10^{14}$ g cm^{-3} as well as at $\rho_0 = \rho_{\rm sat}$. It is typically assumed that the EOS is

---

[1] See Appendix A for a discussion of a linearly parametrized EOS.

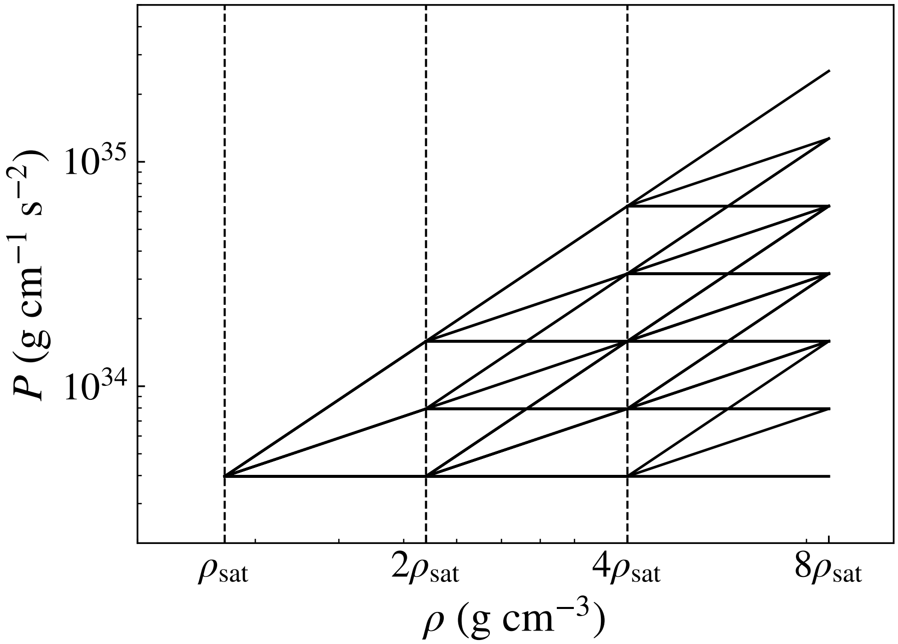

Figure 2.1 Pressure as a function of density for a sample of piecewise polytropes. The equation of state is divided into polytropic segments at three fiducial densities that are uniformly spaced in the logarithm. In each segment, we allow the polytrope in eq. (2.1) to have an index of $\Gamma = 0$, 1, or 2 to illustrate their general behavior.

known up to $\rho_{\rm sat}$; however, Lattimer and Prakash (2001) showed that for a sample of around 30 proposed EOS, the predicted pressures vary by a factor of 5 over the range $0.5\ \rho_{\rm sat} < \rho < \rho_{\rm sat}$, even though these EOS are all meant to be consistent with nuclear physics experiments in this density regime. This is because the extrapolation of pressures from symmetric nuclear matter to neutron-rich matter is poorly constrained. Meanwhile, densities below $\sim 0.5\rho_{\rm sat}$ do not significantly affect the global properties of the star. Therefore, we allowed our parametrization to start at both $0.5\rho_{\rm sat}$ and $\rho_{\rm sat}$, in order to explore these two limits. As for the question of how to space the polytropic segments, the preferred option is to space the segments evenly in the logarithm of the density. A logarithmic spacing more finely samples the low density region of the EOS, which is the region that most affects the resulting neutron star observables (Lattimer and Prakash, 2001; Read et al., 2009a; Özel and Psaltis, 2009). For completeness, we also explored a second possibility: spacing the fiducial densities between each polytropic segment linearly.

We found that the combination of starting the parametrization at $\rho_{\rm sat}$ and spacing the fiducial densities evenly in the logarithm resulted in the smallest errors in mass and radius. We therefore start the first polytrope at $\rho_0 = \rho_{\rm sat}$ and space the remaining fiducial densities evenly in the logarithm between ρ_0 and 7.4 $\rho_{\rm sat}$. We set the last point, $\rho_n = 7.4\ \rho_{\rm sat}$, following the results of Read et al. (2009a) and Özel and Psaltis (2009) who found that the pressure at this density determines the neutron star maximum mass and that pressures at higher densities do not significantly affect the overall shape of the resulting mass-radius curve. We determined the pressure corresponding to each fiducial density by sampling whichever EOS we were parametrizing, i.e., $P_i = P_{\rm EOS}(\rho_i)$. For $\rho \leq \rho_0$, we connected our parametrization to a low-density EOS.

We varied the total number of fiducial densities above $\rho_{\rm sat}$ from 3 to 12. Clearly, as the number of polytropes used to represent the EOS increases, the errors in the observables are expected to reduce. Our goal in the remainder of this chapter is to determine the minimum number of fiducial densities required to reproduce the mass, radius, and moment of inertia of a neutron star to within desired observational uncertainties.

2.2 From EOS to observables

In order to determine how well our parametrizations were able to reproduce the observations predicted by a given EOS, we used the Tolman-Oppenheimer-Volkoff (TOV) equations and solved them to find the mass, radius, and moment of inertia. The TOV equations give the pressure, P, and the enclosed mass, M, of the star as a function of radius, according to eqs. (1.1) and (1.2). Additionally, the energy density, ϵ, is given by

$$d\frac{\epsilon}{\rho} = -P d\frac{1}{\rho}. \tag{2.4}$$

To get the full relation between energy density and mass density, we can integrate eq. (2.4) for $\Gamma \neq 1$ to

$$\epsilon(\rho) = (1+a)\rho c^2 + \frac{K}{\Gamma - 1}\rho^{\Gamma}, \tag{2.5}$$

where a is an integration constant. Along any density section of the EOS, requiring continuity at either endpoint determines a such that eq. (2.5) becomes

$$\epsilon(\rho) = \left[\frac{\epsilon(\rho_{i-1})}{\rho_{i-1}} - \frac{P_{i-1}}{\rho_{i-1}(\Gamma_i - 1)}\right]\rho + \frac{K_i}{\Gamma_i - 1}\rho^{\Gamma_i}, \quad \rho_{i-1} \leq \rho \leq \rho_i \tag{2.6}$$

where K_i and Γ_i are determined as in eqs. (2.2) and (2.3).

Similarly, for the case of Γ=1, eq. (2.4) becomes

$$\epsilon(\rho) = \frac{\epsilon(\rho_{i-1})}{\rho_{i-1}}\rho + K_i \ln\left(\frac{1}{\rho_{i-1}}\right)\rho - K_i \ln\left(\frac{1}{\rho}\right)\rho, \quad \rho_{i-1} \leq \rho \leq \rho_i. \tag{2.7}$$

We used eqs. (2.6) or (2.7) to relate an EOS to the energy density, and then used that energy density to integrate the TOV equations outwards from the center of the star. The radius at which the pressure becomes negligible gives the total mass and radius of the star.

In order to calculate the moment of inertia, we simultaneously solved eqs. (4.1) and (4.2) with two coupled differential equations for the relativistic moment of inertia,

$$\frac{\mathrm{d}I}{\mathrm{d}r} = \frac{8\pi}{3}\frac{(\epsilon + P)}{c^2}\frac{fjr^4}{1 - 2\frac{GM}{rc^2}}, \tag{2.8}$$

and

$$\frac{\mathrm{d}}{\mathrm{d}r}\left(r^4 j \frac{\mathrm{d}f}{\mathrm{d}r}\right) + 4r^3\frac{\mathrm{d}j}{\mathrm{d}r}f = 0, \tag{2.9}$$

where $f(r) \equiv 1 - \frac{\omega(r)}{\Omega}$, $j \equiv e^{-\nu/2}(1 - 2GM/rc^2)^{1/2}$, $\omega(r)$ is the rotational frequency of the local inertial frame at radius r, and Ω is the spin frequency of the star. The boundary conditions for the second-order partial differential eq. (4.5) are

$$\left[\frac{df}{dr}\right]_{r=0} = 0 \tag{2.10}$$

and

$$f(r = R_{\mathrm{NS}}) = 1 - 2\frac{G}{c^2}\frac{I}{R_{\mathrm{NS}}^3}. \tag{2.11}$$

To solve these coupled equations, we integrated eqs. (4.4) and (4.5) outwards from the center of the star, using eq. (4.6) as one boundary condition, and iterated it to find the value of f_0 for which eq. (4.7) is valid.

In this way, we determined the mass, radius, and moment of inertia for a given equation of state.

2.3 Generating mock equations of state

In order to be as general as possible and go beyond the current sample of proposed equations of state, we tested our parametrization on a sample of mock EOS that incorporated extreme but physically allowed behavior, with the hypothesis that if our parametrization could accurately capture these extreme cases, then it would be able to reproduce more reasonable EOS as well.

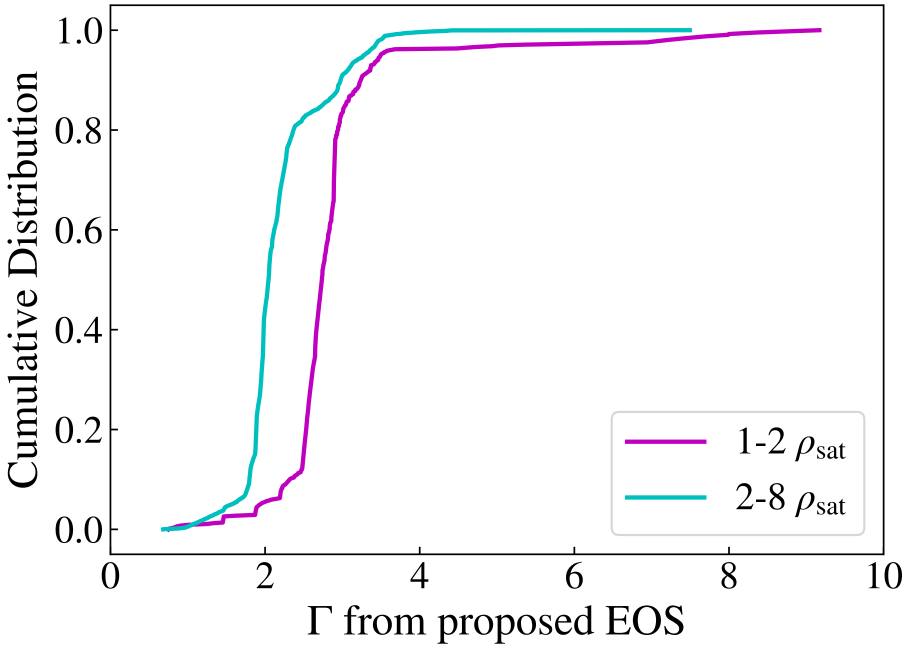

Figure 2.2 Cumulative distribution of polytropic indices, Γ, calculated at all tabulated densities in a given range in a sample of 49 proposed EOS. We found that the majority of polytropic indices lie between $\Gamma \sim 1$ and $\Gamma \sim 5$ and we therefore set the two extreme polytrope options in our mock EOS to have these indices.

For our mock EOS, we assumed the true EOS of neutron stars to be well known up to the nuclear saturation density. We then divided the high-density regime, from 1-8 $\rho_{\rm sat}$, into 15 segments that were evenly-spaced in the logarithm of the density, so that each segment would be small relative to the overall range of densities. The logarithmic sampling also sampled the lower density region better and thus allowed more variability in the region that most affects the global properties of the star (Lattimer and Prakash, 2001; Read et al., 2009a; Özel and Psaltis, 2009). In each of the 15 segments, we allowed our mock equation of state to be one of two extremes, which we describe below (see § 2.4 for the addition of phase transitions to these mock EOS).

We set both the upper and lower extremes of each segment to be polytropes. To determine the polytropic index of each, we looked at a sample of 49 proposed equations of state. This sample of EOS was compiled in order to include a wide variety of physics and calculation methods, as in Read et al. (2009a). Using the tabular data for each of these EOS, we calculated the polytropic indices for all adjacent sets of pressure and density using eq. (2.3) for two density ranges. The cumulative distribution of the resulting polytropic indices is shown in Figure 2.2. We found that the majority of polytropic indices fell between Γ=1 and 5; therefore, we set our nominal upper and lower extremes to have these indices and allowed any sequence of polytropic indices across our density range.

There is, however, an absolute upper bound on the allowed polytropic index that is set by the condition of causality, which requires that the pressure gradient inside a neutron star obey the relation

$$\frac{dP}{d\epsilon} \equiv \left(\frac{c_s}{c}\right)^2 \leq 1, \tag{2.12}$$

where c_s is the local sound speed.

We can use this relation to derive the corresponding bound on Γ by noting that we can write eq. (2.12) as

$$\frac{dP}{d\epsilon} = \frac{dP}{d\rho}\left(\frac{d\epsilon}{d\rho}\right)^{-1} = \left(\frac{c_s}{c}\right)^2. \tag{2.13}$$

For a polytrope, $dP/d\rho = \Gamma P/\rho$, and the mass density-energy density relation of eq. (2.4) can be expanded to

$$\frac{d\epsilon}{d\rho} = \frac{1}{\rho}\left(\epsilon + P\right). \tag{2.14}$$

The polytropic index can therefore be written as

$$\Gamma = \frac{c_s^2}{c^2}\frac{\epsilon + P}{P} \leq \frac{\epsilon + P}{P} \equiv \Gamma_{\text{luminal}}. \tag{2.15}$$

In order to ensure that our upper extreme did not violate causality, we set our upper polytropic index to be the minimum of $\Gamma = 5$ and Γ_{luminal}.

With this set of steps, we obtained the pressure, mass density, and energy density for each segment of our mock equations of state. The mock EOS start at ρ_{sat}, so once the pressure at this density is determined, the above relations will uniquely determine the rest of the behavior of each mock EOS. We introduced further freedom in our mock EOS by allowing two significantly different pressures at the starting point, ρ_{sat}. This is motivated by the fact that such a bifurcation is also seen among the set of proposed EOS. We used the EOS SLy (Douchin and Haensel, 2001) and PS (Pandharipande and Smith, 1975) to determine the lower and higher starting pressures, respectively.

With 15 density-segments, two options for the polytropic behavior along each segment, and two options for the starting pressure, our algorithm produced 2×2^{15} = 65,536 different mock EOS against which we could test our parametrization. However, we excluded any mock EOS that were too soft to produce a 1.9 $M_\odot$ neutron star (Demorest et al., 2010; Antoniadis et al., 2013), reducing our final sample size to 53,343.

2.3.1 The mock EOS

The 53,343 extreme mock equations of state that reached 1.9 $M_\odot$ are shown in Figure 2.3.

All possible trajectories through this grid are indeed included, with the constraint that pressure must always increase with density (i.e., only monotonic behavior in this grid is allowed). The broadening of the mock EOS at high pressures is a result

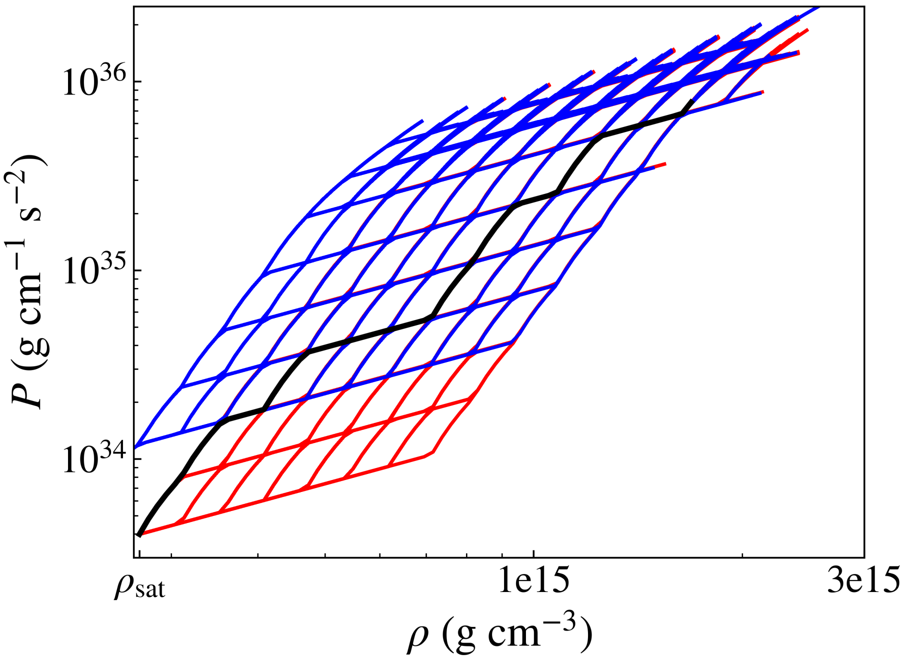

Figure 2.3 The grid of 53,343 extreme, mock equations of state, starting at nuclear saturation density with a pressure corresponding to either the EOS SLy (in red) or PS (in blue). One sample mock EOS is shown bolded in black. Each mock EOS is composed of 15 segments that are spaced evenly in the logarithm between 1 and 8 $\rho_{\rm sat}$. Each segment is a polytrope with either Γ=1 or the minimum of Γ=5 and $\Gamma_{\rm luminal}$. Only EOS that reach 1.9 $M_\odot$ are shown here, leading to the absence of segments in the lower right corner of the parameter space.

of our requirement that the upper polytropic limit must be the minimum of Γ=5 and $\Gamma_{\rm luminal}$.

The corresponding mass-radius curves, calculated according to the method described in § 2.2, are shown in Figure 2.4. As Figure 2.4 demonstrates, starting the mock EOS at the two different pressures corresponding to the two families of proposed EOS allowed us to fully span the range of reasonable radii. With this choice, we achieved a dense sampling of mass-radius curves that span radii from $\sim$ 9-17 km for $M \lesssim 1\ M_\odot$. Furthermore, the mock mass-radius curves include curves that shallowly slope upwards, that are nearly vertical, and that bend backwards, indicating that we have sampled a wide range of possible underlying behavior.

The trend of increasing maximum mass with radius is a result of our causality

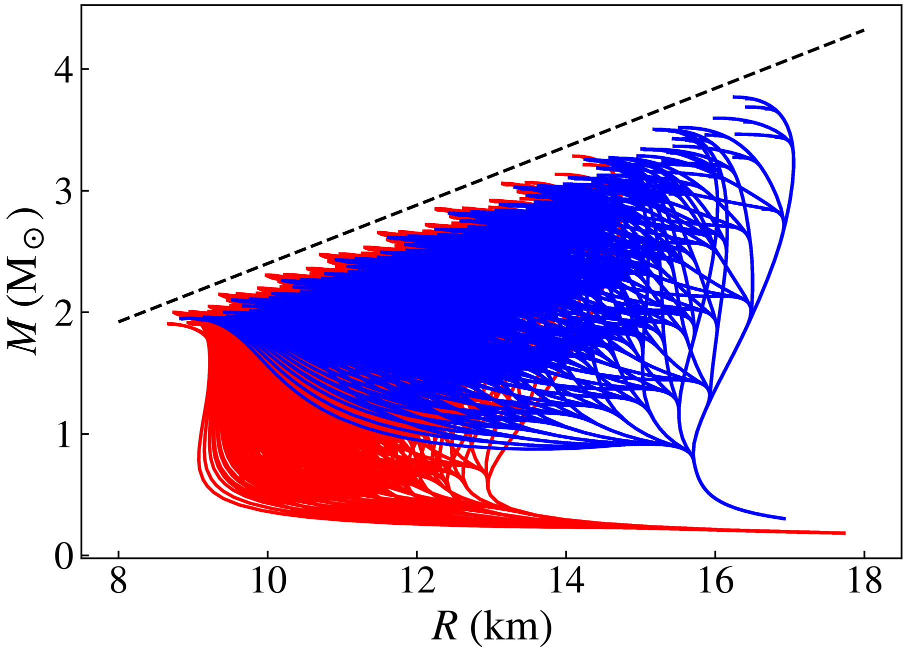

Figure 2.4 Mass-radius curves corresponding to the 53,343 mock EOS shown in Figure 2.3. The red curves are those that started at $\rho_{\rm sat}$ with the corresponding pressure of the EOS SLy; the blue curves use the nuclear saturation pressure of EOS PS. By including both starting pressures in our sample, we are able to densely sample a realistic range of radii of $\sim$ 9-17 km. These mass-radius curves also show a wide range of slopes, indicating that a large range of underlying physics is incorporated in this sample. The dashed line shows the causal relationship of $M_{\rm max} \sim 0.24R(M_\odot/{\rm km})$, derived by Lindblom (1984). The small discrepancy between this line and the observed cutoff in our M-R curves can be attributed to the different EOS that was assumed in the low-density region of the Lindblom (1984) analysis.

constraint. Lindblom (1984) derived the maximum gravitational redshift of a neutron star as a function of mass by assuming that the equation of state is trusted up to $3{\times}10^{14}$g cm^{-3} and configuring the resulting mass of the star to maximize the redshift. As in our analysis, that study required that the relationship between pressure and density inside the star not violate causality. After converting their relationship between the mass and maximum gravitational redshift to a mass-radius relationship, we find that the corresponding relationship of $M_{\rm max} \sim 0.24R(M_\odot/{\rm km})$, shown as the dashed line in Figure 2.4, is very close to what is seen in our mock EOS. The small differences between this relationship and that in our mock EOS can be attributed to the different EOS assumed up to the first fiducial density: Lindblom (1984) assumed the EOS BPS, while we assumed either SLy or PS. Furthermore, they assumed their EOS up to 3×10^{14} g cm^{-3}, while we assumed SLy or PS only up to $\rho_{\rm sat} \sim 2.7 \times 10^{14}$ g cm^{-3}.

2.3.2 Determining the goodness of the parametric representation

We quantified how well our parametrization represented the full EOS and chose the optimal number of sampling points by comparing the radii of our results to those found using the full EOS at three fiducial masses, M=1.4, 1.6, and 1.8 $M_\odot$. We also calculated $\Delta M_{\rm max} \equiv |M_{\rm max}(\text{full}) - M_{\rm max}(\text{parametric})|$ to determine how well our parametrization reproduced the maximum mass predicted by the full EOS. Finally, we calculated the difference in the moment of inertia, $\Delta I_{\rm A}$, predicted by our parametrization and by the full EOS for a star of mass $M = 1.338\ M_\odot$, i.e., the mass of the Pulsar A in the binary system PSR J0737−3039.

Given the typical uncertainties in the mass, radius, and moment of inertia, either with current data or with those expected in the near future, our goal was to reproduce the radii to within half a kilometer, i.e., to require $\Delta R < 0.5$ km at each of the three critical masses. We also required $\Delta M_{\rm max} < 0.1\ M_\odot$. Because the moment of inertia for Pulsar A has not yet been measured, we did not impose strict requirements on $\Delta I_{\rm A}$, but still included this observable in our results to see qualitatively how well it compares to some reasonable predictions for $I_{\rm A}$.

2.3.3 Results of parametrization of mock EOS

Figure 2.5 shows the cumulative distribution of residuals in radius and mass for when various numbers of polytropic segments were included in the parametrization for our full sample of 53,343 extreme mock EOS. We found that our goal of $\Delta R <$ 0.5 km was achieved by sampling the EOS with 5 fiducial densities above $\rho_{\rm sat}$ (i.e., including 5 polytropes). Specifically, using 5 fiducial densities, we found that for 95% of the mock EOS, $\Delta R = 0.50$, 0.44, and 0.48 km at $M = 1.4$, 1.6 and 1.8 $M_\odot$,

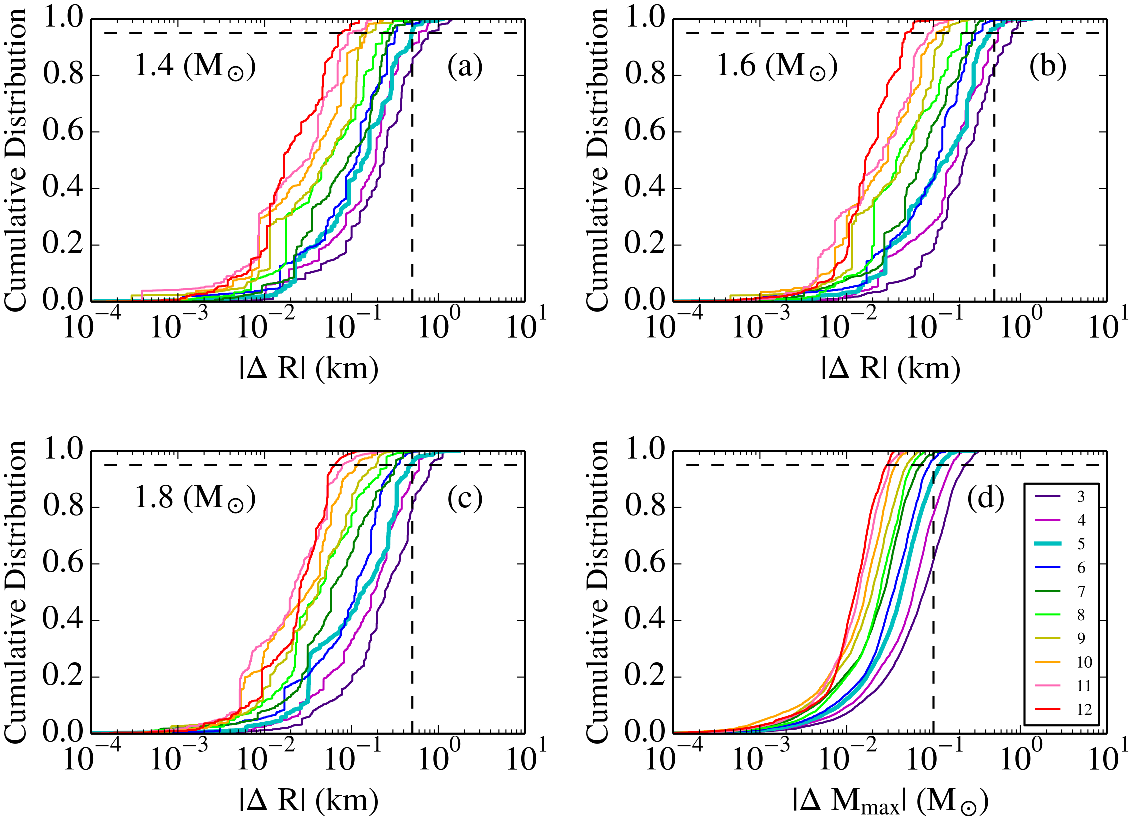

Figure 2.5 *(a)-(c):* Cumulative distributions of the differences in radii between our parametrization and the full EOS for all mock EOS shown in Figure 2.4. The different colors represent the number of fiducial densities above $\rho_{\rm sat}$ (i.e., the number of polytropic segments included in the parametrization). The radius residuals are measured at 1.4, 1.6, and 1.8 $M_\odot$, respectively. The vertical dashed lines mark a residual of 0.5 km; the horizontal dashed lines mark the 95% level of the cumulative distribution. We find that our goal of residuals ≤0.5 km is achieved with 5 fiducial densities. *(d):* Cumulative distribution of the difference in maximum mass between our parametrization and the full EOS. The lines and colors are as for the other three panels, but here the vertical dashed line is shown at 0.1 $M_\odot$, corresponding to our desired maximum residual. This goal is also approximately achieved with 5 fiducial densities.

respectively. In addition, a parametrization with 5 fiducial densities reproduced $M_{\rm max}$ to within 0.12 $M_\odot$ in 95% of the cases.

We also calculated the difference in the moment of inertia for a neutron star with the same mass as Pulsar A in the double pulsar system, i.e., $M_A = 1.338 M_\odot$. The cumulative distribution of these residuals as a function of the number of polytropes included in the parametrizations is shown in Figure 2.6. By sampling the EOS at 5 fiducial densities, we found that the residuals in moment of inertia are less than 0.17×10^{45}g cm^2 in 95% of the cases. The moment of inertia for Pulsar A is expected to be on the order of 10^{45}g cm^2 and is expected to be measured with 10% accuracy (Kramer and Wex, 2009). As a result, depending on the exact value of the forthcoming moment of inertia measurement, 5-6 fiducial densities may be required to recreate the moment of inertia to the 10% accuracy level.

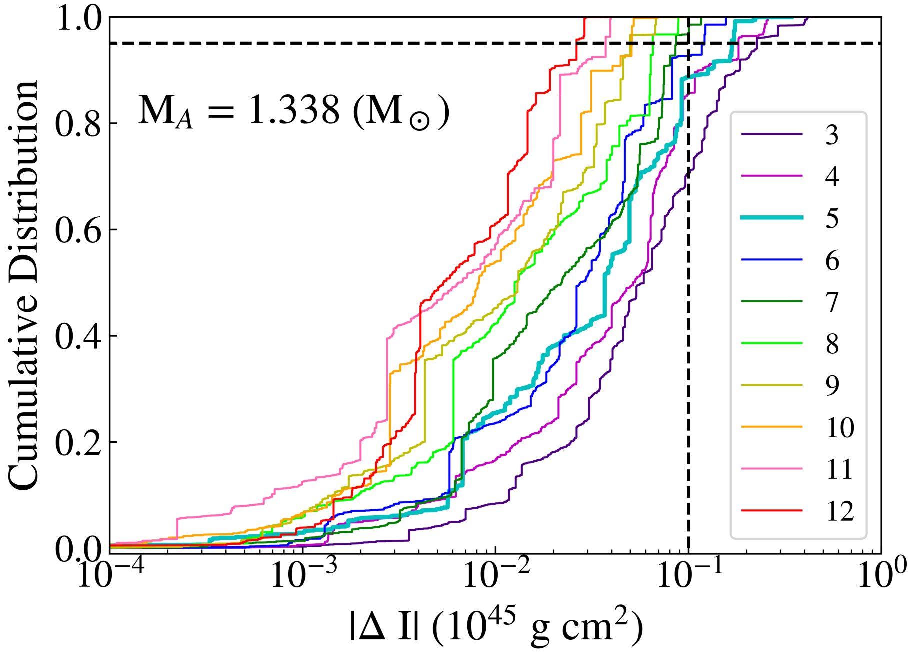

Figure 2.6 Cumulative distribution of the differences in moment of inertia for a star of mass $M_A = 1.338\ M_\odot$, calculated between our parametrization and the full EOS. The different colors represent the number of fiducial densities above ρ_{sat} that we included in our parametrization (i.e., the number of polytropic segments). The vertical dashed line marks a residual of 10% for a hypothetical moment of inertia measurement of 10^{45} g cm^2; the horizontal dashed lines mark the 95% level of the cumulative distribution. With 5 fiducial densities, the moment of inertia residuals are less than 0.17 $\times 10^{45}$ g cm^2 in 95% of cases. We therefore find that, depending on the exact value of the upcoming measurement of the moment of inertia for Pulsar A in the double pulsar system, 5-6 fiducial densities may be needed to reproduce I_A to the 10% accuracy level.

Even a parametrization with just 3 fiducial densities reproduced the radii of

$\sim$80% of our extreme mock EOS to within 0.5 km. However, requiring $\Delta M_{\rm max} < 0.1 M_\odot$ and $\Delta\ I/I \lesssim 10\%$ requires more points. We therefore conclude that, given the most recent observational uncertainties and the continuing prospects for even smaller errors in the near future, a parametrization that samples the EOS at 5 fiducial densities is optimal. Specifically, we recommend spacing the five fiducial densities evenly in the logarithm of the density, such that $(\rho_0, \rho_1, \rho_2, \rho_3, \rho_4, \rho_5) = (1.0, 1.4, 2.2, 3.3, 4.9, 7.4)\ \rho_{\rm sat}$.

2.4 Adding phase transitions to the mock EOS

We also considered more diverse equations of state by allowing there to be a first-order phase transition in the mock EOS described in § 2.3. We allowed only one phase transition per mock EOS, but allowed the phase transition to start in any of our 15 density segments and to last anywhere between 1 and 15 segments. For the remaining segments, the mock EOS was polytropic with an index of Γ=1 or the minimum of Γ=5 and $\Gamma_{\rm luminal}$, as above. With the addition of these phase transitions, there are now $2^N \times N(N+1)/2$ possibilities for N segments of the EOS, for each possible starting pressure. For 15 segments and our two starting pressures (corresponding to the EOS SLy and PS at $\rho_{\rm sat}$), this corresponds to 7,864,320 possibilities for the mock EOS.

We randomly sampled $\sim$175,000 of these mock EOS, with roughly half starting at each of the initial pressures. We then applied our parametrization to each mock EOS. As we did for the original set of mock EOS, we varied the number of polytropic segments in the parametrization between 3 and 12 and calculated the resulting residuals in radius, mass, and moment of inertia. The mass and radius residuals are shown in Figure 2.7. With 5 fiducial densities above $\rho_{\rm sat}$, i.e., the optimal number of polytropic segments found in § 2.3.3, we found that 95% of the radius residuals were less than 0.48, 0.43, and 0.46 km at 1.4, 1.6, and 1.8 $M_\odot$, respectively. These errors are comparable to those from the mock EOS without phase transitions. We also found that 95% of the differences in maximum mass were less than 0.22 $M_\odot$, which is

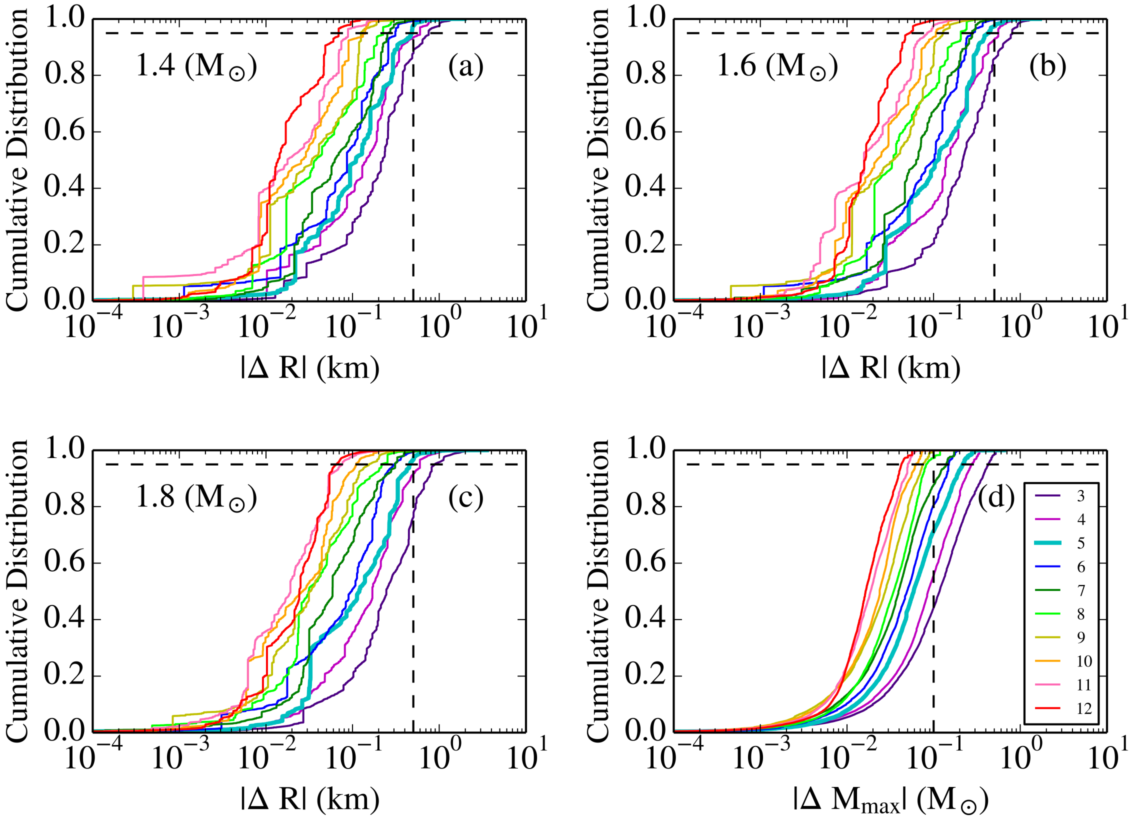

Figure 2.7 Same as Figure 2.5 but for 176,839 randomly sampled mock EOS, each of which include a single first-order phase transition. Approximately half of this sample of mock EOS starts at a pressure corresponding to the EOS SLy at $\rho_{\rm sat}$, while the other half starts at the pressure predicted by the EOS PS at $\rho_{\rm sat}$. We find that a parametrization with five fiducial densities above $\rho_{\rm sat}$ (i.e., five polytropic segments) is sufficient to reproduce the radii at our three fiducial masses to within less than 0.5 km in 95% of cases. The errors in maximum mass are significantly worse than for the sample of mock EOS without phase transitions: 95% of this sample has $\Delta M_{\rm max} < 0.22 M_\odot$ or less.

a larger error than in our previous, less extreme sample of mock EOS. However, 70% of the errors in maximum mass were still less than 0.1 $M_\odot$ for this sample, indicating that this parametrization reasonably recreated the maximum mass for many of our most extreme sample of mock EOS. The error distribution for the moment of inertia was almost identical to the distribution for the sample without phase transitions. We found that a parametrization with 5 fiducial densities reproduced the moment of inertia to within 0.17 $\times 10^{45}$ g cm^2 for 95% of the mock EOS with phase transitions.

The tail end of all four distributions in Figure 2.7 extended to higher errors than did the tail in Figure 2.5. This is because the arbitrarily-placed phase transitions in this sample of mock EOS can make the resulting mass-radius curve have very sharp turn-overs. If a sharp turn-over occurs near one of the fiducial masses at which we measure radius residuals, we will infer an artificially high error. However, the distributions in Figure 2.7 show that the probability of the true EOS falling in this tail is small ($\lesssim$ 5% with 5 fiducial densities). We therefore find that, for the vast majority of cases, a parametrization that samples the EOS at 5 fiducial densities is sufficient to reproduce radius and maximum mass observables to within 0.5 km and 0.1-0.2 $M_\odot$, even if the EOS contains a first-order phase transition at an arbitrary density and over an arbitrary range.

2.5 Application of the parametrization to physically-motivated EOS

Even though we optimized our parametrization using EOS that span a much wider range of possibilities than the currently proposed ones, we nevertheless explored how well this parametrization reproduced the physically-motivated EOS found in the literature. To this end, we applied our optimized parametrization (5 fiducial densities above $\rho_{\rm sat}$) to a sample of 42 proposed EOS,[2] which incorporate a variety of different physical possibilities and calculation methods. (The tabular data for these EOS are compiled in Cook et al. 1994; Lattimer and Prakash 2001; Read et al. 2009a; and Özel and Freire 2016). Our sample included purely nucleonic equations of state, such as: relativistic (BPAL12 and ENG) and nonrelativistic (BBB2) Brueckner-Hartree-Fock EOS; variational-method EOS (e.g. FPS and WFF3); and a potential-method EOS (SLy). We also include models which incorporate more exotic particles, including, for example, a neutron-only EOS with pion condensates (PS), a relativistic mean-field theory EOS with hyperons and quarks (PCL2), and an effective-potential EOS with hyperons (BGN1H1).

---

[2] This sample is smaller than the 49 EOS that we previously cited because we exclude from this subsample any calculated EOS that become acausal, except for the EOS AP4. Even though AP4 reaches a local sound speed of $c_s \sim 1.1c$ by densities of $\rho \sim 6\ \rho_{\rm sat}$ and becomes more acausal thereafter, we do include this EOS, as it is commonly used and included in the literature. We also exclude from this sample two EOS that are not calculated to high enough densities to accommodate our parametrization at 7.4 $\rho_{\rm sat}$.

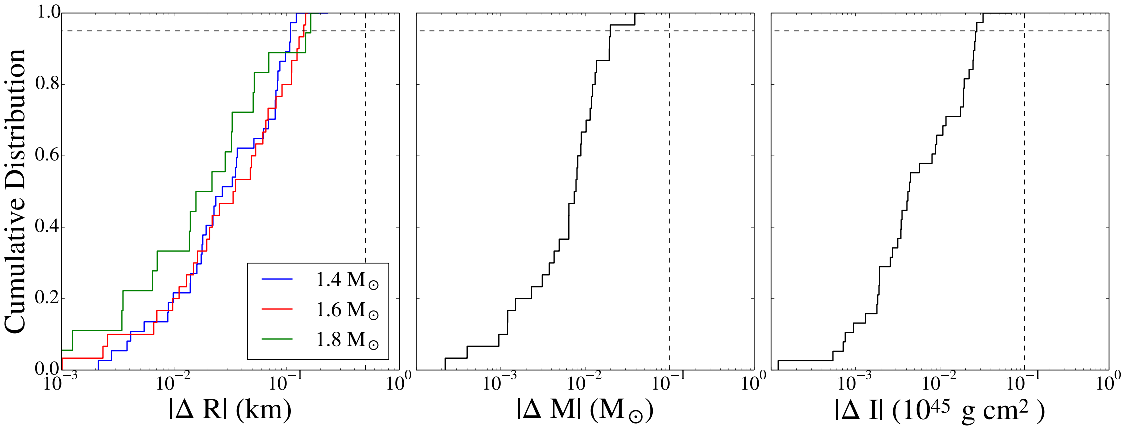

Figure 2.8 Cumulative distribution of the residuals measured between the full EOS and the parametric version for 42 proposed EOS. The parametrization uses 5 fiducial densities above $\rho_{\rm sat}$ (i.e., it includes 5 polytropic segments). *Left panel:* Residuals in radius, as calculated at 1.4, 1.6, and 1.8 $M_\odot$. The vertical dashed line indicates residuals of 0.5 km, while the horizontal line shows the 95% inclusion level (this 95% inclusion line is identical in all three panels). We find that the residuals are less than 0.10, 0.12, and 0.09 km at 1.4, 1.6, and 1.8 $M_\odot$ respectively for 95% of the proposed EOS. *Middle panel:* Differences in maximum mass. The vertical dashed line indicates residuals of 0.1 $M_\odot$. We find that the errors in maximum mass are less than 0.04 $M_\odot$ for 95% of the proposed EOS. *Right panel:* Differences in the moment of inertia for a star of mass $M_A = 1.338 M_\odot$. The vertical dashed line indicates residuals of 10% for a hypothetical moment of inertia measurement of 10^{45} g cm^2. We find that 95% of the proposed EOS have residuals in the moment of inertia of 0.02×10^{45} g cm^2 or smaller.

In applying our parametrization to these proposed EOS, we no longer connected to SLy or PS for $\rho < \rho_{\rm sat}$. Instead, we assumed that each EOS is known up to $\rho_{\rm sat}$, and we therefore used the full EOS that we were parametrizing for the low-density regime. For $\rho > \rho_{\rm sat}$, we applied our parametrization as above. After applying our parametrization, we calculated the resulting residuals in radii at the three fiducial masses,[3] the maximum mass, and the moment of inertia. The residuals for our optimized, 5-polytrope parametrization are shown in Figure 2.8.

---

[3] For every EOS, we only calculated and included the radius resdiual at a given mass if the EOS

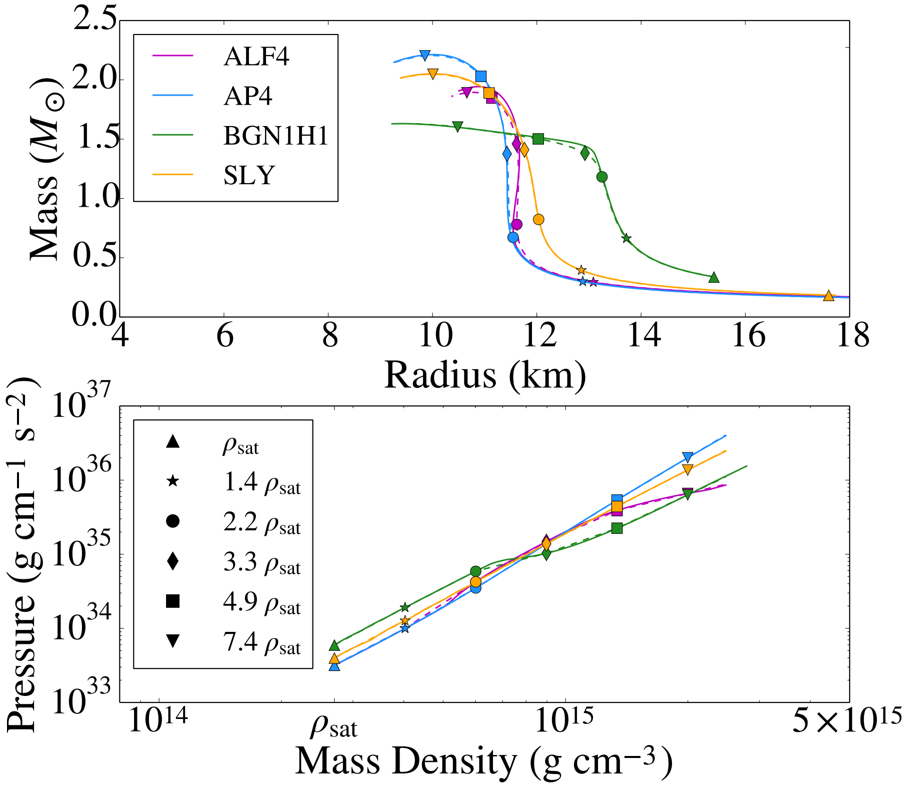

Figure 2.9 *Top:* Mass-radius relations for the EOS AP4, AL4, BGN1H1, and SLy as solid lines. The dashed lines show our parametrization of each, with five fiducial densities above $\rho_{\rm sat}$. The different symbols represent the mass and radius of a star with a central density equal to each fiducial density. *Bottom:* Pressure as a function of mass density for these EOS. The symbols represent the location of each fiducial density. We find that this parametrization reproduces the EOS to very high accuracy in mass-radius space.

The errors in applying the parametrization to the proposed, physically motivated EOS were much lower than for the more extreme, mock EOS. Our optimized parametrization reproduced the radii of ~95% of the proposed EOS to within 0.10, 0.12, and 0.09 km (at 1.4, 1.6, and 1.8 $M_\odot$, respectively) and the maximum masses of 95% of the EOS to within 0.04 $M_\odot$. As examples, we show in Figure 2.9 the full mass-radius relation as well as the one calculated from our parametrized EOS for

---

actually reaches that mass. If, for example, an EOS only produces masses up to 1.7 $M_\odot$, we still included the radius residuals at 1.4 and 1.6 $M_\odot$ and simply excluded the data point at 1.8 $M_\odot$.

several proposed EOS: AP4 (nucleonic), ALF4 (quark hybrid), SLy (nucleonic), and BGN1H1 (includes hyperons). As seen here, the differences in mass-radius space are extremely small.

2.6 Conclusions

In this chapter, we investigated an optimal parametrization of the neutron star equation of state that can be used to interpret neutron star observations. We found that a parametric EOS with five polytropic segments evenly spaced in logarithm between 1 and 7.4 $\rho_{\rm sat}$ was sufficient to reproduce the radii of proposed EOS to within 0.12 km and the maximum mass to within 0.04 $M_\odot$ in 95% of cases. This parametrization was also able to reproduce the radii of our more extreme, mock EOS to within 0.5 km, suggesting that even if a more extreme EOS is proposed or realized in nature, our parametrization will be robust enough to reproduce it well.

The radii of approximately fifteen neutron stars have already been measured, for most of which the masses are also known (Guillot et al., 2013; Guillot and Rutledge, 2014; Heinke et al., 2014; Nättilä et al., 2016; Özel et al., 2016; Bogdanov et al., 2016). Even though the uncertainties in the individual radius measurements are of order $\sim$2 km, combining all the measurements leads to a rather narrow range of predicted neutron star radii. Moreover, these spectroscopic measurements will be independently checked in the near future by, e.g., waveform modeling with NICER (Gendreau et al., 2012). The forthcoming measurement of the moment of inertia, which is a higher-order moment of the mass distribution of the star (Lyne et al., 2004; Kramer and Wex, 2009), and the prospect of eventual measurements of other higher-order moments using gravitational wave observations from coalescing neutron stars (e.g., Read et al. 2009b; Del Pozzo et al. 2013; Agathos et al. 2015) will provide additional constraints. Finally, the recent mass mesaurements of approximately two-solar mass neutron stars (Demorest et al., 2010; Antoniadis et al., 2013) already place strong priors on empirically inferred EOS.

Previous empirical inferences of the equation of state based on existing observations typically relied on functional forms with 3-4 parameters (e.g., Özel et al. 2010a; Steiner et al. 2010; Özel et al. 2016; Steiner et al. 2016). It is difficult to compare the errors produced in these parametrizations directly to our own, as they are not always quantified in mass-radius space. Read et al. (2009a) report errors in their parametrization in pressure vs. density: they find that a four-parameter EOS produced average errors in $\log P$ of 0.013, which corresponds to a fractional error in pressure of $\sim$3%. Similarly, Lindblom and Indik (2012) report errors in their spectral parametrization in energy density vs. enthalpy space: their errors ranged from 1 to 15% when they used $4-5$ spectral parameters. Finally, Steiner et al. (2013) performed a preliminary comparison between five different types of models (e.g., a parametrization of two polytropes and one with four line segments) and found the largest difference in the predicted radii between any two of their models to be 0.8 km; however, these models were not necessarily optimized in terms of the number of parameters.

Ultimately, it is the inverse process of what we have shown that will be of interest: the inference of a parametric EOS from astrophysical measurements. We will address this aspect of the problem in Chapter 3. However, our work here suggests that the uncertainties in the inference of the EOS will be dominated by the quality of the data and the uncertainties in the inversion process itself, rather than those introduced by the parametrization of the EOS.

CHAPTER 3

Bayesian Inference of EOS Pressures†

With this optimally parametrized EOS now in hand, the parameters can be determined using a Bayesian inference scheme. In this chapter, we perform the natural next step to Chapter 2: using Bayesian statistical techniques to infer the pressures of our optimized five-polytrope parameterization given samples of simulated astrophysical measurements. We start in § 3.1 with an introduction to the Bayesian methods that we will use in this chapter. In §3.2, we test the Bayesian inference on a number of equations of state, ranging from simple polytropes to complex EOS with significant phase transitions. We also aim to characterize the effect of measurement uncertainties on our inferred pressures. The role of such uncertainties in the EOS inference has also been considered by, e.g., Steiner et al. (2016) and Alvarez-Castillo et al. (2016). Here, we will consider the effect of measurement uncertainties within the framework of our own parametrization, focusing in particular on the errors associated with each inferred pressure for a variety of EOS and we compare the errors introduced by both the three- and five-polytrope parameterizations.

We find that, if one wants to be fully agnostic about the physics of the EOS at high densities, the full five-polytrope parametrization must be used. This is the only way to ensure that complex structure and/or significant phase transitions are allowed in the inferred EOS. However, if the true EOS is relatively simple or even a single polytrope, the five-polytrope model will lead to over-parametrization. We find that a regularizer can help reduce the effects of the over-parametrization, while still allowing the complexity that is the benefit of the five-polytrope model. Finally, in either case, it is important to use the full five- (or three-) dimensional posterior likelihoods rather than a marginalization, which, as we demonstrate in §3.3, can introduce biases as large as 1 km.

---

†A version of this chapter has been published previously as Raithel, Özel, and Psaltis (2017). *From Neutron Star Observables to the Equation of State. II. Bayesian Inference of Equation of State Pressures.* ApJ, 844, 156. During this work, CR was supported by NSF Graduate Research Fellowship Program Grant DGE-1143953, FO acknowledges support from a fellowship from the John Simon Guggenheim Memorial Foundation, and DP acknowledges support from the Radcliffe Institute for Advanced Study at Harvard University.

3.1 Bayesian inference of EOS pressures

In order to infer the pressures of our parametric EOS, we follow the Bayesian approach of Özel et al. (2016), which we recreate below. (For a similar analysis, see Steiner et al. 2010). The pressures of interest are those at our five fiducial densities, which, as described in Chapter 2, completely determine our piecewise-polytropic EOS.

The posterior that a particular realization of our parametric EOS correctly describes a set of data can be written as

$$P(\mathrm{EOS}|\mathrm{data}) = P(P_1, P_2, P_3, P_4, P_5|\mathrm{data}). \tag{3.1}$$

By Bayes' theorem, we can rewrite this as

$$P(P_1, P_2, P_3, P_4, P_5|\mathrm{data}) = C P(\mathrm{data}|P_1, ..., P_5) \times P_p(P_1, ..., P_5), \tag{3.2}$$

where C is a normalization constant, $P_p(P_1, ..., P_5)$ is the prior on the set of five pressures, and

$$P(\mathrm{data}|P_1, ..., P_5) = \prod_{i=1}^{N} P_i(M_i, R_i|P_1, ..., P_5) \tag{3.3}$$

is the likelihood of a particular realization of N total mass-radius observations, given a set of EOS parameters.

To calculate the likelihood of observing a particular value of (M, R) given an EOS, we compute the probability that the observation is consistent with each point along the predicted M-R curve, and then take the maximum likelihood. That is, we calculate

$$P_i(M_i, R_i|P_1, ..., P_5) = P_{\max}(M_i, R_i|P_1, ..., P_5, \rho_c), \tag{3.4}$$

where we have used the central density, ρ_c, to parametrize the mass-radius curve. In the limit of small errors in either M or R, this method is equivalent to taking the "closest approach" of the curve to the data point.

Finally, the likelihood that an observation of (M_i, R_i) is consistent with a point on the mass-radius curve is given by

$$P_i(M_i, R_i|P_1, ..., P_5, \rho_c) = \frac{1}{2\pi\sigma_{R_i}\sigma_{M_i}} \exp\left\{-\frac{[M_i - M_{\rm EOS}(\rho_c)]^2}{2\sigma^2_{M_i}} - \frac{[R_i - R_{\rm EOS}(\rho_c)]^2}{2\sigma^2_{R_i}}\right\}, \tag{3.5}$$

where σ_{R_i} and σ_{M_i} are the measurement uncertainties associated with the radius and mass, respectively. Here, $R_{\rm EOS}(\rho_c)$ and $M_{\rm EOS}(\rho_c)$ are the radius and mass predicted by the set of pressures, $(P_1, ..., P_5)$, that comprise our parametrized EOS for a particular central density, ρ_c. In order to populate the five-dimensional posterior of eq. (3.2), we use Markov-Chain Monte Carlo simulations following the Metropolis-Hastings algorithm.

3.1.1 Priors on the pressures

For the priors on $(P_1, ..., P_5)$ in eq. (3.2), we employ constraints from physical principles, laboratory nuclear physics experiments, and astrophysical observations. Specifically, we require that:

(1.) The EOS be microscopically stable, i.e.,

$$P_i \ \leq \ P_{i+1}. \tag{3.6}$$

(2.) The EOS remain causal between the fiducial densities, i.e.,

$$\frac{dP}{d\epsilon} = \frac{c_s^2}{c^2} \leq 1, \tag{3.7}$$

where c_s is the local sound speed.

(3.) Each EOS produce a neutron star with a mass of at least 1.97 $M_\odot$, in order to be within 1 σ of the mass measurement of the most massive neutron stars (Antoniadis et al., 2013; Fonseca et al., 2016).

(4.) Pressures $P_1 \geq 3.60$ MeV/fm^3 and $P_2 \geq 11.70$ MeV/fm^3, in order to be consistent with nuclear physics experiments.

Constraint (4) provides lower limits on the pressures at the first two fiducial densities. As noted in Özel et al. (2016), important constraints on the EOS in the density regime around ρ_{sat} are obtained through nucleon-nucleon scattering experiments at energies below 350 MeV and from the properties of light nuclei. Results from such experiments can be extended by assuming two- and three-body potentials at densities near ρ_{sat} (Akmal et al., 1998). However, the interactions at higher densities cannot be written in terms of static few-body potentials. We, therefore, impose this nuclear physics constraint only on the pressures at our two lowest fiducial densities: $\rho_1 = 1.4\ \rho_{\mathrm{sat}}$ and $\rho_2 = 2.2\ \rho_{\mathrm{sat}}$. Because the three-nucleon interaction is always repulsive, the most model-independent lower limit uses only the two-nucleon interaction. Using the Argonne AV8 two-nucleon pressure as calculated in Gandolfi et al. (2014), we find $P(\rho_1)$=3.60 MeV/fm^3 and $P(\rho_2)$=11.70 MeV/fm^3. The AV8 potential is a simplified version of the Argonne AV18 potential (Wiringa et al., 1995); however, as noted in Özel et al. (2016), the two-nucleon interaction pressures are approximately the same for either version of the potential.

3.1.2 Regularizers

We also include a regularizer in our prior distributions, in order to reduce the tendency of our model to over-parameterize simple EOS. The regularizer, ξ, is Gaussian over the second logarithmic derivative of the EOS, i.e.,

$$\xi = \exp\left[-\frac{(d^2(\ln P)/d(\ln\rho)^2)^2}{2\lambda^2}\right], \tag{3.8}$$

where λ is the characteristic scale. We determine a suitable value for λ by calculating $d^2(\ln P)/d(\ln\rho)^2$ at our fiducial densities for a sample of 49 proposed EOS. This sample of EOS was compiled from the literature in order to incorporate a wide variety of physics and calculation methods, as in Read et al. (2009a). The cumulative distribution of second logarithmic derivatives for this sample are shown in Fig. 3.1. From this cumulative distribution, we find that 95% of the derivatives are $\lesssim$ 2. We, therefore, use a characteristic scale of 4 × this value, resulting in $\lambda = 8$ as our Gaussian regularizer. Such a regularizer will apply, at most, a penalty of $\sim$ 3% to the likelihood that we would calculate for an EOS that has second derivatives that occur in our sample of physically-motivated EOS.

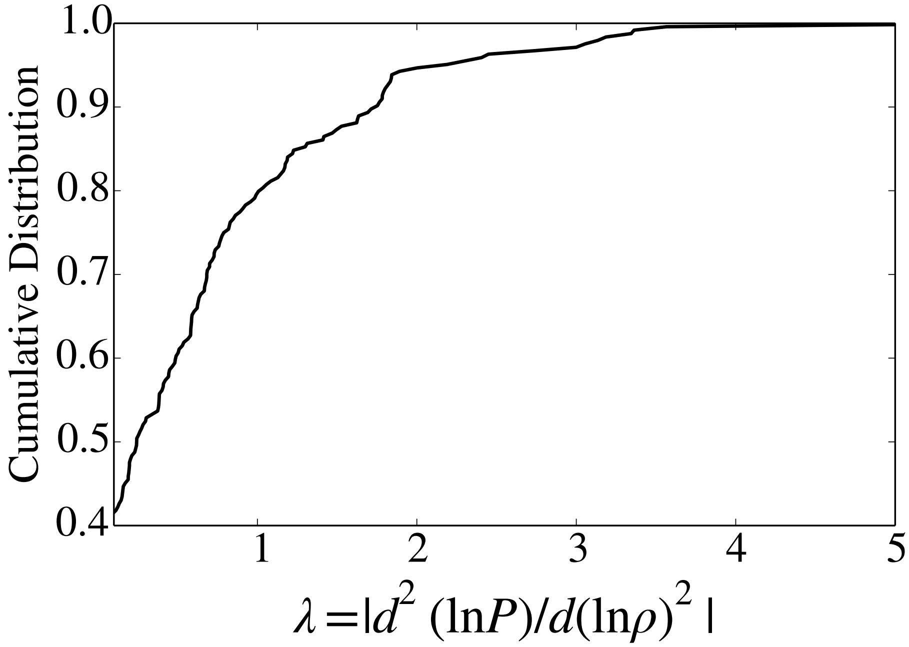

Figure 3.1 Cumulative distribution of the second logarithmic derivative in pressure at our five fiducial densities for a sample of 49 EOS taken from the literature. The majority of second derivatives are $\lesssim 2$. We, therefore, take a conservative value of $\lambda = 8$ in our Gaussian regularizer for this second derivative.

3.2 Testing the Bayesian inference with mock data

In this section, we test the Bayesian inference method described in §3.1 using different sets of mock data. For most of the simulations described below, we assume an underlying EOS and create a realization of a sample of mass-radius data that are equidistant in mass between 1.2 and 2.0 $M_{\odot}$. We assume Gaussian measurement uncertainties with the same dispersions among the data points, which we denote by $\sigma_{\rm M}$ and $\sigma_{\rm R}$. We use a Monte Carlo method to draw a particular realization of simulated measurements from these distributions and apply our Bayesian inference method to this data set. We explore below how well the Bayesian inference method works for different types of underlying EOS, as well as for different number and

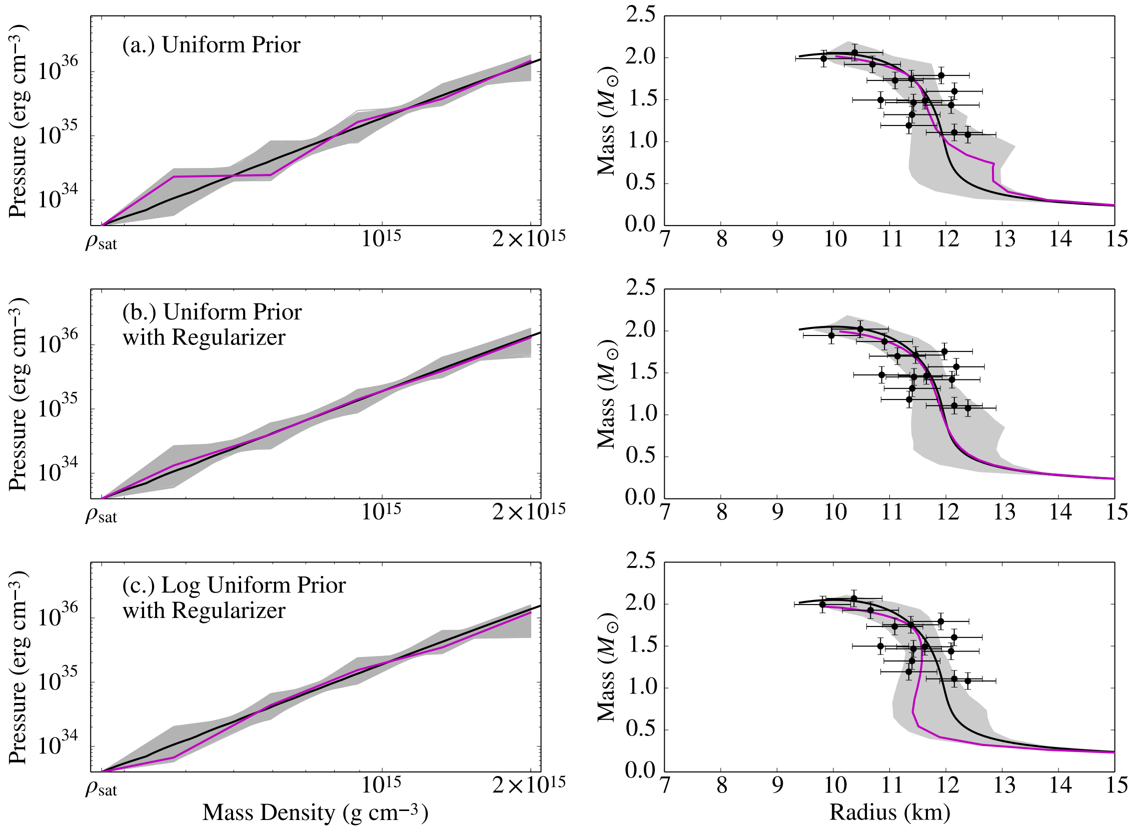

Figure 3.2 *(Top)* Inferred equation of state and mass-radius curve from a sample of mock data, assuming a *uniform* prior distribution of pressures. The mock data are drawn from the nucleonic EOS SLy (Douchin and Haensel, 2001) and are dithered with Gaussian noise corresponding to $\sigma_M = 0.1M_\odot$, $\sigma_R = 0.5$ km. The actual curves for SLy are shown in black. The magenta curve represents the most likely EOS inferred via our Bayesian method. The 68% credibility region is shown in gray. *(Middle)* Identical to top panel, but with our Gaussian regularizer included in the inversion. *(Bottom)* Identical data to the top two panels, but assuming a prior distribution that is *uniform in the logarithm* of pressure and including a Gaussian regularizer. Assuming a uniform distribution leads to a preference towards high pressures in the regions where there are few data to constrain the inversion, while assuming that the pressures are distributed uniformly in the logarithm leads to a preference towards lower pressures. Including the Gaussian regularizer reduces the sensitivity to the choice of prior.

quality of data points.

In Fig. 3.2, we show the result for one realization of mock data drawn from the EOS SLy, with uncertainties of $\sigma_{\rm R} = 0.5$ km and $\sigma_{\rm M} = 0.1\ M_\odot$. EOS SLy is partic-

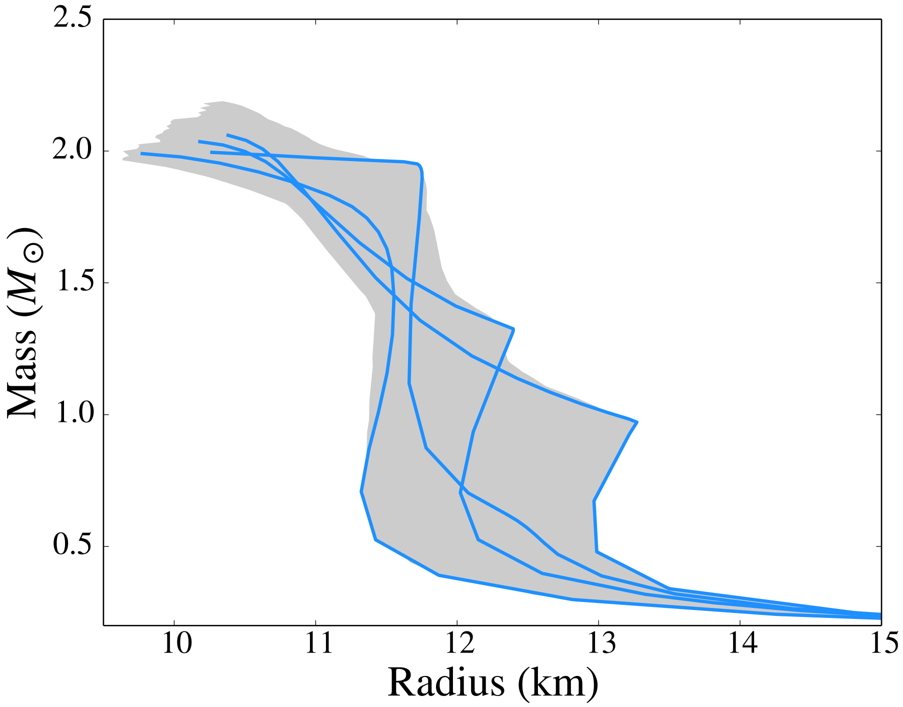

Figure 3.3 Individual mass-radius curves contributing to the shape of the 68% credibility region in the top panel Fig. 3.2. A few individual curves are shown here to emphasize the fact that not all curves that can be drawn through this region will actually have likelihoods within the 68% interval.

ularly challenging for a parametrization like ours that is optimized for potentially more complex EOS because it is practically a single polytrope in the density range of interest. We, therefore, use this example to explore the strengths and limits of the inference as well as of the regularizer.

The black lines in Fig. 3.2 represent the EOS SLy, while the magenta lines show the most-likely inferred EOS found with our Bayesian method. The gray bands represent the 68% credibility regions. For five-dimensional likelihoods, the 68% credibility region is defined as the region where

$$\int\int\int\int\int P(P_1, ..., P_5|\mathrm{data})dP_1dP_2dP_3dP_4dP_5 = 0.68, \qquad (3.9)$$

exactly analogous to the lower-dimensional case. It should be noted that these credibility regions show the spread of possible solutions only, and should not be over-interpreted. That is, there are many curves that may be drawn through these

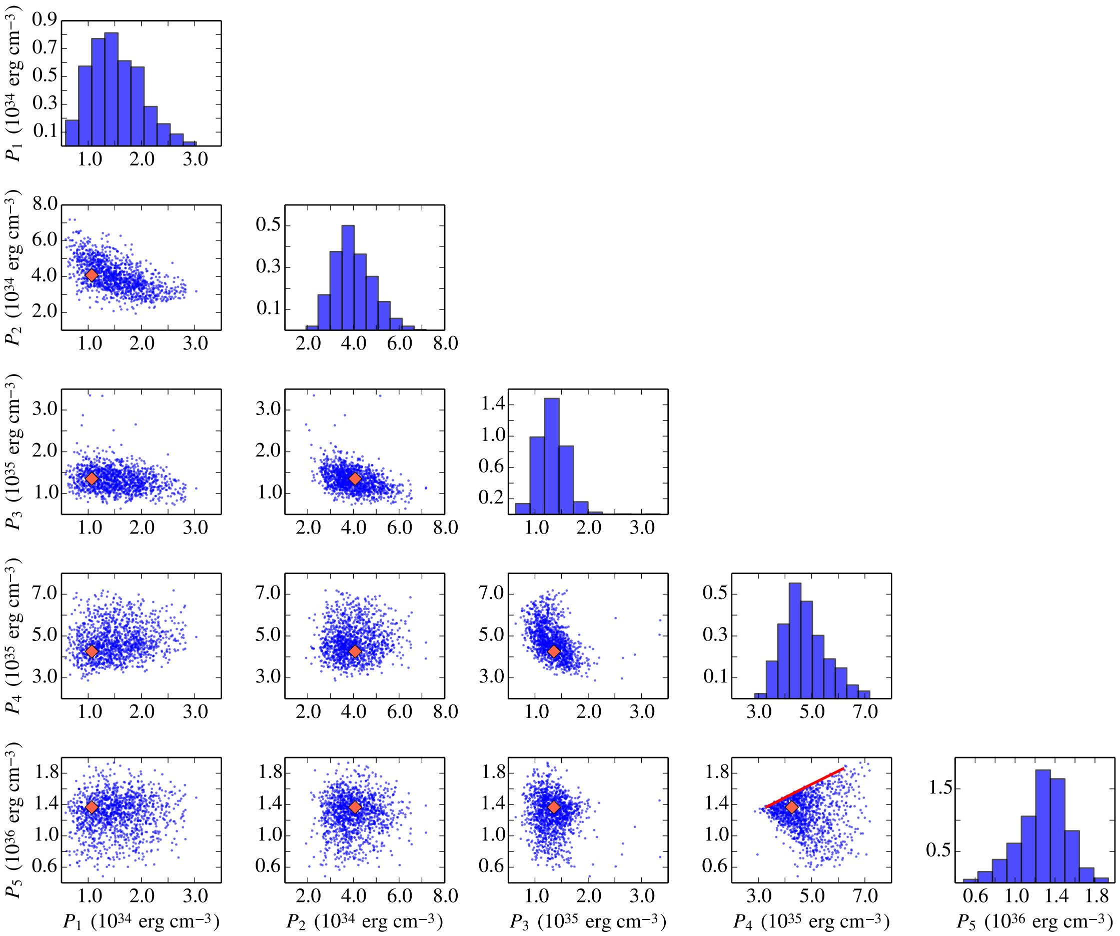

Figure 3.4 Correlation plots for the inferred pressures at our five fiducial densities. The inversion was performed using uniform priors and a Gaussian regularizer ($\lambda = 8$). The red diamonds mark the pressures of the true EOS (SLy) that we are trying to infer. There are slight anti-correlations between adjacent pressures (e.g., P_1 and P_2), but the non-adjacent pressures are relatively uncorrelated. The triangular shape of the P_4 vs. P_5 correlation is due to the causality requirement, which is shown as the red line.

regions that either have very small probabilities or violate one of our priors and are therefore unphysical. For example, the curve that could be drawn along the very edge of any of the bands is much less likely than those truly contained in the 68% credibility region. To emphasize this point further, we show in Fig. 3.3 several of the individual mass-radius curves that contribute to the shape of the 68% credibility region in the top panel of Fig. 3.2. The jagged edge of the contour is created by multiple different mass-radius curves. Indeed, the curve that follows either edge in its entirety is not included in the 68% interval. The same can be said for all of the grayed 68% credibility regions shown throughout this chapter, and thus interpretations of those regions should be made with caution.

In the top panel of Fig. 3.2, we show the results of the inversion using uniform priors in pressure in the absence of any regularizers. The inferred EOS contains several sharp transitions between different polytropic indices. The middle panel shows an inversion for identical data, but in which the Gaussian regularizer has been added to the uniform priors. The stepped behavior that was shown in the top panel is effectively eliminated by the regularizer. With the addition of the regularizer, our inferred, most-likely EOS closely follows SLy. The errors in pressure for our most-likely EOS are all less than 30% for this realization of mock data, while the errors for $P_2 - P_5$ are 3−7%.

Because there is no physical motivation to assume that the prior distribution of the pressures is uniform, we also tested the inversion with priors that are uniform in the logarithm of pressure. The results of this test, with identical data as above and the Gaussian regularizer included, are shown in the bottom panel of Fig. 3.2.

The top panel of Fig. 3.2 shows that assuming a uniform prior introduces a preference towards higher pressures. On the other hand, assuming that prior is uniform in the logarithm of pressures biases the results toward lower pressures. The inversion is particularly sensitive to this bias in the low-mass/low-density region of the EOS, where we lack data. Our Gaussian regularizer helps reduce this bias, as shown in the middle and bottom panels of Fig. 3.2, in which the results are similar for the two types of priors when the regularizer is also included.

In the absence of a regularizer, the freedom introduced by using five polytropes in the parametrization combined with this sensitivity to prior distributions could lead to significantly skewed results, or even the false inference of a phase transition with a perceived high statistical confidence. It is, therefore, important to use a Gaussian regularizer on the second derivative, with characteristic scale $\lambda = 8$, to avoid this sensitivity to over-fitting.

In Fig. 3.4, we explore potential correlations between the inferred parameters for this test. Specifically, we show the correlations for the inversion using uniform priors and the Gaussian regularizer (i.e., the middle panel of Fig. 3.2). There are slight anti-correlations between adjacent inferred pressures, due to fact that, even with the addition of the regularizer, we are still over-parametrizing our model while trying to fit the effectively single-polytrope EOS SLy. Overall, however, the pressures that are not adjacent are uncorrelated with one another. Özel and Psaltis (2009) showed that, for a three-polytrope parametrization, parametrizing with the pressures as free parameters instead of the polytropic indices reduced the correlations between the inferred values. Figure 3.4 shows that the low levels of correlations are maintained here.

In order to ensure that the Bayesian inference works well for other underlying EOS and that the regularizer does not adversely limit our ability to detect potential phase transitions, we tested the method on a number of different EOS as well. As an example,[1] we show in Fig. 3.5 the results of our method obtained for an underlying EOS with significantly more structure than SLy; specifically, we generated a mock EOS with an extreme change in the polytropic index (from $\Gamma = 1$ to $\Gamma = 5$) that occurs in between two of our fiducial densities. This EOS is shown in the black solid line of Fig. 3.5. This was again designed to challenge the inversion procedure, but in the opposite extreme from EOS SLy. Even in this case, the most likely solution still recovers all of the pressures to within $\sim$30%, and recovers P_2 to within 11%.

Some previous studies (e.g., Steiner et al. 2016) have suggested that parametrizing with polytropic segments disfavors phase transitions because polytropes naturally go through the origin. However, continuity between segments, as required in any reasonable parametrization, implies that the power law segments are never required to go through the origin. Small values of the exponent, and hence phase transitions, are thus fully allowed. Moreover, in Fig. 3.5, we show that our parametrization is able to recover a phase transition, even when the phase transition is offset from the fiducial densities.

---

[1] See discussion around Fig. 3.8 for other examples of EOS with a wide range of predicted radii.

Finally, in order to quantify the range of uncertainties in the inferred pressures for different statistical realizations of the mock measurements, we generate a large number of mock data sets drawn from the EOS SLy (as in Figs. 3.2−3.4) and applied our method to each set. We summarize these results in Fig. 3.6, which shows the cumulative distribution of errors in the most likely inferred pressures at each of our five fiducial densities. We find that the pressure at $\rho_2 = 2.2\ \rho_{\rm sat}$ is the best constrained, with errors less than 15% in 95% of the realizations. The other four pressures have errors less than ∼20% in approximately half of the realizations, and are correct to within less than 0.3 dex in every realization, where 1 dex represents an order of magnitude.

3.3 Biases due to marginalization

The Bayesian inference scheme described in §3.1 provides five-dimensional posteriors, $P(P_1, ..., P_5|\text{data})$. While one might explore the marginalized distributions over each pressure, P_i, this can easily lead to misinterpretations. It is possible, for example, that just considering the most likely pressures from each marginalized distribution of P_i will produce an EOS that violates one of our priors. The pressures are coupled to one another and marginalizing over any one dimension removes that dependence. For this reason, we exclusively use the five-dimensional likelihoods to interpret our results.

Another approach that is taken in some earlier studies (e.g., Steiner et al. 2010) is to marginalize the output of the Bayesian inference in mass-radius space, rather than over the pressures. This is done by creating a one-dimensional histogram of the radii over a fixed grid of masses, for all possible mass-radius curves. Analytically, we can derive such a marginalization by first writing the radius and mass as functions of the five pressures and a central density, i.e.,

$$R = R(\rho_c, P_1, ..., P_5) \tag{3.10a}$$

$$M = M(\rho_c, P_1, ..., P_5). \tag{3.10b}$$

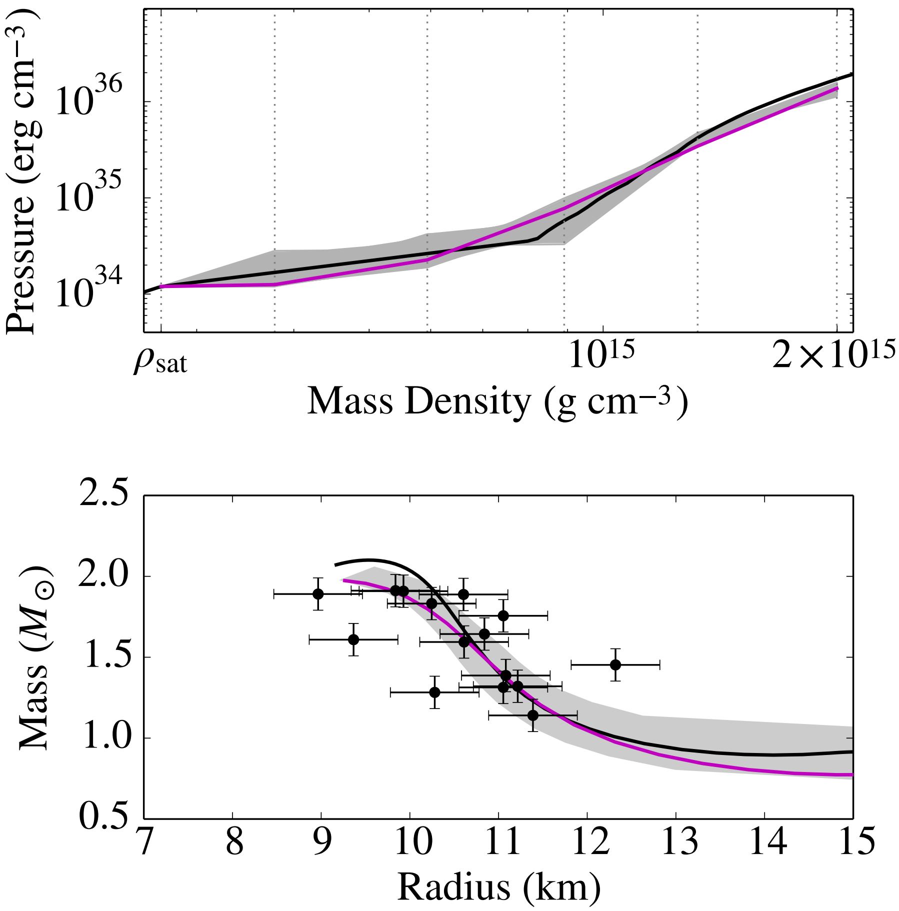

Figure 3.5 Inferred equation of state and mass-radius curve from a sample of mock data, assuming a uniform prior distribution of pressures and a Gaussian regularizer. The mock data are generated from a two-polytrope EOS that we created to have a break in polytropic index that does not line up with our fiducial densities, the locations of which we show with dotted vertical lines to emphasize the misalignment. The generating EOS is shown in black, our most likely inferred EOS is shown in magenta, and the gray regions represent the 68% credibility regions.

For a fixed mass, we can write the radius equation instead as

$$R = R(P_1, ...P_5; M), \tag{3.11}$$

which we can invert to recover P_1 in terms of R and $(P_2, ..., P_5)$ for a fixed mass. One can then express the radius as a function of only the mass by marginalizing

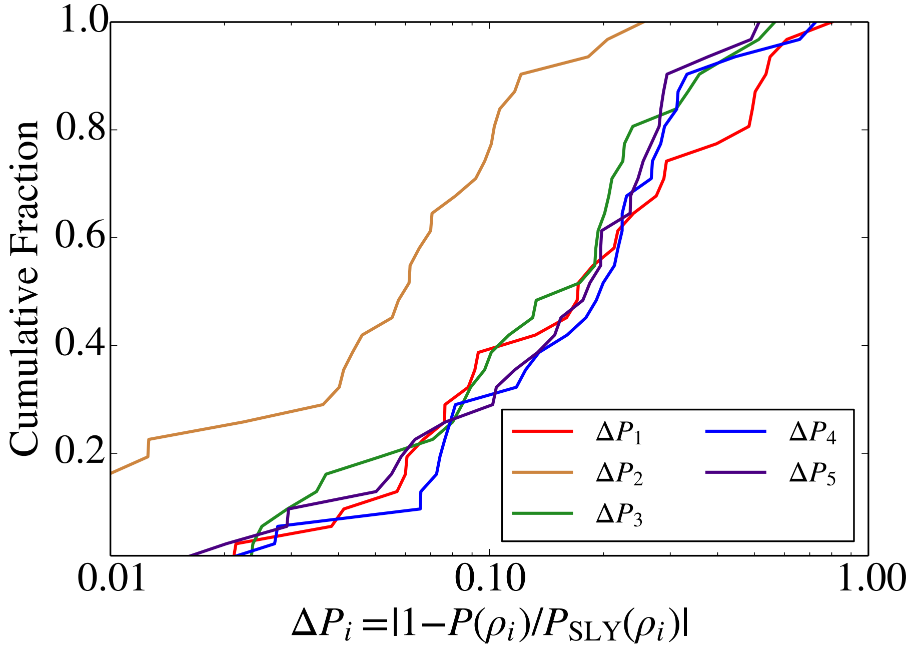

Figure 3.6 Cumulative distribution of the errors in the most likely inferred pressure at each of the five fiducial densities for 32 realizations of mock data. For each realization, we took 15 mock (M, R) data points from the EOS SLy and dithered with noise drawn from Gaussian distributions corresponding to $\sigma_M = 0.1\ M_\odot$ and $\sigma_R = 0.5$ km. We find that P_2 is the best constrained, with errors less than 15% in 95% of cases, while the other pressures have errors less than ∼20% in half of the realizations and are correct to within 0.3 dex in every realization.

across the other four pressures, i.e.,

$$P(R; M) = \int P\left[R(P_2, ..., P_5; M), P_2, ..., P_5\right] \times \hat{J}\left(\frac{R}{P_1}\right) dP_2 ... dP_5, \tag{3.12}$$

where $\hat{J}(R/P_1)$ is the Jacobian that transforms from P_1 to R. This is the analytical equivalent of taking the one-dimensional histogram of radii over a grid of masses.

Equation (3.12) highlights the issues that marginalizing introduces. If the full posterior, $P\left[R(P_2, ..., P_5; M), P_2, ..., P_5\right]$, is relatively flat, then the highly non-linear Jacobian will dominate the resulting marginalization. The marginalization is particularly sensitive to this bias when the data are sparse and have large errors. However, the marginalization can be skewed for any data set, if the posterior distribution is not sharply peaked enough to overcome the influence of the Jacobian.

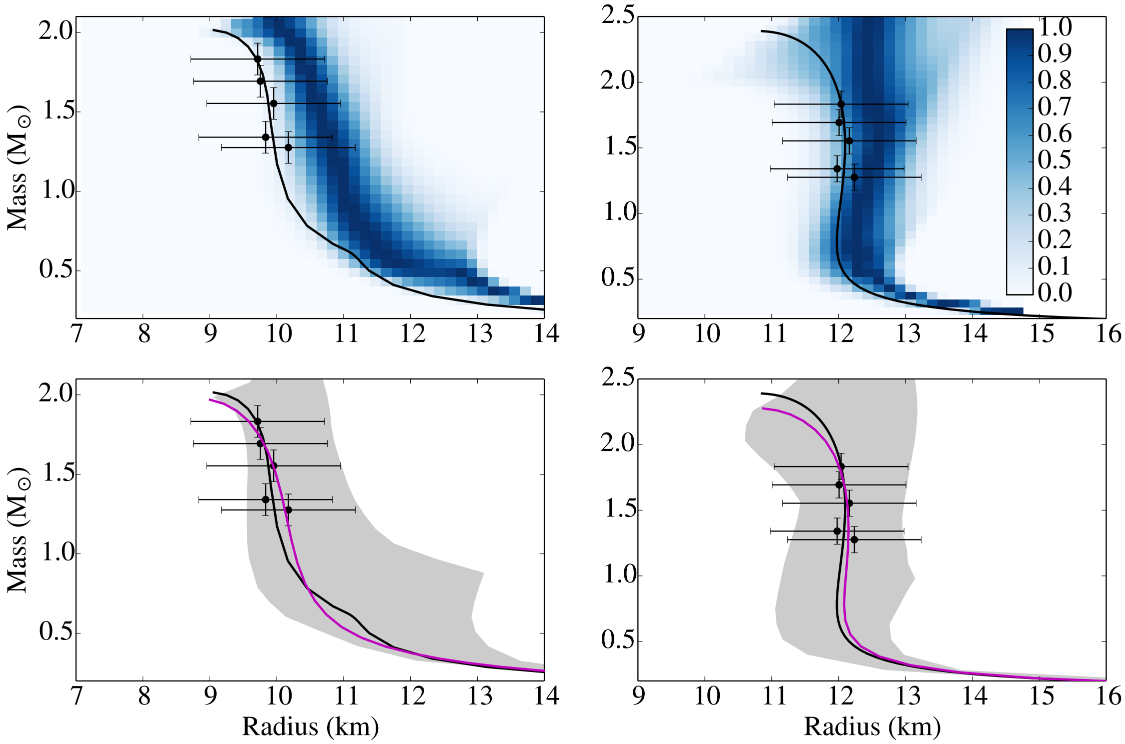

Figure 3.7 Top panel: Marginalization of the most common radii found during the Bayesian inference for two separate EOS (left and right panels). This marginalization is computed using histograms of radii for a fixed grid of masses, for which the analytic equivalent is shown in eq. (3.12). Bottom panel: The probability distribution from the same Bayesian inference. The most likely solution is shown in magenta, while the gray regions show the 68% credibility regions. In both cases, the mock data and generating EOS are shown in black. For the data centered near 10 km, the marginalized contours are offset from the most likely solution by ∼0.5 km. For the data clustered near 12 km, the marginalization bias is smaller but still present.

Indeed, in Fig. 3.7, we show this effect for two different sets of data: one that is clustered around $R \sim 10$ km and one that is clustered around $R \sim 12$ km. Both inversions use 5 simulated (M, R) data points, with masses that are spaced evenly between 1.2 and 1.8 $M_\odot$ and with measurement uncertainties of σ_R=1 km and $\sigma_M = 0.1\ M_\odot$. For the smaller-radii dataset, the marginalized solution is offset by $\gtrsim$ 0.5 km from the data at all masses (upper left panel). The most likely solution, in contrast, goes right through the data (lower left panel). For the larger-radii dataset, the effect is less extreme but still present: the marginalized solution is shifted approximately 0.4 km to the right of the data. The most likely solution, again, goes through every data point. While the marginalized solution is indeed within the error bars of the data, the most likely solution recreates the data almost perfectly for a variety of data. Current radius data have even larger and often overlapping error contours that will make this effect hard to identify by eye. It is, therefore, extremely important that only the full five-dimensional likelihoods be used to identify EOS constraints.

It should be noted that the choice of priors does affect the size and direction of this bias. Here, we use a prior distribution that is uniform in pressure and includes the Gaussian regularizer, while still requiring our other physical constraints (e.g., causality, a 2 $M_\odot$ star, etc.). Using a prior that is uniform in the logarithm of pressure pushes the bias in the other direction, i.e. toward smaller radii, and also pushes our most likely solution in that direction. The effect of the prior is stronger here than in Fig. 3.2 because we have more sparse data.

Figure 3.8 shows the bias of the marginalized solutions for inversions of still more data sets, each of which used uniform priors and the Gaussian regularizer. This figure also shows that the effect persists whether three or five polytropes are included in the parametrization. Each inversion used 5 simulated (M, R) data points clustered near a radius between $\sim 10 - 15$ km, with masses between $1.2 - 1.8$ $M_\odot$, as in Fig. 3.7. We find that the bias is strongest at small radii. For data centered near 9.6 $M_\odot$, the bias is 1.1 km for a three-polytrope parametrization and 0.6 km for our five-polytrope parametrization. We include the results for the three-polytrope parametrization in order to emphasize that this bias is not a result of our specific choice of parametrization, but is a problem stemming from the marginalization of posteriors using sparse data. Given the large biases that can be introduced by the marginalization, it is clear that the marginalized solution should not be trusted. This is particularly true when the data have large, overlapping errors which will make this effect difficult to identify. The maximum likelihood method that we have used throughout this chapter does not suffer any such biases.

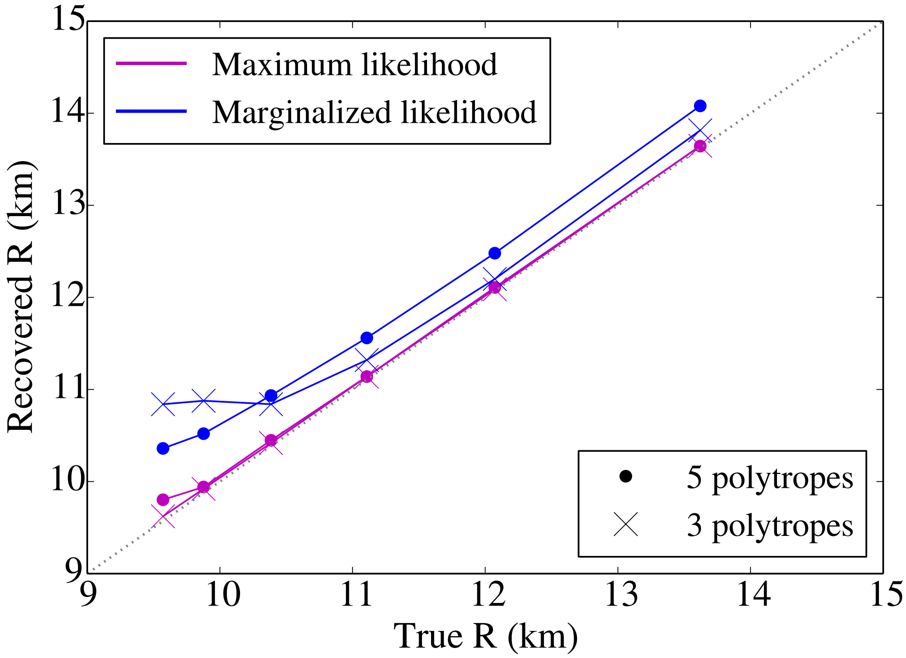

Figure 3.8 Radius recovered in our inversion plotted against the true radius of the underlying EOS. The radii are sampled at four masses between 1.2 and 1.8 $M_\odot$ and then averaged to create each value of R. The gray, dotted line represents a perfect inversion, with no introduced error. The magenta lines show the most likely solution, with circles indicating the solution for our five-polytrope parametrization and crosses indicating the solution for a three-polytrope parametrization. The blue lines and points represent the solutions obtained via marginalization. The most likely solution is consistent with the true value for all radii, while the marginalization solution is only correct for radii $\gtrsim$ 12 km and only for the three-polytrope parametrization. At small radii, the marginalization biases the recovered radii to larger values by as much as ~1 km.

3.4 Conclusions

In this chapter, we developed a Bayesian method that can be used to infer the pressures of a parametrized EOS from a set of neutron star masses and radii. We used a parametrization containing five polytropic segments starting at $\rho_{\rm sat}$, which is the form we found to be optimal in our previous work (Raithel et al., 2016).

We investigated the influence of various priors and measurement uncertainties on the inferred pressures. We found that the freedom introduced by using five polytropic segments in the parametrization (which is necessary to recreate the EOS using next-generation data to within expected uncertainties) caused the inferred EOS to be too stepped in behavior. We, therefore, introduced a regularizer over the second derivative of pressure, to mitigate that freedom without sacrificing the ability to remain agnostic about the dense matter EOS. Combined with uniform priors over the pressures, we were able to show that measurement uncertainties expected in the near future will allow an inference of the pressure at $\rho_2 = 2.2\rho_{\rm sat}$ to within $\sim$15%, for a simple EOS. We were able to recreate the pressures at $\rho_3 - \rho_5$ to within $\sim 20\%$ in approximately half of the realizations, and to within 0.3 dex for all realizations. For a more complicated EOS with a significant break in the power-law indices, we were able to infer the pressures at all densities to within $\sim 30\%$.

Finally, we showed that determining the posterior via marginalization in mass-radius space may lead to significant biases. We found that, for data at small radii, the marginalized mass-radius curves can be biased by nearly +1 km. Previously published EOS inferences from neutron star radius measurements are likely to have been affected by this bias in studies that used such a marginalization. It is better, instead, to use the maximum of the five-dimensional likelihoods computed in the Bayesian inference method. The most likely solutions do not suffer any such bias and were able to recreate the true $M - R$ curve for data at any radius.

It is difficult to compare our results to previous attempts to infer the pressures of a parametrized EOS from data because other studies do not characterize the uncertainties in the same ways. For example, Steiner et al. (2016) report that the maximum uncertainty allowed in their inversion is a factor of 3 in the pressure, purely from the requirement of causality, from their assumed crust EOS, and from the requirement that an EOS produce a star with $M \geq 1.97\ M_\odot$. They report that the maximum uncertainty is closer to a factor of 2 near the central densities of the maximum mass stars. However, these maximum uncertainties are due to the priors of their model only, and would likely be smaller with the inclusion of data.

Using our approach, we find that the EOS can be inferred to high accuracy with the expected quality of next-generation data. Given that the EOS is currently poorly constrained at high densities, the possibility of constraining it to within even

0.3 dex, and possibly to within 15% at 2.2 $\rho_{\rm sat}$, will allow significant advances in our understanding of the physics at work in the ultradense regime.

CHAPTER 4

Model-Independent Mapping from a Moment of Inertia Measurement to the Neutron Star Radius †

While the Bayesian inference scheme of Chapter 3 is the most direct way of constraining the EOS pressures, it can also be useful to perform cross-domain comparisons of neutron star properties, both as a way of further testing the predictions of various EOS and also as a means of checking for systematic biases between different measurements. For example, by comparing a moment of inertia measured from the double pulsar system to the dozen radii measured from X-ray spectra, it becomes possible to confirm the consistency of new measurements before incorporating them into a final EOS inference. These sorts of cross-domain checks are particularly important in the era of sparse data, in which any particular experiment can wield significant constraining power.

While it is trivial to check whether a moment of inertia and radius measurement are consistent with each other given the predictions of a particular EOS, it is less obvious how we can compare such measurements in a model-independent way. If the ultimate goal is still to use these measurements to constrain the EOS, then it is critical to avoid assuming an EOS prematurely. In the following chapters, we introduce a series of new, EOS-independent mappings between various global properties of neutron stars. We start in the present Chapter 4 with a model-independent mapping between the moment of inertia and the neutron star radius. In Chapter 5, we derive a new direct mapping between the tidal deformability of a neutron star merger and the stellar radius. In Chapter 6, we introduce a new way of mapping

---

[†] A version of this chapter has been published previously as Raithel, Özel, and Psaltis (2016). *Model-independent inference of neutron star radii from moment of inertia measurements.* Phys. Rev. C, 93, 3. We thank Norbert Wex, Paulo Freire, and Michael Kramer for numerous useful discussions on this work.

from the tidal deformability directly to the nuclear symmetry energy, for comparison with laboratory-based experiments. Finally, in Chapter 7, we introduce an optimized statistical approach for performing cross-domain comparisons in a robust Bayesian way.

4.1 The moment of inertia in the double pulsar system

We will start with with a new mapping between the moment of inertia and the neutron star radius. With the discovery and continued observations of the double pulsar system, PSR J0737−3039 (Lyne et al., 2004), a neutron star moment of inertia measurement has become imminent. The moment of inertia for Pulsar A in this system can be measured from the periastron advance of the binary orbit, $\dot{\omega}$, due to relativistic spin-orbit coupling, in conjunction with the measurement of the decay of the orbital period, $\dot{P}_b$ (Damour and Schafer, 1988). Such a measurement is expected with up to 10% accuracy within the next five years (Lyne et al., 2004; Kramer and Wex, 2009; Lattimer and Schutz, 2005).

The moment of inertia, which is a higher moment of the mass profile within the neutron star, provides a strong handle on the dense-matter EOS. Indeed, the connection between the moment of inertia and the EOS has previously been explored. For example, Morrison et al. (2004) calculated the moment of inertia for Pulsar A for three classes of EOS and showed that a moment of inertia measurement would let us distinguish between the three classes. Bejger et al. (2005) expanded on this work and further explored the relation between the type of EOS and the resulting moment of inertia. However, both these works rely on individual equations of state at high densities and are limited by the fact that current calculations might be sampling only a restricted range of the physical possibilities.

Neutron star studies and, in particular, measurements of their moments of inertia, more directly constrain the stellar structure and the dense matter EOS than low-energy laboratory experiments. In this chapter, we show how a moment of inertia measurement, I_A, for Pulsar A of the double pulsar system maps directly into the neutron star structure. There are two ways to accomplish this. The first is to assume an EOS throughout the star and solve for the resulting stellar structure. However, as we will demonstrate, the currently proposed EOS already show a spread in their predictions of the moment of inertia for a given stellar radius and it is unclear, given the limited range of physics explored by the current sample of EOS, whether this spread covers the entire range of possibilities. It is therefore unclear what degree of uncertainty would be associated with a neutron star radius, given a moment of inertia measurement.

In order to address this uncertainty, we follow here a second approach that maps the moment of inertia measurements to neutron star structure in a more robust way. We employ a method that assumes an EOS only up to the nuclear saturation density and then configures the remaining mass to either maximize or minimize the moment of inertia. This method is independent of assumptions of the behavior of matter at densities above the nuclear saturation density and, thus, provides the most model-independent constraints on the neutron star structure. We show how even a weak upper bound on I_A places an upper limit on the radius of Pulsar A, which will ultimately provide more stringent constraints on the EOS. Once a more precise measurement of I_A is made, we show that we will be able to constrain the radius to within ±1 km.

4.2 Neutron star moments of inertia for various EOS

We start by showing the widely varying moments of inertia and radii that are predicted for a given neutron star mass, if different EOS are assumed throughout the star. To calculate the moment of inertia predicted by an EOS, we numerically integrate the Tolman-Oppenheimer-Volkoff (TOV) equations for stellar structure simultaneously with a relativistic version of the differential equation for the moment of inertia (Glendenning, 1996).

The TOV equations, which were defined in the introduction and are repeated here for convenience, determine the pressure, P, and the enclosed mass, M, of the star as a function of radius, such that

$$\frac{\mathrm{d}P}{\mathrm{d}r} = -G\frac{(\rho + P/c^2)(M + 4\pi r^3 P/c^2)}{r^2 - \frac{2GMr}{c^2}} \tag{4.1}$$

and

$$\frac{\mathrm{d}M}{\mathrm{d}r} = 4\pi r^2 \rho, \tag{4.2}$$

where ρ is the energy density at an interior radius, r, and

$$\frac{\mathrm{d}\nu}{\mathrm{d}r} = \frac{2G}{c^2}\frac{M + 4\pi r^3 P/c^2}{r^2(1 - 2\frac{GM}{rc^2})}, \tag{4.3}$$

where $e^{-\nu}$ is the g_{tt} component of the metric for a slowly rotating star. The spin frequency of Pulsar A is 44 Hz, so any rotational deformations of the star will indeed be small. Equation (4.3) has the boundary condition $\nu(R_{\mathrm{NS}}) = \ln(1 - 2GM_{\mathrm{NS}}/R_{\mathrm{NS}}c^2)$, where M_{NS} and R_{NS} are the mass and radius of the whole star.

The additional differential equations for the moment of inertia are

$$\frac{\mathrm{d}I}{\mathrm{d}r} = \frac{8\pi}{3}\left(\rho + \frac{P}{c^2}\right)\frac{fjr^4}{1 - 2\frac{GM}{rc^2}}, \tag{4.4}$$

and

$$\frac{\mathrm{d}}{\mathrm{d}r}\left(r^4 j \frac{\mathrm{d}f}{\mathrm{d}r}\right) + 4r^3\frac{\mathrm{d}j}{\mathrm{d}r}f = 0, \tag{4.5}$$

where $f(r) \equiv 1 - \frac{\omega(r)}{\Omega}$, $j \equiv e^{-\nu/2}\left(1 - 2\frac{GM}{rc^2}\right)^{1/2}$, $\omega(r)$ is the rotational frequency of the local inertial frame at radius r, and Ω is the spin frequency of the star. Equation (4.5) is a second-order partial differential equation with the two boundary conditions

$$\left[\frac{df}{dr}\right]_{r=0} = 0 \tag{4.6}$$

and

$$f(r = R_{\mathrm{NS}}) = 1 - 2\frac{I}{R_{\mathrm{NS}}^3}. \tag{4.7}$$

To solve these coupled equations, we integrate eqs. (4.4) and (4.5) outwards from the center of the star, using eq. (4.6) as one boundary condition, and iterate it to find the value of f_0 for which eq. (4.7) is valid.

The final component necessary to integrate these equations is a relation showing how the density depends on the pressure; that is to say, we need some knowledge of the neutron star equation of state. We first compiled a large number of EOS incorporating a variety of different physics and calculation methods, as in Cook et al. (1994); Read et al. (2009a). They include purely nucleonic equations of state, such as: relativistic (BPAL12, ENG, and MPA1) and nonrelativistic (BBB2) Brueckner-Hartree-Fock EOS; variational-method EOS (e.g. FPS and WFF1-3); and a potential-method EOS (SLY). Our sampling also includes models which incorporate hyperons, pion and kaon condensates, and quarks, including, for example: a neutron-only EOS with pion condensate (PS); relativistic mean-field theory EOS with hyperons (GNH3 and H1-3); and an effective-potential EOS with hyperons (BGN1H1).

For each EOS in our list, a given central density results in a unique mass and radius, as well as a moment of inertia. From these results, we choose the central density so that $M_{\rm NS} = 1.338 M_\odot$, i.e., the mass of Pulsar A. The corresponding radius and moment of inertia for each EOS are shown in Fig. 4.1.

The moments of inertia in Fig. 4.1 vary by more than a factor of $\sim$3 and correspond to radii that vary by nearly 10 km. Figure 4.1 also shows the empirical relation for moments of inertia,

$$I \simeq (0.237 \pm 0.008) M R^2 \left[1 + 4.2 \frac{M \mathrm{km}}{M_\odot R} + 90 \left(\frac{M \mathrm{km}}{M_\odot R} \right)^4 \right], \tag{4.8}$$

obtained in Lattimer and Schutz (2005) by fitting to a sample of EOS which do not show significant softening at supranuclear densities and which are not self-bound. In principle, this fit could provide tight constraints on R given a measurement of the moment of inertia. However, the range of neutron star radii that correspond to a given value of the moment of inertia is limited by the sample selection of EOS; it remains possible that the true neutron star EOS has not yet been formulated and is not within the uncertainties in this fit.

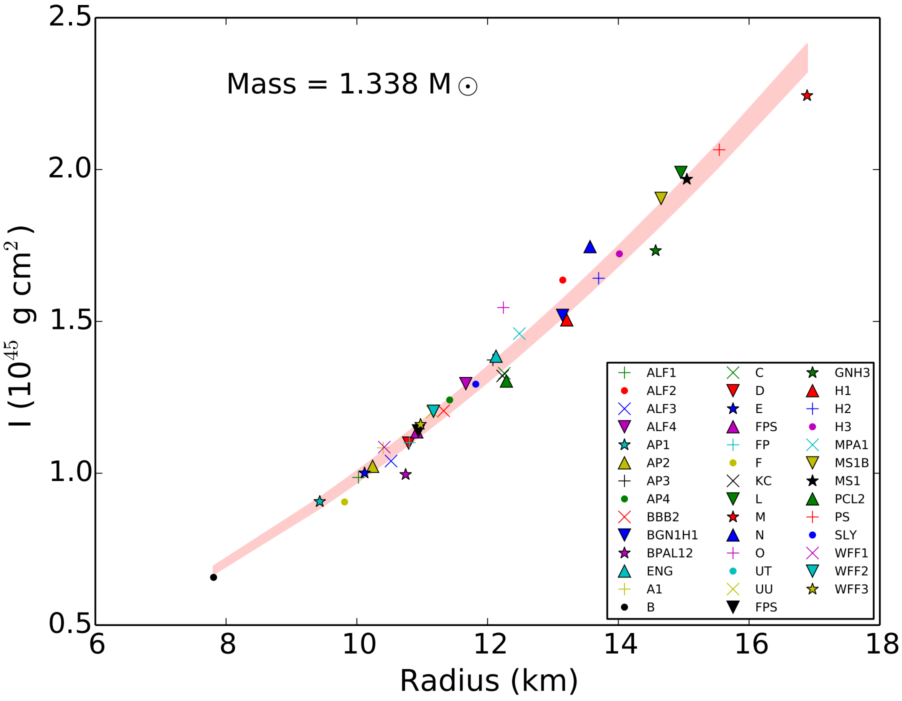

Figure 4.1 Radii and moments of inertia predicted by 41 different equations of state for a neutron star of mass $M_A = 1.338 M_\odot$. The red shaded region is the approximate range of moments of inertia by Lattimer and Schutz (2005) for EOS that do not show extreme softening at supranuclear densities. Even though their approximation follows the general trend, it does not span the entire range of radii that correspond to a given value of the moment of inertia.

4.3 Absolute bounds on the moment of inertia

As shown in Fig. 4.1, the various EOS differ by a large degree in their predictions for the moment of inertia and the corresponding radius. We present here a less model-dependent method of determining the neutron star structure from a future moment of inertia measurement. It is well known that the various EOS agree well up to $\rho \sim \rho_{\rm sat}$, in the regime where there is experimental data to constrain the models. Our goal is to determine the bounds that can be placed on the moment of inertia without assuming further knowledge of any EOS.

To accomplish this, we followed the formalism of Sabbadini and Hartle (1977). We assumed an EOS only in the outer layer of the star, at densities below some fiducial density, ρ_0. Interior to ρ_0, we assumed one of two configurations to either maximize or minimize the resulting moment of inertia.

The configuration that maximizes the moment of inertia is the one that places as much mass as possible away from the center the star while still maintaining physical stability (see Fig. 4.2). This corresponds to a constant density core of mass M_c and radius R_c, such that

$$\rho_\mathrm{c} = \frac{M_\mathrm{c}}{4\pi R_\mathrm{c}^3/3} \geq \rho_0. \tag{4.9}$$

For $r < R_\mathrm{c}$, we keep the density constant, but still vary M and P according to the TOV equations to maintain hydrostatic equilibrium. Having determined the structure of the neutron star in this way, we then determined the moment of inertia, as described above.

We repeated this calculation starting from different stellar radii, R_NS, but keeping the mass constant to $M_\mathrm{NS} = 1.338 M_\odot$. For each radius, we determined whether the resulting core is stable using the condition

$$\frac{4\pi}{3} R_\mathrm{c}^3 \rho_\mathrm{c} \leq M_\mathrm{c} \leq \frac{2}{9} R_\mathrm{c} \left[1 - 6\pi R_\mathrm{c}^2 P_\mathrm{c} + (1 + 6\pi R_\mathrm{c}^2 P_\mathrm{c})^{1/2}\right], \tag{4.10}$$

(see (Sabbadini and Hartle, 1973)) which requires that the matter inside the core be a perfect fluid at all densities and that it can be described by a one-parameter EOS; that the energy density, ρ, is non-negative; and that both the pressure, P, and its derivative with respect to ρ, $dP/d\rho$, are non-negative.

The minimum moment of inertia configuration, on the other hand, concentrates as much mass as close to the center of the star without causing the star to collapse. This corresponds to two constant density cores, with $\rho_\mathrm{c} = \rho_0$ and $\rho_\mathrm{inner} \geq \rho_\mathrm{c}$ (see Fig. 4.2). The inner core radius, R_inner, was determined by iteratively solving for the radius which maximizes the mass at the center of the star while still maintaining stability according to eq. (4.10).

As discussed in Sabbadini and Hartle (1977), this configuration technically requires infinite pressure at the center of the star. We assumed the pressure to be constant but finite for a small, innermost core in order to avoid numerical issues due to the infinity, and calculated the moment of inertia for the resulting stellar structure.

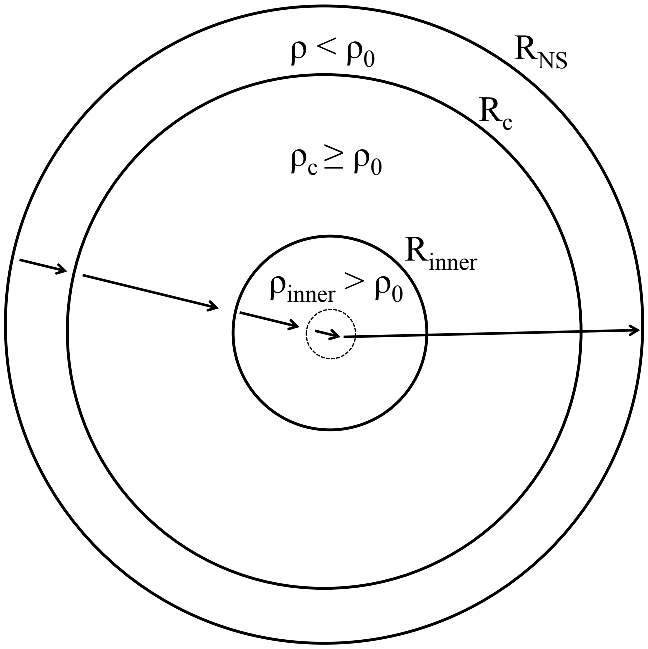

Figure 4.2 Stellar configuration for the extremes of the moment of inertia. The outermost envelope is the region where we assume a low-density EOS. The maximum moment of inertia configuration does not have the region denoted by $\rho_{\rm inner}$. The minimum moment of inertia configuration requires $\rho_{\rm c} = \rho_0$.

To be even more conservative, we calculated maximum and minimum moments of inertia for two cases: trusting the various EOS up to $\rho_0 = \rho_{\rm sat}$ and trusting the EOS up to $\rho_0 = 0.5\rho_{\rm sat}$. We first chose AP4 (a version of the APR equation of state) to use as a representative EOS for the integration up to $\rho = \rho_0$, as AP4 was constructed to fit low-density data (Akmal et al., 1998). We show the resulting bounds on I_A in Fig. 4.3.

We then varied this assumption and used other EOS for the low-density portion of the integration, the results of which are shown in Fig. 4.4. We also show in this figure an example moment of inertia measurements with 10% accuracy. We show that even for the extreme configurations that are obtained for the maximum and minimum I_A, we constrain the radius to within ±1 km. This constraint can become even tighter if additional considerations about the neutron star structure are incorporated. For example, the observation of a 2 $M_\odot$ neutron star already places a fairly EOS-independent lower limit on the radius by excluding radii less than 8.3 km (Özel et al., 2010c).

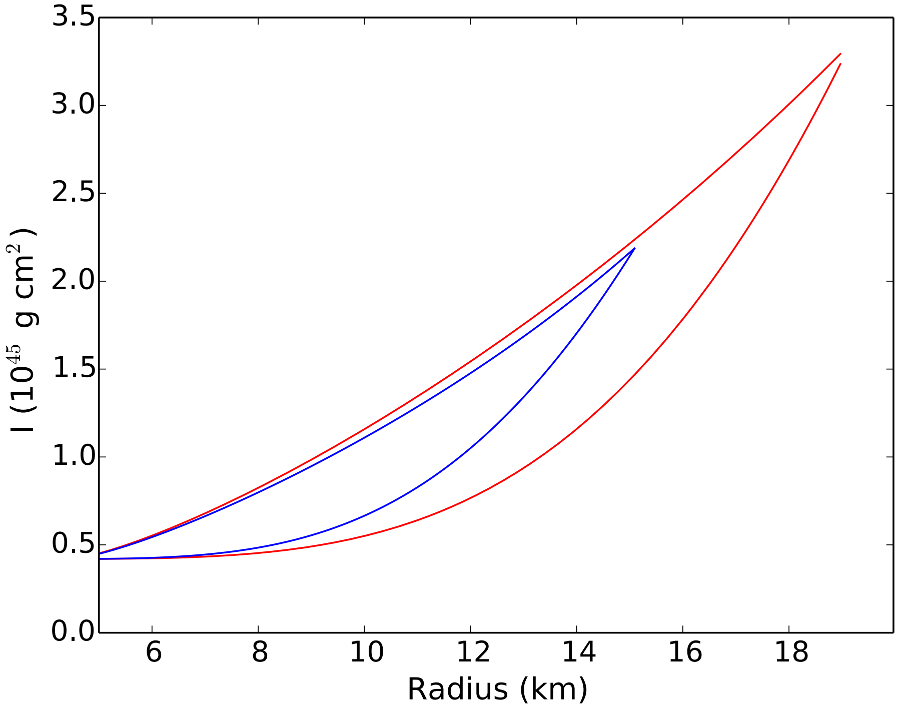

Figure 4.3 Extreme bounds on the moment of inertia of Pulsar A as a function of its radius. The blue curve assumes the EOS, AP4, up to $\rho_0 = \rho_{\rm sat}$, while the red curve assumes AP4 up to $\rho_0 = 0.5\ \rho_{\rm ns}$. Interior to ρ_0, one of two constant-density configurations was assumed, corresponding to whether we were maximizing or minimizing the moment of inertia.

Figure 4.4 shows that these bounds depend very weakly on the low-density EOS; i.e., assuming different EOS produces roughly the same bounds on the radius of Pulsar A, given a measurement of I_A. This is expected since all EOS agree fairly well with each other up to $\rho \sim \rho_{\rm sat}$. Therefore, a moment of inertia measurement of a pulsar of known mass will directly lead to a model-independent measurement of its radius. This is important for a direct comparison of a moment of inertia measurement to other astrophysical measurements of neutron star radii such as those

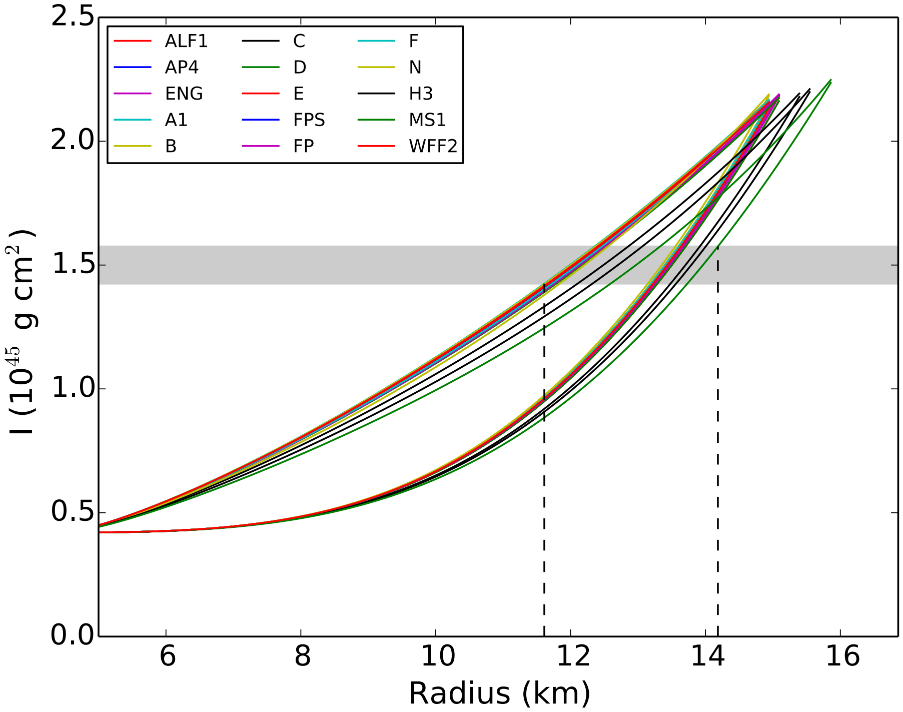

Figure 4.4 Extreme bounds on the moment of inertia of Pulsar A, using different EOS for the integration up to $\rho_0 = \rho_{\rm sat}$. The shaded region represents a sample measurment of the moment of inertia to 10% accuracy, which will lead to absolute bounds on the radius of approximately ±1 km.

from spectroscopic methods (Özel et al., 2016), without requiring any assumptions about the EOS. It will also potentially allow measurements of neutron star radii at different masses.

As in the case of neutron star radii, the measurement of the moment of inertia will directly lead to quantitative constraints on the ultradense matter equation of state (Lattimer and Prakash, 2001; Read et al., 2009a; Özel and Psaltis, 2009; Lattimer and Steiner, 2014). As an example, a measurement of the moment of inertia with 10% uncertainty can be directly translated into constraints on the magnitude S and the slope L of the symmetry energy at nuclear saturation density. Quantitatively, for a measurement of $I = 1.3 \times 10^{45}$ g cm^2 for Pulsar A with a 10% uncertainty, the framework presented in this chapter will lead to a radius inference with a similar level of uncertainty. This leads to a measurement of the pressure at nuclear saturation density of $P_{\mathrm{sat}} \sim 2.6$ MeV fm^{-3}, with only somewhat larger uncertainty, as well as of the symmetry energy parameter $L \sim 3P_{\mathrm{sat}}/\rho_{\mathrm{sat}} \simeq 48 \pm 10$ MeV.

CHAPTER 5

Gravitational Wave Events as a Direct Probe of the Neutron Star Radius [†]

We now turn to a new, direct mapping between the tidal deformability measured from a binary neutron star merger and the neutron star radius. We find that, when the chirp mass is specified, the effective tidal deformability of the binary system is surprisingly independent of the component masses of the individual neutron stars, and instead depends primarily on the ratio of the chirp mass to the neutron star radius. Thus, a measurement of the effective tidal deformability can be used to directly measure the neutron star radius. We use this new mapping to constrain the neutron star radius to $9.8 < R < 13.2$ km, at 90% credibility, independently of the assumed masses for the component stars (assuming a flat prior in the tidal deformability; see also Chapter 7 for other choices of priors). The result can be applied generally, to probe the stellar radii in any neutron star-neutron star merger with a well-measured chirp mass. The approximate mass independence disappears for neutron star-black hole mergers. Finally, we discuss a Bayesian inference of the equation of state that uses the measured chirp mass and tidal deformability from GW170817 combined with nuclear and astrophysical priors and discuss possible statistical biases in this inference.

[†] A version of this chapter has been published previously as Raithel, Özel, and Psaltis (2018). *Tidal Deformability from GW170817 as a Direct Probe of the Neutron Star Radius.* ApJL, 857, 2. Some figures and text have been updated using results from Raithel (2019), *Constraints on the neutron star equation of state from GW170817.* EPJA, 55, 90. We thank Sam Gralla for useful discussions on this work. During both projects, CR was supported by the NSF Graduate Research Fellowship Program Grant DGE-1143953, while FO and DP were supported by NASA grant NNX16AC56G.

5.1 Gravitational waves and the EOS

The first detection of gravitational waves from a neutron star-neutron star merger (GW170817, Abbott et al. 2017c) marks the start of a new era in the study of neutron stars, their associated transient events, and the dense-matter equation of state. The electromagnetic counterpart that accompanied the event (Abbott et al., 2017d) has confirmed neutron star mergers as the sources of at least some short-duration gamma-ray bursts, as has long been theorized (Eichler et al., 1989; Narayan et al., 1992; Berger, 2014), as well as the source of kilonovae, predicted to be powered by the radioactive decay of merger ejecta (Li and Paczyński, 1998; Metzger et al., 2010). Information about the component neutron stars and their underlying equation of state is encoded in the waveform itself, which was observed by the two LIGO and one Virgo detectors for ∼3000 orbital cycles prior to the merger (Abbott et al., 2017c).

Several studies have already placed constraints on fundamental neutron star properties using these observations. For example, Margalit and Metzger (2017) used the combined gravitational wave and electromagnetic signals to set an upper limit on the maximum neutron star mass, which is a sensitive constraint on the equation of state at high densities (Özel and Psaltis, 2009). In another work, Rezzolla et al. (2017) inferred the maximum neutron star mass from the event without relying on models of the electromagnetic signal, instead using only the quasi-universal relations that describe neutron stars and simple models of kilonovae.

The observed gravitational waveform can also be used to place direct constraints on the neutron star EOS. In one of the first quantitative studies exploring EOS effects on the waveform from the coalescence of two neutron stars, Read et al. (2009b) showed that a realistic waveform would deviate significantly from a point-particle waveform and that this could be observed with Advanced LIGO. The degree of the deviation depends on the underlying EOS and, as a result, could be used to differentiate between EOS that differ in radius by only ∼1 km (Read et al., 2009b, 2013; Lackey and Wade, 2015).

The magnitude of the deviation is strongest at later times in the inspiral and during the merger, i.e., in the phases where numerical relativity would be necessary to model the waveforms. Nevertheless, Flanagan and Hinderer (2008) found that the early phase of the inspiral depends cleanly on a single EOS-dependent parameter: the tidal Love number, λ. The tidal Love number measures the ratio of the star's tidally-induced quadrupolar deformation, $Q^{(\mathrm{tid})}$, to the tidal potential caused by a binary companion, $\varepsilon^{(\mathrm{tid})}$, i.e.,

$$\lambda \equiv -\frac{Q^{(\mathrm{tid})}}{\varepsilon^{(\mathrm{tid})}} \tag{5.1}$$

or, in dimensionless form,

$$\Lambda \equiv \frac{\lambda}{M^5} \equiv \frac{2}{3} k_2^{(\mathrm{tid})} \left(\frac{Rc^2}{GM}\right)^5 , \tag{5.2}$$

where R is the radius of the neutron star and M is its mass. Following the convention of Flanagan and Hinderer (2008), we call k_2 the tidal apsidal constant. The tidal apsidal constant depends both on the equation of state and the compactness (GM/Rc^2) of the particular star. For realistic, hadronic equations of state, k_2 has been constrained to lie in the range $\sim 0.05 - 0.15$ (Hinderer, 2008; Hinderer et al., 2010; Postnikov et al., 2010).

The individual Love numbers for the two stars, Λ_1 and Λ_2, cannot be disentangled in the observed gravitational waveform. Instead, what is measured is an effective tidal deformability of the binary, $\widetilde{\Lambda}$, which is a mass-weighted average of Λ_1 and Λ_2 that we describe in detail in §5.2. The expectation is thus that $\widetilde{\Lambda}$ would measure a mass-weighted compactness for the two neutron stars. Similarly, the two component masses are not measured directly; rather, the chirp mass is.

We report here on a new simplification that arises in the effective tidal deformability of the binary when the chirp mass is measured accurately. We find that $\widetilde{\Lambda}$ depends primarily on the ratio of the chirp mass to the neutron star radius. Thus, we find that $\widetilde{\Lambda}$ can be used as a direct probe of the neutron star radius, rather than of the compactness as is typically assumed.

In §5.2, we describe the measured properties of GW170817. We show in §5.3 that the effective tidal deformability is approximately independent of the component masses, when the chirp mass is specified. In §5.4, we use the Newtonian limit to show analytically that the mass-independence arises from an inherent symmetry in the expression for the effective tidal deformability. In §5.5, we use this new mapping between $\widetilde{\Lambda}$ and R to place new constraints on the neutron star radius, and we compare to existing constraints from X-ray observations. Finally, in §5.6, we perform an example Bayesian inference of the neutron star EOS from the measured tidal deformability and chirp mass and a limited number of prior physical constraints and discuss important statistical biases that can occur in such inference schemes.

5.2 Properties of GW170817

The properties of GW170817 were inferred by matching the observed waveform with a frequency-domain post-Newtonian waveform model (Sathyaprakash and Dhurandhar, 1991), with modifications to account for tidal interactions (Vines et al., 2011), point-mass spin-spin interactions (Mikóczi et al., 2005; Arun et al., 2011; Bohé et al., 2015; Mishra et al., 2016), and effects due to spin-orbit coupling (Bohé et al., 2013). The LIGO analysis using these models is summarized in Abbott et al. (2017c) and references therein.

One of the most tightly constrained properties that was inferred is the chirp mass, defined as

$$\mathcal{M}_c = \frac{(m_1 m_2)^{3/5}}{(m_1 + m_2)^{1/5}} = m_1 \frac{q^{3/5}}{(1+q)^{1/5}}, \tag{5.3}$$

where m_1 and m_2 are the masses of the primary and the secondary neutron stars, respectively, and we have introduced the mass ratio, $q \equiv m_2/m_1$. The chirp mass was constrained to $\mathcal{M}_c = 1.188^{+0.004}_{-0.002}\ M_\odot$ at the 90% confidence level, independent of the particular waveform model or priors chosen (Abbott et al., 2017c).

By assuming low-spin priors, as is consistent with the binary neutron star systems that have been observed in our Galaxy, the component masses were inferred from the chirp mass to lie within the ranges $m_1 \in (1.36, 1.60)\ M_\odot$ and $m_2 \in (1.17, 1.36)\ M_\odot$, with a mass ratio of $q \in (0.7, 1.0)$, all at the 90% confidence level (Abbott et al., 2017c). These masses are consistent with the range of masses observed masses in other neutron star systems (see Özel and Freire 2016 for a recent review of neutron star mass measurements).

GW170817 also provided constraints on the effective tidal deformability of the system, defined as

$$\widetilde{\Lambda} \equiv \frac{16}{13} \frac{(m_1 + 12m_2)m_1^4\Lambda_1 + (m_2 + 12m_1)m_2^4\Lambda_2}{(m_1 + m_2)^5}, \tag{5.4}$$

(Flanagan and Hinderer, 2008; Favata, 2014). In eq. (5.2), we saw that the dimensionless tidal Love number depends only on the stellar compactness and the tidal apsidal constant, which in turn depends on the equation of state and compactness. Combining these expressions, we can explicitly write the dependence of the effective tidal deformability on neutron star properties as $\widetilde{\Lambda} = \widetilde{\Lambda}(m_1, m_2, R_1, R_2, \mathrm{EOS})$.

Abbott et al. (2017c) constrain the effective tidal deformability for GW170817 to be $\widetilde{\Lambda} \leq 800$ at the 90% confidence level, which disfavors EOS that predict the largest radii stars. In the following analysis, we will show that this measurement can also be used to directly constrain the radii of the individual neutron stars, independently of the component masses.

5.2.1 Updated analysis of GW170817

The LIGO-Virgo collaboration published a revised analysis of GW170817, roughly one year after the initial detection (Abbott et al., 2019). This revised analysis improved on the initially-published constraints by re-calibrating the Virgo data, extending the range of frequencies included, using a new set of waveform models that go beyond the post-Newtonian approximation, and incorporating source distance measurements from the electromagnetic counterpart. With the new analysis, the chirp mass was revised down slightly to $\mathcal{M}_c = 1.186^{+0.001}_{-0.001}\ M_\odot$ and more detailed information on the tidal deformability was provided. In particular, the LIGO-Virgo collaboration reported a 90% highest posterior density interval of $\widetilde{\Lambda} = 300^{+420}_{-230}$ (Abbott et al., 2019). The majority of this chapter is primarily based on work (Raithel et al., 2018) that was published prior to the 2019 reanalysis, and thus the main results use the initially-published values for $\mathcal{M}_c$ and $\widetilde{\Lambda}$. However, Fig. 5.1 and § 5.5

come from a more recent review paper (Raithel, 2019), which incorporates the updated values for $\mathcal{M}_c$ and $\widetilde{\Lambda}$. We will make explicit which values for $\mathcal{M}_c$ and $\widetilde{\Lambda}$ we are using throughout this chapter, but the conclusions all remain the same for either choice.

5.3 Effective tidal deformability for GW170817

We start with a simple illustration of our key result. Figure 5.1 shows the effective tidal deformabilities as a function of the stellar radii for a number of realistic EOS. For each EOS, we calculated these tidal deformabilities for various values of m_1 that lie within the mass range inferred for GW170817 (shown in different symbols). The corresponding values for m_2 are calculated assuming a fixed chirp mass, corresponding to the revised value of $\mathcal{M}_c = 1.186\ M_\odot$.

We find that $\widetilde{\Lambda}$ is almost entirely insensitive to the mass of the component stars for the relevant mass range and depends instead primarily on the radius of the star. In particular, $\widetilde{\Lambda}$ changes by nearly an order of magnitude between $R = 10$ km and $R = 15$ km, but, for a given radius, changes negligibly for masses spanning the full range of $m_1 = 1.36 - 1.6\ M_\odot$.

An upper limit of $\widetilde{\Lambda} \lesssim 800$ immediately excludes radii above ∼13 km at the 90% confidence level, without requiring detailed knowledge of m_1. As shown in Figure 5.1, this rules out the EOS that predict the largest radii, such as the hyperonic EOS H4 (Lackey et al., 2006) and the field theoretic nucleonic EOS with a low symmetry energy of 25 MeV, MS1b (Müller and Serot, 1996).

The trend found in Figure 5.1 is for a sample of six EOS. However, this result is more general, as we will now show. It has been reported previously that the individual tidal deformabilities of neutron stars obey a universal relationship with stellar compactness (Yagi and Yunes, 2013). In particular, Yagi and Yunes (2017) found that the relationship can be written as

$$C = a_0 + a_1 \ln \Lambda + a_2 (\ln \Lambda)^2, \tag{5.5}$$

where $C \equiv GM/Rc^2$ is the compactness and the coefficients were fit to be $a_0 =$

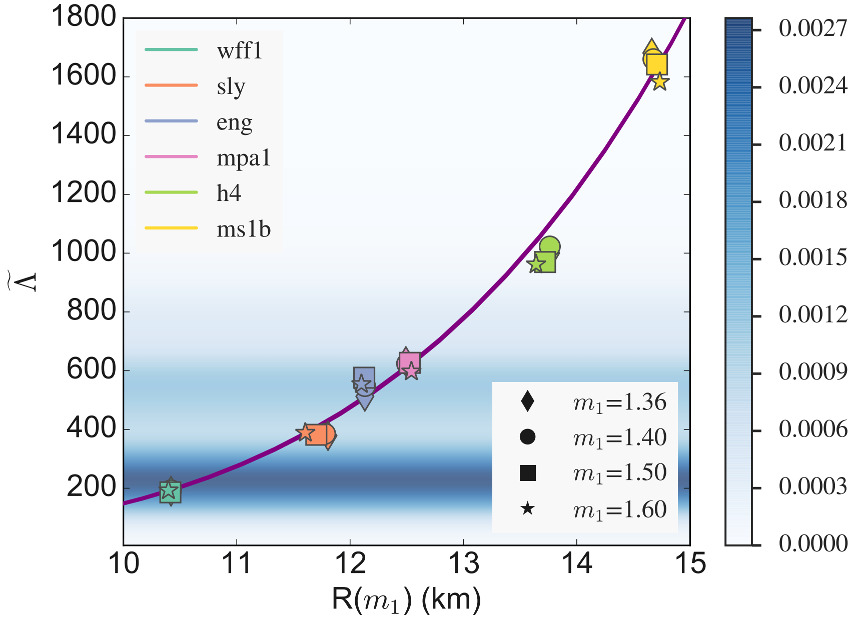

Figure 5.1 Effective tidal deformability of the binary system as a function of the radius of the primary neutron star. The tidal deformability is calculated for various primary masses (corresponding to the different symbols) using several proposed equations of state (corresponding to the different colors). The mass of the secondary neutron star is found assuming the revised chirp mass, $\mathcal{M}_c = 1.186\ M_\odot$, from the re-analysis of GW170817 (Abbott et al., 2019). Additionally, overlaid in blue is the one-dimensional posterior distribution of $\widetilde{\Lambda}$ for GW170817, as digitized from Abbott et al. (2019) for the PhenomPNRT model. The thin purple swatch corresponds to the quasi-Newtonian expansion of eq. (5.9) for $q = 0.7 - 1.0$. We find that $\widetilde{\Lambda}$ is relatively insensitive to m_1 but scales strongly with radius, and that GW170817 strongly favors small radii $\lesssim 13\ km$.

$0.360, a_1 = -0.0355$, and $a_2 = 0.000705$. The relation holds to within 6.5% for a wide variety of neutron star EOS (Yagi and Yunes, 2017).

To see if the trend we have found between $\widetilde{\Lambda}$ and R holds generically for a wide range of EOS, we use the universal relation of eq. (5.5) to calculate the individual tidal deformabilities, Λ_1 and Λ_2. We then calculate the effective tidal deformability for the binary system, shown as the solid lines in Figure 5.2 for three different radii. We find that when we use this universal relation to represent a much larger sample of EOS, the trend holds. The effective tidal deformability of the binary depends extremely weakly on the component masses but strongly on the radii of the stars.

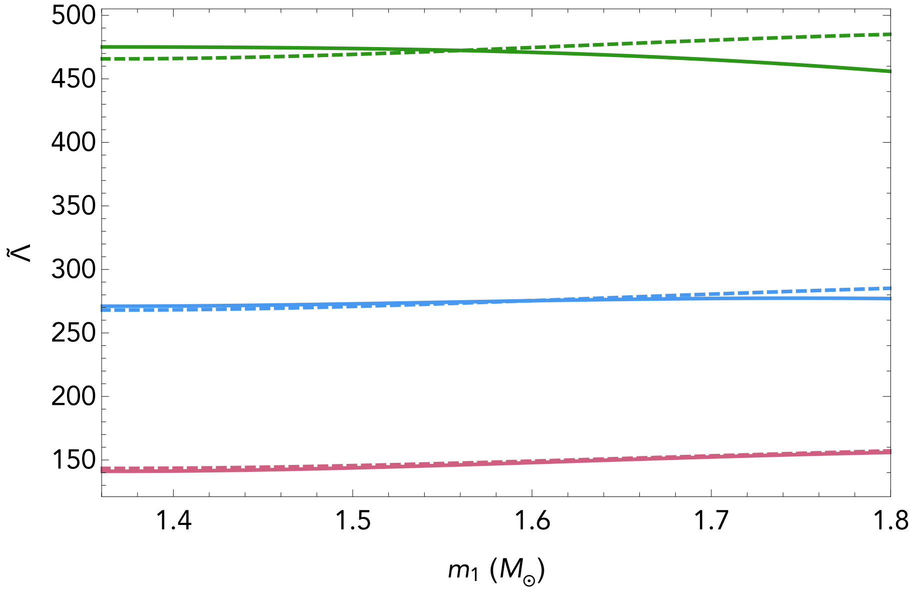

Figure 5.2 Effective tidal deformability of the binary system as a function of the primary mass, m_1, when the chirp mass is held fixed at $\mathcal{M}_c = 1.188\ M_\odot$. We calculate $\widetilde{\Lambda}$ for three fixed radii, R=10, 11, and 12 km, shown in purple, blue, and green, respectively. The solid lines show the tidal deformability calculated using the empirically-fit universal relation between the tidal deformability of each neutron star and its compactness from Yagi and Yunes (2017), while the dashed lines show the quasi-Newtonian approximation for Λ_i from eq. (6.15). The quasi-Newtonian approximation is a good approximation to the full GR result.

The weak dependence of $\widetilde{\Lambda}$ on the component masses is surprising and has not been reported before. It renders $\widetilde{\Lambda}$ a direct probe of the neutron star radius, rather than of the compactness as is typically assumed. We turn now to an analytic explanation of the origin of this result.

5.4 Effective tidal deformability in the Newtonian limit

In order to see why the dependence on mass in eq. (5.4) for $\widetilde{\Lambda}$ is so weak, we turn to the Newtonian limit. Yagi and Yunes (2013) showed that the Newtonian expression for the tidal Love number of a star governed by a polytropic EOS with index $n = 1$

(which is appropriate for the majority of realistic EOS) is simply

$$\Lambda_N = \frac{15-\pi^2}{3\pi^2}\left(\frac{Rc^2}{Gm}\right)^5 . \tag{5.6}$$

The full relativistic expression for the tidal deformability of a star is given by Damour and Nagar (2009) for a given compactness and a parameter y, which is the logarithmic derivative of a metric function, H, at the stellar surface. The full expression is far more complicated than what we have introduced so far, but we find that a relatively simple redshift correction to Λ_N qualitatively reproduces the universal results computed for more realistic EOS. We call this correction the "quasi-Newtonian" expression and define it as

$$\Lambda_{qN} = \frac{15-\pi^2}{3\pi^2}\left(\frac{Rc^2}{Gm}\sqrt{1-\frac{2Gm}{Rc^2}}\right)^5 . \tag{5.7}$$

This corresponds to equation (96) of Damour and Nagar (2009) with $\beta \approx 1$.

We can combine this with eq. (5.4) to write the quasi-Newtonian effective tidal deformability as

$$\widetilde{\Lambda}_{qN} = \frac{16}{13}\left(\frac{15-\pi^2}{3\pi^2}\right)\left(\frac{Rc^2}{Gm_1}\right)^5 \frac{(1+12q)\left(1-\frac{2Gm_1}{Rc^2}\right)^{5/2} + (1+12/q)\left(1-\frac{2Gqm_1}{Rc^2}\right)^{5/2}}{(1+q)^5}, \tag{5.8}$$

where we have assumed that the radii for the two neutron stars are the same, as is approximately true for $n=1$ polytropic EOS. Finally, we can eliminate m_1 in favor of $\mathcal{M}_c$ and q using eq. (6.17), yielding an expression for $\widetilde{\Lambda}_{qN}$ in terms of only q, $\mathcal{M}_c$, and R.

This quasi-Newtonian form of $\widetilde{\Lambda}_{qN}$ is much simpler to work with, but is it a good enough approximation? We show $\widetilde{\Lambda}$ and $\widetilde{\Lambda}_{qN}$ as functions of m_1 in Figure 5.2 as the solid and dashed lines, respectively, for fixed radii of R=10, 11, and 12 km and fixed $\mathcal{M}_c = 1.188\ M_\odot$. We find that the quasi-Newtonian approximation provides a reasonable approximation of the full expression for $\widetilde{\Lambda}$, calculated using the quasi-universal relations. We can, therefore, use $\widetilde{\Lambda}_{qN}$ to understand its dependence on the masses.

Expressing $\widetilde{\Lambda}_{qN}$ as a series expansion around $q = 1$, we find

$$\widetilde{\Lambda}_{qN} = \widetilde{\Lambda}_0 \left(1 + \delta_0(1-q)^2\right) + \mathcal{O}\left((1-q)^3\right), \tag{5.9}$$

where

$$\widetilde{\Lambda}_0 = \frac{15-\pi^2}{3\pi^2}\xi^{-5}(1-2\xi)^{5/2}, \tag{5.10}$$

$$\delta_0 = \frac{3}{104}(1-2\xi)^{-2}\left(-10+94\xi-83\xi^2\right), \tag{5.11}$$

and we have introduced

$$\xi = \frac{2^{1/5}G\mathcal{M}_c}{Rc^2} \tag{5.12}$$

as an “effective compactness.”

We note that expanding near $q = 1$ is not a restrictive choice. The known population of neutron stars is observed to have a relatively small range of masses and the observed mass distribution of double neutron stars is even narrower, suggesting that most astrophysical merger scenarios will have q near unity (see Özel and Freire 2016).

From eqs. (5.9-5.12), we see that the effective tidal deformability of the binary, $\widetilde{\Lambda}$, scales approximately as R^5 for a given $\mathcal{M}_c$. When the mass ratio is close to unity, the individual masses add only a small correction. For the measured chirp mass of GW170817, we calculate the expansion coefficients for a few radii in Table 5.1. We note that the mass dependence only enters at order $(1-q)^2$. Furthermore, the weak dependence on mass becomes even weaker as the radius increases. Even for $R = 10$ km, the mass dependent term adds at most a $\sim$4% correction to $\widetilde{\Lambda}_{qN}$ for the mass ratio range inferred for GW170817.

We show this quasi-Newtonian expansion for a range of q values, $q \in (0.7, 1.0)$, as the purple band in Figure 5.1 and find that it accurately recreates the trend observed in that sample of EOS. Moreover, the width of this purple band – caused by the uncertainty in q – is so narrow that the quasi-Newtonian expansion effectively allows for a one-to-one mapping between $\widetilde{\Lambda}$ and R.

Table 5.1. $\widetilde{\Lambda}_{qN}$ expansion terms for the initial chirp mass ($\mathcal{M}_c = 1.188$) measured from GW170817.

Radius	$\widetilde{\Lambda}_0$	Expansion
$R = 10$ km	143.4	$1 + 0.041\left(\frac{1-q}{1-0.7}\right)^2 + \mathcal{O}\left(\frac{1-q}{1-0.7}\right)^3$
$R = 11$ km	268.0	$1 + 0.029\left(\frac{1-q}{1-0.7}\right)^2 + \mathcal{O}\left(\frac{1-q}{1-0.7}\right)^3$
$R = 12$ km	465.8	$1 + 0.020\left(\frac{1-q}{1-0.7}\right)^2 + \mathcal{O}\left(\frac{1-q}{1-0.7}\right)^3$
$R = 13$ km	764.6	$1 + 0.014\left(\frac{1-q}{1-0.7}\right)^2 + \mathcal{O}\left(\frac{1-q}{1-0.7}\right)^3$

5.5 Comparison to existing radius constraints

With the analytic, one-to-one mapping derived in eq. (5.9), we can now convert the measured posterior distribution in $\widetilde{\Lambda}$ to a poster distribution on the radius, according to

$$P(R) = P(\widetilde{\Lambda})\left|\frac{\partial\widetilde{\Lambda}}{\partial R}\right|. \tag{5.13}$$

Using the updated posteriors on $\widetilde{\Lambda}$ for GW170817 (Abbott et al., 2018), the corresponding constraints on the radius are shown in Fig. 5.3, for a range of mass ratios. GW170817 implies a 90% highest posterior density interval of $9.8 < R < 13.2$ km (for $q = 1$), with distinct likelihood peaks at $\sim$10.8 km and 12.3 km. Note, however that these results are influenced by the fact that $\widetilde{\Lambda}$ was originally measured assuming a flat prior over $\widetilde{\Lambda}$. By instead assuming a flat prior in the radius, the inferred radii will be slightly smaller (see Chapter 7 for further discussion).

Figure 5.3 also shows, as the gray, dashed line, the radius inferred from a sample of 12 X-ray radii measurements, under the assumption that all neutron stars share a common radius and are governed a mono-parametric EOS (Özel et al., 2016). The gravitational wave constraints on R are consistent with, though slightly broader than those inferred from such X-ray measurements (for a more detailed comparison, see Chapter 7). Finally, Fig. 5.3 indicates that the inferred radii are approximately

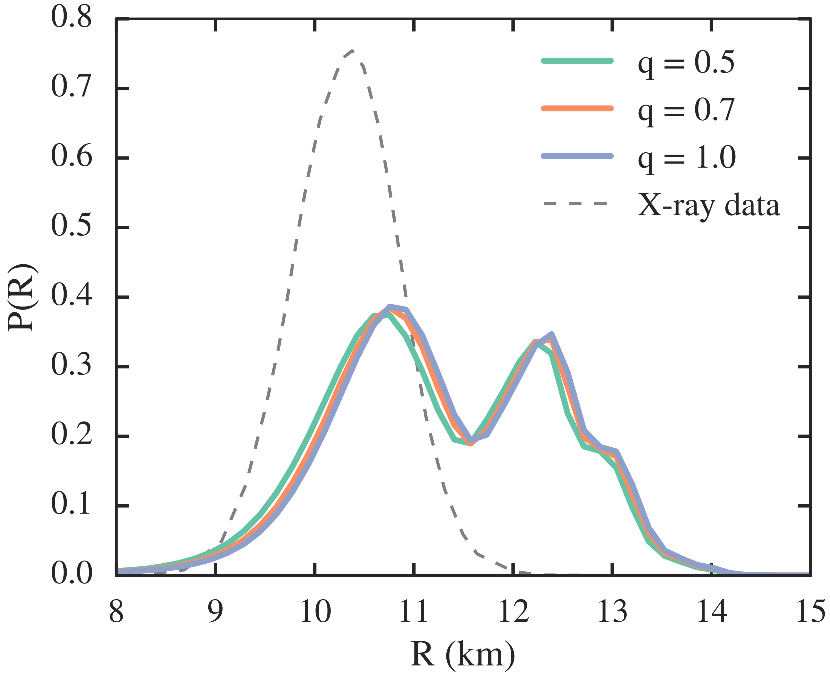

Figure 5.3 Posterior distribution in radius from GW170817 for three different mass ratios, shown in the different colors. The updated posterior distribution for $\widetilde{\Lambda}$ (which assumes a flat prior in $\widetilde{\Lambda}$; Abbott et al. 2019) has been converted to posteriors in radius using the quasi-Newtonian expansion of eq. (5.9). The resulting 90% highest-posterior density interval corresponds to $9.8 < R < 13.2$ km, for $q = 1$, with likelihood peaks at $R \sim$10.8 and 12.3 km. The gray dashed line represents the composite posterior in radius from 12 spectroscopic X-ray measurements, under the assumption that all neutron stars share a common radius (Özel et al., 2016). There is approximate agreement between the X-ray data and the higher probability peak of the inferred radius from GW170817.

independent of the mass ratio, as expected from the weak q-dependence discovered in eq. (5.9).

The measured constraints on $\widetilde{\Lambda}$ can also be used to directly constrain the EOS, using the type of Bayesian inference scheme that was discussed in Chapter 3. The LIGO-Virgo Collaboration performed such an inference using a spectral parameterization of the EOS (Lindblom, 2010) and incorporating astrophysical priors on the neutron star maximum mass to further constrain the parameter space. At the

90% confidence level, the resulting EOS constraints correspond to predicted radii of $R_1 = 11.9^{+1.4}_{-1.4}$ km and $R_2 = 11.9^{+1.4}_{-1.4}$ km (Abbott et al., 2018), which are consistent with the constraints shown in Fig. 5.3. Using this spectral EOS sampling, the LIGO-Virgo collaboration also reported direct constraints on the pressure, finding the pressure at twice the nuclear saturation density to be $3.5^{+2.7}_{-1.7} \times 10^{34}$ dyn/cm^2, and at $6\rho_{\rm sat}$ $9.0^{+7.9}_{-2.6} \times 10^{35}$ dyn/cm^2, at the 90% confidence level (Abbott et al., 2018).

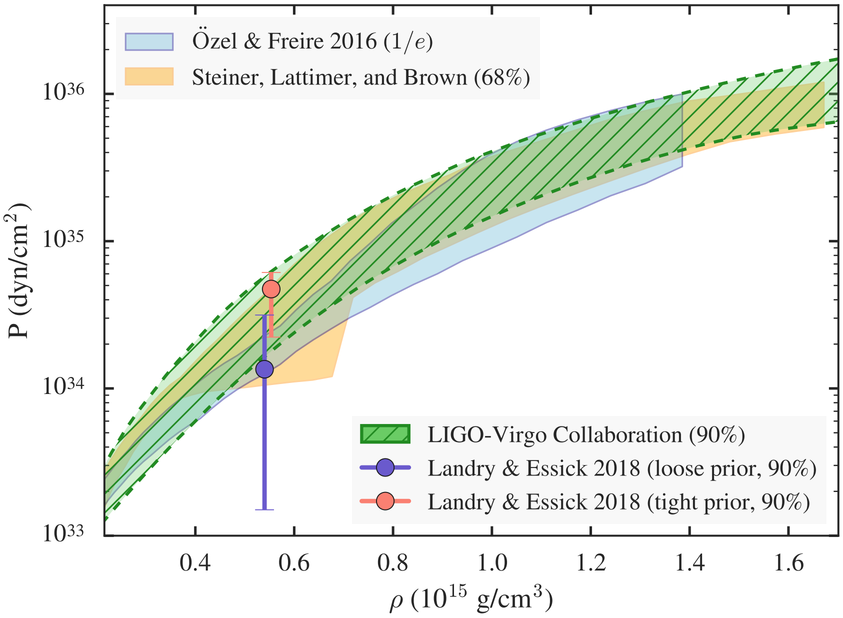

Figure 5.4 Ensemble of EOS constraints from X-ray radius measurements and GW170817. The orange and blue bands represent the EOS inferred from X-ray measurements of neutron star radii in Steiner et al. (2013) and Özel and Freire (2016), respectively. It should be noted that the blue band spans the range of inferred EOS with posterior likelihoods that fall within $1/e$ of the maximum likelihood, while the orange band represents the 68% credibility interval. The green hatched band corresponds to the new constraints inferred from GW170817 with the LIGO-Virgo parametric inference, at 90% credibility (Abbott et al., 2018). Finally, the symbols show the constraints at $2\rho_{\rm sat}$ from a non-parametric analysis of GW170817, with error bars representing the 90% confidence intervals (Landry and Essick, 2019). While these analyses report their constraints with differing confidences, the results indicate that the constraints from GW170817 are approximately consistent with existing inferences from X-ray measurements.

In an independent analysis, Landry and Essick (2019) employed a non-parametric inference of the EOS using priors generated with Gaussian processes that are conditioned on a set of realistic EOS. In a Monte Carlo integration, synthetic EOS are drawn from these non-parametric priors and used to predict the tidal deformabilities for given component masses. These macroscopic properties are then compared with the observed data to calculate the EOS likelihoods. The authors argue that this method can more faithfully recreate complicated EOS, which may have phase transitions or other discontinuities. For GW170817, they find the pressure at twice the nuclear saturation density to be $1.35^{+1.8}_{-1.2} \times 10^{34}$ dyn/cm^2, for the case in which the prior was only loosely trained on the realistic EOS, and $4.73^{+1.4}_{-2.5} \times 10^{34}$ dyn/cm^2, for the case in which the prior was tightly trained on the sample EOS. For GW170817, this method thus produces results consistent with the LIGO-Virgo parametric analysis (Abbott et al., 2018).

These EOS constraints are summarized in Fig. 5.4. The orange and blue bands represent the EOS inferred from X-ray measurements of neutron star radii in Steiner et al. (2013) and Özel and Freire (2016), respectively. In addition to using radius measurements from X-ray bursts and quiescent low-mass X-ray binaries, both of these studies also required consistency in the EOS with low-energy nucleon-nucleon scattering data as well as sufficient pressure to support a maximum mass of $\gtrsim 2\ M_{\odot}$. Atop these previous X-ray constraints, Fig. 5.4 also shows the new constraints inferred from GW170817 using the parametric Bayesian inference of Abbott et al. (2018) (green hatched band). The non-parametric constraints of Landry and Essick (2019) are shown as the purple and orange symbols, for the case of loose and tight priors, respectively. While these analyses all report constraints at different confidence levels, it is clear that the two types of observations (X-rays and gravitational waves) give approximately consistent results. With additional data– both of new gravitational wave sources and of new X-ray radii with potentially smaller uncertainties – the constraints will become even tighter.

5.6 Bayesian inference of the radius

Given these promising constraints on the EOS from gravitational wave data, we now turn to a discussion of the biases that can be introduced by marginalizing the posteriors in a Bayesian inference scheme. The issue of marginalization of a multi-dimensional posterior space was first introduced in Chapter 3. Here, we explore the issue in the context of an inference using gravitational wave data directly. Because this work was performed prior to the publication of the full posterior information on $\widetilde{\Lambda}$, we perform a sample inference, in which we take the constraint on $\widetilde{\Lambda} \leq 800$ to correspond to a Gaussian distribution, centered at $\widetilde{\Lambda}_{\rm obs} = 400$ with a dispersion of $\sigma_{\widetilde{\Lambda}} = 243$. We also use the initial inferred chirp mass from GW170817, which is constrained to $\mathcal{M}_c = 1.188^{+0.004}_{-0.002}\ M_\odot$.

In our sample inference, we incorporate a variety of astrophysical and nuclear physics priors, including that the EOS is microscopically stable and causal at all pressures, that the lowest two pressures exceed the limit placed by two-nucleon interaction, and that all EOS must produce a neutron star of at least 1.97 $M_\odot$, in order to be within 1σ of the measurements of the most massive neutron stars (Antoniadis et al., 2013; Fonseca et al., 2016). We assume a uniform prior on the pressures. In order not to over-parametrize the EOS, while still allowing the possibility of complex behavior to be inferred, we also include a Gaussian regularizer over the second derivative of the pressure ($\lambda = 2$), which penalizes sharp phase transitions. For further details on the set-up of our Bayesian inference, see Chapter 3.

In addition to the above priors, which were extensively studied in Chapter 3, we also place an *upper* limit on the maximum mass, $M_{\rm max} < 2.33\ M_\odot$, which is the upper limit of the 90% credibility level found in Rezzolla et al. (2017). This maximum mass was inferred from GW170817 assuming only the quasi-universal neutron star relations and simple models of kilonovae and is thus fairly model-independent.

The likelihood of a particular EOS is given by

$$P(\text{EOS}|\mathcal{M}_{\rm c}, \widetilde{\Lambda}) = P_{pr}(\text{EOS}) P(\mathcal{M}_c, \widetilde{\Lambda}|\text{EOS}), \tag{5.14}$$

where $P_{pr}(\text{EOS})$ represents the set of the priors on the EOS, which we describe above. Because of the high accuracy in the measurement of the chirp mass, we fix it to the observed value, and use that to set m_2 for any given m_1. Then, eq. (5.14) can be written as

$$P(\mathrm{EOS}|\widetilde{\Lambda}) = P_{pr}(\mathrm{EOS}) \times \frac{1}{\sqrt{2\pi}\sigma_{\widetilde{\Lambda}}} \exp\Big\{ -\frac{[\widetilde{\Lambda}_{\mathrm{EOS(m_1,m_2)}} - \widetilde{\Lambda}_{\mathrm{obs}}]^2}{2\sigma^2_{\widetilde{\Lambda}}} \Big\}, \tag{5.15}$$

where $\widetilde{\Lambda}_{\mathrm{EOS(m_1,m_2)}}$ is the effective tidal deformability for a particular set of the two masses, m_1 and m_2, of each EOS that maximizes the likelihood. We choose to use the maximum likelihood, rather than integrating over all combinations of m_1 and m_2 to avoid biasing our results, as discussed in Chapter 3.

To populate the posteriors in eq. (5.15), we run a Markov Chain Monte Carlo (MCMC) simulation with $\sim 10^6$ points. For each EOS that is tested in our MCMC, we also calculate the corresponding mass-radius relation using the standard TOV equations. In the left panel Figure 5.5, we show the mass-radius relations corresponding to the highest-likelihood solutions from our MCMC. The solid magenta line shows the most likely solution, while the pink shaded band corresponds to the range of EOS with probabilities within $1/\sqrt{e}$ of the maximum value. Figure 5.5 also shows, as the black dashed line, the radius that corresponds to the most likely value of $\widetilde{\Lambda} = 400$ using the quasi-universal relation of eq. (5.9). Both our analytic expansion of the $\widetilde{\Lambda}-$radius relationship and the full Bayesian inference presented here imply radii of ~ 11.7 km, for these sample data. This Bayesian method can be used to robustly infer the EOS as additional measurements of $\widetilde{\Lambda}$ and $\mathcal{M}_c$ are made from future neutron star merger events

To demonstrate the biases introduced by marginalization, we show in the middle and right panels of Figure 5.5 the results of our MCMC after they have been marginalized in mass-radius space, as is frequently presented in some other studies (e.g., Steiner et al., 2017; Most et al., 2018). This method of marginalization involves calculating the posteriors over radius in a fixed grid of masses. However, because there are far more large-radii EOS that produce a 2 $M_\odot$ neutron star, marginalizing in this way effectively weights the large radii solutions much more heavily than any

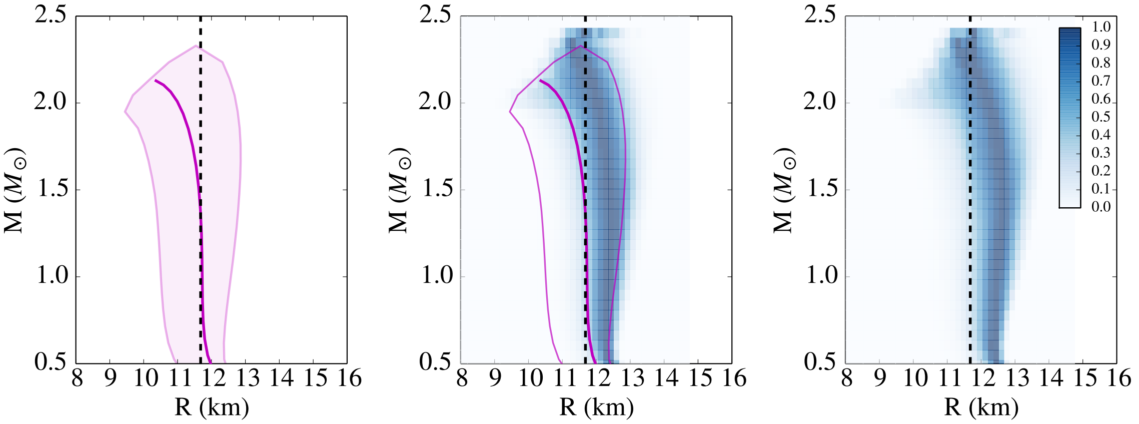

Figure 5.5 Left: Mass-radius relations corresponding to the most-likely EOS in our Bayesian inference, with a sample distribution for $\widetilde{\Lambda}$ centered at $\widetilde{\Lambda} = 400$ and a fixed chirp mass of $\mathcal{M}_c = 1.188\ M_\odot$. The solid magenta line corresponds to the most-likely EOS, while the pink band corresponds to the range of EOS with posteriors within $1/\sqrt{e}$ of the maximum value. The black dashed line shows the analytic prediction from our $\widetilde{\Lambda} - R$ relation of eq. (5.9). We find excellent agreement between our $\widetilde{\Lambda} - R$ prediction and the full Bayesian inference. Middle: Same as left panel, but showing, in addition, the marginalized posteriors over the neutron star radii for a fixed grid of masses. These marginalized likelihoods are shown in blue. By marginalizing the posteriors in this way, the results are skewed to higher radii and away from the maximum likelihood solution. Right: Marginalized likelihoods for an inference with only the priors and no data. These marginalized posteriors are nearly identical to the marginalized posteriors from the inference that incorporated data from a $\widetilde{\Lambda} = 400$ centered Gaussian. This method of marginalization over-weights the prior on the EOS pressures imposed by the observation of a 1.97 $M_\odot$ neutron star. The results of the marginalization are less sensitive to the input data and are not reliable.

other priors, or even than the data themselves. This can be seen in the middle panel of Figure 5.5, which shows that the marginalized solution leads to an inferred radius of ∼12.2 km, even though the maximum likelihood solution occurs at ∼11.7 km. To further illustrate the point, we show in the right panel of Figure 5.5 the marginalized posteriors for an inference with only priors and no data at all. The marginalized posteriors with no data are effectively identical to the marginalized posteriors for the inference that incorporated data from a $\widetilde{\Lambda} = 400$ centered Gaussian. This method of marginalization weights the 2 $M_\odot$ prior so heavily that the data are effectively ignored. We suspect that this bias also affects the posteriors presented in other works, e.g. Most et al. (2018).

5.7 Black hole-neutron star mergers

Finally, we comment that black hole-neutron star mergers are another source of gravitational waves that may contain information about the neutron star EOS. The tidal Love number of a black hole is zero (Damour and Nagar, 2009; Binnington and Poisson, 2009), which greatly simplifies the effective tidal deformability of eq. (6.16). However, this simplification also destroys the inherent symmetry in eq. (6.16), which is the source of the mass independence in the neutron star-neutron star merger scenario. Without this symmetry, a series expansion of $\widetilde{\Lambda}$, as in eq. (5.9), includes a correction term of order $(1 - q)$.

Due to the lower-order terms of $\mathcal{O}(1-q)$, there persists a stronger dependence on the mass of the components. Thus, the effective tidal deformability measured from a neutron star-black hole merger does not directly probe the radius, as in the case of a neutron star-neutron star merger. Instead, a measurement of $\widetilde{\Lambda}$ will primarily probe the neutron-star compactness.

5.8 Conclusions

In this chapter, we found that the effective tidal deformability is approximately independent of the component masses for a neutron star-neutron star merger, when the chirp mass is specified. Because this surprising result is difficult to see analytically in the full GR case, we introduce a quasi-Newtonian approximation that closely reproduces the results found in full GR. In the quasi-Newtonian limit, we find that the masses of the stars only enter at order $\mathcal{O}\left((1-q)^2\right)$, where q is the mass ratio. We find that, for the chirp mass measured from GW170817, this introduces at most a 4% mass correction to the effective tidal deformability for the entire range of mass ratios. Thus, the effective tidal deformability can be considered as approximately independent of the neutron star masses. This makes $\widetilde{\Lambda}$ a direct probe of the neutron star radius. For GW170817, we find that the revised posteriors on $\widetilde{\Lambda}$ (assuming a flat prior in $\widetilde{\Lambda}$) constrain the neutron star radius to $9.8 < R < 13.2$ km, at 90% credibility. We find that these constraints are consistent with previous measurements from the X-ray community.

We also incorporate other astrophysical priors and constraints from nuclear physics in order to perform an example Bayesian inference of the pressures in a parametric EOS, from the initial $\mathcal{M}_c$ value inferred in GW170817 and a sample interpretation of the initial upper limit on $\widetilde{\Lambda}$. We show that significant biases can be avoided by robustly examining the maximum likelihood solutions in the multidimensional parameter space, rather than introducing a marginalization in mass-radius space. The marginalization tends to weight particular priors more heavily than the actual data, which causes the resulting answer to skew systematically towards larger radii. Finally, in the case of a neutron star-black hole merger, we find that the vanishing Λ for the black hole breaks the symmetry in $\widetilde{\Lambda}$ and makes it depend more strongly on the component masses. Thus, a measurement of $\widetilde{\Lambda}$ for a neutron star-black hole merger probes the compactness of the neutron star, but cannot be used as a direct probe of the radius.

Using the methods we have developed in this chapter, future gravitational wave events can be used to directly and robustly constrain the neutron star radius, providing new constraints on the EOS.

CHAPTER 6

Connecting Gravitational Wave Events to Fundamental Nuclear Parameters [†]

Motivated by the new one-to-one mapping between $\widetilde{\Lambda}$ and R that was found in Chapter 5 and by the long-known correlation between the radius and the nuclear symmetry energy, in this chapter, we introduce a new method for mapping from a tidal deformability to fundamental nuclear parameters. We focus in particular on the low-order coefficients of the nuclear symmetry energy: namely, the value of the symmetry energy at the nuclear saturation density, S_0, and the slope of the symmetry energy, L_0. We find that the gravitational wave data are relatively insensitive to S_0, but that they depend strongly on L_0 and point to lower values of L_0 than have previously been reported, with a peak likelihood near $L_0 \sim 23$ MeV. Finally, we use the inferred posteriors on L_0 to derive new analytic constraints on higher-order nuclear terms.

6.1 Motivations for studying the nuclear symmetry energy

Determining the nuclear symmetry energy is one of the main goals of modern nuclear physics. The symmetry energy, which characterizes the difference in energy between pure neutron matter and matter with equal numbers of protons and neutrons, is typically represented as a series expansion in density, with coefficients that represent the value of the symmetry energy at the nuclear saturation density, S_0, the slope, L_0, the curvature, $K_{\rm sym}$, and the skewness $Q_{\rm sym}$, as well as higher-order terms. The symmetry energy is one of the two main components in nuclear formulations of the dense-matter EOS; the other being the energy of symmetric matter, which can similarly be broken down into nuclear expansion terms.

[†] A version of this chapter has been published previously as Raithel and Özel (2019). *Measurement of the Nuclear Symmetry Energy Parameters from Gravitational-wave Events.* 885, 2, 121. We thank Dimitrios Psaltis, Kent Yagi, Andrew Steiner, and Zack Carson for useful conversations related to this work. This work was supported by NSF Graduate Research Fellowship Program Grant DGE-1746060 and support from NASA grant NNX16AC56G.

Of these expansion terms, only the low-order parameters can be experimentally constrained, as a result of the limited densities and energies that can be reached in laboratory-based experiments. For example, experimental constraints on S_0 and L_0 have been inferred by fitting nuclear masses, by measuring the neutron skin thickness, the giant dipole resonance, and electric dipole polarizability of ^{208}Pb, and by observing isospin diffusion or multifragmentation in heavy ion collisions (Tsang et al., 2012; Lattimer and Lim, 2013; Oertel et al., 2017). However, there exist only limited experimental constraints on K_{sym} and no direct constraints on Q_{sym} (Lattimer and Lim, 2013).

The symmetry energy also plays a key role in a number of astrophysical phenomena, from determining the neutron star radius (Lattimer and Prakash, 2001), to affecting the gravitational wave emission during neutron star mergers (e.g., Fattoyev et al. 2013), r-process nucleosynthesis in merger ejecta (Nikolov et al., 2011), and the outcomes of core-collapse supernovae (e.g., Fischer et al. 2014). In the new gravitational wave era, measurements of the tidal deformability of neutron stars offer a promising way to observationally constrain the symmetry energy. The first detection of gravitational waves from a neutron star-neutron star merger, GW170817, constrained the effective tidal deformability of the binary system to $\widetilde{\Lambda} \lesssim 900$ (Abbott et al., 2017c). Subsequent work refined these constraints to $\widetilde{\Lambda} = 300^{+420}_{-230}$ (90% highest posterior density) for a system with chirp mass $\mathcal{M}_c = 1.186^{+0.001}_{-0.001}\ M_{\odot}$, for low-spin priors (Abbott et al., 2019).[1]

Already, several analyses have set initial constraints on nuclear parameters using the tidal deformability of GW170817. Malik et al. (2018) found evidence of correlations between linear combinations of nuclear parameters and the neutron star radius, tidal love number, and tidal deformability, for a wide range of EOS. They used the inferred bounds on $\Lambda_{1.4}$ from GW170817, i.e., the tidal deformability of a 1.4 $M_\odot$ neutron star, to constrain the symmetric nuclear parameters as well as $K_{\rm sym}$, for given choices of L_0. Carson et al. (2019) expanded this work to include a broader set of EOS and used updated posteriors on $\widetilde{\Lambda}$ to calculate the posteriors for various nuclear parameters. In quoting final constraints on the high-order nuclear parameters, the authors of both studies either limit L_0 to a pre-determined range or marginalize over priors on L_0. However, one might expect $\widetilde{\Lambda}$ to be particularly sensitive to L_0, as a result of the direct mapping between $\widetilde{\Lambda}$ and the neutron star radius (Raithel et al., 2018; De et al., 2018; Raithel, 2019) and the tight correlation between the radius and L_0 (Lattimer and Prakash, 2001).

---

[1] Throughout this chapter, we will exclusively use the low-spin prior results for GW170817, as is most relevant for binary neutron stars in our Galaxy.

In a more general analysis that allowed for variable L_0, Zhang and Li (2019) showed that a precision measurement of $\Lambda_{1.4}$ maps to a plane of constraints on L_0, $K_{\rm sym}$, and $Q_{\rm sym}$. They found that the tidal deformability is sensitive to the higher-order symmetry terms ($K_{\rm sym}$ and $Q_{\rm sym}$), and conclude that there is no unique mapping between $\Lambda_{1.4}$ and L_0. Krastev and Li (2019) extended this work and showed that the mapping gets even more complicated when the isotriplet/isosinglet interaction is allowed to vary. They found that assuming different density-dependences of the symmetry energy can result in identical values of the $\Lambda_{1.4}$, implying that there can be no one-to-one mapping between the tidal deformability and individual nuclear parameters.

While there may be no unique mapping of Λ to individual nuclear parameters when the parameters are allowed to vary fully independently, we find that a more restricted parameter space is often sufficient to reproduce a wide range of EOS. With a well-motivated parameter reduction, we will show that it becomes possible to directly map from the tidal deformability to nuclear parameters.

In this chapter, we introduce a framework to reduce the allowed space of nuclear parameters and we show that constraints can, indeed, be placed directly on the slope of the symmetry energy. Our method does not rely on priors from nuclear experiments. We only assume that the density-dependence of the EOS can be represented with a single-polytrope around the nuclear saturation density, which decreases the parameter space significantly. This dimension-reduction allows us to map from observed constraints on $\widetilde{\Lambda}$ directly to L_0, independently of any nuclear priors. We find that the tidal deformability is relatively insensitive to S_0, as has been assumed in the above analyses. However, we find that $\widetilde{\Lambda}$ is quite sensitive to L_0 and that GW170817 implies a relatively small value of $11.5 \lesssim L_0 \lesssim 64.8$ MeV, with a most likely value of $L_0 = 23$ MeV. These constraints are approximate, but they point to values of L_0 that are in modest conflict with those inferred from nuclear physics experiments and theory. While our constraints extend to large values of L_0 that are consistent with the results from past nuclear studies, this overlap occurs at lower likelihood. Moreover, we find that our most likely value of $L_0 = 23$ MeV lies outside of the range of previously-derived constraints. Finally, we use the inferred posterior on L_0 to analytically constrain combinations of the higher-order nuclear terms. We find that combinations of K_{sym} and K_0 can be constrained by GW170817, and that combinations of K_{sym}, Q_0, and Q_{sym} can also be constrained.

We start in §6.2 with an overview of the nuclear EOS formalism that we will use in this chapter. We introduce our polytropic approximation of these EOS in §6.3. In §6.4, we map the measurement of $\widetilde{\Lambda}$ from GW170817 to posteriors over L_0. Finally, in §6.5, we use the posterior on L_0 to constrain linear combinations of the higher-order nuclear parameters.

6.2 Nuclear expansion of the equation of state

We start by introducing the EOS formalism that we will use to connect the tidal deformability from a gravitational wave event to nuclear parameters. As discussed in the introduction, we use this standard formalism to decompose the EOS into a symmetric matter part and the symmetry energy, which we can generically write as

$$E_b(n, Y_p) = E_0(n) + E_{\mathrm{sym}}(n)(1-2Y_p)^2, \tag{6.1}$$

where $E_b(n, Y_p)$ is the energy per baryon for a given density n and proton fraction Y_p, $E_0(n)$ is the energy of symmetric matter, and $E_{\mathrm{sym}}(n)$ is the symmetry energy.

We represent the symmetric energy term with a series expansion and keep terms to third order, i.e.,

$$E_0(n) = B_0 + \frac{K_0}{18}u^2 + \frac{Q_0}{162}u^3 + \mathcal{O}(u^4), \tag{6.2}$$

where the expansion is performed around the nuclear saturation density, $n_{\rm sat}$, and $u \equiv (n/n_{\rm sat}) - 1$. Here, B_0 is the bulk binding energy of symmetric matter at $n_{\rm sat}$, and K_0 and Q_0 represent the incompressibility and skewness of symmetric matter.

Similarly, we expand the symmetry energy around u and write

$$E_{\rm sym}(n) = S_0 + \frac{L_0}{3}u + \frac{K_{\rm sym}}{18}u^2 + \frac{Q_{\rm sym}}{162}u^3 + \mathcal{O}(u^4), \tag{6.3}$$

where S_0 represents the symmetry energy at $n_{\rm sat}$ and L_0, $K_{\rm sym}$ and $Q_{\rm sym}$ give the slope, curvature, and skewness of the symmetry energy, respectively.

Such expansions are commonly used in representing neutron star matter because the coefficients can be linked to nuclear physics parameters near the saturation density. While experimental constraints on certain of these parameters exist, in order to be as general as possible, we will only assume knowledge of the bulk binding energy term and fix it to $B = -15.8$ MeV (Margueron et al., 2018a). We will leave the remaining six parameters $(K_0, Q_0, S_0, L_0, K_{\rm sym}, Q_{\rm sym})$ free.

We can convert from the energy per particle to the pressure using the standard thermodynamic relation,

$$P(n, Y_p) = n^2 \left\{ \frac{\partial [E_b(n, Y_p) + E_e(n, Y_p)]}{\partial n} \right\}\Bigg|_{Y_p, S}, \tag{6.4}$$

where S is the entropy, and we have formally included the electron contribution to the total energy, $E_e(n, Y_p)$. However, for the current analysis, we neglect the contribution of electrons and assume that the total energy is dominated by the baryons.

The pressure for our nuclear expansion is then

$$P(n, Y_p) = \left(\frac{n^2}{3n_{\rm sat}}\right)\left[\frac{K_0}{3}u + \frac{Q_0}{18}u^2 + \left(L_0 + \frac{K_{\rm sym}}{3}u + \frac{Q_{\rm sym}}{18}u^2\right)(1-2Y_p)^2\right]. \tag{6.5}$$

For a cold star in β-equilibrium, the proton fraction is uniquely determined by the density and the symmetry energy, according to

$$\frac{Y_p}{(1-2Y_p)^3} = \frac{64 E_{\rm sym}(n)^3}{3\pi^2 n(\hbar c)^3} \tag{6.6}$$

where $\hbar$ is the Planck constant and c is the speed of light. (For a derivation of this relationship and an analytic solution for Y_p, see Appendix A of Chapter 9).

In order to simplify the subsequent calculations, we perform an additional series expansion on the neutron excess parameter and define

$$(1-2Y_p)^2 \approx a + bu + cu^2 + \mathcal{O}(u^3), \tag{6.7}$$

keeping terms up to second-order, as in eq. (6.5). The coefficients of this expansion depend on the symmetry energy parameters of up to the same order, i.e., $a = a(S_0), b = b(S_0, L_0)$, and $c = c(S_0, L_0, K_{\rm sym})$.[2] Thus, keeping terms to second order, we can write the nuclear expansion of the pressure as

$$\begin{aligned} P(n, Y_p) = &\left(\frac{n^2}{3n_{\rm sat}}\right) \times \\ &\left\{aL_0 + \left(bL_0 + \frac{K_0 + aK_{\rm sym}}{3}\right)u + \left(cL_0 + \frac{bK_{\rm sym}}{3} + \frac{Q_0 + aQ_{\rm sym}}{18}\right)u^2\right\}. \end{aligned} \tag{6.8}$$

6.3 Polytropic approximation

While the expansion derived in §6.2 is useful for its direct connection to nuclear parameters, it is also complicated. The pressure of eq. (6.8) depends on 6 nuclear parameters: S_0, K_0, Q_0, L_0, $K_{\rm sym}$, and $Q_{\rm sym}$. However, many studies have shown that a wide range of EOS can be approximated with piecewise polytropic parametrizations (e.g., Read et al. 2009a; Özel and Psaltis 2009; Steiner et al. 2010; Raithel et al. 2016). The pressure of a single-polytrope is given by

$$P(n) = K_{\rm poly} n^{\Gamma}, \tag{6.9}$$

where the polytropic constant $K_{\rm poly}$ and index Γ are free parameters. The possibility of modeling the EOS with a few number of polytropes motivated us to explore whether the pressure in eq. (6.8) truly depends on all six nuclear parameters independently, or whether, as we will show, the parameter space can be further restricted. In this section, we will show that modeling the full pressure of eq. (6.8) with a single polytrope near the nuclear saturation density reasonably captures the density dependence. We will then use this simplified model to derive constraints on nuclear parameters using data from GW170817.

---

[2] We provide a `Mathematica` notebook to calculate these coefficients, along with corresponding `C` routines, at `https://github.com/craithel/Symmetry-Energy`.

Our goal is to approximate the nuclear expansion pressure of eq. (6.8) with the polytropic pressure of eq. (6.9). We require that these two expressions match at $n_{\rm sat}$ and then extrapolate to higher densities using the polytropic index. This requirement uniquely determines the polytropic constant, so that our simplified nuclear pressure can be written as

$$P(n) = \frac{aL_0 n_{\rm sat}}{3}\left(\frac{n}{n_{\rm sat}}\right)^{\Gamma}. \tag{6.10}$$

At low densities of $n \leq 0.5\ n_{\rm sat}$, we fix the EOS to the nuclear EOS SLy (Douchin and Haensel, 2001). For $0.5\ n_{\rm sat} \leq n < n_{\rm sat}$, we perform a power-law interpolation, to ensure matching between SLy and the polytropic approximation.

While our goal is to use the single-polytrope expression of eq. (6.10), we also need to ensure that the EOS remains causal at all densities. This results in an upper limit on Γ which changes with the density and which can be calculated as follows. We start with the definition of the sound speed,

$$\left(\frac{c_s}{c}\right)^2 = \frac{\partial P}{\partial \epsilon} \leq 1, \tag{6.11}$$

where $\epsilon = (E + mc^2)n$ is the total internal energy density, m is the baryon mass, c_s is the local sound speed, and c is the speed of light. For a polytropic EOS,

$$\frac{\partial P}{\partial \epsilon} = \frac{\Gamma P}{\epsilon + P}. \tag{6.12}$$

Thus, the maximum polytropic index, corresponding to $c_s/c = 1$, is simply

$$\Gamma_{\rm luminal} = \frac{\epsilon + P}{P}. \tag{6.13}$$

Whenever we implement eq. (6.10) throughout this chapter, we use the minimum of Γ and $\Gamma_{\rm luminal}$ to ensure that causality is always obeyed. This results in a slight decrease in Γ at high densities for some EOS.

We infer a reasonable range for our baseline values of Γ by generating a sample of 5,000 test EOS using eq. (6.8). The EOS are created by drawing independent values of each of the six nuclear parameters ($K_0, Q_0, S_0, L_0, K_{\rm sym}$, and $Q_{\rm sym}$) from the experimentally-constrained distributions reported in Table I of Margueron et al. (2018b) (a similar approach was taken in Carson et al. 2019). We exclude any EOS that become hydrostatically unstable. We also require that the analytic expression for Y_p derived from eq. (6.6) be positive and less than 0.5 (i.e., neutron rich) across the same density range. Finally, we require that the sound speed of each nuclear EOS remains causal across a density range of $n \sim 1-3\ n_{\rm sat}$. We choose this density range in order to focus our analysis on the regime that is responsible for determining the neutron star radius, and hence the effective tidal deformability (Lattimer and Prakash, 2001; Raithel et al., 2018). Moreover, the nuclear expansion formalism is not necessarily valid at higher densities. At lower densities, we will instead use a realistic, calculated EOS in the following analysis.

We fit each EOS in our sample with the simplified pressure model of eq. (6.10), fixing L_0 and S_0 to their drawn values. We perform the fit across the same density range, $n = 1 - 3n_{\rm sat}$. We show the resulting distribution of Γ values in Fig. 6.1. We find that nearly all of the EOS constructed with the nuclear expansion formalism can be represented with a polytropic index of $\Gamma \approx 3-4$, with a most common fit value of $\Gamma \sim 3.5$. Moreover, we find that the residuals between the full nuclear expansion EOS and our polytropic approximation are small. Figure 9.8 shows the distribution of the residuals from the sample of EOS fits at a range of densities. At each density, we calculate the residual as $(P_{\rm full} - P_{\rm poly})/P_{\rm full}$, where $P_{\rm full}$ corresponds to the full nuclear expansion of eq. (6.8) and $P_{\rm poly}$ corresponds to the polytropic approximation of eq. (6.10). The top panel of Fig. 9.8 shows the histogram of the residuals, including their sign. The bottom panel shows the cumulative distribution of the magnitudes of the residuals. The residuals are small at low densities, where the tidal deformability is expected to be determined and where the nuclear expansion formalism still applies. At 2 $n_{\rm sat}$, the error introduced by our polytropic approximation is $\lesssim$17% for 90% of the EOS sample.

Table 6.1. Error in the polytropic approximation of a nuclear EOS for seven realistic EOS.

EOS	S_0	L_0	Γ_{poly}	$R_{1.4}$	$\delta R_{1.4}$	$k_{2,\ 1.4}$	$\delta k_{2,\ 1.4}$	$\Lambda_{1.4}$	$\delta\Lambda_{1.4}$
SFHx	28.7	23.2	3.98	12.02	0.04	0.09	0.03	399.96	0.20
SFHo	31.6	47.1	3.15	11.93	0.02	0.08	0.00	338.03	0.09
DD2	31.7	55.0	3.59	13.26	0.04	0.10	0.04	706.10	0.20
FSUGold	32.6	60.4	2.95	12.59	0.04	0.08	0.02	440.40	0.22
TMA	30.7	90.1	2.85	13.89	0.06	0.11	0.10	969.05	0.34
TM1	37.0	111.0	2.91	14.52	0.05	0.10	0.08	1162.94	0.30
NL3	37.4	118.5	3.42	14.82	0.03	0.11	0.03	1392.54	0.18

Note. — The first three columns list the EOS and its published symmetry energy parameters, in MeV. Γ_{poly} provides our fit to the EOS across the density range 1-3 n_{sat}. $R_{1.4}$ (in km), $k_{2,1.4}$, and $\Lambda_{1.4}$ represent the stellar properties of a 1.4 $M_{\odot}$ star, calculated using the full tabulated EOS. The columns labeled δQ provide the fractional error between each stellar property calculated using the full EOS and using the polytropic approximation of eq. (6.10).

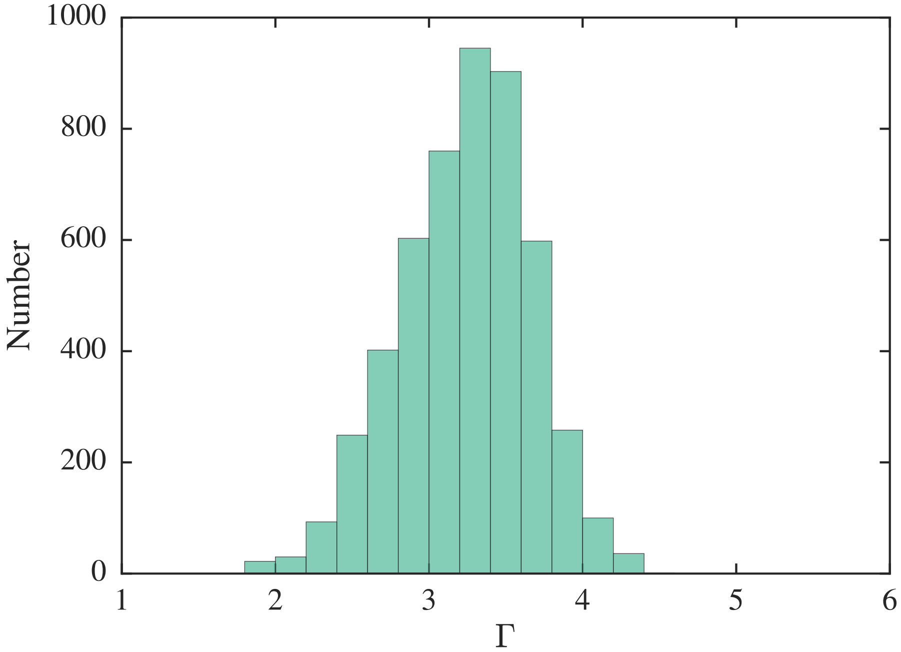

Figure 6.1 Distribution of polytropic indices fit to a sample of 5,000 nuclear expansion EOS using eq. (6.10). Each EOS was constructed using eq. (6.8) with the six nuclear parameters, ($K_0, Q_0, S_0, L_0, K_{\rm sym}$, and $Q_{\rm sym}$), independently drawn from experimentally-constrained distributions. We find that nearly all of the EOS can be with with $\Gamma = 3-4$, while the most common Γ is ~ 3.5

In addition to the large sample of mock EOS, we also calculate the errors introduced by our polytropic approximation for seven realistic EOS. For each realistic EOS in this sample, we use the full EOS[3] to calculate the tidal apsidal constant for a 1.4 $M_\odot$ star, $k_{2,1.4}$; the radius of the corresponding star, $R_{1.4}$; and $\Lambda_{1.4}$ (see §6.4 for more details on how these quantities are calculated). We report these values in Table 6.1. We then calculate the same quantities using the polytropic approximation. We start by fitting the tabulated EOS with a single polytropic index, $\Gamma_{\rm poly}$, between $1-3$ $n_{\rm sat}$, while keeping the pressure at $n_{\rm sat}$ fixed to the coefficient of eq. (6.10) for the S_0 and L_0 of each EOS. We list the published values of S_0 and L_0[4] and the

---

[3] In practice, to simplify the calculation, we use a many-polytrope approximation. In this case, we use 20 polytropes to represent the pressure between 1 and 10 $n_{\rm sat}$, which should be more than sufficient.

[4] These values are compiled from the `CompOSE` database, https://compose.obspm.fr/home/.

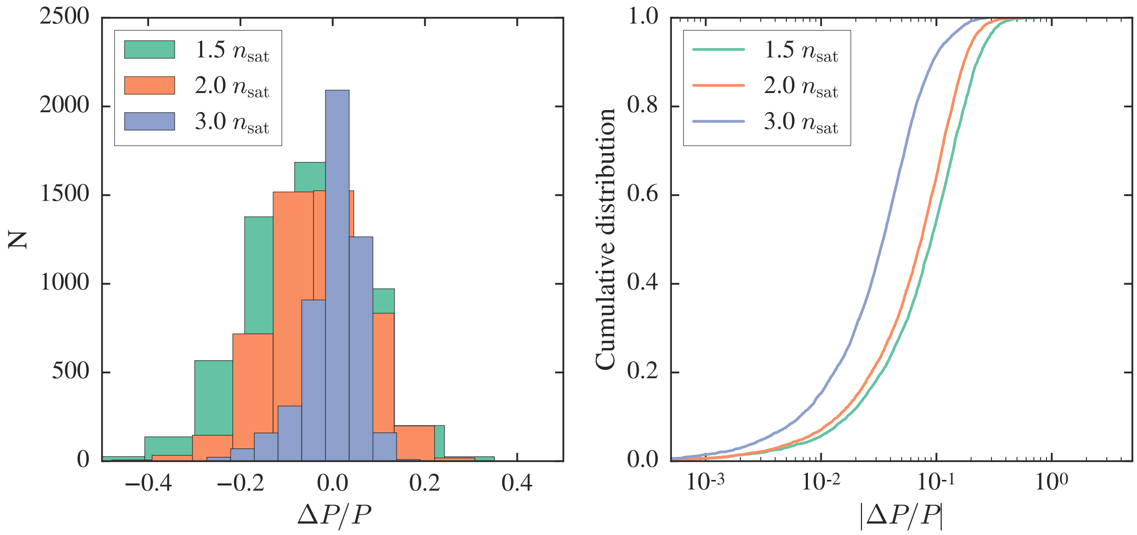

Figure 6.2 Left: Distribution of residuals between the pressure of the full nuclear expansion in eq. (6.8) and our single-polytrope approximation of eq. (6.10), calculated at various fiducial densities (shown in the different colors). Right: Cumulative distribution of the same residuals. We find that the single-polytrope approximation reasonably captures the overall density-dependence of the pressure. At densities of 2 $n_{\rm sat}$, which are expected to determine the neutron star radius and hence the tidal deformability, the errors of our polytropic approximation are $\lesssim$17% for 90% of the EOS in our sample.

fit value for $\Gamma_{\rm poly}$ in Table 6.1. We then use $\min(\Gamma_{\rm poly}, \Gamma_{\rm luminal})$ for densities above $n_{\rm sat}$, and at low densities ($n < 0.5\ n_{\rm sat}$), we use the full, tabulated EOS. We connect between these two regimes with a power-law interpolation. Table 6.1 also shows the fractional error in each quantity, Q, defined as

$$\delta Q = \frac{Q_{\rm EOS} - Q_{\rm poly}}{Q_{\rm EOS}}, \tag{6.14}$$

where Q is calculated using either the full EOS, $Q_{\rm EOS}$, or the polytropic approximation of eq. (6.10), $Q_{\rm poly}$.

We find very small errors in $R_{1.4}$ and $k_{2,1.4}$, which propagate to slightly larger errors in $\Lambda_{1.4}$ of $\lesssim 30\%$, as a result of the strong radius-dependence of $\Lambda \sim R^5$ (see eq. 6.15). Although the errors in $\Lambda_{1.4}$ are modest, we find that our approximation tends to *under*-estimate $\Lambda_{1.4}$, compared to the full EOS. In the following analysis, we will show that the direction of this bias actually acts to further reinforce our results.

We revisit this point in §6.4. Finally, we note that there is no clear correlation between the value of L_0 and the size of the residual for these EOS.

We, therefore, conclude that the single-polytrope approximation reasonably recreates the EOS for most combinations of the nuclear parameters. While this approximation is not exact, it is a useful technique that will allow us to explore the parameter-dependence of $\widetilde{\Lambda}$ in a new way. Our simplified model depends only on S_0 and L_0, thereby reducing a six-dimensional parameter space to two dimensions. This will allow us to directly map from $\widetilde{\Lambda}$ to S_0 and L_0, without requiring us to fix or marginalize over the higher-order terms.

6.4 Relating the tidal deformability to the symmetry energy

Using the framework for pressure introduced in §6.3, we can now connect the observed constraints on $\widetilde{\Lambda}$ from a gravitational wave event to nuclear parameters. We start with the general expression for the tidal deformability of a single star,

$$\Lambda_i = \frac{2}{3} k_2 \left(\frac{G m_i}{R_i c^2} \right)^{-5}, \tag{6.15}$$

where m_i is the mass of the star, R_i is the stellar radius, and, following the convention of Flanagan and Hinderer (2008), we call k_2 the tidal apsidal constant. The tidal apsidal constant depends both on the compactness of the star, as well as the overall density gradient of the particular EOS (Hinderer, 2008; Hinderer et al., 2010; Postnikov et al., 2010).

We follow the method outlined in Hinderer et al. (2010) for constructing a set of augmented Oppenheimer-Volkoff equations. We integrate these stellar structure equations to calculate the stellar mass, radius, and tidal apsidal constant for a given central density. We then compute the effective tidal deformability of the binary system as

$$\widetilde{\Lambda} = \frac{16}{13} \frac{(m_1 + 12 m_2) m_1^4 \Lambda_1 + (m_2 + 12 m_1) m_2^4 \Lambda_2}{(m_1 + m_2)^5}, \tag{6.16}$$

where the subscripts indicate the component stars in the binary system.

We show the effect of L_0 on each of these stellar properties in Fig. 6.3. For demonstrative purposes, in this figure we have fixed S_0=32 MeV and Γ = 3.5, as

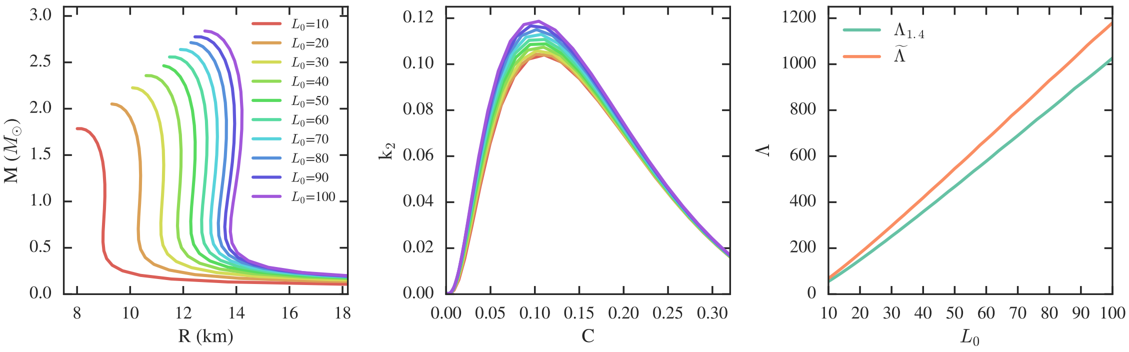

Figure 6.3 Left: Mass-radius curves for our polytropic approximation with varying values for L_0 (in MeV). Middle: Tidal apsidal constants for the same EOS, as a function of stellar compactness ($C = Gm/Rc^2$). Right: Tidal deformability as a function of L_0. In all three panels, we have fixed S_0 to 32 MeV and $\Gamma = 3.5$. In the right panel, $\widetilde{\Lambda}$ is calculated assuming the $q = 0.87$ and $\mathcal{M}_c = 1.186\ M_\odot$, as was observed for GW170817. Within the polytropic approximation, we find that smaller values of L_0 correspond both to smaller radii and to smaller values of k_2, resulting in a smaller tidal deformability.

well as the component masses for calculating $\widetilde{\Lambda}$ (see below for the effect of varying each of these assumptions). We show the mass-radius relations for a variety of L_0 in the left panel of Fig. 6.3. The middle panel panel shows the tidal apsidal constant as a function of the stellar compactness, for the same set of L_0 values. We find that smaller values L_0 lead to both smaller radii and to smaller tidal apsidal constants. Both of these trends act to reduce the tidal deformability of the star (see eq. 6.15), as shown in the right panel of Fig. 6.3. We find that the dependence on L_0 persists both for $\Lambda_{1.4}$ and for the binary tidal deformability, $\widetilde{\Lambda}$. Thus, we expect that the measurement of $\widetilde{\Lambda}$ from a gravitational wave event should have significant constraining power on L_0.

From eq. (6.16) and Fig. 6.3, it is clear that $\widetilde{\Lambda}$ depends on the stellar masses and radii, with an additional dependence on the EOS through k_2. By introducing the chirp mass,

$$\mathcal{M}_c = \frac{(m_1 m_2)^{3/5}}{(m_1 + m_2)^{1/5}} = m_1 \frac{q^{3/5}}{(1+q)^{1/5}}, \tag{6.17}$$

and the mass ratio $q \equiv m_2/m_1$, we can explicitly write the dependences of $\widetilde{\Lambda}$ as $\widetilde{\Lambda}(\mathcal{M}_c, q, R_1, R_2, \mathrm{EOS})$. This is a particularly convenient choice because, for gravitational wave events, we expect the chirp mass to be precisely measured and the mass ratio to also be constrained. This was indeed the case for GW170817, for which the the chirp mass was determined to be $\mathcal{M}_c = 1.186^{+0.001}_{-0.001}\ M_\odot$ and the mass ratio was constrained to $q \in (0.73, 1.00)$ at the 90% confidence level (Abbott et al., 2019).

Additionally, we note that, given the masses of each star, the EOS can be used to uniquely determine the corresponding radii.[5] Within the polytropic approximation of eq. (6.10), the EOS depends only on S_0, L_0, and Γ, where Γ is narrowly constrained to be $\sim 3-4$ for a wide range of realistic EOS. We can, therefore, summarize the dependences of the tidal deformability as $\widetilde{\Lambda} = \widetilde{\Lambda}(\mathcal{M}_c, q, S_0, L_0, \Gamma)$.

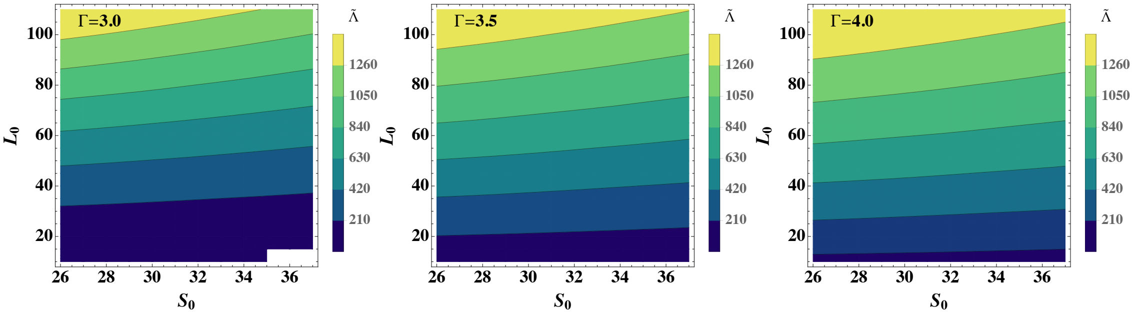

Figure 6.4 The effective tidal deformability of the binary system, as a function of S_0 and L_0. We calculate $\widetilde{\Lambda}$ using the polytropic approximation of the nuclear EOS, shown in eq. (6.10). From left to right, the polytropic index is fixed to $\Gamma = 3$, 3.5, or 4. In all panels, we fix the chirp mass and mass ratio to their central values of $q = 0.87$ and $\mathcal{M}_c = 1.186\ M_\odot$ for GW170817. We find that $\widetilde{\Lambda}$ is only weakly dependent on S_0, but that it is quite sensitive to L_0. The constraints on $\widetilde{\Lambda} = 300\ (+420/-230)$ from GW170817 (Abbott et al., 2019) point to relatively small values of L_0.

We have already shown that $\widetilde{\Lambda}$ depends sensitively on L_0 for fixed S_0 and Γ. In order to explore the full, more general dependences of $\widetilde{\Lambda}$, we perform a grid search across the range $S_0 \in (26, 38)$ MeV and $L_0 \in (10, 110)$ MeV. For each set of values, we construct an EOS according to eq. (6.10), fixing the mass ratio to $q = 0.7, 0.87$, or 1.0 and fixing Γ to 3, 3.5, or 4. In all cases, we fix the chirp mass to the central value from GW170817 of 1.186 $M_{\odot}$. For each combination of parameters, we compute the mass, radius, and tidal apsidal constant by numerically integrating the augmented TOV equations and then compute $\widetilde{\Lambda}$ using eqs. (6.15-6.17). We show the resulting contours of $\widetilde{\Lambda}$ as a function of S_0 and L_0 in Fig. 6.4. The three panels correspond to three different choices of Γ, with fixed $q = 0.87$. We find that the particular choice of q does not significantly affect these or our later results, so we fix q to the central value of 0.87 from GW170817 for the remainder of this analysis. We also note that for some combinations of parameters, such as when Γ and L_0 are very small and S_0 is large, the EOS becomes too soft to support the masses of the stars inferred from GW170817. We indicate these unphysical combinations by leaving the contours white in Fig. 6.4, and we attribute zero probability to them in the following analysis.

---

[5] While there do exist some EOS for which the mass-to-radius mapping is not unique (notably, the so-called "twin-stars," which can have identical masses and different radii; see, e.g., Glendenning and Kettner 2000), these EOS have complex structure that cannot be represented with single polytropes. We, therefore, neglect these special cases for the present study.

We find that $\widetilde{\Lambda}$ is only weakly dependent on S_0, especially for smaller values of $\widetilde{\Lambda}$, as are preferred by the current gravitational wave data. In contrast, $\widetilde{\Lambda}$ depends quite sensitively on L_0. We, therefore, focus on L_0 in the following analysis and fix S_0 to a characteristic value of 32 MeV (Li and Han, 2013; Oertel et al., 2017).

This final simplification renders $\widetilde{\Lambda}$ as a function only of L_0, for fixed Γ. We can, therefore, transform the measured posterior on $\widetilde{\Lambda}$ to a posterior on L_0, according to

$$\mathcal{P}(L_0) = \mathcal{P}(\widetilde{\Lambda}) \left(\frac{\partial \widetilde{\Lambda}}{\partial L_0} \right) , \tag{6.18}$$

where we calculate the Jacobian term numerically.

We show the resulting one-dimensional posteriors on L_0 in Fig. 6.5. Figure 6.5 also shows two current sets of constraints on L_0, in dark and light green from Lattimer and Lim (2013) and Oertel et al. (2017), respectively, which are based on a combination of astrophysical observations of neutron stars, nuclear experiments, and theory. Earlier constraints on $43 < L_0 < 52$ MeV (68% confidence) were calculated using neutron star radii alone (Steiner and Gandolfi, 2012). On the other hand, theoretical calculations of the neutron matter EOS using quantum Monte Carlo

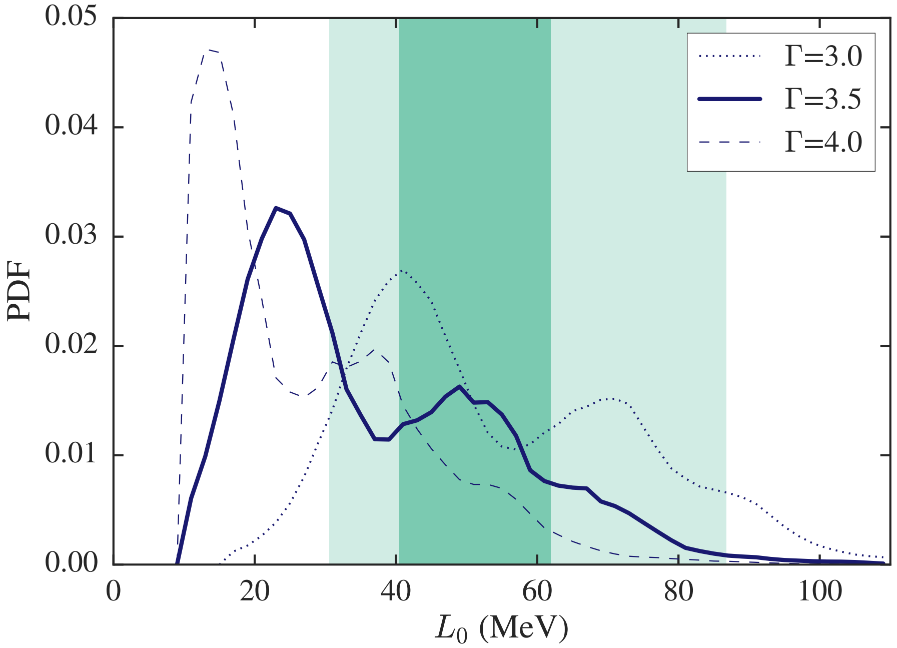

Figure 6.5 One-dimensional posterior in L_0, from GW170817 for $q = 0.87$ and S_0=32 MeV, for three choices of Γ. The dark and light green bands show the combined constraints on L_0 from previous neutron star observations, nuclear experiments, and theory, as calculated in Lattimer and Lim (2013) and Oertel et al. (2017), respectively. We find that the gravitational wave data point towards smaller values of L_0 than these previous studies have found.

methods (Gandolfi et al., 2012) or chiral effective field theory (Hebeler et al., 2013) produce comparable constraints, of $L_0 = 31.3 - 63.6$ MeV and $L_0 = 32.4 - 57.0$ MeV, respectively. We use the summary results from Lattimer and Lim (2013) and Oertel et al. (2017) to encompass these theoretical, observational, and experimental constraints.

We find that the gravitational wave data imply smaller values of L_0 than these previous studies have found. In particular, for $\Gamma = 3.5$, we find a 90% highest-posterior density interval of $11.5 < L_0 < 64.8$ MeV, with a peak likelihood at $L_0 = 23$ MeV. There is a small correlation between the choice of Γ and the inferred constraints on L_0, with choices of larger values of Γ leading to lower values of L_0. We also note that the likelihoods have low-probability tails that extend to quite high values of L_0, which are consistent with the existing experimental constraints. We find roughly equal probability for values of L_0 above or below 30 MeV ($\Gamma = 3.5$), indicating that it is equally likely that L_0 is consistent or inconsistent with the experimental constraints from Oertel et al. (2017), but that these constraints are likely inconsistent with those of Lattimer and Lim (2013). For both $\Gamma = 3.5$ or 4, the peak likelihoods in L_0 lie outside the allowed constraints from either Lattimer and Lim (2013) and Oertel et al. (2017). For $\Gamma = 3$, the peak likelihood falls at the lower limit of the constraint from Lattimer and Lim (2013).

As we noted in §6.3, our polytropic approximation does introduce small errors into the global stellar properties. In particular, we find that for realistic EOS, our polytropic approximation tends to underestimate the tidal deformability. From the right-hand panel of Fig. 6.3, it can be seen that having smaller values of $\Lambda_{1.4}$ effectively pushes the constraints on L_0 to larger values. Thus, the gravitational wave data may prefer even smaller L_0 than we have found here.

However, we note that much smaller values of L_0 may be inconsistent with the observations of neutron stars with $M \approx 2\ M_\odot$ (Demorest et al., 2010; Antoniadis et al., 2013; Fonseca et al., 2016). Within our framework, we find $M_{\max} \geq 2\ M_\odot$ for EOS with $L_0 \gtrsim 20\ MeV$ for $\Gamma = 3.5$ (see the left panel of Fig. 6.3). In contrast, for smaller values of Γ, such low values of L_0 result in EOS with insufficient pressure to support massive neutron stars. For $\Gamma = 3.0$, we find that L_0 must be $\gtrsim 45$ MeV to support $M_{\max} \geq 2\ M_\odot$. Thus, while our most-likely constraints on L_0 are consistent with the observations of massive neutron stars, there is little freedom to reduce L_0 much further, if we take into account this additional observational constraint.

Several recent studies connecting GW170817 to the nuclear EOS have either restricted L_0 to priors similar to those of Lattimer and Lim (2013) and Oertel et al. (2017) or directly marginalized over such priors (Malik et al., 2018; Carson et al., 2019). While the posteriors on L_0 presented here are not exact, they do suggest that GW170817 points toward small values of L_0 that may be in tension with such priors. We, therefore, conclude that it is important to explore the dependence of gravitational wave data on L_0 directly, in order to gain new information on L_0 itself as well as to avoid biasing the interpretation of higher-order parameters.

6.5 Constraints on higher-order nuclear parameters

In §6.4, we showed that GW170817 directly maps to constraints on L_0 using our polytropic approximation of the nuclear expansion. In this section, we turn to the higher-order nuclear terms. In particular, we will show that by taking the polytropic approximation in eq. (6.10), we can place constraints on the allowed combinations of the remaining four nuclear parameters.

We start by equating the polytropic approximation and the full nuclear expansion, and match terms of equivalent order, i.e.,

$$\begin{aligned} aL_0(u+1)^{\Gamma-2} = aL_0 + \left(bL_0 + \frac{K_0 + aK_{\rm sym}}{3}\right) u \\ + \left(cL_0 + \frac{bK_{\rm sym}}{3} + \frac{Q_0 + aQ_{\rm sym}}{18}\right) u^2. \end{aligned} \tag{6.19}$$

For this expression to be true at all densities, the terms of equivalent order must all sum to zero. For example, setting $\Gamma = 3$ implies the constraints

$$(a-b)L_0 - \frac{K_0 + aK_{\rm sym}}{3} = 0 \tag{6.20a}$$

$$cL_0 + \frac{bK_{\rm sym}}{3} + \frac{Q_0 + aQ_{\rm sym}}{18} = 0. \tag{6.20b}$$

Likewise, setting $\Gamma = 4$ implies

$$(2a-b)L_0 - \frac{K_0 + aK_{\rm sym}}{3} = 0 \tag{6.21a}$$

$$(c-a)L_0 + \frac{bK_{\rm sym}}{3} + \frac{Q_0 + aQ_{\rm sym}}{18} = 0. \tag{6.21b}$$

For $\Gamma = 3.5$, we introduce one final series expansion on the left-hand side of eq. (6.19) to simplify $(u+1)^{1.5} \approx 1 + (3/2)u + (3/8)u^2 + \mathcal{O}(u^3)$. Using this approximation, we can again require terms of the same order to sum to zero, and we find

$$\left(\frac{3a}{2} - b\right) L_0 - \frac{K_0 + aK_{\rm sym}}{3} = 0 \tag{6.22a}$$

$$\left(c - \frac{3a}{8}\right) L_0 + \frac{bK_{\rm sym}}{3} + \frac{Q_0 + aQ_{\rm sym}}{18} = 0, \tag{6.22b}$$

where we recall that $a = a(S_0), b = b(S_0, L_0)$, and $c = c(S_0, L_0, K_{\rm sym})$.

Thus, for a given choice of Γ, we have two independent sets of constraints: the first connects the parameter set $\{S_0,\ L_0,\ K_0$, and $K_{\rm sym}\}$, while the second connects $\{S_0,\ L_0,\ K_{\rm sym},\ Q_0,\ Q_{\rm sym}\}$. In the following, we will use the posterior on L_0 from §6.4 to constrain the remaining combinations of higher-order terms using these relationships.

We start with the first set of constraints, on $\{S_0,\ L_0,\ K_0$, and $K_{\rm sym}\}$. These constraints correspond to eqs. (6.20a), (6.21a), and (6.22a). As in § 6.4, we fix S_0=32 MeV and find that this choice does not strongly affect the results. We then use the 90%-credible interval on L_0 from Fig. 6.5 to bound the allowed range of $K_{\rm sym} - K_0$ values. We show the resulting constraints in Fig. 6.6 for each Γ. In this figure, the light shaded regions represent the bounds on the $K_{\rm sym} - K_0$ relationship allowed by the 90%-credible interval on L_0. The dark solid lines indicate the $K_{\rm sym} - K_0$ relationship corresponding to the most likely value of L_0, for a given Γ.

We find that GW170817 places tight constraints on linear combinations of K_0 and $K_{\rm sym}$. For the three values of Γ, fixing L_0 to its maximum likelihood value from Fig. 6.5 yields

$$\Gamma = 3.0: \quad K_{\rm sym} = 108.43 - 1.201 K_0 \tag{6.23a}$$

$$\Gamma = 3.5: \quad K_{\rm sym} = 94.40 - 1.201 K_0 \tag{6.23b}$$

$$\Gamma = 4.0: \quad K_{\rm sym} = 72.57 - 1.201 K_0. \tag{6.23c}$$

These equations correspond to the dark, solid lines in Fig. 6.6. The coefficient in front of K_0 is the same in all three cases because it is given simply by $1/a$ and hence depends only on S_0. The constant term depends on S_0, L_0, and the coefficients of L_0 in eqs. (6.20a), (6.21a), and (6.22a), and thus varies slightly with the choice of Γ.

Previous studies have constrained K_0 by fitting nuclear models to measurements of the isoscalar giant monopole resonance. Depending on the analysis methods, the results range from quite narrow, $K_0 = 248 \pm 8$ MeV (Piekarewicz, 2004) and

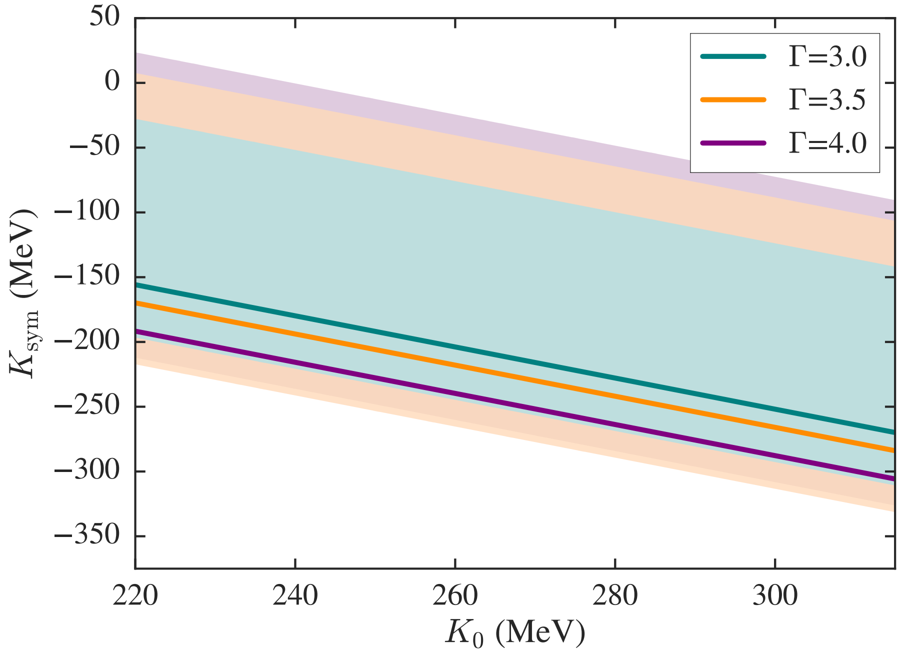

Figure 6.6 Two-dimensional constraints on $K_{\rm sym}$ and K_0, from GW170817. The shaded regions bound the $K_{\rm sym} - K_0$ space allowed by eqs. (6.20a), (6.21a), and (6.22a), for S_0=32 MeV and L_0 corresponding to the 90% confidence intervals from Fig. 6.5. The dark, solid lines represent the $K_{\rm sym} - K_0$ relationship corresponding to the most likely value of L_0 from Fig. 6.5 for each Γ. We find that GW17017 constrains $K_{\rm sym}$ to values $\lesssim 70$ MeV, for a wide range K_0.

$K_0 = 240 \pm 20$ MeV (Shlomo et al., 2006), to broader bounds of $K_0 = 250 - 315$ MeV (Stone et al., 2014). If we take the broadest range of these allowed values and assume $220 < K_0 < 315$ and combine this with our results in Fig. 6.6, we find that $-330 \lesssim K_{\rm sym} \lesssim 25$, at 90% confidence. This constraint on $K_{\rm sym}$ is broader than, but consistent with previous results, including the constraint of $K_{\rm sym} = -111.8 \pm 71.3$ MeV that was derived from universal relations between $K_{\rm sym}$ and lower-order expansion terms (Mondal et al., 2017).

Using the tidal deformability from GW170817, Malik et al. (2018) found constraints of $-112 < K_{\rm sym} < -52$ MeV or $-140 < K_{\rm sym} < 16$ MeV, depending on their choice of prior for L_0. In a similar analysis, Carson et al. (2019) derived constraints of $-259 \leq K_{\rm sym} \leq 32$ MeV, after marginalizing over L_0. Our results, which are derived with the polytropic approximation and no priors on L_0, are consistent with both of these analyses. However, if we take the $K_{\rm sym}(K_0)$ relationship that corresponds to the maximum likelihood in L_0 (i.e., the dark solid lines in Fig. 6.6), we find that the data point to smaller values of $K_{\rm sym}$, below the lower bound from the Malik et al. (2018) study and on the lower end of the Carson et al. (2019) constraints. This is likely a consequence of the fact that these studies both used priors that either forbade or disfavored low values of L_0, such as those we find in this chapter.

Finally, we turn to the second set of constraints on the parameters $\{S_0,\ L_0,\ K_{\rm sym},\ Q_0,\ Q_{\rm sym}\}$. As we did above, we will fix $S_0 = 32$ MeV and use the maximum likelihood in L_0. We can then use eqs. (6.20b), (6.21b), and (6.22b) to calculate the relationship between the remaining four parameters. For the most likely value of L_0, we find

$$\Gamma = 3.0: \quad K_{\rm sym} = 103.4 - 1.73 Q_0 - 1.44 Q_{\rm sym} \tag{6.24a}$$

$$\Gamma = 3.5: \quad K_{\rm sym} = 253.3 - 1.53 Q_0 - 1.28 Q_{\rm sym} \tag{6.24b}$$

$$\Gamma = 4.0: \quad K_{\rm sym} = 311.8 - 1.44 Q_0 - 1.20 Q_{\rm sym}. \tag{6.24c}$$

To our knowledge, no nuclear experiments have constrained Q_0 or $Q_{\rm sym}$ and only broad theoretical bounds have been calculated. For example, Zhang et al. (2017) found $-800 < Q_0 < 400$ MeV based on analyses of energy density functionals. Nevertheless, future experiments or astrophysical observations may one day provide stricter bounds on Q_0 or $Q_{\rm sym}$. Within our polytropic framework, any such measurements can then be used to constrain the correlated parameters using these analytic relationships.

6.6 Conclusions

In this chapter, we have introduced a new approximation of the nuclear EOS which allows for a direct mapping from measured $\widetilde{\Lambda}$ constraints to the symmetry energy parameters. We have shown that a wide sample of nuclear EOS can be reasonably represented with a single-polytrope approximation in the density range of interest, which simplifies the EOS to depend only on S_0, L_0, and Γ, rather than the full six nuclear parameters. Moreover, we find that $\widetilde{\Lambda}$ is relatively insensitive to S_0. With many future gravitational wave detections expected in the coming years, this framework will make it possible to map the gravitational wave event directly to L_0 or to combinations of higher-order nuclear parameters.

With this parameter-space reduction and focusing on the existing measurement of $\widetilde{\Lambda}$ from GW170817, we were able to map from the full posterior on $\widetilde{\Lambda} = 300^{+420}_{-230}$ (Abbott et al., 2019) to posteriors on L_0. We find that GW170817 points to significantly smaller values of L_0 than have been previously been reported, with a peak likelihood of $L_0 \sim 23$ MeV. We additionally use these posteriors on L_0 to constrain combinations of higher-order nuclear parameters, finding tight constraints on the allowed combinations of $K_{\rm sym}$ and K_0, as well as constraints on $K_{\rm sym}, Q_0$, and $Q_{\rm sym}$.

We note that the final constraints on L_0 depend slightly on the choice of Γ and, of course, will depend on the robustness of our polytropic approximation. If the true combination of $K_0, Q_0, S_0, L_0, K_{\rm sym}$, and $Q_{\rm sym}$ produce an EOS with significant sub-structure, then our single-polytrope approximation is not the optimal approach. Moreover, if the dense-matter EOS contains a phase transition to quark matter, then the polytropic approximation will be inadequate and, depending on the particular formulation, the relationship between the tidal deformability and L_0 may be significantly weaker as well (e.g., Zhu et al. 2018).

Nevertheless, the results in this chapter indicate that gravitational wave data can significantly constrain the slope of the symmetry energy for nuclear EOS. This is an important point. Previous studies connecting GW170817 to the nuclear EOS have either fixed the allowed range of L_0 or marginalized over L_0 (Malik et al., 2018; Carson et al., 2019), using priors from nuclear physics that we find to be in modest conflict with the values inferred from GW170817. As the LIGO/Virgo team continue to observe new gravitational wave events and further pin down the tidal deformability of neutron stars, it will become increasingly important to develop robust approaches to constrain the nuclear parameters in model-independent ways.

CHAPTER 7

Optimized Statistical Approach for Comparing Multi-Messenger Neutron Star Data[†]

With the wealth of new results coming in from electromagnetic observations of astrophysical sources, gravitational wave detections of binary systems, and laboratory-based nuclear experiments – as well as the new direct mappings that let us directly compare these results, as developed in Chapters 4-6 – we are now in an era of true multi-messenger constraints on the neutron star EOS. In this chapter, we explore the statistical biases that can arise when such multi-messenger data are mapped to a common domain for comparison. We find that placing Bayesian priors individually in each domain of measurement can lead to biased constraints. Using the first two binary neutron star mergers as an example, we show that a uniform prior in the tidal deformability can produce inflated evidence for large radii, even in the absence of a measured signal. We present a new prescription for defining Bayesian priors consistently across different experiments, which will allow for robust cross-domain comparisons. Finally, using this new prescription, we provide a status update on multi-messenger EOS constraints on the neutron star radius.

7.1 Overview of multi-messenger data for neutron stars

We start with a brief overview of current multi-messenger observations of neutron stars. On the astrophysical side, X-ray observations of surface emission from neutron stars in low-mass X-ray binaries (LMXBs) have constrained the radii of at least a dozen sources (Özel et al. 2009; Güver et al. 2010; Guillot et al. 2013; Guillot and Rutledge 2014; Heinke et al. 2014; Nättilä et al. 2016; Özel et al. 2016; Bogdanov et al. 2016; for a recent review, see Özel and Freire 2016). Under the assumption that all neutron stars have a common radius, these measurements combine to yield a narrowly-constrained radius of $R = 10.3 \pm 0.5$ km (Özel et al., 2016). Additionally, the NICER collaboration recently reported the first radius constraint for an isolated X-ray pulsar (Bogdanov et al., 2019), which is quite broad but seems to favor relatively large radii, $R = 12.71^{+1.14}_{-1.19}$ km, for a multi-component, phenomenological set of pulse-profile models (Riley et al., 2019). The LIGO-Virgo collaboration has also now detected two likely binary neutron star mergers. The first event, GW170817, provided strong constraints on the effective tidal deformability of the binary neutron star system, $\widetilde{\Lambda} = 300^{+430}_{-220}$ (Abbott et al., 2017c, 2019). While there was no strong detection of tidal effects in the second event, GW190425, the masses from this event render it likely to be a second binary neutron star system, which some studies have already used in placing new, multi-messenger constraints on the neutron star EOS (The LIGO Scientific Collaboration et al., 2020; Dietrich et al., 2020; Landry et al., 2020).[1]

[†] A version of this chapter has been submitted for publication to ApJ as Raithel, Özel, and Psaltis, (2020, submitted). *Optimized statistical approach for comparing multi-messenger neutron star data.* This work was supported in part by Chandra Grant GO7-18037X. CR was supported by NSF Graduate Research Fellowship Program Grant DGE-1746060.

In addition to these astrophysical measurements, a wide variety of nuclear experiments have placed complementary constraints on the low-density portion of the EOS. For example, the two-body potential can be constrained from nucleon-nucleon scattering data at energies below 350 MeV and from the properties of light nuclei, which directly informs the EOS at densities near the nuclear saturation density, $n_{\rm sat}$ (Akmal et al., 1998; Morales et al., 2002). Experimental constraints are also often expressed in terms of the nuclear symmetry energy, which characterizes the difference in energy between pure neutron matter and symmetric nuclear matter. The value of the nuclear symmetry energy at $n_{\rm sat}$ and its slope, L_0, have been constrained by fits to nuclear masses; by measurements of the neutron skin thickness, the giant dipole resonance, and electric dipole polarizability of ^{208}Pb; and by observations of isospin diffusion or multifragmentation in heavy ion collisions (e.g., Danielewicz 2003; Centelles et al. 2009; Roca-Maza et al. 2013; Tamii et al. 2011; Tsang et al. 2012; see Oertel et al. 2017 for a recent review).

---

[1] The LIGO Scientific Collaboration et al. (2020) does point out that, due to the weak measurement of tidal effects, it remains possible that GW190425 contains at least one black hole. Throughout this chapter, we will assume that GW190425 was, in fact, a binary neutron star merger, as is assumed in the majority of the discovery paper (The LIGO Scientific Collaboration et al., 2020).

With this diversity of data, the question then arises of how one might robustly compare the results across the various domains. In this chapter, we will provide one self-consistent method for comparing posteriors on the neutron star EOS from different types of experimental data, for any domain in which the prior is defined. This method allows one to directly compare previously-published posteriors on observable neutron star properties. As such, this approach is different from, but complementary to full Bayesian inferences, which attempt to combine multi-messenger data to constrain the parameters of the EOS itself (for further discussion, see § 7.2). For the properties considered in this chapter, we will focus specifically on recent constraints from X-ray observations of the neutron star radius, gravitational waves constraints on $\widetilde{\Lambda}$, and nuclear experiments constraining L_0. As we will show, defining priors self-consistently across the multiple domains is critical for ensuring unbiased constraints.

We start in § 7.2 with an overview of currently-used approaches for cross-domain comparisons of neutron star data and we highlight some common pitfalls of these methods, which motivate this work. In §7.3, we provide a brief review of Bayesian statistics, in order to define the issues that arise when defining priors across different domains. We then introduce consistent sets of Bayesian priors for the various domains of comparison that are relevant for EOS constraints and we comment on the use of a Jeffreys' prior to solve this problem. In §7.4, we derive a set of analytic transformation equations that facilitate the mapping of posteriors between any two domains, making use of previously-published mappings between the nuclear symmetry energy and the radius, as well as between the radius and the binary tidal deformability. These transformation functions allow for diverse sets of archival posteriors to be compared self-consistently. In §7.5, we apply the newly-derived priors to the concrete example of the measured tidal deformability from GW170817 and GW190425. The choice of priors strongly dominates for the weakly-informative GW190425, but for both events, the choice of a uniform prior in the tidal deformability inflates the evidence for large radii, while a uniform prior in R points towards smaller radii. Finally, in §7.6, we combine a set of archival posteriors from X-ray observations, the two gravitational wave events, and a recent study using heavy-ion collisions and we present summary constraints on the neutron star radius.

7.2 Motivation and past work

Many studies have attempted to address the question of how to combine multi-messenger data to constrain the neutron star EOS. Currently, there are several different approaches that are commonly used in the literature. In this section, we will give an overview of these methods and will highlight that, in the absence of a community consensus on the appropriate prior distributions to assume, the particular choice of priors can significantly affect the resulting constraints.

One way of combining multi-messenger data is to perform a Bayesian inference, in which a single set of priors is defined in the EOS domain and likelihoods are sampled in all domains of measurements (e.g., Steiner et al., 2010; Wade et al., 2014; Steiner et al., 2016; Özel et al., 2016; Raithel et al., 2016; Riley et al., 2018; Landry and Essick, 2019). Even though a Bayesian inference is, in principle, robust, there are still choices to be made when setting up the framework. For example, while certain priors are widely agreed upon, such as the requirement for the EOS to maintain thermodynamic stability and for the sound speed to remain subluminal, others, such as which parametrization to use or what priors to place on the parameters of a particular model, are still being debated. Several studies have explored the role of the EOS priors in inferences from X-ray radii (e.g., Steiner et al., 2016) or from gravitational waves (e.g., Carney et al., 2018), and have found that the result is indeed sensitive to the choice of parametrization. In order to avoid this sensitivity, Landry and Essick (2019) recently introduced a non-parametric inference scheme, which uses Gaussian processes trained on a sample of theoretical EOS models. While this approach allows for more direct characterization of the errors of the inferred EOS function, it too requires a choice when defining the priors. In Landry and Essick (2019), the priors are conditioned on a set of published EOS, which may reflect historical trends more than the true range of possible physics.

Additionally, Bayesian inference schemes tend to be computationally expensive. Calculating each likelihood requires an integration of the TOV equations to compute masses, radii, and tidal deformabilities for every EOS sampled within the inference scheme. As a result, it remains common to instead make use of archival (i.e., published or publicly available) posteriors on intermediate parameters, such as R or $\widetilde{\Lambda}$ (see Riley et al. 2018 for further discussion).

Archival posteriors can provide a useful consistency check between astrophysical observations and a proposed EOS, at low computational cost. This provides an alternative method for using multi-messenger data to inform EOS theory. For example, many recent EOS analyses (e.g., Krastev and Li, 2019; Lim and Holt, 2019; Blaschke et al., 2020; Christian and Schaffner-Bielich, 2020; Fattoyev et al., 2020; Khanmohamadi et al., 2020; Marczenko et al., 2020) have compared the predictions of their models to some combination of posteriors on $\Lambda_{1.4}$ from GW170817, posteriors on R from GW170817, as inferred either through a Bayesian inference (e.g., using a spectral EOS, as in Abbott et al., 2018) or using quasi-universal relations (e.g., Annala et al., 2018; De et al., 2018; Most et al., 2018; Raithel et al., 2018; Coughlin et al., 2019; Radice and Dai, 2019; Raithel, 2019), and posteriors on R from the recent NICER measurement (Miller et al., 2019; Riley et al., 2019). Other studies have sought to incorporate more directly different types of measurements, combining, for example, nuclear constraints on L_0 with the LIGO posteriors on $\widetilde{\Lambda}$ (Malik et al., 2018; Carson et al., 2019) and additionally with NICER posteriors on R (Zimmerman et al., 2020), or directly comparing constraints from different sources (e.g., Raithel 2019 for a comparison of LMXB posteriors and radii inferred from posteriors on $\widetilde{\Lambda}$; or Raithel and Özel 2019 for a comparison of posteriors on $\widetilde{\Lambda}$

and nuclear constraints on L_0).

However, each of the above studies combines sets of posteriors that assume different – and, as we will show, incompatible – sets of priors. These mixed priors imply inconsistent assumptions about the universe that cannot be held simultaneously. For example, the radius measurements that come from NICER or LMXBs tend to assume a flat prior in R. In contrast, the LIGO posteriors on the tidal deformability of GW170817 assume a flat prior in $\widetilde{\Lambda}$ (Abbott et al., 2017c, 2019), and any radius constraints from GW170817 that were inferred using the quasi-universal relations between $\widetilde{\Lambda}$ and R also implicitly assume this flat-in-$\widetilde{\Lambda}$ prior. Because $\widetilde{\Lambda}$ is a strong function the neutron star radius (De et al. 2018; Raithel et al. 2018), a flat distribution of $\widetilde{\Lambda}$ implies a distribution of radii that strongly favors large radii. Similarly, a flat prior distribution in the spectral indices of an EOS predicts a distribution of radii and tidal deformability that increases with larger values (see, e.g., Fig. 2 of Jiang et al. 2020). Because L_0 also depends on $R_{1.4}$ (Lattimer and Prakash, 2001), a flat distribution in L_0 implies a non-uniform distribution in R and $\widetilde{\Lambda}$ as well. Because of these non-linear relationships, flat priors in R, $\widetilde{\Lambda}$, L_0, and the spectral EOS indices are fundamentally incompatible with one another.

Combining posteriors that assume inconsistent priors can lead to biased conclusions, which we demonstrate with a simple example in Fig. 7.1. We start by requiring consistency between a particular theoretical EOS (shown as either dashed or dotted lines, for two sample EOS) and a set of two archival posteriors on the radius. In this example, one set of posteriors comes from a fictitious X-ray radius measurement (shown in green; assumes a flat-in-R prior) and the second set of posteriors comes from GW170817 (excluded 90% bounds shown with the purple hatched band; derived assuming a flat-in-$\widetilde{\Lambda}$ prior). When combining these inconsistent priors, we would falsely conclude that the dashed EOS is incompatible with the joint data, while the dotted EOS is allowed. However, if we instead transform the GW170817 radius constraint to assume a prior that is consistent with the X-ray measurement (i.e., flat-in-R; shown in orange), we find that, in fact, the dotted EOS is ruled out by the joint posteriors, while the dashed EOS is allowed, at 90% confidence. Similar false conclusions can be drawn whether the consistent set of priors is ultimately defined in the radius domain, the $\widetilde{\Lambda}$-domain, or some other domain altogether. Clearly, defining priors self-consistently is necessary for deriving unbiased constraints.

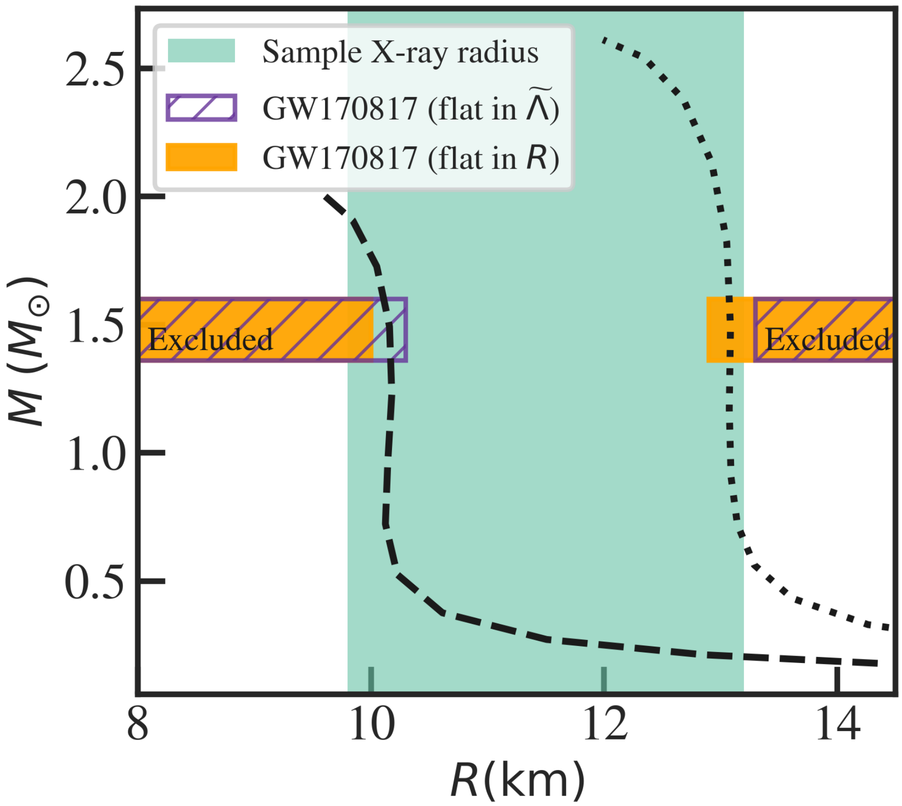

Figure 7.1 Example consistency check between two theoretical EOS (shown as dashed and dotted lines) and a collection of astrophysical data. A fictitious, broad radius constraint from an X-ray observation is shown in green. We also show the 90%-confidence exclusion bounds on the radius that are inferred from the LIGO posteriors on $\widetilde{\Lambda}$ (Abbott et al., 2019), with two different choices of priors. In the purple hatched band, we show the radii that are excluded if one assumes a flat prior in $\widetilde{\Lambda}$, as was used by the LIGO-Virgo collaboration. The orange band shows the radii that are excluded if a flat prior in radius is instead assumed (we will derive these bounds in §7.5). If the X-ray radius measurement, which assumes a flat-in-R prior, and the raw gravitational wave constraint, which assumes a flat-in-$\widetilde{\Lambda}$ prior, are combined, then the dashed EOS would be ruled out at 90%-confidence, while the dotted EOS would be allowed. In contrast, if we require consistent priors that are both defined as flat-in-R (green and orange), then the dotted EOS would be rejected, while the dashed EOS would be consistent with both measurements.

While this conclusion may be a general feature of Bayesian statistics, our goal in this chapter is to demonstrate the importance of maintaining self-consistent priors and provide a method for doing so, specifically within the context of the neutron star literature, where it remains common to combine inconsistent priors and where the definition of a "non-informative" prior varies across subfields. Most work highlighting the role of priors in constraining the neutron star EOS has focused on Bayesian inference schemes, and hence focuses on priors that are defined within the EOS domain (e.g., Steiner et al., 2016; Carney et al., 2018). Here, we focus on priors that are defined in external, observable domains, specifically for use in transforming the archival posteriors on R, L_0 and $\widetilde{\Lambda}$ that are widely used for cross-domain comparisons.

7.3 Defining Bayesian priors

We start with a general review of Bayesian statistics, in order to illustrate the problems that can arise when performing cross-domain comparisons of archival posteriors. Bayes' theorem states that, when modeling some collection of data with a set of parameters $\vec{\theta}$, the posterior distribution on $\vec{\theta}$ is given by

$$P(\vec{\theta}|\text{data}) = P_{\text{pr}}(\vec{\theta})\mathcal{L}(\text{data}|\vec{\theta}), \tag{7.1}$$

where $P_{\text{pr}}(\vec{\theta})$ represents the Bayesian prior on $\vec{\theta}$ and $\mathcal{L}(\text{data}|\vec{\theta})$ represents the likelihood of observing the measured data given a particular set of values for $\vec{\theta}$.

We can transform this measurement of $\vec{\theta}$ to a new set of parameters, $\vec{\phi}$, with a simple transformation of variables,

$$P(\vec{\phi}|\text{data}) = P(\vec{\theta}|\text{data})\mathcal{J}\left(\frac{\vec{\theta}}{\vec{\phi}}\right), \tag{7.2}$$

where $\mathcal{J}$ represents the Jacobian of transformations. In the case that $\vec{\theta}$ and $\vec{\phi}$ are both single parameters, the Jacobian is simply $|\partial\theta/\partial\phi|$. From eq. (7.2), it is clear that, depending on the nature of this Jacobian, even a broad posterior on $\vec{\theta}$ can potentially lead to stringent constraints on $\vec{\phi}$, simply by the transformation of variables. While this is a general feature of Bayesian priors (e.g., Chapter 1.3 of Box and Tiao, 1992), it becomes particularly relevant for neutron star EOS inferences, in which key parameters of interest – namely, L_0, R, and $\widetilde{\Lambda}$ – are high-powered functions of one another. As a result, requiring simultaneous consistency between a theoretical EOS and a set of posteriors that assume flat priors in more than one of these domains (as in e.g., Krastev and Li 2019; Lim and Holt 2019; Blaschke et al. 2020; Christian and Schaffner-Bielich 2020; Fattoyev et al. 2020; Khanmohamadi et al. 2020; Marczenko et al. 2020), can potentially lead to false conclusions (as shown in Fig. 7.1).

In order to avoid such biases, it is necessary to decide, a priori, what one wants to take as "known" about the population of neutron stars or about the behavior of nuclear matter, and then define priors in the other domains accordingly. There is freedom to choose the domain in which the initial set of priors is defined, but once that choice is made, it fixes the priors for the other variables. In the following, we provide transformation functions that can be used to map a prior on L_0, R, or $\widetilde{\Lambda}$ to the other domains, for use in self-consistent cross-domain comparisons.

We start with priors that are defined with respect to the slope of the nuclear symmetry energy. If we consider L_0 to be the fundamental variable on which we want to define the prior, then we can define corresponding priors on R and $\widetilde{\Lambda}$ according to

$$P_{\mathrm{pr;\ L_0}}(L_0) = P_{\mathrm{pr}}(L_0) \tag{7.3a}$$

$$P_{\mathrm{pr;\ L_0}}(R) = P_{\mathrm{pr}}(L_0)\left|\frac{\partial R}{\partial L_0}\right|^{-1} \tag{7.3b}$$

$$P_{\mathrm{pr;\ L_0}}(\widetilde{\Lambda}) = P_{\mathrm{pr}}(L_0)\left|\frac{\partial R}{\partial L_0}\right|^{-1}\left|\frac{\partial \widetilde{\Lambda}}{\partial R}\right|^{-1}. \tag{7.3c}$$

In these equations, we have introduced a short-hand notation for the prior, $P_{\mathrm{pr;\ X}}(Y)$, which indicates a Bayesian prior on the measurement of a variable Y that is defined with respect to a given prior on X. In defining the transformation of variables, we have chosen to expand the derivatives so that we ultimately have only two derivatives to calculate: $\partial R/\partial L_0$ and $\partial \widetilde{\Lambda}/\partial R$. This choice is particularly convenient because functions for $R(L_0)$ and $\widetilde{\Lambda}(R)$ have been previously reported in other works, as we will review in §7.4.

If we instead choose the radius as the fundamental variable over which to define the prior, then the corresponding priors on the gravitational wave and nuclear parameters are given by

$$P_{\mathrm{pr;\ R}}(L_0) = P_{\mathrm{pr}}(R)\left|\frac{\partial R}{\partial L_0}\right| \tag{7.4a}$$

$$P_{\mathrm{pr;\ R}}(R) = P_{\mathrm{pr}}(R) \tag{7.4b}$$

$$P_{\mathrm{pr;\ R}}(\widetilde{\Lambda}) = P_{\mathrm{pr}}(R)\left|\frac{\partial \widetilde{\Lambda}}{\partial R}\right|^{-1}, \tag{7.4c}$$

where a natural choice for a minimally-informative prior might be a bounded uniform distribution on R.

For the sake of completeness, we also include the set of self-consistent priors that are defined with respect to $\widetilde{\Lambda}$,

$$P_{\mathrm{pr;}\ \widetilde{\Lambda}}(L_0) = P_{\mathrm{pr}}(\widetilde{\Lambda})\left|\frac{\partial \widetilde{\Lambda}}{\partial R}\right|\left|\frac{\partial R}{\partial L_0}\right| \tag{7.5a}$$

$$P_{\mathrm{pr;}\ \widetilde{\Lambda}}(R) = P_{\mathrm{pr}}(\widetilde{\Lambda})\left|\frac{\partial \widetilde{\Lambda}}{\partial R}\right| \tag{7.5b}$$

$$P_{\mathrm{pr;}\ \widetilde{\Lambda}}(\widetilde{\Lambda}) = P_{\mathrm{pr}}(\widetilde{\Lambda}). \tag{7.5c}$$

For the flat prior on $\widetilde{\Lambda}$ that the LIGO-Virgo collaboration assumed for GW170817 (Abbott et al., 2017c, 2019), eq. (7.5) represents the corresponding set of priors that are implied for R and L_0.

Finally, we note that, in this chapter, we focus on prior distributions that are flat in the variable of interest, in order to be consistent with the many published measurements that employ a flat prior in either R, $\widetilde{\Lambda}$, or L_0. Lacking other information on what the distributions for these parameters should be, a flat distribution is a reasonable choice. A truly uninformative prior – e.g., the Jeffreys' prior, for which the posterior is invariant to transformations of the prior (Jeffreys, 1946) – might be a more robust choice. However, the Jeffreys' prior is only well-defined for a particular experiment. For example, a Jeffreys' prior on $\widetilde{\Lambda}$ can be derived from the

Fisher information matrix for a gravitational wave measurement. The posterior for such a measurement will be invariant under a transformation of the Jeffreys' prior to, say, the radius, which can also be used to parameterize the strain data. But, the Jeffreys' prior for R that is derived from the gravitational wave data will not be the same as the Jeffreys' prior for R that would be derived from an X-ray measurement, which involves a different Fisher information matrix. In other words, there is no "global" Jeffreys' prior that can be defined for independent experiments that measure the radius, tidal deformability, and symmetry energy. Thus, even if one were to adopt the Jeffreys' prior for one domain of interest, eqs. (7.3)-(7.5) would still be necessary to transform that prior to the other domains.

7.4 Transformation functions

We now turn to deriving the transformation functions needed to calculate the priors in eqs. (7.3)-(7.5). For each transformation function, we make use of the appropriate relationships and provide the corresponding derivatives.

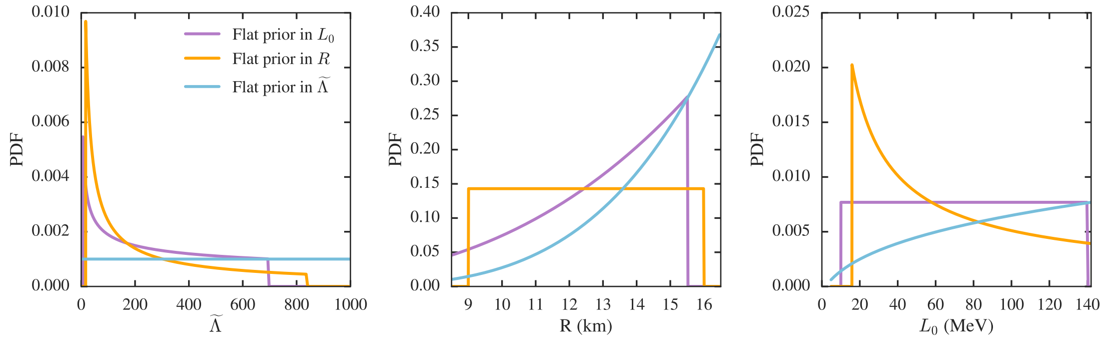

Figure 7.2 *Left*: Prior distributions mapped to the domain of $\widetilde{\Lambda}$. *Center*: Prior distributions mapped to the domain of R. *Right*: Prior distributions mapped to the domain of L_0. The purple lines represent the case of a uniform prior in L_0, which has been transformed to each of the domains using eq. (7.3). The orange lines represent a uniform prior in R, which has been transformed according to eq. (7.4). The blue lines represent a uniform prior in $\widetilde{\Lambda}$, after transformation according to eq. (7.5).

7.4.1 From the nuclear symmetry energy to the neutron star radius

We start at the microscopic level, with the mapping between the the slope of the nuclear symmetry energy, L_0, and the neutron star radius. Many previous studies have found evidence of strong correlations between these parameters (e.g., Lattimer and Prakash, 2001; Steiner et al., 2013; Alam et al., 2016). Here, we use the approximate relation

$$R_{1.4} \simeq (4.51 \pm 0.26) \left(\frac{L_0}{\mathrm{MeV}} \right)^{1/4} \mathrm{km}, \tag{7.6}$$

which was calculated as a function of pressure for a sample of realistic EOS in Lattimer and Lim (2013) and later translated to be a function of L_0 in Tews et al. (2017). The derivative is then simply

$$\frac{\partial R}{\partial L_0} \simeq (1.128 \pm 0.065) \left(\frac{L_0}{\mathrm{MeV}} \right)^{-3/4} \frac{\mathrm{km}}{\mathrm{MeV}}, \tag{7.7}$$

where we have assumed $R \approx R_{1.4}$, as is reasonable for EOS with nearly vertical mass-radius relations.

7.4.2 From tidal deformability to the neutron star radius

We now turn to the relationship between the radius and the effective tidal deformability measured from a gravitational wave event. Several studies have shown that $\widetilde{\Lambda}$ is effectively a mono-parameteric function of the neutron star radius (De et al., 2018; Raithel et al., 2018), which scales quite strongly as $\widetilde{\Lambda} \sim R^{5-6}$, where the exponent varies according to the slightly different assumptions made in these analyses. We use the formalism of Chapter 5 to exactly calculate $\partial\widetilde{\Lambda}/\partial R$ below.

In that study, we used a quasi-Newtonian framework for calculating $\widetilde{\Lambda}$, in which

$$\widetilde{\Lambda} \approx \widetilde{\Lambda}_0 \left[1 + \delta_0 (1-q)^2 \right] + \mathcal{O}\left((1-q)^3 \right), \tag{7.8}$$

where

$$\widetilde{\Lambda}_0 = \frac{15 - \pi^2}{3\pi^2} \xi^{-5} (1 - 2\xi)^{5/2}, \tag{7.9}$$

$$\delta_0 = \frac{3}{104} (1 - 2\xi)^{-2} \left(-10 + 94\xi - 83\xi^2 \right), \tag{7.10}$$

and ξ was introduced as an effective compactness, defined as

$$\xi \equiv \frac{2^{1/5} G \mathcal{M}_c}{R c^2}. \tag{7.11}$$

In these equations, $\mathcal{M}_c$ is the chirp mass, q is the mass ratio of the binary (defined such that $q \leq 1$), G is the gravitational constant, and c is the speed of light. Combining these results, one finds that the radius-dependence of the binary tidal deformability scales approximately as $\widetilde{\Lambda} \sim R^6$.

In this framework, the derivative of $\widetilde{\Lambda}$ is then given by

$$\frac{\partial \widetilde{\Lambda}}{\partial R} \approx \frac{\partial \widetilde{\Lambda}_0}{\partial R} \left\{ 1 + \left[\delta_0 + \widetilde{\Lambda}_0 \left(\frac{\partial \delta_0}{\partial R} \right) \left(\frac{\partial \widetilde{\Lambda}_0}{\partial R} \right)^{-1} \right] (1-q)^2 \right\}, \tag{7.12}$$

where we neglect the higher-order terms and we use the auxillary derivatives given by

$$\frac{\partial \delta_0}{\partial R} = -\frac{\delta_0 \xi}{R} \left[\frac{54 + 22\xi}{-10 + 114\xi - 271\xi^2 + 166\xi^3} \right] \tag{7.13}$$

and

$$\frac{\partial \widetilde{\Lambda}_0}{\partial R} = \frac{5 \widetilde{\Lambda}_0 \xi}{R} \left(\frac{1}{\xi} + \frac{1}{1 - 2\xi} \right). \tag{7.14}$$

The importance of the 2nd-order correction term in eq. (7.12) increases with the chirp mass, $\mathcal{M}_c$, and with the mass asymmetry of the binary. That is, larger values of $\mathcal{M}_c$ and smaller values of q will both act to increase the coefficient of the 2nd-order term. However, even for a very large $\mathcal{M}_c = 1.44\ M_\odot$, as was measured for GW190425, and for $q = 0.7$, as was the lower limit for both GW170817 and GW190425, the correction term is at most 4%. Thus, we neglect the 2nd-order correction term and simply approximate

$$\frac{\partial \widetilde{\Lambda}}{\partial R} \approx \frac{\partial \widetilde{\Lambda}_0}{\partial R}, \tag{7.15}$$

which scales approximately as R^5.

7.4.3 Summary of transformations

We now apply these transformation functions to compute the priors in eqs. (7.3)-(7.5). For each fundamental variable, we assume a bounded uniform distribution.

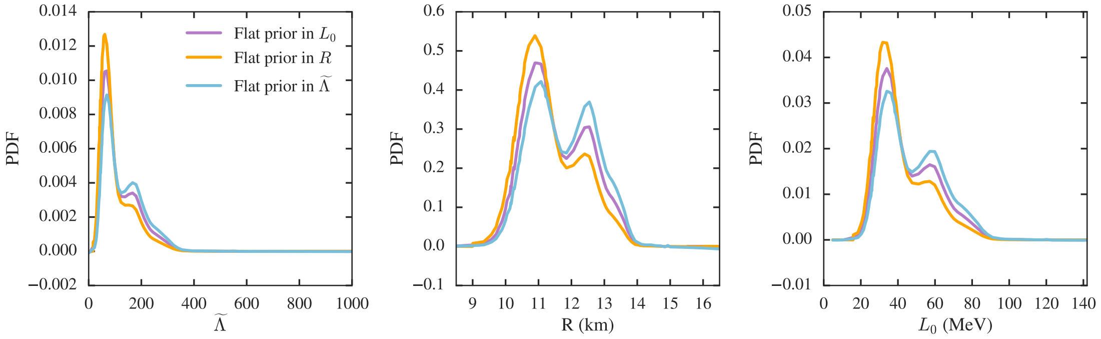

Figure 7.3 *Left*: Posteriors on $\widetilde{\Lambda}$ from GW170817, after reweighting for each set of priors and mapping to the chirp mass of event GW190425. The purple line indicates the case of a uniform distribution in L_0; the orange line represents a uniform prior in R; and the blue line represents a uniform prior in $\widetilde{\Lambda}$, as was originally used by the LIGO-Virgo Collaboration. *Center*: Constraints on R inferred from each posterior on $\widetilde{\Lambda}$. *Right*: Constraints on L_0 inferred from each posterior on $\widetilde{\Lambda}$.

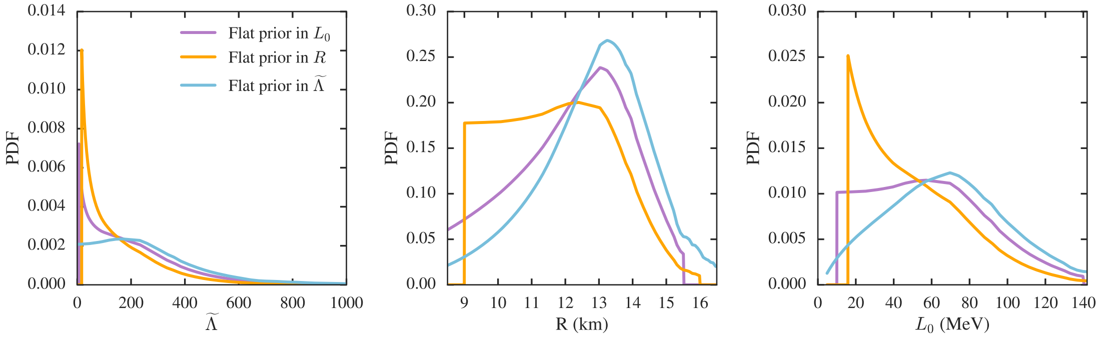

Figure 7.4 Same as Fig. 7.3, but for the posteriors on $\widetilde{\Lambda}$ measured from GW190425. The measurement of $\widetilde{\Lambda}$ was much less significant for this event compared to GW170817, and thus the choice of prior strongly influences the subsequent inference of R or L_0. In particular, for the original prior assumed by the LIGO-Virgo collaboration, the low-significance constraint on $\widetilde{\Lambda}$ implies an artificial measurement of R.

We bound the uniform prior on $\widetilde{\Lambda}$ to be positive and less than 1200, which is well above the limits that were derived for either GW170817 (with an adjusted chirp mass of $\mathcal{M}_c = 1.44\ M_\odot$)[2] or GW190425. We bound the uniform prior on R to be between 9 and 16 km, in order to broadly encompass all viable physics formulations and current measurements. Finally, we bound the uniform prior on the slope of the symmetry energy such that $L_0 \in [10, 140]$ MeV, in order to be approximately consistent with a wide range of experimental results (for a review, see, e.g., Lattimer 2012).

---

[2] The binary tidal deformability is a mass dependent quantity. In order to compare the results from GW170817 and GW190425 directly, we need to re-weight $\widetilde{\Lambda}$ from the two events to have the

We show the resulting transformations of these priors in Fig. 7.2. In blue, we show the original case of a uniform prior on $\widetilde{\Lambda}$, as was used by the LIGO-Virgo collaboration for both GW170817 and GW190425. The middle panel shows how the flat prior in $\widetilde{\Lambda}$ maps to a highly informative prior in R, which is biased towards large radii. The right panel shows that a flat prior in $\widetilde{\Lambda}$ is moderately biased towards larger values of L_0. Figure 7.2 also shows how a uniform prior in R or L_0 transforms to the other domains, in orange and purple lines, respectively. Clearly, a "non-informative" prior in one domain can be highly informative in a different domain.

Figure 7.2 also demonstrates the incompatibility of assuming flat priors in more than one of these domains. For example, a flat prior in R assigns equal probability to stars with radii of 10 or 15 km, whereas a flat prior in $\widetilde{\Lambda}$ assigns $8.5\times$ more probability to the larger star. A flat prior in L_0 implies that the 15 km star is $\sim 3\times$ more likely than the 10 km star. While any of these may be a valid prior distribution to choose, they clearly describe very different physical assumptions.

7.5 Example application to gravitational wave data

With these transformation functions in hand, we now turn to a concrete example, in order to further highlight how the interpretation of some specific measurements can rely on the priors. In this section, we will calculate posteriors for $\widetilde{\Lambda}$ using priors that are minimally informative in either $\widetilde{\Lambda}$, R, or L_0. We will then map each set of posteriors to constraints on R and L_0, in order to illustrate the sensitivity of the

---

same chirp mass. Thus, we adjust the chirp mass of GW170817 to match the central value of the chirp mass for GW190415, $\mathcal{M}_c = 1.44\ M_{\odot}$, in order to facilitate this comparison. For the chirp-mass adjusted posteriors on $\widetilde{\Lambda}$ from GW170817, see The LIGO Scientific Collaboration et al. (2020).

resulting constraints to the particular choice of priors.

We start with the posteriors on $\widetilde{\Lambda}$ from GW170817, which were measured assuming a flat prior in $\widetilde{\Lambda}$ (Abbott et al., 2017c, 2019). These posteriors are shown in blue in the left panel of Fig. (7.3), for an adjusted chirp mass of $\mathcal{M}_c = 1.44\ M_{\odot}$. We then modify the published posterior to calculate the posterior that would have been inferred had the prior been uniform in radius (shown in orange) or uniform in L_0 (shown in purple). We calculate these new posteriors as

$$P(\widetilde{\Lambda}|\text{data}) = P_{\text{old}}(\widetilde{\Lambda}|\text{data}) \left[\frac{P_{\text{pr, new}}(\widetilde{\Lambda})}{P_{\text{pr, old}}(\widetilde{\Lambda})} \right], \tag{7.16}$$

where $P_{\text{pr, new}}(\widetilde{\Lambda})$ indicates the new prior, which is given by eq. (7.3c) for the case of a uniform prior in L_0 or by eq. (7.4c) for the case of a uniform prior in R . Here, $P_{\text{pr, old}}(\widetilde{\Lambda})$ represents the original, uniform prior on $\widetilde{\Lambda}$ and $P_{\text{old}}(\widetilde{\Lambda}|\text{data})$ represents the original, published posterior. By dividing the reported posterior by the old prior, we recover the original likelihood.

We then transform each of the three, new posteriors on $\widetilde{\Lambda}$ to find the corresponding constraints on R, according to

$$P(R|\text{data}) = P(\widetilde{\Lambda}|\text{data}) \left| \frac{\partial \widetilde{\Lambda}}{\partial R} \right|. \tag{7.17}$$

We similarly transform the posteriors on $\widetilde{\Lambda}$ to constraints on L_0, according to

$$P(L_0|\text{data}) = P(\widetilde{\Lambda}|\text{data}) \left| \frac{\partial \widetilde{\Lambda}}{\partial R} \right| \left| \frac{\partial R}{\partial L_0} \right|. \tag{7.18}$$

The inferred constraints on R and L_0 are shown in the middle and right panels of Fig. 7.3, respectively. At 68% confidence (highest-posterior density), the radius is constrained to $R = 10.9^{+1.8}_{-0.6}$ km for uniform priors in L_0, $R = 10.9^{+0.8}_{-0.7}$ km for uniform priors in R, and $R = 11.1^{+1.8}_{-0.6}$ km for uniform priors in $\widetilde{\Lambda}$. There is a small difference between the inferred constraints, depending on which choice of prior is used. In particular, assuming a flat prior in $\widetilde{\Lambda}$ or L_0 leads to evidence for slightly larger radii compared to the radii that are inferred when a flat prior distribution in R is assumed. Accordingly, radius constraints that are derived from posteriors on

$\widetilde{\Lambda}$ which assume a flat-in-$\widetilde{\Lambda}$ prior (e.g., Annala et al., 2018; De et al., 2018; Raithel et al., 2018; Coughlin et al., 2019; Radice and Dai, 2019) will tend to favor larger radii, purely as an artifact of the prior. This effect will be important to take into account when comparing gravitational wave constraints on R to X-ray constraints on R, which typically assume priors that are flat in the radius. However, the data for GW170817 are constraining enough that the overall effect of the prior remains small for this event.

In contrast, Fig. 7.4 shows that the constraints inferred from $\widetilde{\Lambda}$ for GW190425 are much more sensitive to the choice of the prior. As for GW170817, the LIGO-Virgo collaboration reported posteriors on $\widetilde{\Lambda}$ assuming a uniform prior distribution on $\widetilde{\Lambda}$ (The LIGO Scientific Collaboration et al., 2020). However, unlike GW170817, the resulting posteriors for GW190425 essentially represent a non-detection: the authors state that they lack the requisite sensitivity to detect matter effects for this system (The LIGO Scientific Collaboration et al., 2020). Nevertheless, they report constraints on $\widetilde{\Lambda}$, the neutron star EOS, and R, assuming that GW190425 is indeed a binary neutron star system based on its component masses. Following suit, we re-weight the reported posteriors on $\widetilde{\Lambda}$ to determine the posteriors that would have been inferred had a uniform prior in R or L_0 instead been used, according to eq. (7.16). The resulting posteriors, and their transformations to R and L_0, are shown in Fig. 7.4.

We find that the choice of prior strongly influences the resulting constraints on R and L_0 for GW190425. In particular, the assumption of a flat prior in $\widetilde{\Lambda}$ leads to the inference of quite large radii, $R = 13.2^{+1.5}_{-1.7}$ km (68% credibility interval), even though no significant matter effects were detected in the actual measurement. The inference of large radii is purely an artifact of the transformation of variables. If we instead use a uniform prior in the radius, then the corresponding constraints on R are also relatively uniform, as one would expect from a non-detection, such that it does not make sense to report a 68% credibility interval. We find that the constraints on R are essentially flat across the range of 9-13 km, with values of $R \gtrsim 13$ km disfavored. Figure 7.4 thus demonstrates that the prior outweighs the actual data for this event. Moreover, Fig. 7.4 demonstrates that comparing in the radius domain, when the measurement and original prior were defined in the $\widetilde{\Lambda}$ domain, can produce inflated evidence for large radii, even in the absence of a measured signal.

The conclusion that the prior outweighs the data for GW190425 may be obvious when the posteriors are examined in the domain in which they are made. In this case, the relatively flat posterior measured for $\widetilde{\Lambda}$ is clearly mostly consistent with the flat prior that was assumed, and we can conclude that the event was not very informative. The picture becomes less clear, however, when transforming to a different domain and then making comparisons in that domain. In fact, several studies are already starting to compare the radii inferred from GW190425, which are completely prior-dominated, to the predictions of theoretical EOS (e.g., Blaschke et al., 2020; Marczenko et al., 2020). Even when made only at a qualitative level, such comparisons provide false evidence for large radii, while the data themselves bear little-to-no constraining power.

The two gravitational wave events that have been detected so far are relatively straightforward to identify as "strongly" and "weakly" constraining events. However, in the coming years, it is likely that the LIGO-Virgo collaboration will measure many events whose constraints on $\widetilde{\Lambda}$ fall in the more intermediate category of constraining power. When interpreting these events, it will be important to not only define priors that are consistent with one another, but to explicitly acknowledge which domain the priors are defined within and to understand how that choice influences subsequent transformations to other observable quantities.

7.6 Composite constraints on the neutron star radius

With the new prescription for defining priors introduced in this chapter, we now present summary constraints on the neutron star radius, using the latest results from X-ray data, gravitational waves, and nuclear constraints on L_0.

These results are summarized in Figure 7.5 for two choices of priors. In this

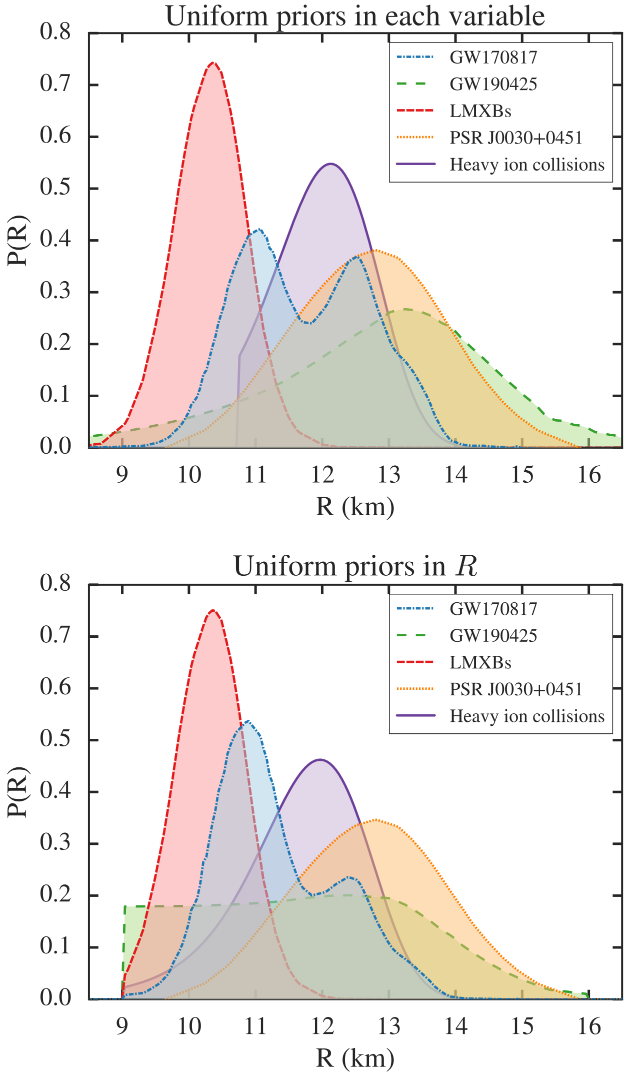

Figure 7.5 *Top*: Constraints on the neutron star radius from X-ray observations, gravitational wave inference, and nuclear experimental data, assuming a uniform prior in each of the measured quantities (i.e., $\widetilde{\Lambda}, R$, and L_0). *Bottom*: Constraints on the neutron star radius from the same data, but now assuming a uniform prior in the radius. We find that using prior distributions that are chosen to be minimally-informative in the radius results in more evidence for smaller radii.

figure, we include likelihoods from GW170817 (in blue, Abbott et al., 2019) and GW190425 (in green, The LIGO Scientific Collaboration et al., 2020), X-ray constraints on the radii of 12 neutron stars in LMXBs (in red, Özel et al. 2016; for an alternative set of LMXB X-ray radius constraints, see, e.g., Steiner et al. 2013), the X-ray timing results from NICER for PSR J0030+0451 (in orange, Riley et al., 2019), and a recent constraint on L_0 from an analysis of single and double ratios of neutron and proton spectra from heavy-ion collisions (in purple, Morfouace et al., 2019). While we only include a single constraint on L_0, we note that this posterior ($L_0 = 49.6 \pm 13.7$ MeV, with values below 32 MeV or above 120 MeV forbidden[3]) is consistent with the results of a recent meta-analysis of several dozen studies that determined $L_0 = 58.7 \pm 28.1$ MeV (Oertel et al., 2017). Thus, we include the Morfouace et al. (2019) results in Fig. 7.5 as a representative and recent example of Bayesian constraints on L_0.

The top panel of Fig. 7.5 shows the composite posteriors on R assuming uniform priors in the domain of each measurement, as is commonly done in the literature; i.e., uniform priors on $\widetilde{\Lambda}$ for the gravitational wave events, uniform priors on R for the X-ray data, and uniform priors on L_0 for the heavy-ion collision inference. In contrast, the bottom panel of Fig. 7.5 shows the constraints on R that are derived when a uniform prior on R is assumed for each measurement. Figure 7.5 illustrates that using a uniform prior in each variable leads to more evidence for larger radii from the $\widetilde{\Lambda}$ and L_0 measurements, while the radius measurements that are made in directly in this domain remain relatively small. Thus, by mixing posteriors with inconsistent priors, the resulting constraints become muddled. In contrast, when we define the priors self-consistently in the radius domain, the resulting constraints are overall shifted to slightly smaller radii and a clearer picture emerges. We note that one could also define the priors self-consistently with respect to $\widetilde{\Lambda}$ or L_0 or even a different parameter altogether, in which case the inferred radii may shift to slightly larger values, compared to the bottom panel of Fig. 7.5, but would, again, provide an internally consistent picture.

---

[3] The constraints from Morfouace et al. (2019) assume a uniform prior for $32 < L_0 < 120$ MeV. Because the prior goes to zero outside of this range, we cannot rigorously recover the likelihood for very large or small values of L_0. Instead, when we re-weight the posterior to use a prior that is uniform in R, we simply assume that the likelihood continues as the inferred Gaussian outside of this range.

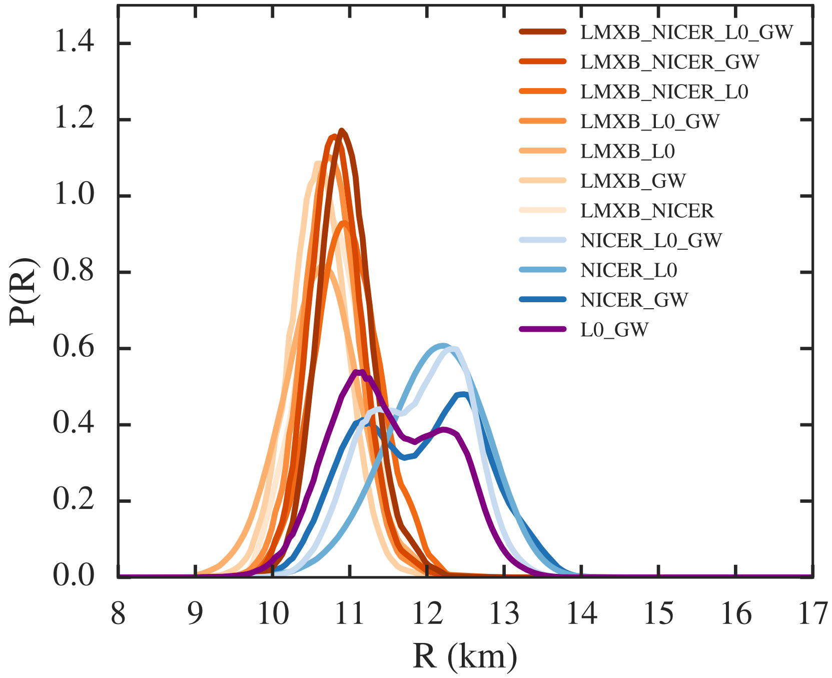

Figure 7.6 Joint posterior distribution on the radius, determined by various combinations of experimental data. Orange lines correspond to any combination of experimental results that include the 12 LMXB sources. Blue lines indicate combinations that include the NICER source, PSR J0030+0451, as the only X-ray data. The purple line shows the constraints inferred from only gravitational wave and nuclear contraints; i.e., with no X-ray data.

Finally, Fig. 7.6 shows the joint posterior distribution for various combinations of these experimental and observational constraints, with uniform priors defined in the radius domain. The orange lines show the joint posterior distributions for any combination of experimental constraints that include the data for the 12 LMXB sources, with the darkest orange line representing the joint posterior including all of the data shown in Fig. 7.5. The blue lines represent the joint posteriors for any combination of data that include the NICER pulsar as the only X-ray source. Finally, the purple line represents the joint posterior for just the nuclear and the gravitational wave constraints (i.e., excluding all X-ray sources).

We find that the data from the 12 LMXB sources (as analyzed by Özel et al. 2016) are the most constraining measurement included in this chapter. Any joint posteriors that contain these data point to $R \sim 10 - 11.5$ km. Moreover, small radii are supported by *any* combination of results that exclude the NICER data, including the combination of gravitational wave and L_0 constraints alone. In contrast, if the NICER source is included as the only X-ray data, then the resulting radii are much larger, $R \sim 12 - 13$ km. Currently, the NICER collaboration has published radius constraints for just a single source, PSR J0030+0451, using a multi-component, phenomenological pulse-profile model to fit the data. As more physical pulse-profile models are developed and more sources are included in the analysis, it will be interesting to see whether this systematic offset persists.

Given the current tension between the NICER constraints and the LMXB and gravitational wave constraints, it is all the more crucial to consider the role of the prior when combining these posteriors. Different choices of the prior – either on exterior parameters like L_0, R, or $\widetilde{\Lambda}$, as considered in this chapter, or on the parameters of the EOS itself – will provide a different relative weight to each of these measurements. Thus, by naively picking a particular prior, one may also be granting more constraining power to a particular type of experiment. Of course, if the chosen prior is well-motivated, then this is exactly what should happen. However, we raise the issue here to point out that – for the current state of sparse, and sometimes conflicting, neutron star data – the choice of even "non-informative" priors can significantly affect the resulting analysis and should be not be adopted naively.

As the community continues to work towards ever-more stringent constraints on the neutron star radius, these joint posteriors can be helpful for understanding the relative constraining power of each additional measurement and how this compares to the information provided by the prior. Joint posteriors can also help to identify systematic offsets between different types of measurements. For a recent example of a comparison of joint posteriors in a fully Bayesian inference that also includes a treatment for systematic offsets, see Al-Mamun et al. (2020). Finally, we note again that regardless of which data are included in any meta-analysis, defining the priors to be self-consistent is an important step towards getting unbiased constraints.

7.7 Conclusions

With the recent flood of multi-messenger constraints on the neutron star EOS, it is important to start identifying the statistical biases that enter into comparisons of these diverse data sets. In this chapter, we have highlighted the importance of defining a consistent set of priors and of understanding the role that those priors play, when transforming to different domains. We introduced a general prescription for calculating consistent priors and derived the relevant transformation functions so that archival posteriors from different experiments can be robustly compared.

Using the example of GW170817 and GW190425, we showed that assuming a Bayesian prior that is "non-informative" in $\widetilde{\Lambda}$ leads to a highly-informative constraint on R, even in the absence of a measured signal. In particular, a flat prior in $\widetilde{\Lambda}$ biases the resulting constraint on R to large values, whereas with a flat prior in the radius provides evidence for slightly smaller radii.

As the community continues to collect more and higher quality data, the relative importance of the priors should diminish. We have already shown this for the case of radius constraints inferred from $\widetilde{\Lambda}$ for GW170817, for which the choice of prior does not strongly affect the resulting posterior. However, for gravitational waves in particular, we may see far more low-significance events than we do GW170817-like events. Thus, if we hope to use the future constraints on $\widetilde{\Lambda}$ to compare with other radius measurements, it is important to account for the role of the assumed priors.

As new events – gravitational and otherwise – continue to be observed, the general prescription introduced in this chapter will facilitate increasingly stringent, and statistically robust, constraints on the neutron star EOS.

CHAPTER 8

The Birth Mass Distribution of Neutron Stars and Black Holes[†]

In the final chapters of this dissertation, we will consider the additional insight into neutron stars can be gained through simulations of dynamical phenomena. We start in this chapter with a study of the neutron star and black hole birth mass distributions. In this work, we use the observed distributions of neutron star and black hole masses to directly confront the predictions of stellar evolution models and one-dimensional neutrino-driven supernova simulations, which were provided by co-author Tuguldur Sukhbold and collaborator Thomas Ertl. We find excellent agreement between the black hole and low-mass neutron star distributions created by these simulations and the observations. We show that a large fraction of the stellar envelope must be ejected, either during the formation of stellar-mass black holes or prior to the implosion through tidal stripping due to a binary companion, in order to reproduce the observed black hole mass distribution. We also determine the origin of one of the bimodal peaks of the neutron star mass distribution, finding that the low-mass peak (centered at $\sim 1.4\ M_{\odot}$) originates from progenitors with $M_{\rm ZAMS} \approx 9 - 18\ M_{\odot}$. The simulations fail to reproduce the observed peak of high-mass neutron stars (centered at $\sim$1.8 $M_{\odot}$) and we explore several possible explanations. We argue that the close agreement between the observed and predicted black hole and low-mass neutron star mass distributions provides new promising evidence that these stellar evolution and explosion models are accurately capturing the relevant stellar, nuclear, and explosion physics involved in the formation of compact objects.

[†] A version of this chapter has been published previously as Raithel, Sukhbold, and Özel (2018). *Confronting Models of Massive Star Evolution and Explosions with Remnant Mass Measurements.* ApJ, 856, 1. We thank Thomas Ertl for his help with the simulations used in this study and for many discussions on this work. We thank Dimitrios Psaltis, Nathan Smith, and Jeremiah Murphy for helpful discussions and comments on this work. We also thank Casey Lam for her input on our reported fit coefficients. During this work, CR was supported by the NSF Graduate Research Fellowship Program Grant DGE-1143953, TS was partially supported by NSF grant PHY-1404311 to John Beacom, and FO was supported in part by a fellowship from the John Simon Guggenheim Memorial Foundation as well as by NASA grant NNX16AC56G.

8.1 Previous studies of the compact object mass distribution

The masses of compact objects that are formed through massive star evolution are relics of the various physical processes that take place during the star's lifetime and subsequent death. First, whether the star explodes and forms a neutron star or implodes to form a black hole is largely determined by the advanced-stage evolution in the stellar core. Beyond the star's fate, the pre-supernova core structure also influences the mass of the resulting neutron star following a successful explosion. If instead the star implodes, the black hole mass is affected by the star's mass loss history. Second, the key processes that take place during the core collapse itself, such as neutrino transport and multi-dimensional turbulence, can also influence the nature of the outcome. Furthermore, the dense matter equation of state plays a role in determining the possible range of neutron star and black hole masses, setting both the maximum neutron star mass and potentially the minimum black hole mass. Because the mass distribution of compact objects is collectively shaped by each of these processes, it has the potential to provide insight into the fundamental physics underlying stellar evolution, the supernova (SN) explosion mechanism, and the dense matter equation of state.

Observationally, the mass distribution can be inferred from the known sample of neutron star and black hole masses. Many black hole masses have been measured from X-ray binary systems, while over 30 precision neutron star masses have been measured from double neutron stars and millisecond pulsars (for a recent review of the latter, see Özel and Freire 2016). To infer the black hole mass distribution, Özel et al. (2010b) combined measurements from 16 low-mass X-ray binaries, finding that it follows an exponential decline. Farr et al. (2011) fit a similar sample of black hole masses from 15 low-mass X-ray binaries, but also included black holes from 5 high-mass X-ray binaries. They found that the low-mass population follows a power-law distribution, while the combined population follows an exponential decline. The mass distribution of neutron stars has also been measured, with an ever-growing and precise sample (Thorsett and Chakrabarty, 1999; Özel et al., 2012; Kiziltan et al., 2013; Antoniadis et al., 2016). The most recent study by Antoniadis et al. (2016) inferred a bimodal distribution, possibly indicating two separate formation channels for creating neutron stars.

From the theoretical side, there have been recent new developments in our understanding of the evolution of massive stars and the modeling of their explosions. In particular, during the advanced stages of core evolution of massive stars, the interplay of convective burning episodes of carbon and oxygen gives rise to final pre-supernova structures that are non-monotonic in initial mass (Sukhbold and Woosley, 2014). The pre-supernova core structure of a massive star, i.e., the density gradient surrounding the iron core, is known to play a pivotal role in determining whether the star explodes or implodes (e.g., Burrows et al. 1995). Several recent studies have explored the connection between this final core structure and the landscape of neutrino-driven explosions of massive stars through numerical and semi-analytical approaches (O'Connor and Ott, 2011; Ugliano et al., 2012; Pejcha and Thompson, 2015; Ertl et al., 2016; Sukhbold et al., 2016; Müller et al., 2016; Murphy and Dolence, 2017). While these works differ in their scope and complexity, all find that there is no single initial mass below which stars only explode and above which only implode. Instead, they recover a much more complicated landscape of explosions as dictated by the pre-supernova evolution of massive stars.

A number of previous studies have explored the connection between the supernova mechanism and the observed distribution in compact objects. For example, Pejcha et al. (2012) used the mass distribution of double neutron stars to constrain the entropy coordinate in the progenitor at which the explosion must originate. In another work, Kochanek (2014) related the observed mass distribution of black holes to the core compactness of the progenitor star, in order to constrain core-collapse

SN models. Both studies, however, used mass cuts, rather than realistic explosion simulations, to determine the predicted remnant masses.

Sukhbold et al. (2016; hereafter, S16) surveyed the explosion outcomes, including the nucleosynthesis yields, light curves, and compact remnants, for a large set of stellar models using a novel one-dimensional neutrino-driven explosion mechanism, based on Ugliano et al. (2012) and Ertl et al. (2016). While three-dimensional models are the gold standard in understanding SN explosions, they are computationally expensive and prohibit an exploration of a large parameter space. Furthermore, although great progress is being made in multi-dimensional explorations of the problem, a consensus has not yet been reached in the community (Janka et al. 2016, and references therein). Though simplified, the one-dimensional treatment in S16 allows for large parameter-space studies. In that work, the authors explored the outcomes due to various parameterizations of the central engine applied to 200 pre-SN stars with initial masses between 9 and 120 $M_{\odot}$. They performed a preliminary comparison of the remnant masses produced in their simulations to the observed populations of black holes and neutron stars, and found reasonable agreement in the produced mass range. However, the comparison was qualitative as they did not properly weight the observed masses or explore any observational biases.

This new, fine grid of stellar evolution models, combined with a simplified, parametric explosion mechanism and combined with a better quantitative understanding of remnant mass distributions, now make it possible to confront these theoretical models with remnant mass observations in a systematic way. One potential difficulty in such a comparison, however, is that the theoretical models describe single-star evolution, while all precision mass measurements come from binary systems. We argue that a meaningful comparison can nevertheless be made for the following reasons.

For late-time mass transfers (cases B and C; Smith 2014), the He-core mass, which is the main determinant for the final pre-SN structure (Sukhbold and Woosley, 2014), is not appreciably affected by the mass transfer. Thus, for these scenarios, the remnant outcome will not be strongly affected by binary evolution. On the other hand, in early stable mass transfers via Roche-lobe overflow, the He core mass can be affected. However, this effect can be at least partially encompassed by a stronger mass loss efficiency in the single-star models. In other words, even though the models here describe single star evolution, due to the uncertain nature of mass loss (e.g., Renzo et al., 2017), the single star models can be representative of some close binary scenarios. We revisit this point in §8.6.3. For millisecond pulsars, which are spun up by accretion from their binary companion *after* forming, Antoniadis et al. (2016) found that the accretion rates onto the neutron star are very inefficient, and that the observed masses must be close to their birth masses. Thus, we take the approach in this chapter that comparing the remnant masses measured from binary systems to theoretical models of single-star evolution indeed can provide a reasonable first constraint on the theoretical models.

With these motivations, we directly confront the stellar evolution models and SN outcomes of S16 with the observed black hole and neutron star mass distributions. We describe the stellar evolution and supernova models in more detail in §8.2. In §8.3, we review the current collection of observed compact object masses. In §8.4, we compute the simulated black hole mass distribution, in order to compare it to the observed distribution on a level playing field. We find that the fraction of the stellar envelope that must be ejected during the SN implosion in order to recreate the observed black hole mass distribution is quite large. In §8.5, we compute the mass distribution of neutron star remnants and find surprisingly close agreement between the simulated outcomes and low-mass peak of the observed bimodal distribution of Antoniadis et al. (2016). We explore the origin of this peak and find that it originates from progenitors with zero-age main sequence masses ($M_{\rm ZAMS}$) in the range $M_{\rm ZAMS} \approx 9 - 18\ M_{\odot}$. We discuss in §8.6 possible explanations for the lack of high-mass neutron stars and LIGO-mass black holes in the simulations. Finally, we discuss the possible implications of our inferred distributions for stellar evolution and explosion models more generally.

8.2 Pre-SN stellar evolution and explosion

The nucleosynthesis yields, remnant masses, and light curves due to neutrino-driven explosions from a wide range of solar metallicity massive stars were surveyed recently in S16. In the following, we briefly highlight aspects of that work that are relevant to the present study.

All of the progenitor models used in S16 were computed using the one-dimensional implicit hydrodynamics code `KEPLER` (Weaver et al., 1978). The main progenitor set consists of 200 non-rotating, solar metallicity models with initial masses between 9 and 120 $M_{\odot}$, and were mostly compiled from Woosley and Heger (2007), Sukhbold and Woosley (2014), and Woosley and Heger (2015). Between the initial masses of 13 and 30 $M_{\odot}$, the models were calculated with 0.1 $M_{\odot}$ increments. As will be shown in §8.5, the large number of models with fine resolution in initial mass space were critical in uncovering discrete branches in the neutron star mass distribution.

Mass loss rates from Nieuwenhuijzen and de Jager (1990) were employed in all models. While the lightest stars don't lose much mass throughout their evolution, the mass loss gradually strengthens with increasing initial mass. The entire envelope was lost for stars with initial masses above 40 $M_{\odot}$ and a Wolf-Rayet wind from Wellstein and Langer (1999) was adopted for these stars. Due to coarse sampling in mass space for high-M_{ZAMS} stars and due to the assumed input physics, nearly all Wolf-Rayet pre-SN stars lost their He-envelopes as well, and, therefore, died as carbon-oxygen (CO) cores.

Although the He core mass, and hence the final pre-supernova structure, is insensitive to mass loss for the lighter stars that don't lose all of their envelope, the masses of black holes that are formed if the star implodes have an appreciable dependence on the adopted prescription of mass loss. For stars with $M_{\mathrm{ZAMS}} < 40\ M_{\odot}$, the amount of envelope remaining sets the range of possible black hole masses upon implosion, while for stars with $M_{\mathrm{ZAMS}} > 40\ M_{\odot}$, the final star mass approximately sets the possible black hole mass.

The final fates of `KEPLER` pre-supernova progenitors were modeled from the onset of core collapse through core bounce and to either a successful explosion or implosion with the Prometheus-Hot Bubble code (`P-HOTB`, Janka and Mueller 1996; Kifonidis et al. 2003). `P-HOTB` is a one-dimensional Eulerian hydrodynamics code with a simplified gray neutrino-transport solver and a high density equation of state (Lattimer and Swesty 1991, with K=220 MeV). The simulations were run for sufficiently long times in order to determine the final mass cuts and explosion energies. For technical details and further discussion see Ugliano et al. (2012) and Ertl et al. (2016).

A major improvement of the recent studies such as S16, Ugliano et al. (2012), and Ertl et al. (2016) over the previous surveys is that the explosion outcomes were free from arbitrary mass cuts and directly dialed-in explosion energies (e.g., Woosley et al. 2002; Chieffi and Limongi 2013; Nomoto et al. 2013). This was achieved by calibrating the free parameters of an analytic proto-neutron star (PNS) cooling model to reproduce the observables of SN1987A for five different models of the progenitor star: W15, W18, W20, N20, and S19.8. Each model resulted in a particular choice of parameters (which we call the "central engine," henceforth) and each central engine was then applied to the 200 `KEPLER` pre-supernova models. Furthermore, S16 improved the low ZAMS-mass end compared to Ugliano et al. (2012) by adding SN 1054 as a calibration anchor and interpolating the core parameters to account for the reduced PNS contraction in the case of small PNS masses (see S16 for details). Finally, each explosion yielded a unique set of observational outcomes, including the remnant mass, that is characterized by the pre-supernova core structure of the progenitor. This, in turn, allowed us to construct the expected compact remnant mass distributions for each central engine.

Figure 8.1 shows the baryonic remnant masses produced by one sample engine (W18) as a function of the initial progenitor mass. A successful explosion results in a neutron star for most models (purple), but in a very small number of cases that experienced significant amount of fallback, a light black hole is formed (gray stars). Since such fallback black holes occur infrequently and only at relatively high mass

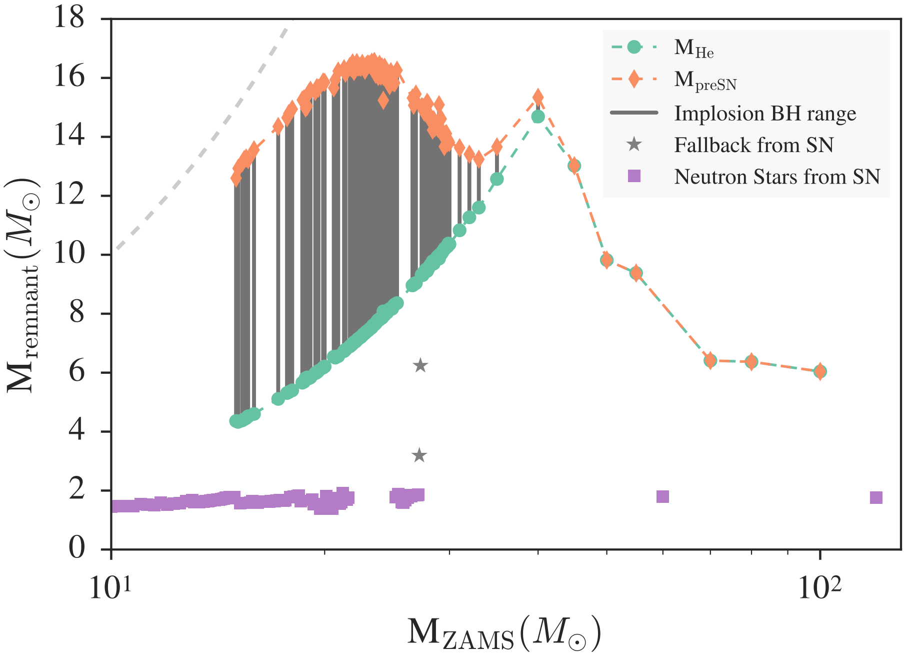

Figure 8.1 Baryonic remnant masses as a function of the progenitor ZAMS mass, for the central engine W18. Neutron star remnant masses from successful explosions are shown in purple. The range of possible black hole masses, shown in gray, is bound by the He-core mass (green circles) and pre-SN mass (orange diamonds) of the progenitor, because an uncertain fraction of the stellar envelope may be ejected either during the formation of the black hole, via the Nadyozhin-Lovegrove mechanism (Nadezhin, 1980; Lovegrove and Woosley, 2013), or prior to the implosion by tidal stripping from a binary companion. The gray dashed line denotes the initial progenitor mass. Note the co-existence of neutron star and black hole outcomes between $M_{\rm ZAMS} \sim 15 - 21\ M_\odot$ and 25–$28 M_\odot$.

models, we omitted them from our analysis.[1]

Although a failed explosion would certainly form a stellar-mass black hole, its exact mass is not well determined for progenitors that retain some amount of envelope by the time of implosion (i.e., for stars with $M_{\rm ZAMS} < 40\ M_\odot$). A weak shock, which is launched by the loss of the proto-neutron star binding energy in the Nadyozhin-Lovegrove effect, may be able to eject a fraction or all of the remaining envelope (Nadezhin, 1980; Lovegrove and Woosley, 2013; Coughlin et al., 2017; Fernández et al., 2017). Additionally, it is possible that some of the progenitor envelope may be stripped by a binary companion prior to the implosion. If common Type I-b/c SNe arise from progenitors that have lost their envelope to a companion (e.g., Dessart et al. 2012, 2015), it would not be surprising to if some of these stripped cores fail to explode. Thus, we might expect that a fraction of all remnant black holes come from the collapse of stripped cores. The black hole masses from stellar implosions (gray lines in Fig. 8.1) are thus bounded by the He-core (green circles) and the final pre-SN (orange diamonds) masses of the progenitor, and ultimately depend on how much of the stellar envelope gets ejected during or prior to the implosion. We analyze this further in §8.4.

---

[1] We verified that the fallback black holes do not affect our conclusions by repeating the analysis described in §8.4 and including an additional branch to model them with a Gaussian distribution. We found no significant change to our results.

Finally, we note the presence of large intervals in $M_{\rm ZAMS}$-space over which the outcomes switch between neutron stars and black holes in Fig. 8.1. As has previously been reported, the explodability of the pre-SN star is not determined by only the initial mass (O'Connor and Ott, 2011; Ugliano et al., 2012; Pejcha and Thompson, 2015; Ertl et al., 2016; Sukhbold et al., 2016; Müller et al., 2016; Murphy and Dolence, 2017). For example, Ertl et al. (2016) propose a new two-dimensional parameter space to characterize pre-SN stars and to predict whether a neutron star or a black hole forms following core collapse. Specifically, a separatrix can be drawn in this space such that any model that falls above it will explode, while models below it will implode. In this framework, we interpret the large intervals of neutron star or black hole outcomes to result from repeated crossings of this separatrix as the initial mass varies and the core structure changes. In addition, there are also smaller intervals in initial-mass space, such as between $M_{\rm ZAMS} \sim 15$ and 21 $M_\odot$ and between 25 and 28 $M_\odot$ in which the locus of pre-SN stars in this parameter space straddles the separatrix and, correspondingly, the outcome frequently changes. As a result, even very small changes in the initial conditions may turn a successful explosion into an implosion or vice versa. We, therefore, interpret the outcomes in these mass ranges not as rapid oscillations between the two types of remnants but rather as the co-existence of two channels with different likelihoods (see also the discussion in Clausen et al. 2015). We show this probabilistic interpretation of outcomes in Fig. 8.2, where we plot the relative fraction of neutron stars produced, $f_{\rm NS}$, as a function of the initial mass. We identify several regions where the outcomes can be only neutron stars, only black holes, or a combination of the two. We use these branches to appropriately weight the remnant outcomes when comparing the simulated and observed mass distributions in §8.4-8.5.

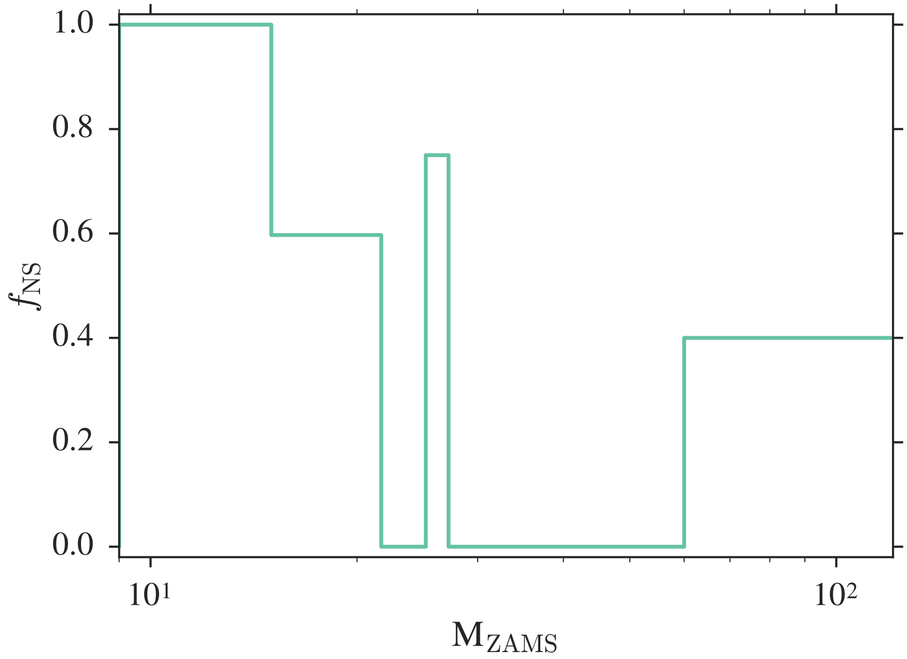

Figure 8.2 Fraction of neutron stars formed as a function of progenitor initial mass, for the outcomes shown in Fig. 8.1. The initial mass has been binned to produce the minimum number of bins while still capturing whether a mass region has only neutron star outcomes, only black hole outcomes, or some combination of the two.

8.3 Observations of remnant masses

The simulation outcomes described in §8.2 can be directly compared to the observed masses of compact objects, as we will describe in §8.4 and 8.5. First, however, we review the current status of the measurements. The observed masses, which are summarized in Fig. 8.3, come from a few primary types of observations: timing and spectra of X-ray binaries containing stellar-mass black holes, timing of millisecond pulsars with white dwarf companions as well as of the double neutron stars, and, most recently, the detection of gravitational waves from black hole-black hole mergers and the first neutron star-neutron star merger.

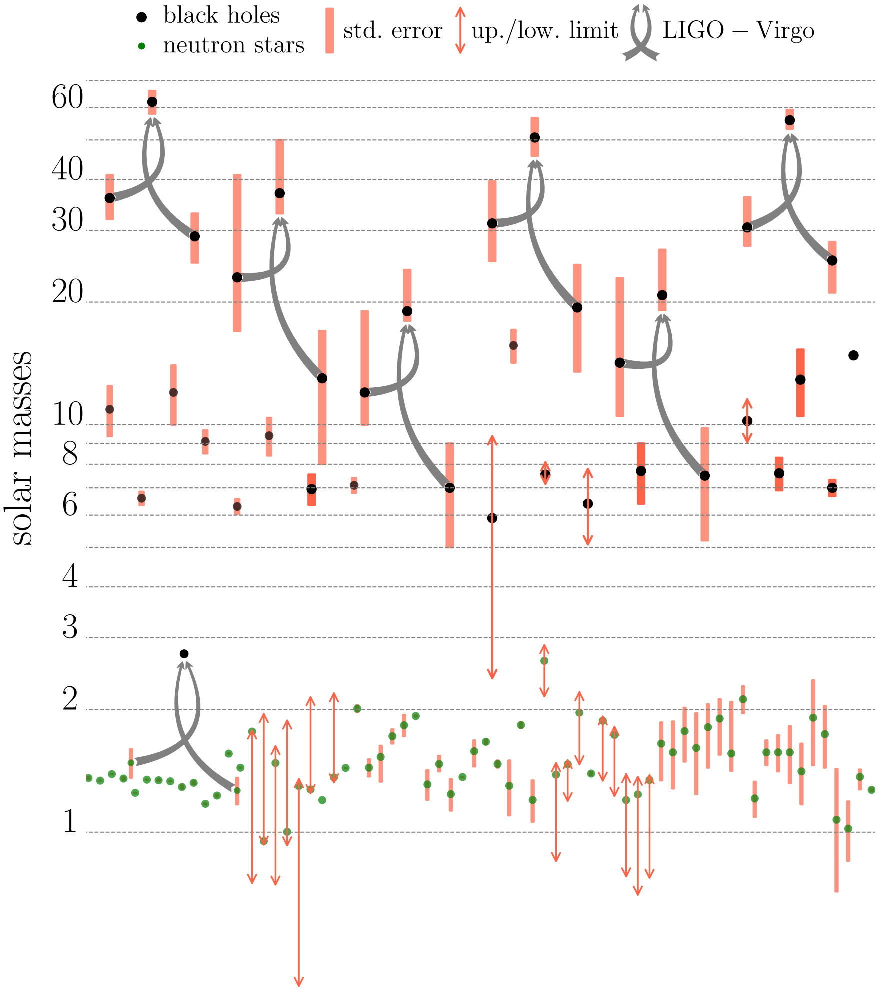

Figure 8.3 Observed masses of neutron stars and black holes. The green points show neutron stars, while the black points show black holes. The red vertical lines represent the error bars for each measurement. The red vertical arrows denote upper and lower measurement limits, and should not be taken as Gaussian uncertainties. The gray arrows connect the progenitors to the outcome mass for each of the six confirmed and one candidate detection of gravitational waves from merging black holes and neutron stars.

Black hole masses are typically measured dynamically from X-ray binaries. Data on 23 confirmed black hole X-ray binaries and on 32 additional transient systems with candidate black hole members have been compiled in Özel et al. (2010b). From these data, masses are provided for 16 confirmed black holes, based on some combination of constraints on the mass ratio, inclination angle, or the mass function for the system. A similar compilation can be found in Farr et al. (2011), which focused on the masses of 15 black holes in low-mass X-ray binaries undergoing Roche-lobe overflow, as well as 5 black holes in wind-fed, high-mass X-ray binaries. Several masses in Fig. 8.3 are also taken from the more recent compilation found on the StellarCollapse website,[1] from Wiktorowicz et al. (2014), and the references therein. Finally, the most recent estimate on GX 339-4 by Heida et al. (2017) has also been included in Fig. 8.3.

Neutron star masses are also measured dynamically, but with different methods. While spectra from an optically bright companion can be used to constrain the neutron star mass, the majority of masses are measured from radio pulsar timing. In particular, for millisecond pulsars with white dwarf companions, the measurement of any post-Keplerian parameters in the pulsar timing residuals can be used to constrain the pulsar mass, when combined with the mass function. Precision masses for 32 millisecond pulsars were recently summarized in Antoniadis et al. (2016). Precision masses for the sub-population of double neutron stars are also determined from the timing measurement of at least two post-Keplerian parameters. For a recent review of all neutron star mass measurements, see Özel and Freire (2016).[2]

Finally, there has been a new addition to these families of mass measurements, thanks to the first detections of gravitational waves by LIGO and subsequently, the LIGO-Virgo Collaboration. To date, five confirmed detections have been made from the mergers of binary black holes (Abbott et al., 2016c,d, 2017b; The LIGO Scientific Collaboration et al., 2017a,b). The sixth set of gravitational wave black holes shown

---

[1] http://www.stellarcollapse.org/bhmasses

[2] The neutron star masses can be found at:

http://xtreme.as.arizona.edu/NeutronStars/data/pulsar_masses.dat in Fig. 8.3 is from the candidate black hole-black hole merger LVT151012 (Abbott et al., 2016b). As shown in Fig. 8.3 and as we will discuss more in §8.6.1, some of these black hole masses are larger than had previously been observed or even thought possible. Additionally, the first detection of gravitational waves from a neutron star-neutron star merger was recently announced (Abbott et al., 2017c), and offers a new way of adding measurements to the collection of neutron star masses as well.

The most uncertain of these masses are those that come from the measurement of a single post-Keplerian parameter in a neutron star or black hole binary, with no additional constraints on the system. Such measurements provide only an upper and lower limit to the component masses, which we represent in Fig. 8.3 with vertical red arrows. These arrows represent a likely mass range for an assumed isotropic distribution of binary inclination and should not be interpreted as Gaussian uncertainties. We also note that Fig. 8.3 does not include any measurements with only an upper or lower limit; we include only points with both an upper and lower limit, or with well-defined error bars. All error bars (shown as the solid red lines) represent the 68% confidence intervals, except for the LIGO masses, which denote 90% confidence intervals. Finally, we note that the black hole mass measurement for NGC 300 X-1 has been excluded due to the likely asymmetric irradiation of stellar winds, which contaminates the mass measurement (Tom Maccarone, priv. communication).

8.4 Black hole mass distribution

Our goal is to directly compare the outcomes of the S16 stellar evolution and SN simulations with the measured remnant masses discussed above. We first focus on the models that produce remnant masses larger than the maximum, theoretically-allowed neutron star mass and, therefore, yield black holes.

The observed masses of compact objects have previously been fit with simple functional forms. The functional forms have been chosen to provide a theoretically motivated description of the data and to help facilitate a direct comparison between the observations and theory. We, therefore, start by creating analytic functions

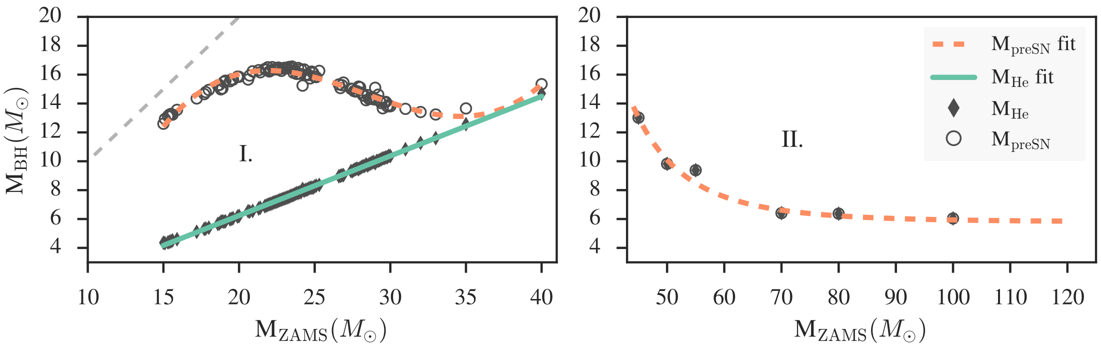

Figure 8.4 Same as Fig. 8.1, but only showing the implosion black holes. Solid diamonds indicate black holes that are formed from the collapse of only the He- or CO-core; open circles indicate black holes formed from the collapse of the entire star. We also label the two progenitor mass ranges, across which we fit the black hole masses with analytic functions. We show the fits to the remnants of implosions in which the entire star collapsed and in which only the core collapsed in orange dashed and green solid lines, respectively.

to model the remnant masses as a function of their ZAMS progenitor masses. By convolving these functions with the initial mass function (IMF), we determine the expected distribution, which can then be directly compared to the observed distribution.

Figure 8.4 shows the black hole remnant masses calculated in the simulations described in §8.2 for engine W18. For simplicity, we only show the outcomes from one particular engine in Fig. 8.4, but we include results from all of the following five engines from S16 in our analysis: W15, W18, W20, N20, and S19.8. Each model produces qualitatively similar results to those shown in Fig. 8.4, so we average the results from each model in the following analysis.

In Fig. 8.4, we also identify two different branches of mass outcomes, so that each branch is well-approximated by a single function. The branches are divided as follows: Branch I spans $15 \leq M_{\rm ZAMS} \leq 40 M_{\odot}$, which corresponds to the range of red supergiant models that retained significant amounts of the envelope upon implosion. Branch II spans $45 \leq M_{\rm ZAMS} \leq 120 M_{\odot}$, which corresponds to the range of models that lost all of their envelopes and die as Wolf-Rayet stars.

In Branch I of the black hole masses, the outcomes are bounded by two possibilities: (1) He-core implosion, which occurs in the event that the entire hydrogen envelope is ejected by a weak shock during the black hole formation or has been tidally stripped by a binary companion prior to the collapse, or (2) implosion of the entire pre-SN stellar mass. In our modeling of these outcomes, we allow for a variable fraction of the envelope to be ejected, which we denote as $f_{\rm ej}$. For the more massive progenitors in Branch II, which do not retain their hydrogen and helium envelopes, $f_{\rm ej}$ has no physical meaning. For these models, the only scenario considered is the collapse of the CO-core.

Accordingly, the filled diamonds in Fig. 8.4 indicate that the entire stellar envelope was ejected prior to or during the implosion and only the core collapsed to form the black hole. We represent remnant masses from this scenario as $\rm M_{BH,core}$, which have an ejection fraction, $f_{\rm ej} = 1$. On the other end of the spectrum, open circles indicate that the entire pre-SN star collapsed to form the black hole. We specify remnant masses from this scenario as $\rm M_{BH,all}$, with ejection fractions of $f_{\rm ej} = 0$.

The gaps between these branches are due to the discrete sampling of the S16 simulations. For Branch I, we separately fit the outcomes from core-only implosions and the implosions in which the entire star collapses with simple functional forms. For Branch II, we consider only the outcomes of core-only implosions. We select the functions from a set of power-law or first-, second-, or third-order polynomials, by minimizing the RMS of the residuals. If the RMS of the residuals is $< 1\%$ for more than one of the polynomials, we take the lowest-order function. However, we note that the conclusions we find are largely independent of the particular models chosen.

The functions for $\rm M_{BH,core}$ and $\rm M_{BH,all}$ differ quite significantly from each other in Branch I because $\rm M_{BH,core}$ depends on the assumed input physics in the stellar modeling but does not depend on the mass loss for this range of progenitor masses, whereas $\rm M_{BH,all}$ is highly sensitive to the particular mass loss prescription and its efficiency. In contrast, for the stars in Branch II, the final masses of the resulting CO-cores are strongly dependent on both the assumed red supergiant and Wolf-

Table 8.1. Fraction of outcomes that yield black holes in each branch of Fig. 8.4 for the five central engine models included in our analysis.

Branch	$X_{\mathrm{BH,W15}}$	$X_{\mathrm{BH,W18}}$	$X_{\mathrm{BH,W20}}$	$X_{\mathrm{BH,N20}}$	$X_{\mathrm{BH,S19.8}}$	$X_{\mathrm{BH,Avg}}$
I	0.686	0.635	0.878	0.500	0.474	0.635
II	0.875	0.750	1.00	0.500	0.500	0.725

Rayet mass loss prescriptions, but the resulting core uniquely determines the black hole mass.

In Branch I, we find that the outcomes from implosions in which only the He-core collapses ($f_{\mathrm{ej}} = 1$) are well-fit by a linear model and find

$$M_{\mathrm{BH,core}}(M_{\mathrm{ZAMS}}) = -2.024 + 0.4130 M_{\mathrm{ZAMS}}, \quad 15 \leq M_{\mathrm{ZAMS}} \leq 40 M_{\odot}. \tag{8.1}$$

with residuals of 0.9%.

For the outcomes in Branch I for the implosions in which the entire star collapses ($f_{\mathrm{ej}} = 0$), we find that a third-order polynomial with parameters

$$\begin{aligned} M_{\mathrm{BH,all}}(M_{\mathrm{ZAMS}}) = 16.28 + 0.00694(M_{\mathrm{ZAMS}} - 21.872) - 0.05973(M_{\mathrm{ZAMS}} - 21.872)^2 \\ + 0.003112(M_{\mathrm{ZAMS}} - 21.872)^3, \quad 15 \leq M_{\mathrm{ZAMS}} \leq 40 M_{\odot} \end{aligned} \tag{8.2}$$

is necessary to keep the residuals ∼1%. A second-order polynomial fit produces larger residuals of ∼4%.

In Branch II, we only consider the implosion of the CO-core, since there is no remaining envelope at these high masses. We find that fitting these outcomes with a power-law model is sufficient and find

$$M_{\mathrm{BH,core}}(M_{\mathrm{ZAMS}}) = 5.795 + 1.007 \times 10^9 (M_{\mathrm{ZAMS}})^{-4.926}, \quad 45 \leq M_{\mathrm{ZAMS}} \leq 120 M_{\odot}. \tag{8.3}$$

with residuals of ∼9%. This larger residual is due to a single data point. Fitting instead with a second- or third-order polynomial improved the residuals by less than

$\sim$0.5% and made no significant change to the final distribution, so we chose to use the simpler power-law model.

In order to probe regimes in which there may be partial ejection fractions, we can extrapolate from our fits of the special cases of $f_{\rm ej} = 0$ or 1, using the approximation

$$M_{\rm BH}(M_{\rm ZAMS}; f_{\rm ej}) = f_{\rm ej} M_{\rm BH,core}(M_{\rm ZAMS}) + (1 - f_{\rm ej}) M_{\rm BH,all}(M_{\rm ZAMS}). \tag{8.4}$$

We use this formalism for its simplicity but also note that the pre-SN core structures and the binding energy outside the He-cores are not identical in models where the stars retain some of their envelopes. As a result, the ultimate fraction of the envelope that gets ejected upon implosion is likely not the same for all progenitor masses. Considering the uncertain nature of this mechanism, in this work we adopt a simple scenario where $f_{\rm ej}$ has the same value for all applicable stars, in order to explore its effect on the resulting black hole mass distribution.

Using this combined model for each branch, we calculate the probability of a particular black hole remnant mass as

$$P(M_{\rm BH}|M_{\rm ZAMS}; f_{\rm ej}) = \left| \frac{dM_{\rm BH}(M_{\rm ZAMS}; f_{\rm ej})}{dM_{\rm ZAMS}} \right|^{-1} \delta[M_{\rm ZAMS} - M_{\rm ZAMS}(M_{\rm BH})], \tag{8.5}$$

where the δ-function encapsulates the relationship between $M_{\rm ZAMS}$ and $M_{\rm BH}$ at the value at which the probability distribution is evaluated. Finally, to get the distribution of black holes for each branch, we marginalize over the progenitor masses, i.e.,

$$P(M_{\rm BH}; f_{\rm ej}) = \int P(M_{\rm BH}|M_{\rm ZAMS}; f_{\rm ej}) P(M_{\rm ZAMS}) dM_{\rm ZAMS}, \tag{8.6}$$

where for the probability of finding a particular mass, $M_{\rm ZAMS}$, in the initial mass distribution, we use the Salpeter IMF,

$$P(M_{\rm ZAMS}) = C(M_{\rm ZAMS})^{\alpha}, \tag{8.7}$$

with α=-2.3 and C=0.065 (Salpeter, 1955).

We weight the probability of each branch by a value, $X_{\rm BH}$, which represents the fraction of outcomes in that branch that produced black holes. These weighting fractions, which are shown in Table 8.1 for each engine, reflect the fact that the explosion outcomes can form either neutron stars or black holes in certain mass ranges, as discussed in §8.2, and need to be treated probabilistically. Note that we do not include fallback cases in the number of successful black holes, but do include them in the number of possible outcomes.

8.4.1 Comparing the simulated and observed black hole mass distributions

We calculate the final black hole mass distribution by summing the probability contributions for each branch, as found in eq. (8.6), and weighting each contribution by the ratios, $X_{\rm BH}$, of Table 8.1. We include in this analysis the results from each of the five central engines, which we average together. We show the resulting black hole mass distribution, for various ejection fractions, in Figure 8.5.

We find that, in general, the smaller the ejection fraction, the narrower the expected mass distribution. This is because the pre-SN mass is less sensitive to the initial mass in Branch I than the He-core mass is, as shown in Fig. 8.4. Additionally, we find that smaller ejection fractions produce larger black holes, as expected. For an ejection fraction of 0, the distribution is confined to $M_{\rm BH} \sim 12 - 16\ M_\odot$, with sharp peaks at ~ 13 and $16\ M_\odot$. In contrast, we find that an ejection fraction of 0.9 leads to a mass distribution with a soft decay, spanning from $M_{\rm BH} \sim 5 - 12\ M_\odot$.

In the bottom panel of Fig. 8.5, we show two black hole mass distributions inferred from the observed black hole masses in our Galaxy. The first distribution was calculated in Özel et al. (2010b) from black hole masses measured from 16 low-mass X-ray binaries. The resulting distribution was well-fit by a decaying exponential. The second distribution was calculated similarly by Farr et al. (2011) from mass measurements of 15 black holes in low-mass X-ray binaries and 5 black holes in high-mass, wind-fed X-ray binaries. In this study, they fit several different models to the data and found strong evidence for an exponentially decaying profile of the

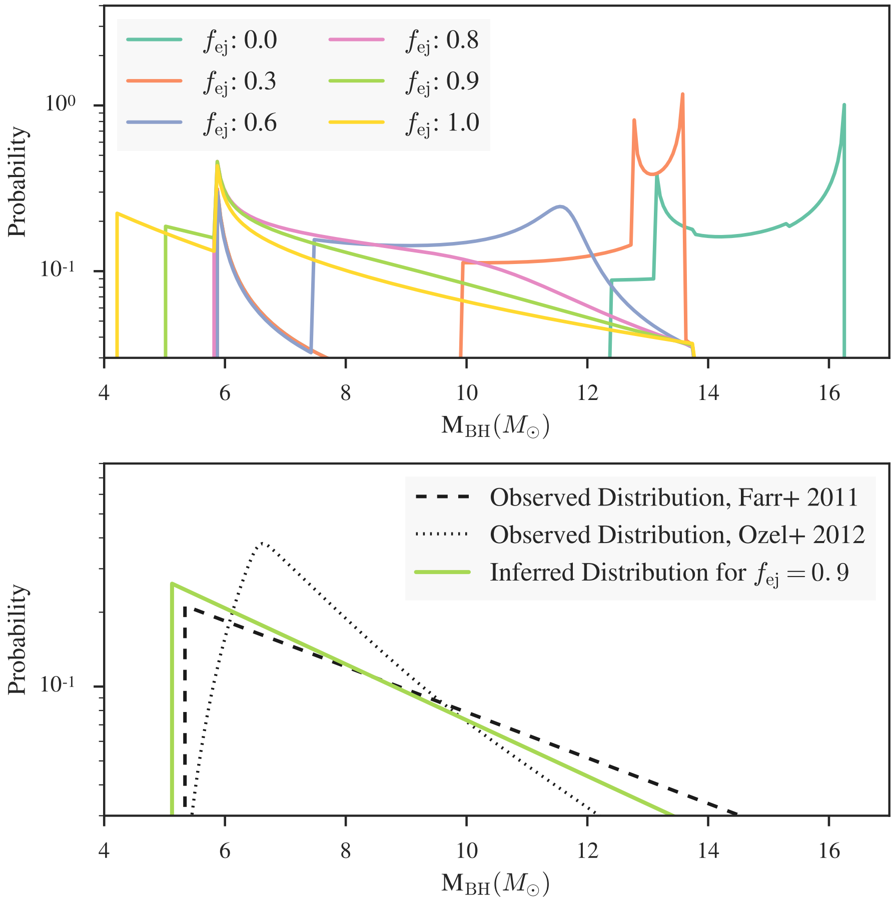

Figure 8.5 *Top:* Mass distribution of black holes averaged from the simulations for all five central engines. Different colors represent different fractions of the stellar envelope that are ejected either during the implosion, by a weak shock, or prior to the implosion, via tidal stripping by a binary companion. *Bottom:* Comparison to the observed mass distributions of Farr et al. (2011) and Özel et al. (2012), shown in the black dashed and dotted lines, respectively. Here, the green line represents the distribution that would be inferred from the underlying simulated distribution for $f_{\rm ej} = 0.9$, if a decaying exponential form is assumed. We find that to recreate the observed distribution, a relatively large ejection fraction is required.

form,

$$P(M_{\rm BH}; M_{\rm min}, M_0) = \frac{\exp(M_{\rm min}/M_0)}{M_0} \times \begin{cases} \exp(-M_{\rm BH}/M_0), & M_{\rm BH} \geq M_{\rm min} \\ 0, & M_{\rm BH} < M_{\rm min} \end{cases}, \quad (8.8)$$

where $M_{\rm min}$ is the minimum black hole mass, which was found to be 5.3268 $M_{\odot}$, and M_0 is a scale mass found to be 4.70034 $M_\odot$ (Farr et al., 2011).

In order to make the comparison between these observed distributions and our simulated distribution more directly, we note that the substructure in the simulated distributions is finer than the typical uncertainties in the observations and would not be observable as is. Thus, we also calculate the distribution that would be inferred from the underlying simulated distribution, by drawing 200 random black hole masses from the simulated distribution and fitting them with the exponential decay model of eq. (8.8). This "inferred," simulated distribution is shown for $f_{\rm ej} = 0.9$ in the bottom panel of Fig. 8.5, and shows close agreement with the observed distribution in our Galaxy.

Finally, we calculate the likelihood of the "inferred" distributions for each ejection fraction, assuming the same functional form of eq. (8.8). We calculate the likelihood as

$$\mathcal{L} = \exp\left[-\sum_i \frac{(P_{\rm inferred}(M_{\rm BH,i}; f_{\rm ej}) - P_{\rm obs}(M_{\rm BH,i}))^2}{P_{\rm obs}(M_{\rm BH,i})} \right], \tag{8.9}$$

where $P_{\rm obs}(M_{\rm BH,i})$ is the probability given in eq. (8.8) for the inferred parameters from Farr et al. (2011), for black holes above the minimum mass of Farr et al. (2011) in our sampling. We show these likelihoods in Fig. 9.8, and find that ejection fractions of $f_{\rm ej} \gtrsim 0.9$ have the highest likelihoods, given the observed mass distribution. This implies not only that the S16 simulations are closely reproducing the black hole masses observed in our Galaxy, but also that a large fraction of the stellar envelope must be ejected in order to form the observed black holes, either during the implosion itself or beforehand, through tidal stripping from a binary companion.

Finally, we note that, for all ejection fractions in the solar-metallicity models of S16, there appear to be no black holes with masses above $12 - 16$ $M_\odot$. This is particularly interesting in light of the recent inferences of black holes with $M \geq 22$ $M_\odot$ that have been made with the first LIGO and Virgo gravitational wave detections (Abbott et al., 2016c,d, 2017b; The LIGO Scientific Collaboration et al., 2017b), as can be seen in Fig. 8.3. We discuss this further in §8.6.1.

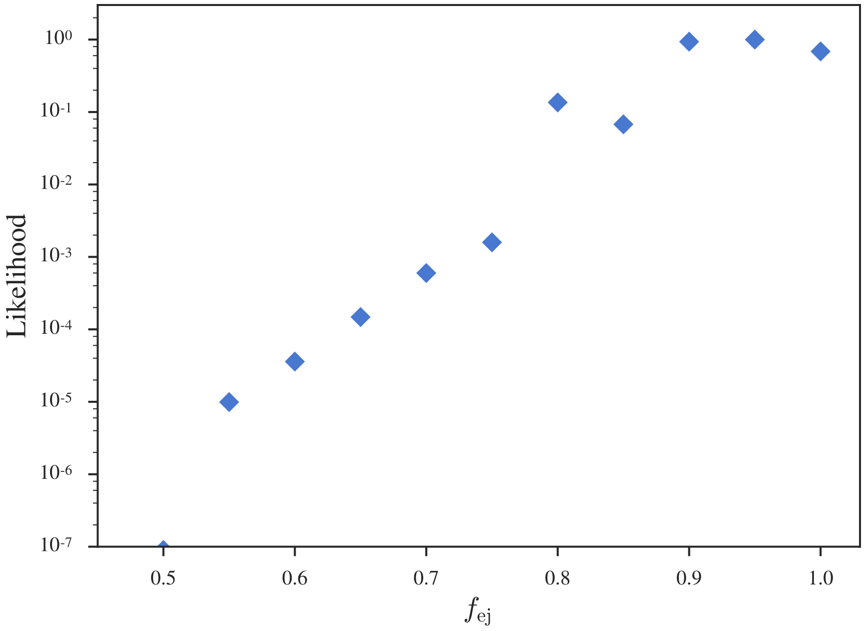

Figure 8.6 Likelihood that the inferred, simulated distribution matches the observed distribution of black hole masses, for various ejection fractions. We find that the likelihood peaks when a relatively large fraction of the stellar envelope has been ejected, $f_{\rm ej} > 0.9$.

8.5 Neutron star mass distribution

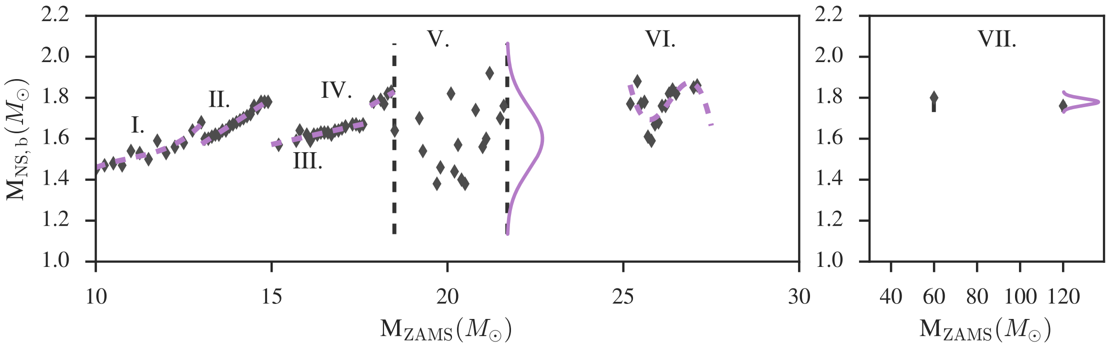

Figure 8.7 Neutron star baryonic masses as a function of the progenitor mass, for engine W18. We identify 7 distinct branches in this distribution. The analytic functions that we fit to each branch are shown in purple.

We calculate the neutron star mass distribution with the same method that we used for the black hole distribution of §8.4. Figure 8.7 shows the neutron star remnant masses for various progenitors, as calculated with the W18 engine. The neutron star masses produced by the five different engines that we used in §8.4 are offset slightly from one another, although each give approximately similar results. As a result, in order to avoid introducing artificial noise by combining these slightly different sets of outcomes, we only include engine W18 in the following analysis and take it to be representative of all five models.

Within the neutron star remnant masses, we identify 7 distinct segments that we fit with simple analytic functions, as in §8.4. We show the analytic functions that we fit to each branch in Fig. 8.7 in purple.

We find that the first branch is best fit by a third-order polynomial with parameters

$$\begin{aligned} M_{\rm NS,b}(M_{\rm ZAMS}) = 2.24 + 0.508(M_{\rm ZAMS} - 14.75) \\ + 0.125(M_{\rm ZAMS} - 14.75)^2 + 0.0110(M_{\rm ZAMS} - 14.75)^3, \\ 9 \leq M_{\rm ZAMS} \leq 13 M_\odot. \end{aligned} \tag{8.10}$$

The RMS of the residuals to this fit is $\sim 1.3\%$. Here, $M_{\rm NS,b}$ is the baryonic mass of the neutron star. The baryonic masses are the natural output of the stellar evolution and explosion models, which we will later convert to gravitational masses.

We find that Branches II−IV are sufficiently fit with linear models, with residuals $< 1\%$ for

$$M_{\rm NS,b}(M_{\rm ZAMS}) = 0.123 + 0.112 M_{\rm ZAMS}, \quad 13 < M_{\rm ZAMS} < 15 M_\odot, \tag{8.11}$$

$$M_{\rm NS,b}(M_{\rm ZAMS}) = 0.996 + 0.0384 M_{\rm ZAMS}, \quad 15 \leq M_{\rm ZAMS} < 17.8 M_\odot. \tag{8.12}$$

and

$$M_{\rm NS,b}(M_{\rm ZAMS}) = -0.020 + 0.10 M_{\rm ZAMS}, \quad 17.8 < M_{\rm ZAMS} < 18.5 M_\odot. \tag{8.13}$$

We find Branch V to be approximately randomly distributed, and thus fit it with a Gaussian distribution, i.e.,

$$P(M_{\rm NS,b}|M_{\rm ZAMS}) = \frac{1}{\sqrt{2\pi}\sigma}\exp\,[-(M_{\rm NS,b} - M_0)^2/2\sigma^2], \tag{8.14}$$

where M_0 and σ are the mean and standard deviation of the distribution. For Branch V ($18.5 \leq M_{\rm ZAMS} < 21.7 M_\odot$), we find the standard deviation to be $\sigma = 0.155$ and the mean to be $M_0 = 1.60\ M_\odot$.

Branch VI is best fit by a third-order polynomial with parameters

$$\begin{aligned} M_{\rm NS,b}(M_{\rm ZAMS}) = 3232.29 &- 409.429(M_{\rm ZAMS} - 2.619) \\ &+ 17.2867(M_{\rm ZAMS} - 2.619)^2 - 0.24315(M_{\rm ZAMS} - 2.619)^3, \\ &\qquad 25.2 \leq M_{\rm ZAMS} < 27.5 M_\odot, \end{aligned} \tag{8.15}$$

with residuals ~3%.

Finally, we fit Branch VII ($60 \leq M_{\rm ZAMS} \leq 120 M_\odot$) with a Gaussian distribution and find $\sigma = 0.016$ and $M_0 = 1.78\ M_\odot$. It should be noted, however, that Branch VII contains only two points; as a result, the parameters of this particular fit should be interpreted with caution. We show the Gaussian distributions on the right side of each $M_{\rm ZAMS}$ range in Fig. 8.7.

We use the analytic functions for Branches I–IV and VI to calculate the probability distribution of neutron star masses, according to

$$P(M_{\rm NS,b}|M_{\rm ZAMS}) = \left|\frac{dM_{\rm NS,b}(M_{\rm ZAMS})}{dM_{\rm ZAMS}}\right|^{-1} \delta[M_{\rm ZAMS} - M_{\rm ZAMS}(M_{\rm NS,b})], \tag{8.16}$$

For Branches V and VII, we simply use the fitted Gaussian distribution for $P(M_{\rm NS,b}|M_{\rm ZAMS})$.

Finally, we marginalize the probabilities of each branch by

$$P(M_{\rm NS,b}) = \int P(M_{\rm NS,b}|M_{\rm ZAMS})P(M_{\rm ZAMS})dM_{\rm ZAMS}, \tag{8.17}$$

and use the IMF of eq. (8.7) for $P(M_{\rm ZAMS})$, as in §8.4. We calculate the total distribution by summing the probability contributions from each branch, weighted by the fraction of outcomes that produce neutron stars ($X_{\rm NS}$) in that branch. We list

Table 8.2. Fraction of outcomes that yield neutron stars in each branch of Fig. 8.7.

Branch	$X_{\mathrm{NS,\ W18}}$
I	1.00
II	1.00
III	0.679
IV	0.833
V	0.500
VI	0.652
VII	0.400

Note. — Only the W18 engine results were included in our analysis of neutron star distributions.

these fractions in Table 8.2. We show the neutron star baryonic mass distribution, along with the contributions from each branch, in Fig. 8.8.

We convert from the baryonic ($M_{\mathrm{NS,b}}$) to the gravitational ($M_{\mathrm{NS,g}}$) mass distribution with the transformation

$$P(M_{\mathrm{NS,g}}) = P(M_{\mathrm{NS,b}}) \left| \frac{dM_{\mathrm{NS,b}}}{dM_{\mathrm{NS,g}}} \right|^{-1}, \tag{8.18}$$

where $M_{\mathrm{NS,g}}$ is the gravitational mass and we calculate the derivative using the relationship between binding energy (BE) and baryonic and gravitational masses,

$$M_b = M_g + \mathrm{BE}. \tag{8.19}$$

For the binding energy, we use the Lattimer and Prakash (2001) approximation

$$BE = M_{\mathrm{NS,g}} \times \left(\frac{0.6\beta}{1 - 0.5\beta} \right), \tag{8.20}$$

where $\beta \equiv GM_G/Rc^2$ is the neutron star compactness. We find that the gravitational mass distribution depends only weakly on the choice of radius in the binding energy approximation, so we use a characteristic value of 12 km.

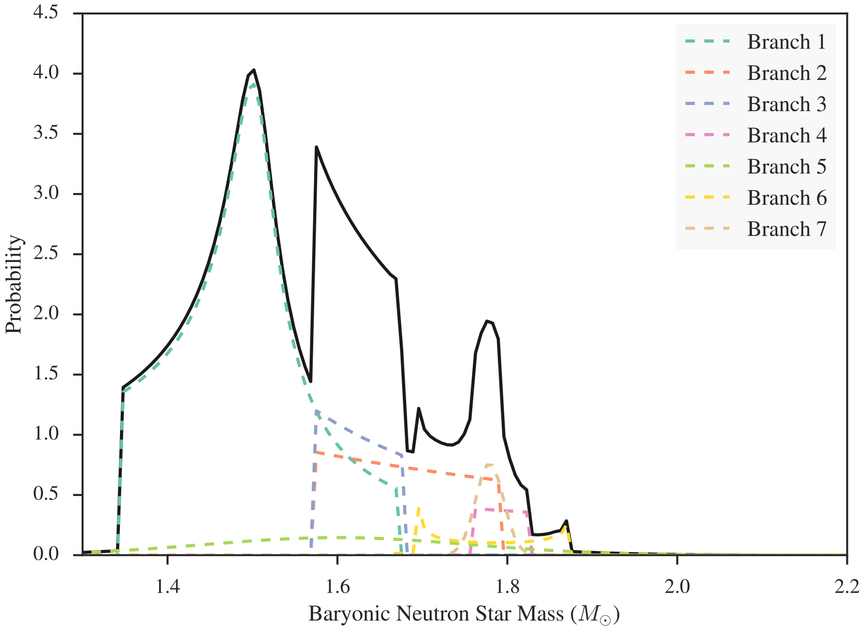

Figure 8.8 Baryonic mass distribution of neutron stars from the S16 simulations. The overall distribution is shown in black. The various dashed colors represent the contributions from each branch of ZAMS progenitors.

8.5.1 Comparing the simulated and observed pulsar mass distributions

We calculate the gravitational mass distribution as described in §8.5 and show the outcome as the dotted line in Fig. 8.9. However, because the substructure between the various peaks is finer than could be detected with realistic observational uncertainties as before, we also compute and show in the same figure the Gaussian distribution that would be inferred from this underlying distribution. We calculate this Gaussian by drawing 200 points from the underlying distribution and fitting with a single Gaussian function, i.e.,

$$P(M_{\mathrm{NS,g}}) = \frac{1}{\sqrt{2\pi}\sigma} \exp^{-(M-M_0)/2\sigma^2} . \tag{8.21}$$

We show the most-likely value for the mean, M_0, and standard deviation, σ in Table 8.3 and the resulting distribution in green in Fig. 8.9. Finally, we also include in Fig. 8.9 the observed neutron star mass distribution inferred from 33 millisecond pulsars in Antoniadis et al. (2016) in orange. The parameters of the low-mass peak of the Antoniadis et al. (2016) distribution, shown in Table 8.3, agree within 1-σ with the inferred parameters from the S16 distribution.

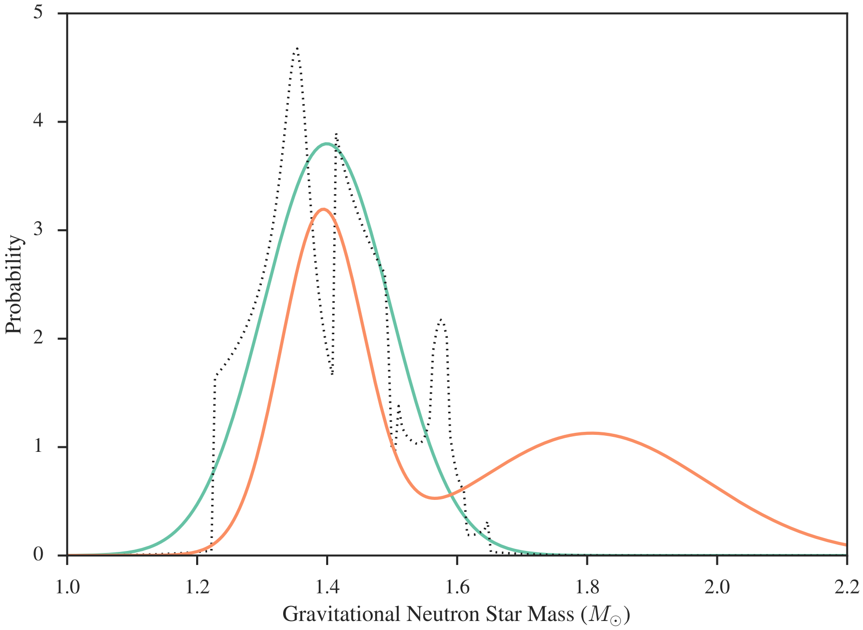

Figure 8.9 The gravitational mass distribution of neutron stars predicted from the S16 simulations (black dotted line) and the Gaussian distribution that would be inferred from the mock data that we produced from the full simulated distribution (green line). The orange line shows the observationally determined mass distribution of millisecond pulsars from Antoniadis et al. (2016). We find that the simulated mass distribution aligns very closely with the low-mass component of the observed distribution.

We can determine the origin of the low-mass peak of the observed distribution by comparing with the simulated distributions of each branch, which are shown in Fig. 8.8. We find that progenitors in Branches I−III, i.e. with $M_{\rm ZAMS} = 9 - 17.8 M_\odot$, are the dominant contributors to the low-mass peak that agrees well with the observed one.

We also see that the narrow peak at $M_{\rm NS,g} \sim\ 1.6\ M_\odot$ originates primarily from progenitors in Branch VII, with a modest enhancement from Branch IV. Because branch VII contains only two neutron stars that are fit with a Gaussian, its properties could easily be affected by a larger number of simulations in that mass range and it

Table 8.3. Gaussian Parameters for low-mass neutron star peak in Fig. 8.9

Source of distribution	M_0 ($M_\odot$)	σ
Antoniadis et al. (2016) observations	1.393	0.064
S16 simulations	1.399	0.098

should be interpreted with caution. Finally, Branches V and VI contain very broad distributions and correspondingly do not contribute significantly to any particular peak.

In the overall comparison of neutron star masses, we find excellent agreement between the simulated distribution and the low-mass peak of the observed mass distribution. We wish to emphasize here that this is a highly constrained comparison, with no parameters that can be adjusted in either distribution to improve their relative alignment. As described in §8.2, the simulations are calibrated only to reproduce the energetic properties of SN 1987A and SN 1054. The alignment that we see in Fig. 8.9, in addition to the alignment in the black hole mass distribution, therefore, seem to be a natural consequence of calibrating to the global energetic properties. Therefore, we argue that this level of agreement in the mass distributions provides a strong and independent validation of these stellar evolution and explosion models.

8.6 Missing high-mass remnants

In the analyses of §8.4 and 8.5, we found that the remnant mass distributions predicted by the S16 simulations show close agreement with both the observed black hole mass distribution and low-mass neutron star distribution, offering new evidence in support of these models. However, these simulations do not produce the high-mass LIGO black holes that can be seen in Fig. 8.3 and are missing the high-mass component of the observed pulsar mass distribution. In this section, we explore possible explanations for these discrepancies.

8.6.1 High-mass black holes

The recent detection of gravitational waves from black hole binary GW150914 provided the first observational evidence of "heavy" stellar-mass black holes ($M \gtrsim 25\ M_\odot$). The black holes in this binary were inferred to have masses of 29^{+4}_{-4} and $36^{+5}_{-4}\ M_\odot$ (Abbott et al., 2016d). In an initial characterization, Abbott et al. (2016a) proposed that the formation of such massive black holes via single-star evolution requires weak winds, which in turn requires an environment with metallicity $Z \lesssim 1/2\ Z_\odot$. Subsequent detections have found further evidence of additional "heavy" stellar-mass black holes (Abbott et al., 2016c, 2017b; The LIGO Scientific Collaboration et al., 2017b).

The mass range of implosion outcomes due to a sample central engine applied to low metallicity progenitors is illustrated in Figure 8.10. The models are the ultra-low metallicity ($10^{-4} Z_\odot$) "U-series" set from Sukhbold and Woosley (2014), which consists of 110 models with initial masses between 10 and 65 $M_\odot$. At such a low metallicity, mass loss is negligible and both the He core and final pre-supernova masses increase monotonically with initial mass. At lower initial mass, the explosion landscape is similar to the solar metallicity models, since the pre-supernova core structure in these stars are not strongly affected by metallicity. For more massive models, however, the cores are significantly harder to explode. Indeed, with the adopted sample central engine, all stars implode above $M_{\rm ZAMS} > 30\ M_\odot$. From this figure, it is clear that black holes can be formed with $M_{\rm BH} \gtrsim 25 M_\odot$, when the metallicity is sufficiently reduced.

An alternate channel for heavy stellar-mass black hole formation from single stars has recently been proposed in the form of strong magnetic fields. Petit et al. (2017) showed that for progenitor stars with $M_{\rm ZAMS}$ in the range $40 - 80\ M_\odot$, the presence of strong surface magnetic fields can significantly quench mass loss by magnetically confining a fraction of wind material to the star's surface. For a

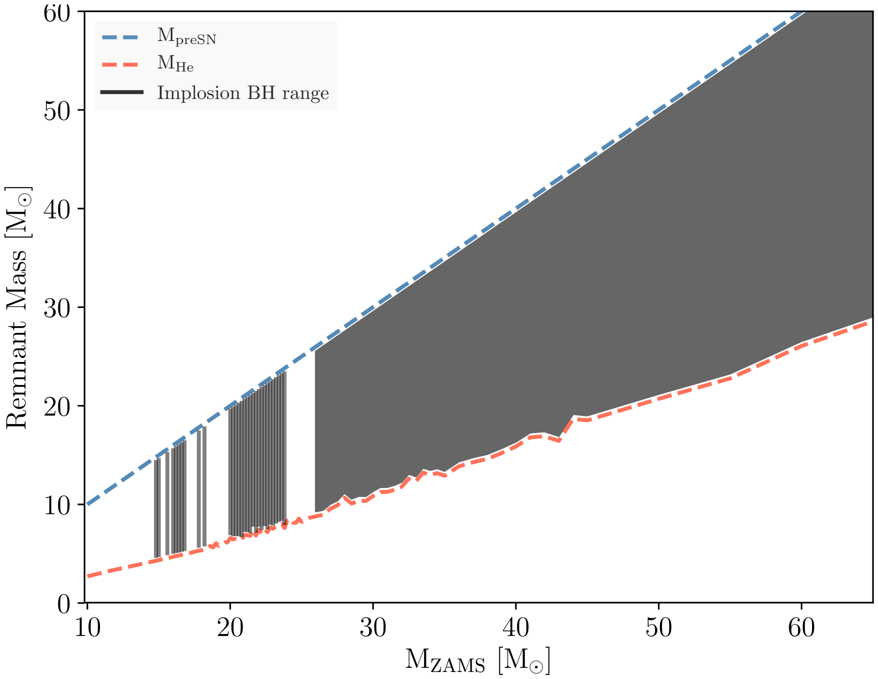

Figure 8.10 The range of possible black hole masses, bound by the pre-SN and He core masses of imploding progenitors, are shown for the ultra-low $10^{-4}\ Z_\odot$ metallicity models and a sample central engine (N20). The input physics in these models are identical to the those employed in this chapter, with the exception of the reduced metallicity. Compared to the models with solar metallicity shown in Fig. 8.4, the mass loss here is negligible and thus the implosions from the heaviest models allow the formation of heavy stellar mass black holes.

strongly magnetic 80 $M_\odot$ star, this reduces the mass lost during the main-sequence evolution by 20 $M_\odot$, which is the equivalent mass loss reduction achieved by reducing the stellar metallicity to $Z \sim 1/30\ Z_\odot$ for a non-magnetic star (Petit et al., 2017). The S16 simulations do not include magnetic fields or rotation, but such a model offers another possible mechanism for producing black holes in the regime that was probed by the LIGO detection, without reducing the metallicity.

Numerous studies have also explored the effect of binary evolution for producing heavy stellar mass black holes. Typically, simulations of binary massive star evolution result in the formation of a common envelope, via Roche lobe overflow (e.g., Voss and Tauris 2003). Accretion through the common envelope could, in principle, increase the mass of a star's He core and hence the mass of the post-SN black hole remnant to what was observed in the LIGO detections (Belczynski et al., 2016; Kruckow et al., 2016; Woosley, 2016; Eldridge and Stanway, 2016; Stevenson et al., 2017). However, there remain many uncertainties in the common-envelope physics used that affect the possible outcomes (see, e.g., Ivanova et al. 2013).

It is possible to avoid the uncertainties and pitfalls of the common envelope scenario by requiring a close binary orbit. In this mechanism, the close companions tidally spin up one another. The rapid rotation then induces mixing that is faster than the chemical gradient build-up due to nuclear burning, so that the stars remain chemically homogeneous throughout hydrogen burning. This keeps the stars from developing massive hydrogen envelopes and thus offers a way in which the stars could evolve to black holes without ever undergoing significant mass transfer. It has been shown that in such models, it is indeed possible to form heavy black holes, with $M \gtrsim 25\ M_\odot$ (de Mink and Mandel, 2016; Mandel and de Mink, 2016; Marchant et al., 2016). However, there remain large uncertainties in the efficiency of the mixing processes involved and in the impact of stellar winds on the orbital evolution, making it unclear whether this channel is likely or even possible (Mandel and de Mink, 2016).

Finally, many studies have found that dynamical assembly of black hole binaries in dense stellar clusters can also produce more massive black holes, via multi-body encounters, mass segregation, and gravitational focusing. These processes favor heavier black holes, which are already easier to form in the low-metallicity environments of globular clusters (Mapelli, 2016; O'Leary et al., 2016; Rodriguez et al., 2016; Askar et al., 2017; Park et al., 2017). If this is the primary way in which LIGO-mass black holes are formed, the single-star evolution framework of S16 and this chapter would not apply.

As a final remark, there may still be an upper bound on the expected masses of "heavy" stellar-mass black holes that might play a role in the above formation mechanisms. A recent analysis by Woosley (2017) predicts that no black holes with masses between $\sim$52 and 133 $M_\odot$ should be found in nature in close binary systems due to pulsational pair-instability effects. While this is in agreement with the current massive black hole detections by the LIGO-Virgo collaboration, mergers within a Hubble time from more complicated systems with more than two components could violate this bound.

8.6.2 Missing high-mass neutron stars

In §8.5, we also found that the high-mass peak of the observed neutron star mass distribution of Antoniadis et al. (2016) was not reproduced by the S16 simulations, despite very close agreement in the low-mass regime. Indeed, the S16 simulations do not produce any neutron stars with masses above $M_{\rm NS,g} > 1.7\ M_{\odot}$ and it is possible that the lack of high-mass neutron stars could imply incomplete physics in the stellar evolution models. Recent work by Sukhbold et al. (2017), which employs updated physics and a denser grid of models, finds the pre-SN core structures to be intrinsically multi-valued, including for the mass range $14 < M_{\rm ZAMS} < 19\ M_{\odot}$. Without performing full explosions of the pre-SN models, that study finds tantalizing evidence that neutron stars with $M_{\rm NS,g} \sim 1.9\ M_{\odot}$ can be made by the most massive stars with a significant second oxygen shell burning ($M_{\rm ZAMS} \sim 15\ M_{\odot}$). Whether these new models can recreate the high-mass peak of neutron star distribution will be explored in a future work.

Alternatively, the discrepancy would disappear if the observed high-mass peak is due to accretion rather than a second population of neutron star birth masses. However, Antoniadis et al. (2016) argue against such a path: they highlight several examples of high-mass neutron stars with companions that would be too small to allow significant accretion, inferring that the birth masses must be $\gtrsim 1.7\ M_{\odot}$. Even if we allow some accretion and lower the high-mass component to $1.7\ M_{\odot}$, such a population of neutron stars is still missing from the simulations. We discuss two other possibilities below.

Effect of rotation

More massive neutron stars are generally made by more massive main sequence stars, yet only a few models with $M_{\mathrm{ZAMS}} > 30\ M_{\odot}$ successfully explode in the neutrino-driven formalism of S16. The effects of rotation are expected to be important in the deaths of these heavier stars (e.g., Heger et al., 2005), and therefore the inclusion of rotation in the modeling of both the evolution and explosion may result in more successful explosions at higher initial mass and consequently in more massive neutron stars.

8.6.3 Effect of binary evolution

It is also possible that the explodability of the pre-SN stars and the resulting compact object masses are influenced by binary evolution. The potential impact of binary evolution is particularly important to consider in our comparison, since the observed black hole and pulsar masses all come from binary systems, while the models of S16 assume single-star evolution.

While the reproduction of observed compact object mass distributions in this study may suggest that binary effects are negligible, such an argument is not conclusive. As an example, single-star models had historically reproduced the observed populations of massive stars, even though binary effects were known to be important in $\sim$70% of those stars. It was eventually shown that the assumed mass loss rates had been set $3-10$ times too high in the single-star models and were effectively compensating for mass loss due to binary Roche-lobe overflow or common envelope evolution (see Smith 2014 for a review). It is natural to ask whether the single-star models of S16 may similarly include physics that is mimicking binary effects.

Given the uncertain nature of mass loss (e.g., Renzo et al., 2017), the prescriptions employed in the models of S16 may well be overestimating what is really experienced by single massive stars. In the current work, we cannot quantify to what extent the final pre-SN masses of the S16 progenitors or the ejections fractions inferred in §8.4 are influenced by binary effects. However, we can qualitatively say that the net mass loss effects from binaries would have to closely match the combined result from the employed mass loss prescriptions (Nieuwenhuijzen and de Jager, 1990; Wellstein and Langer, 1999) and the relatively high envelope ejection fraction of $f_{\rm ej}$ ∼0.9, in order to reproduce the agreement we find with the observed remnant masses.

Another important consideration is the assumed initial mass function. The formation of binary systems requires a specific set of conditions, and the formation of binaries that remain bound even after one member explodes requires an even more restrictive scenario. The mass function of binaries that can produce compact objects with bound companions, therefore, might differ from that of isolated stars. Throughout our analysis, we used the Salpeter IMF. It is possible that using a more representative mass function could increase the weighting given to the high-mass stars, and perhaps enhance a high-mass peak of neutron stars. Fully exploring such a binary mass function could be carried out using detailed population synthesis models. We note, however, that in the case of the high-mass neutron star peak, given the absence of neutron stars with masses above 1.7 $M_{\odot}$ in the S16 results, modifying the initial mass function alone is unlikely to produce the missing high-mass peak.

8.7 Conclusions

In this chapter, we directly confronted the outcomes from the stellar evolution models and neutrino-driven explosion simulations of S16 with the observed neutron star and black hole mass distributions. Given that the central engines of the simulations were calibrated only to reproduce the ^{56}Ni mass, kinetic energy, and neutrino burst timescale of SN 1987A and the kinetic energy of SN 1054, it is perhaps surprising that the remnant mass distribution from these simulations agrees so closely with the observed black hole mass distribution and the low-mass distribution neutron stars. This degree of agreement can be taken as evidence that the stellar evolution and explosion models we studied here have reached a point where they are accurately capturing the relevant stellar, nuclear, and explosion physics involved in the formation of compact objects.

In comparing the simulated and observed mass distributions, we find that the stellar evolution and explosion models are able to accurately reproduce the observed black hole distribution (Özel et al., 2010b; Farr et al., 2011), if a large fraction of the stellar envelope is ejected during the SN ($f_{\rm ej} \sim 0.9$). However, the solar-metallicity models we use in this chapter do not produce heavy stellar-mass black holes, the existence of which have recently been confirmed by the LIGO gravitational wave detections. We show that similar models to those used in S16 can indeed produce heavier black holes, if the metallicity is sufficiently reduced. We also review alternate mechanisms that may produce such black holes, including via rapid rotation in binary evolution or strong magnetic fields in single-star evolution, but large uncertainties remain in the current understanding of these mechanisms.

We also find very close agreement between the simulated distribution of neutron star masses and the low-mass peak of the observed bimodal distribution found by Antoniadis et al. (2016); specifically, that the simulated and observed Gaussian distributions agree to within their 1-σ uncertainties. From the S16 simulations, we determine that the low-mass neutron stars originate from progenitors with $M_{\rm ZAMS} \approx 9 - 18\ M_\odot$. However, the simulations do not reproduce the observed high-mass peak at $M_{\rm NS,g} \sim 1.8\ M_\odot$. In fact, the simulated distribution ends below $M_{\rm NS,g} \sim 1.7\ M_\odot$. We explore several possibilities for this discrepancy, including that the high-mass formation channel might require consideration of the binary mass function (as opposed to the single-star IMF we use here), or consideration of additional physics, such as the impact of rotation on the explodability of high-mass progenitors.

The method we have developed here, of directly confronting the simulated outcomes with measured mass distributions, will allow further tests of new models and ultimately will allow us to better understand the formation of compact objects. With the framework developed here, other formation channels may be tested as well, offering a new way to constrain stellar evolution and explosion models.

CHAPTER 9

Finite-Temperature Extension for Cold Neutron Star EOS [†]

The astrophysical observations discussed in this dissertation so far – from measurements of neutron star masses and radii, to the moment of inertia and even the tidal deformability, which is set early in the inspiral of a neutron star merger – all place constraints on the EOS of cold, neutron-rich matter. Meanwhile, nuclear physics experiments, such as those discussed in Chapter 6 probe the EOS of hot, symmetric matter. In between these two regimes lie many dynamical phenomena, such as the core-collapse supernovae discussed in Chapter 8, the formation and cooling of proto-neutron stars, and the late-stages of a binary neutron star merger, all of which depend on the EOS at finite temperatures for matter with varying proton fractions. In this chapter, we introduce a new framework to accurately extend any cold nucleonic EOS, including piecewise polytropes, to arbitrary temperature and proton fraction for use in numerical simulations of dynamical phenomena.

9.1 Dynamical phenomena and the finite-temperature EOS

Many dynamical phenomena, including core collapse supernovae, the formation and subsequent cooling of proto-neutron stars, and both the electromagnetic and gravitational signals from neutron star mergers, depend sensitively on the neutron star EOS at densities where the EOS is not well understood. In addition, for these dynamical phenomena, there are two further complications. First, temperatures may range from below the Fermi temperature, for which "cold" EOS suffice, to temperatures of up to 10-100 MeV in neutron star mergers (e.g., Oechslin et al. 2007). Second, the composition may range from nearly pure neutron matter to symmetric matter, with some dynamical timescales shorter than the timescale required to establish β-equilibrium. While astrophysical observations of stationary neutron stars probe the cold EOS in β-equilibrium and laboratory experiments constrain the hot EOS of symmetric matter, extrapolations between the two regimes remain difficult. (For a schematic representation of these various regimes, see Fig. 9.1. For recent reviews, see e.g., Lattimer and Prakash 2016; Özel and Freire 2016.) Such extrapolations to arbitrary proton fraction and temperature add further uncertainty to the EOS and complicate numerical simulations of these phenomena.

[†] A version of this chapter has been published previously as Raithel, Özel, and Psaltis (2019). *Finite-temperature Extension for Cold Neutron Star Equations of State.* ApJ, 875, 1. We thank Vasileios Paschalidis for useful discussions and comments on this work. CR was supported during this project by NSF Graduate Research Fellowship Program Grant DGE-1143953. FO and DP acknowledge support from NASA grant NNX16AC56G.

In the zero-temperature limit, a large number of EOS have been calculated, ranging from purely nucleonic models (e.g., Baym et al. 1971; Friedman and Pandharipande 1981; Akmal et al. 1998; Douchin and Haensel 2001) to models incorporating quark degrees of freedom using state-of-the-art results from perturbative QCD (e.g., Fraga et al., 2014). Laboratory experiments and neutron-star observations do not yet have sufficient power to distinguish between these models. Furthermore, it is likely that these EOS do not span the full range of possible physics. This possibility has motivated the creation of a large number of parametric EOS, as were first introduced by Read et al. (2009a) and Özel and Psaltis (2009). These parametric models do not require a priori knowledge of the high-density nuclear physics governing the EOS and, hence, can be used to probe unknown physics from neutron star observations.

A much smaller number of EOS that self-consistently incorporate finite-temperature effects have been calculated to date. Among the most well-known of these are the LS model, which is based on finite-temperature compressible liquid drop theory with a Skyrme nuclear force (Lattimer and Swesty, 1991); as well as the EOS of Shen et al. (1998), which was calculated using relativistic mean field (RMF) theory with a Thomas-Fermi approximation. More recently, the statistical model developed in Hempel and Schaffner-Bielich (2010) has been applied to an additional

~10 combinations of RMF models and nuclear mass tables.

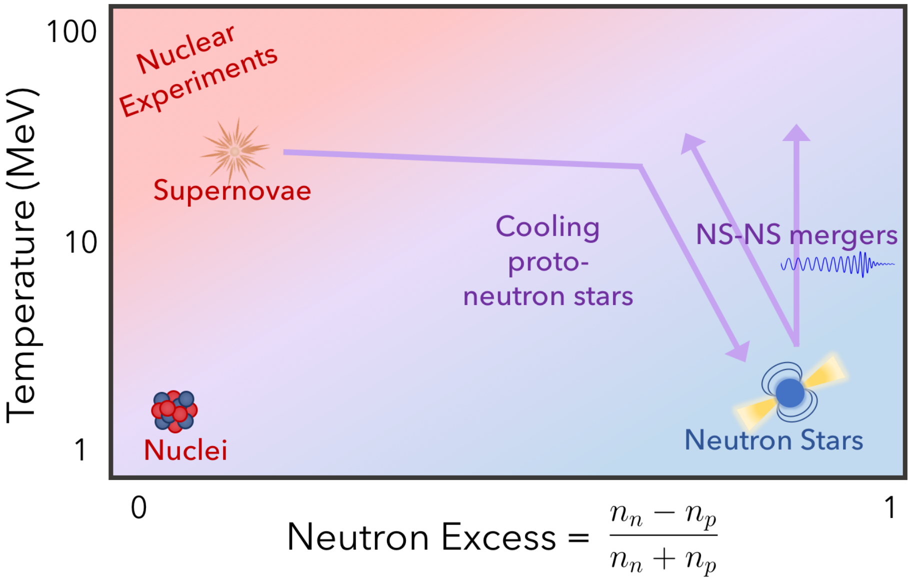

Figure 9.1 Cross-section of a phase diagram, containing temperature as a function of neutron excess, where neutron excess is defined as the difference between neutron and proton densities, n_n and n_p, compared to the total baryon density. The approximate regimes probed by various terrestrial and astrophysical phenomena are indicated. The dense-matter EOS is primarily constrained by observations of neutron stars and by laboratory data from nuclei and nuclear experiments. Many dynamical phenomena, such as neutron star mergers, supernovae, and the cooling of proto-neutron stars, lie in the intermediate regions of parameter space where the temperature is non-zero and the matter can be at a variable proton fraction.

Just as parametrizations of the cold EOS have proven useful in representing a broader range of physics, so too would a parametric finite-temperature EOS be useful for incorporating EOS effects into supernova and merger calculations. To this end, many authors have employed so-called "hybrid EOS," in which a thermal component for an ideal fluid is added to an arbitrary cold EOS to account for heating (Janka et al., 1993). The ideal-fluid thermal component is parametrized in terms of a simple adiabatic index as $P_{\rm th} = \epsilon_{\rm th}(\Gamma_{\rm th} - 1)$, where $P_{\rm th}$ and $\epsilon_{\rm th}$ are the thermal pressure and energy density and $\Gamma_{\rm th}$ is the adiabatic index, which is assumed to be constant. Such an approach is computationally simple, but neglects the effect of degeneracy on the thermal pressure. At high densities and finite temperatures, part of the available energy acts to lift degeneracy, rather than contributing additional thermal support. This causes a net reduction in the thermal pressure at high densities, compared to the prediction for an ideal fluid.

The density-dependence of these thermal effects depends directly on the density-dependence of the nucleon effective mass, as has been shown for many EOS (Constantinou et al., 2014, 2015). Constantinou et al. (2015) performed a Sommerfeld expansion to approximate the thermal properties at next-to-leading order and showed that the expansion terms require both the effective mass and its derivatives. Given a complete expression for the density-dependence of the effective mass, they showed that this formalism can be used to accurately approximate the thermal properties of a wide variety of EOS. Constantinou et al. (2017) later expanded this work and showed that the formalism can be used to recreate even models beyond mean field theory, such as the two-loop exchange model of Zhang and Prakash (2016).

The strong dependence of thermal properties on the effective mass can also be seen in the behavior $\Gamma_{\rm th}$. For example, Constantinou et al. (2015) compared two EOS with similar zero-temperature properties but with different single-particle potentials, and hence different density-dependences in their nucleon effective masses. They found substantially different thermal properties for the two EOS and that a constant $\Gamma_{\rm th}$ model failed to describe either EOS. Zhang and Prakash (2016) also found a strong density-dependence in $\Gamma_{\rm th}$ for their two-loop exchange model. These results indicate that $\Gamma_{\rm th}$ has a significant density-dependence for a diverse range of analytic models, which is not captured in the constant $\Gamma_{\rm th}$ approximation of the hybrid EOS.

Neglecting the effect of degeneracy on the thermal pressure has important consequences for dynamical simulations as well. For example, Bauswein et al. (2010) compared the properties of a neutron star-neutron star merger that would be predicted by a hybrid EOS and by more realistic EOS. Specifically, they compared the Shen et al. (1998) and Lattimer and Swesty (1991) EOS to hybrid EOS that were constructed from the zero-temperature versions of these same EOS with either $\Gamma_{\rm th} = 1.5$ or 2. They found that using the hybrid EOS predicts post-merger frequencies from a hypermassive neutron star that are 50-250 Hz smaller than what is found with a realistic finite-temperature EOS. Moreover, the lifetime of the hypermassive remnant can deviate by a factor of two from the more realistic value and the post-collapse accretion disk mass around the resulting black hole can differ by up to 30% when the simplified thermal effects are used (Bauswein et al., 2010). These results all suggest that it is indeed important to account for the effect of degeneracy on the thermal pressure when simulating neutron star mergers.

The Sommerfeld expansion results of Constantinou et al. (2015) can be used to explicitly correct a hybrid EOS to include degenerate effects, as long as the particle interactions and potentials of the cold EOS are known. However, requiring knowledge of the potentials of the cold EOS renders these corrections inapplicable to piecewise-polytropic EOS or other parametric forms of the EOS that are agnostic in their descriptions of the microphysics.

The goal of this chapter is to develop a physically-motivated framework for incorporating the thermal pressure that maintains the wide applicability of the hybrid EOS approach. With such a model, it will be possible to robustly add thermal effects to any cold EOS in β-equilibrium, without having to make the simplifying assumptions of an ideal fluid at all densities. The framework we present in this chapter is specific to neutron-proton-electron (n-p-e) matter, but could be generalized to include more exotic particles. We also include a symmetry-energy dependent correction that extrapolates the proton fraction away from β-equilibrium. The complete model thus allows us to build an EOS at finite-temperature and arbitrary proton fraction from any cold n-p-e EOS in neutrinoless β-equilibrium, including piecewise-polytropic EOS. Moreover, the model is analytic and in closed-form and thus can be calculated efficiently in dynamical simulations.

We start in §9.2 with a brief review of existing finite-temperature EOS and a discussion of the regimes in which thermal effects become important. In §9.3, we outline our model. We provide the symmetry-energy dependent extrapolation to arbitrary proton fraction in §9.4. In §9.5, we introduce our M^*-approximation of the thermal effects. We summarize the model in §9.6, in which all of the relevant equations can be found in Boxes I and II. Finally, we quantify the performance of our model in §9.7. We find that with a relatively small set of parameters, our complete model is able to recreate existing finite-temperature EOS with introduced errors of $\lesssim$20%, for densities above the nuclear saturation density.

9.2 Overview of finite-temperature EOS

Before introducing our new approximation for the pressure at arbitrary proton fraction and temperature, we will first briefly review the finite-temperature EOS that have been previously developed.

Two of the most widely-used finite-temperature EOS are the models of Lattimer and Swesty (1991, hereafter LS), which is based on a finite-temperature liquid drop model with a Skyrme nuclear force, and Shen et al. (1998, hereafter STOS) which is an RMF model that is extended with the Thomas-Fermi approximation. An additional eight EOS have been calculated with the framework of Hempel and Schaffner-Bielich (2010, hereafter, HS), which is a statistical model that consists of an ensemble of nuclei and interacting nucleons in nuclear statistical equilibrium and, hence, goes beyond the single nucleus approximation that both LS and STOS assume. Each HS EOS represents the nucleons with an RMF model and additionally includes excluded volume effects. Of the RMF models that have been used with the HS method, six are nucleonic: TMA (Toki et al., 1995), TM1 (Sugahara and Toki, 1994), NL3 (Lalazissis et al., 1997), FSUGold (Todd-Rutel and Piekarewicz, 2005), IUFSU (Fattoyev et al., 2010), DD2 (Typel et al., 2010); while the models BHB$\Lambda\phi$ and BHBΛ include hyperons with and without the repulsive hyperon-hyperon interaction mediated by the ϕ meson, respectively (Banik et al., 2014). Additionally, Steiner et al. (2013) created a set of two finite-temperature EOS, SFHo/x, that also used the statistical method of HS, but with new RMF parameterizations and constraints from neutron star observations. There are also the EOS of G. Shen, which are based on a virial expansion and nuclear statistical equilibrium calculations at low densities and RMF calculations at high densities, using the models FSUGold

(Shen et al., 2011a) and NL3 (Shen et al., 2011b). Tables of these various EOS can be found on the website of M. Hempel,[1] `stellarcollapse.org`, and/or the `CompOSE` database.[2]

More recently, several new finite-temperature EOS have been added to the `CompOSE` database. These include the SLY4-RG model, which is calculated in nuclear statistical equilibrium using a Skyrme energy functional (Gulminelli and Raduta, 2015; Raduta and Gulminelli, 2018), as well as chiral mean field theory models, which include hyperons as additional degrees of freedom (e.g., Dexheimer, 2017), generalized relativistic density functional models (e.g., Typel, 2018), and models calculated using a variational method applied to two- and three-body nuclear potentials (e.g., Togashi et al., 2017).

For the sake of simplicity in the following analysis, we will focus on a subset of these EOS and will include only models that are nucleonic. In particular, our sample will include STOS as well as the eight nucleonic EOS calculated with the HS method, to represent the models based on RMF theory. We will also include LS (with a compression modulus $K = 220$ MeV) and SLY4-RG, to represent non-relativistic models with Skyrme nuclear forces.

In spite of the increasing number of finite-temperature EOS that have been calculated, they nevertheless span a relatively limited range of physics, especially when compared to the diversity of cold EOS models. In order to span a broader range of possible physics, many authors have used the so-called "hybrid EOS," which assume that the thermal pressure is given simply by an ideal-fluid term that can be added to any cold EOS. The hybrid EOS were first introduced by Janka et al. (1993) and have been used in many subsequent works (for recent reviews, see Shibata and Taniguchi, 2011; Faber and Rasio, 2012; Baiotti and Rezzolla, 2017; Paschalidis and Stergioulas, 2017). In these hybrid EOS, the thermal pressure is written as

$$P_{\rm th,hybrid}(n,T) = nE_{\rm th,hybrid}(n,T)(\Gamma_{\rm th}-1), \tag{9.1}$$

where $E_{\rm th,hybrid}(n,T)$ is the thermal contribution to the energy per baryon, n is the baryon number density, and $\Gamma_{\rm th}$ is the thermal adiabatic index and is constrained to be $1 \leq \Gamma_{\rm th} \leq 2$. In the hybrid approximation, $\Gamma_{\rm th}$ is assumed to be constant.

---

[1] https://astro.physik.unibas.ch/people/matthias-hempel/equations-of-state.html

[2] https://compose.obspm.fr/home/

Following Etienne et al. (2008), the hybrid temperature-dependence of $E_{\rm th,hybrid}$ is included as an ideal fluid plus a contribution from relativistic particles, i.e.,

$$E_{\rm th,hybrid}(n,T) = \frac{3}{2}k_B T + \frac{4\sigma}{c}\frac{f_s}{n}T^4, \tag{9.2}$$

where k_B is the Boltzmann constant, T is the temperature, and $\sigma \equiv \pi^2 k_B^4/[60\hbar^3 c^2]$ is the Stefan-Boltzmann constant, with $\hbar$ the Planck constant and c the speed of light. The parameter f_S represents the number of ultra-relativistic species that contribute to the thermal pressure. For $k_B T \ll 2m_e c^2$, where m_e is the mass of an electron, photons will dominate and f_S=1. For $k_B T \gg 2m_e c^2$, electrons and positrons become relativistic as well and yield $f_S = 1 + 2 \times (7/8) = 11/4$. Finally, for $k_B T \gtrsim 10$ MeV, thermal neutrinos and anti-neutrinos appear, rendering $f_s = 11/4 + 3 \times (7/8) = 43/8$. If right-handed neutrinos were to exist, this would become $f_s = 11/4 + 3 \times 2 \times (7/8) = 8$.

We note that all 12 EOS discussed above neglect neutrinos in their calculations. The STOS EOS additionally neglects leptons and photons, which we add in wherever we use STOS in this chapter. For the STOS thermal lepton and photon contribution, we use eq. (9.2) with the appropriate lepton density. For the cold lepton energy, we add the contribution for a degenerate gas of relativistic electrons. Because all the EOS neglect neutrinos, we will also neglect neutrinos in our comparisons and thus we will calculate f_S only as

$$f_S = \begin{cases} 1, & k_B T < 1 \text{ MeV}, \\ 11/4, & k_B T \geq \text{ 1MeV}. \end{cases} \tag{9.3}$$

We, therefore, account for the degrees of freedom introduced by the possible presence of ultra-relativistic positrons. However, throughout this chapter, we will assume that the population of positrons is small and that their contribution to the pressure or energy at higher densities is negligible. If there were a scenario in which the population of positrons were significant compared to the electrons, one would have to explicitly account for the positrons in particle-counting as well as in imposing charge neutrality.

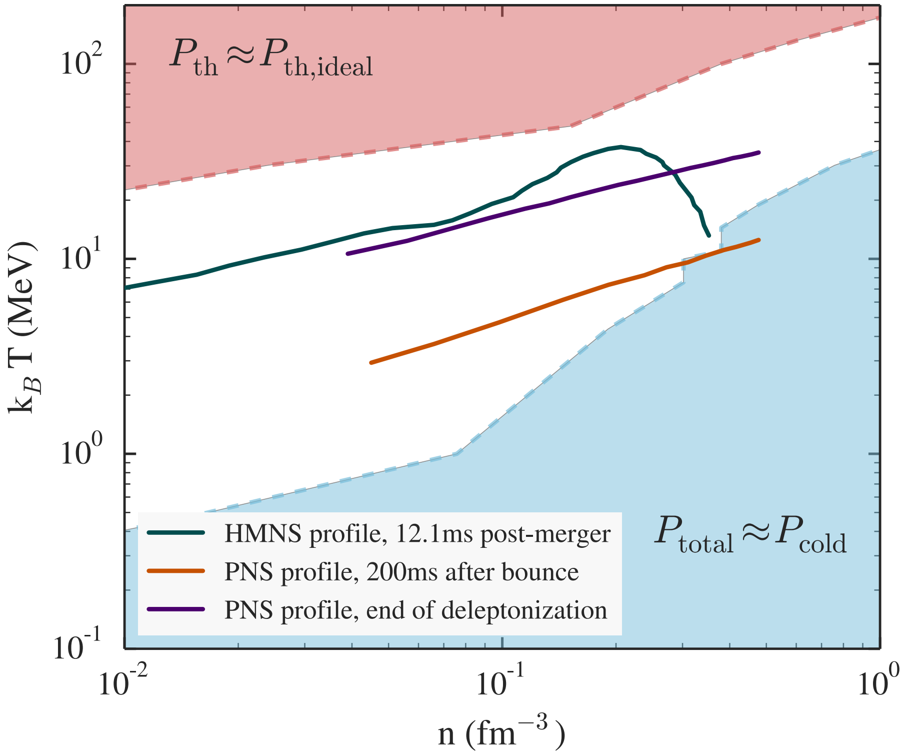

Figure 9.2 Phase diagram for regimes of interest in neutron star simulations. The blue shaded region represents the regime where the total pressure is dominated by the cold pressure, to within 1%, for the STOS EOS with proton fraction $Y_p = 0.1$. The red shaded region represents the $T - n$ range where the thermal pressure is dominated by the ideal-fluid pressure ($P_{\text{th}} = nk_BT$), to within 1%, for the same EOS and fixed Y_p. The white range in between these two extremes represents the phase space in which degenerate thermal effects are important. For comparison, the green line shows the profile of a hypermassive neutron star (HMNS) remnant 12.1 ms after a neutron star merger from the simulations of Sekiguchi et al. (2011) using the STOS EOS. The orange and purple lines show the profiles of a proto-neutron star (PNS) 200 ms after the bounce in a core-collapse supernova simulation and at the end of de-leptonization in the same simulation, both with a bulk version of the LS EOS (Camelio et al., 2017).

In order to highlight the regimes where a realistic finite-temperature EOS and the hybrid approximation differ, we show a phase diagram in Fig. 9.2. In this plot, we show various regions calculated for the EOS STOS, all at a fixed proton fraction of $Y_p = 0.1$. The total pressure, P_{total}, is thus calculated at $Y_p = 0.1$ and a given temperature. The cold contribution, P_{cold}, is calculated at the same Y_p and at zero-temperature.[3] Finally, the thermal contribution, P_{th}, is defined as $P_{\text{total}} - P_{\text{cold}}$ for the same proton fraction.

In this figure, the blue shaded region shows the regime where the total pressure is dominated by the cold pressure; there, the thermal pressure of STOS contributes $< 1\%$ of the total pressure. The red shaded region represents the regime where the thermal pressure can be approximated by the ideal fluid pressure ($P_{\text{th,ideal}} = nK_BT$), to within 1%. The white region between these two extremes represents the range of parameter space in which the thermal pressure is important but the ideal-fluid approximation does not yet apply. In this white region, the effects of degeneracy on the thermal pressure cannot be neglected.

For comparison, we also show in Fig. 9.2 the projected temperature-density profiles from three different simulations of relevant astrophysical phenomena. The green line shows the profile of a hypermassive neutron star remnant 12.1 ms after the merger of two 1.35 $M_\odot$ neutron stars, as simulated using the EOS STOS (Sekiguchi et al., 2011). The orange and purple lines both come from numerical simulations of the evolution of a proto-neutron star using a bulk-version of the LS EOS. The orange line gives the profile of the proto-neutron star at 200 ms after the core bounce, while the purple line shows the profile of the proto-neutron star at the end of the de-leptonization phase (Camelio et al., 2017). We note that these profiles are not necessarily calculated at $Y_p = 0.1$, but we include them nevertheless to show the approximate relevant temperatures and densities for such phenomena.

In order to further explore the dependence on the proton fraction, we also calculated the regime where degeneracy dominates for increasing values of Y_p. We find that as the proton fraction increases towards $Y_p = 0.5$, the white degeneracy region in Fig. 9.2 shrinks, but still largely encompasses the shown profiles. We thus find that all of these simulations primarily probe the phase space where degenerate thermal effects are important. This suggests that using the hybrid approximation, instead of the full thermal pressure, may bias the outcomes from such simulations.

---

[3] We note that, throughout this chapter, we use the coldest HS calculation, performed at $k_BT = 0.1$ MeV, as an approximation of the zero-temperature EOS. Even though the STOS EOS is calculated at $T = 0$ MeV, we use the $k_BT = 0.1$ MeV table as our cold component for this EOS as well, in order to maintain consistency with the HS set of EOS.

9.3 Generic model of a finite temperature EOS

In order to construct a finite-temperature EOS at arbitrary proton fraction, our model must be able to extrapolate from β-equilibrium to an arbitrary Y_p, as well as from cold matter to an arbitrary temperature. This will naturally introduce dials into our model that can be adjusted to represent a wide range of physics, based on the symmetry energy, its slope, and the strength of particle interactions we wish to include. Moreover, we will show that with a small set of parameters, the EOS that are currently in use in the literature can be replicated to high accuracy.

We start with our model in general terms, for which we will derive analytic expressions in the following sections. Our final model will be for the complete energy per baryon, $E(n, Y_p, T)$, separated into analytic, physically-motivated terms. A summary of the final equations can be found in Boxes I and II in §9.6.

We can expand the energy per particle of nuclear matter, $E_{\rm nucl}$, about the neutron excess parameter, $(1-2Y_p)$, to second order as

$$E_{\rm nucl}(n, Y_p, T) = E_{\rm nucl}(n, Y_p = {}^1\!/\!_2, T) + E_{\rm sym}(n, T)(1-2Y_p)^2, \tag{9.4}$$

where $E_{\rm nucl}(n, Y_p = {}^1\!/\!_2, T)$ represents the energy of symmetric nuclear matter and

$$E_{\rm sym}(n, T) \equiv \frac{1}{2}\frac{\partial^2 E_{\rm nucl}(n, Y_p, T)}{\partial(1-2Y_p)^2}\bigg|_{Y_p=1/2} \tag{9.5}$$

is the symmetry energy. The proton fraction is related to the overall baryon density, n, according to

$$Y_p = \frac{n_p}{n} = \frac{N_p}{N_n + N_p}, \tag{9.6}$$

where n_p is the proton density, N_p is the total number of protons, and N_n is the total number of neutrons. Throughout this chapter, we enforce charge-neutrality, which requires that the proton and electron densities balance. Thus, the electron density, n_e, can be written as

$$n_e = Y_p n. \tag{9.7}$$

Finally, by requiring that the baryonic components combine to give the total density n, we can write the neutron density as

$$n_n = (1 - Y_p)n. \tag{9.8}$$

We can further expand eq. (9.4) by separating the energy of cold, symmetric matter from its thermal contribution, i.e.,

$$\begin{aligned} E_{\text{nucl}}(n, Y_p, T) =& E_{\text{nucl}}(n, Y_p = {}^1\!/\!_2, T = 0) \\ &+ E_{\text{nucl,th}}(n, Y_p = {}^1\!/\!_2, T) \\ &+ E_{\text{sym}}(n, T)(1 - 2Y_p)^2. \end{aligned} \tag{9.9}$$

Here and throughout the chapter, we use the subscript "*th*" to indicate the thermal contribution to a variable, after the cold component has been subtracted.

In order to write the energy with respect to a cold EOS in β-equilibrium, as is often most relevant to start from in the study of neutron stars, we eliminate the cold, symmetric term in eq. (9.9) to yield

$$\begin{aligned} E_{\text{nucl}}(n, Y_p, T) =& E_{\text{nucl}}(n, Y_{p,\beta}, T = 0) \\ &+ E_{\text{nucl,th}}(n, Y_p = {}^1\!/\!_2, T) \\ &+ E_{\text{sym}}(n, T)(1 - 2Y_p)^2 \\ &- E_{\text{sym}}(n, T = 0)(1 - 2Y_{p,\beta})^2, \end{aligned} \tag{9.10}$$

where $Y_{p,\beta}$ represents the proton fraction of a zero-temperature system in β-equilibrium. We note that the proton fraction depends on the density, i.e., $Y_{p,\beta} = Y_{p,\beta}(n)$, but for simplicity we suppress this in our notation.

Finally, we must add the contribution of leptons and photons to this expression. The zero-temperature energy from relativistic degenerate electrons is given by

$$E_{\text{lepton}}(n, Y_p, T = 0) = 3KY_p(Y_p n)^{1/3}, \tag{9.11}$$

where the extra factor of Y_p comes from our definition of E as the energy per baryon, combined with eqs. (9.6) and (9.7). Here, $K \equiv (3\pi^2)^{1/3}(\hbar c/4)$. Additionally, there will also be a thermal contribution, $E_{\rm lepton,th}(n, Y_p, T)$, which we derive in §9.5.

Thus, our skeletal model for the total energy is given by the following set of equations:

$$E(n, Y_p, T) = E(n, Y_p, T = 0) + E_{\rm th}(n, Y_p, T) \tag{9.12a}$$

$$\begin{aligned} E(n, Y_p, T = 0) = {} & E(n, Y_{p,\beta}, T = 0) \\ & + E_{\rm sym}(n, T = 0)\left[(1 - 2Y_p)^2 - (1 - 2Y_{p,\beta})^2\right] \\ & + 3K\left(Y_p^{4/3} - Y_{p,\beta}^{4/3}\right) n^{1/3} \end{aligned} \tag{9.12b}$$

$$\begin{aligned} E_{\rm th}(n, Y_p, T) = {} & E_{\rm nucl,th}(n, Y_p = {}^1\!/_2, T) \\ & + E_{\rm lepton,\ th}(n, Y_p, T) \\ & + E_{\rm sym,th}(n, T)(1 - 2Y_p)^2. \end{aligned} \tag{9.12c}$$

From these relations, we can derive the pressure via the standard thermodynamic relation,

$$P \equiv -\left.\frac{\partial U}{\partial V}\right|_{N_q,S} = n^2 \left.\left[\frac{\partial E(n, T = 0)}{\partial n}\right]\right|_{Y_p,S} \tag{9.13}$$

where U is the total energy, V is the volume, N_q is the number of each species q, and S is the total entropy. From eq. (9.6), it is clear that evaluating these derivatives at constant N_q is equivalent to evaluating them at constant Y_p. In this chapter, we will mainly plot results in terms of pressure. We summarize the complete expressions for pressure in Box II of §9.6.

While this set of expressions may seem to have a large number of terms, this separation allows these terms to be represented analytically. Moreover, as we will show, the parameters of each term are linked directly to physics on which there are experimental constraints and of which further constraints are the motivation of many observations of astrophysical neutron stars: namely, the value of the symmetry energy at the saturation density, the slope of the symmetry energy, and the strength of interactions between particles.

9.4 Derivation of the cold symmetry energy in the Fermi Gas limit

We turn first to the symmetry energy correction term, $E_{\mathrm{sym}}(n,T)$ of eq. (9.4). The symmetry energy is defined as the per-nucleon difference in energy between symmetric matter and pure neutron matter. In other words, the symmetry energy represents the excess energy of matter with unequal numbers of protons and neutrons. In nuclear models, the symmetry energy is typically calculated as an expansion around the nuclear saturation density, for matter with $Y_p = 1/2$. In eq. (9.4), we perform the expansion with respect to the proton fraction and, in the following section, will introduce a density-dependence to extrapolate beyond the saturation density, where the coefficients of our approximation are experimentally constrained. In this section, we will provide the approximation for $E_{\mathrm{sym}}(n,T)$ at zero-temperature. For the thermal contribution to the symmetry energy, which turns out to be negligible, see §9.5.

It is particularly useful to parameterize the symmetry energy in terms of its separate kinetic and potential components at zero-temperature (e.g., Tsang et al., 2009; Steiner et al., 2010), modified by a parameter η to account for short-range correlations due to the tensor force acting between a spin-triplet or isospin-singlet proton-neutron pair. These correlations can significantly reduce the kinetic symmetry energy to even a negative value at the saturation density, compared to the kinetic energy of an uncorrelated Fermi gas model (Xu and Li, 2011; Vidaña et al., 2011; Lovato et al., 2011; Carbone et al., 2012; Rios et al., 2014; Hen et al., 2015). In this framework, we parameterize the symmetry energy of eq. (9.12b) as

$$E_{\mathrm{sym}}(n,T=0) = \eta E_{\mathrm{sym}}^{\mathrm{kin}}(n) + \left[S_0 - \eta E_{\mathrm{sym}}^{\mathrm{kin}}(n_{\mathrm{sat}})\right]\left(\frac{n}{n_{\mathrm{sat}}}\right)^{\gamma}, \tag{9.14}$$

as in Li et al. (2015). Here, $E_{\mathrm{sym}}^{\mathrm{kin}}(n)$ is the "kinetic" symmetry energy, arising from the change in the Fermi energy of a gas at density n as the relative proton/neutron fraction changes, $n_{\mathrm{sat}} = 0.16\ \mathrm{fm}^{-3}$ is the nuclear saturation density,[4] and the second term represents the "potential" symmetry energy which accounts for the interactions between particles. Because the exact form of the potential symmetry energy is not well known, it is anchored at the saturation density by the magnitude of the overall symmetry energy, $S_0 \equiv E_{\rm sym}(n_{\rm sat})$, and is given an arbitrary density-dependence through the constant γ.

---

[4] We note that n_{sat} does vary slightly among the EOS in our sample, but we fix the value to $n_{\mathrm{sat}} = 0.16\ \mathrm{fm}^{-3}$ in order to more easily compare the various EOS. We find that this does not significantly affect the results.

In contrast, the kinetic energy term can be calculated directly from the nuclear momentum distribution. The kinetic energy of a free Fermi gas is given simply by

$$\frac{\varepsilon_{k,q}}{n} = \frac{3}{5} E_f(n_q) \tag{9.15}$$

where $\varepsilon_{k,q}$ is the kinetic energy per particle, q represents the particle (either a neutron or proton), and $E_f(n)$ is the Fermi energy,

$$E_f(n_q) = \frac{\hbar^2}{2m} \left(3\pi^2 n_q\right)^{2/3}, \tag{9.16}$$

in which m is the mass of the relevant particle. For our approximation, we will neglect the small difference between the proton and neutron mass and simply take $m \approx m_n$, where m_n is the neutron mass.

By taking the difference between symmetric matter and pure neutron matter, the kinetic symmetry energy as a function of the total density is then

$$\begin{aligned} E_{\rm sym}^{\rm kin}(n) &= \frac{3}{5}\left[2E_f\left(n_p = n_n = \frac{1}{2}n\right) - E_f(n_n = n)\right] \\ &= \frac{3}{5}\left(2^{1/3} - 1\right) E_f(n). \end{aligned} \tag{9.17}$$

We can also eliminate the parameter η in eq. (9.14) by introducing the constant L, which is related to the overall slope at the saturation density via,

$$L \equiv 3n_{\rm sat} \left[\frac{\partial E_{\rm sym}(n, T=0)}{\partial n}\right]\Bigg|_{n_{\rm sat}}. \tag{9.18}$$

Combining eqs. (9.14) and (9.18), we can solve for η in terms of the quantities S_0 and L, which are constrained by nuclear physics experiments for matter near $Y_p = 1/2$ (Lattimer and Lim, 2013). We find

$$\eta = \frac{5}{9}\left[\frac{L - 3S_0\gamma}{(2^{1/3} - 1)\,(2/3 - \gamma)\, E_f(n_{\rm sat})}\right], \tag{9.19}$$

Table 9.1. Symmetry energy parameters characterizing each EOS at $k_B T = 0.1$ MeV.

EOS	S_0 (MeV)	L (MeV)	γ
TM1	36.95	110.99	0.75
TMA	30.66	90.14	0.66
NL3	37.39	118.49	0.62
FSG	32.56	60.43	1.11
IUF	31.29	47.20	0.52
DD2	31.67	55.03	0.91
STOS	36.95	110.99	0.77
SFHo	31.57	47.10	0.41
SFHx	28.67	23.18	-0.04[5]
LS	29.3	74.0	1.05
SLY4-RG	32.04	46.00	0.35

Note. — S_0 and L are fixed to the values predicted for each EOS, while γ is a fit parameter. All fits are performed for densities above $n \geq 0.01$ fm^{-3} and n_{sat}=0.16 fm^{-3}

thereby leaving one free parameter, γ, which is constrained by nuclear experiments to lie in the range $\sim$ 0.2 to 1.2 (see, e.g., Fig. 2 of Li et al. 2015; Tsang et al. 2009).

We thus have a complete expression for the symmetry energy that depends only on the three parameters γ, S_0, and L which, in principle, can be constrained by nuclear experiments. We can now use this functional form to fit for γ, by combining it with the following relationship between the symmetry energy and $Y_{p,\beta}$ for charge-neutral n-p-e matter in neutrinoless β-equilibrium,

$$\frac{Y_{p,\beta}}{(1-2Y_{p,\beta})^3} = \frac{64}{3\pi^2 n}\left[\frac{E_{\rm sym}(n,T=0)}{\hbar c}\right]^3 \tag{9.20}$$

(for a derivation of this relation, see, e.g., Blaschke et al., 2016, or Appendix B). When solved for $Y_{p,\beta}$, this becomes

$$Y_{p,\beta} = \frac{1}{2} + \frac{(2\pi^2)^{1/3}}{32}\frac{n}{\xi}\left\{(2\pi^2)^{1/3} - \frac{\xi^2}{n}\left[\frac{\hbar c}{E_{\rm sym}(n,T=0)}\right]^3\right\}, \tag{9.21}$$

where, for simplicity, we have introduced the auxilary quantity ξ, defined as

$$\xi \equiv \left[\frac{E_{\rm sym}(n,T=0)}{\hbar c}\right]^2 \times \left\{24n\left[1+\sqrt{1+\frac{\pi^2 n}{288}\left(\frac{\hbar c}{E_{\rm sym}(n,T=0)}\right)^3}\right]\right\}^{1/3}. \tag{9.22}$$

For each of the EOS in our sample, we stitch together a complete cold EOS at β-equilibrium from the publically-available tables at fixed Y_p, by requiring that $\mu_e + \mu_p - \mu_n = 0$, where μ_i is the chemical potential of each species. We then use the corresponding density-dependent proton fraction, $Y_{p,\beta}$, to fit for γ using eqs. (9.14)-(9.20) and keeping S_0 and L fixed for each EOS. We perform the fits using a standard least-squares method and limit the density range to $n \geq 10^{-2}$ fm^{-3}. In principle, eqs. (9.14)-(9.20) apply only to n-p-e matter, which will be uniform only above $0.5n_{\rm sat}$. However, in practice, we find a very small difference in the fits for γ whether we include densities above $0.5n_{\rm sat} = 0.08$ fm^{-3} or whether we start the fits at a slightly lower but still astrophysically relevant cutoff of $n = 10^{-2}$ fm^{-3}. We show the resulting fit values in Table 9.1.

We note that the range of EOS provided in Table 9.1 is intentionally broad. While the symmetry energy parameters of some of these EOS disagree with the combined set of experimental constraints (see Lattimer and Lim 2013 for a recent review), or are in disagreement with certain theoretical considerations such as chiral effective field theory results for pure neutron matter (see, e.g., Krüger et al., 2013), they are all consistent with at least some experimental constraints on S_0 and L.

We find that γ spans roughly the range of experimentally-allowed values, between 0.15 and 1.0, as expected, with the exception of SFHx. SFHx has an extremely low value of L, which makes the result of the fit highly sensitive to the density range that is included. For consistency, we still constrain the densities to $n \geq 10^{-2}$ fm^{-3} for the fit to this EOS; however, the inferred value for γ ranges from the reported value of -0.04 up to 0.18, depending on where the density cutoff is placed. Thus, the particular value for γ for SFHx should be taken with some caution.

We have here used eq. (9.20) to fit for γ from the β-equilibrium proton fractions of realistic EOS. We wish to also emphasize that eq. (9.20) can, of course, be used to calculate $Y_{p,\beta}$, given a choice of S_0, L, and γ. Once these three parameters are specified, eqs. (9.21)-(9.22) can be used to calculate $Y_{p,\beta}$ for any EOS. As a result, all that is required of the cold EOS is knowledge of the run of pressure with density. This feature makes it possible to apply our model to piecewise polytropes or other families of parametric EOS that may not directly calculate $Y_{p,\beta}$.

We show an example of the performance of this model for $E_{\mathrm{sym}}(n, T = 0)$ in Fig. 9.3 for the EOS NL3 (Lalazissis et al., 1997, 1999) and DD2 (Typel et al., 2010). We show these two EOS as representative samples, with NL3 representing the family of EOS with larger L values and DD2 representing the EOS with smaller symmetry energy slopes (see Table 9.1). The top panel of Fig. 9.3 shows the zero-temperature pressure predicted by NL3 and DD2 at $Y_p = 0.1$ as blue and orange diamonds, respectively. The colored lines show our model: starting with the corresponding EOS in β-equilibrium, adding the symmetry energy correction of eqs. (9.14)-(9.19), and correcting for the leptons, all according to eq. (9.12b). For these models, we take the values of S_0, L, and γ for each EOS from Table 9.1. We note that we are plotting pressures, but could have similarly shown the energy. We use eq. (9.13) to convert the equations of this section to pressures; for the complete set of pressure

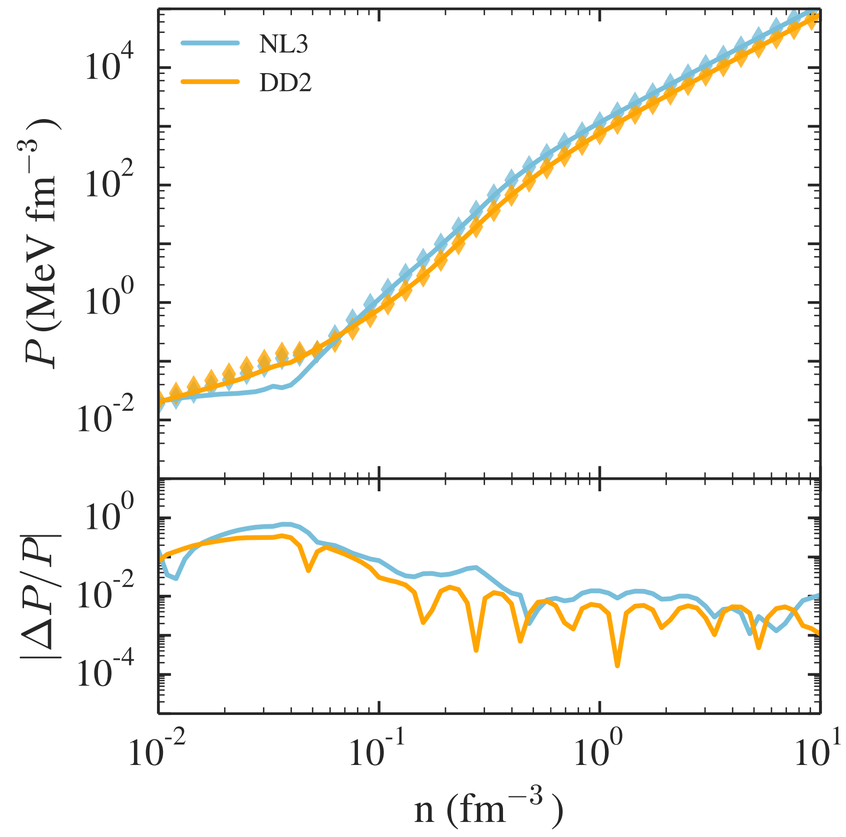

Figure 9.3 Top: Pressure as a function of density for EOS NL3 and DD2, at $k_BT = 0.1$ MeV and $Y_p = 0.1$, as blue and orange diamonds, respectively. The solid lines show our model of the pressure, calculated using eqs. (9.12b) and (9.14-9.20). Our model starts with the respective EOS in β-equilibrium and adds the appropriate symmetry energy and lepton corrections to extrapolate to $Y_p = 0.1$. For S_0, L, and γ, we use the values listed in Table 9.1. Bottom: Residuals between the true EOS at $Y_p = 0.1$ and our model. We find that our model extrapolates from β-equilibrium to $Y_p = 0.1$ reasonably well, especially at high densities where the model introduces an error of $\lesssim 1\%$ compared to using the full EOS.

expressions, see §9.6 and Box II.

The bottom panel of Fig. 9.3 shows the residuals between our model and the pressure predicted by each EOS at $Y_p = 0.1$. We find that our model performs very well at densities above 0.5 $n_{\rm sat}$, with errors $\lesssim 10\%$. At the highest densities, using our model compared to the full EOS introduces errors of only $\sim$1%. The residuals for the other EOS in our sample are comparably small.

For Y_p=0.3, we find the residuals between our model and NL3 and DD2 are comparable to those shown in Fig. 9.3. We, therefore, conclude that this model reasonably captures the Y_p-dependence of the cold EOS, for a large range of L values.

We thus have an expression for the symmetry energy at zero-temperature that depends only on n, Y_p, S_0, L, and the narrowly-constrained parameter γ. There are two possible routes for creating a finite-temperature EOS with this framework. One possibility is to start from a cold, physically-motivated EOS, which will provide predicted values for S_0, L, and $Y_{p,\beta}$. In this case, eq. (9.20) can be used to fit for γ. We have provided such fits for the EOS in our sample in Table 9.1. Alternatively, a cold, parametric EOS can be chosen, for which the underlying physics are not specified. In this case, a user can freely specify S_0, L, and γ, which will uniquely specify $Y_{p,\beta}$. For the EOS in our sample, we find that this approach is able to accurately extrapolate from β-equilibrium to arbitrary proton fraction, introducing errors of $\lesssim 10\%$ for densities of interest (above 0.5 $n_{\rm sat}$), and errors of $\lesssim 3\%$ at high densities.

9.5 Thermal contribution to the energy

We now turn to the thermal energy, which was first defined in eq. (9.12c) as

$$\begin{aligned} E_{\rm th}(n, Y_p, T) = {} & E_{\rm nucl,th}(n, Y_p = 1/2, T) \\ & + E_{\rm sym,th}(n, T) \times (1 - 2Y_p)^2 \\ & + E_{\rm lepton,th}(n, Y_p, T). \end{aligned}$$

It is useful to further divide the thermal energy into density regimes, over which the matter displays distinct behaviors. At the lowest densities, the contribution from relativistic leptons and photons dominates. At intermediate densities, an ideal-fluid description suffices. However, at high densities, matter can remain partially degenerate even at intermediate-to-high temperatures. In the high-density regime, some of the available energy goes into lifting the degeneracy of the particles rather than adding thermal support and, accordingly, the thermal pressure can dip well below the prediction for an ideal fluid. (See Fig. 9.6 for the markedly different behaviors in thermal pressure across these three regimes.)

It is, therefore, convenient to write the thermal energy as

$$E_{\text{th}}(n, Y_p, T) = \begin{cases} E_{\text{rel}}(n, T), & n < n_1 \\ E_{\text{ideal}}(T), & n_1 < n < n_2 \\ E_{\text{th,deg.}}(n, Y_p = 1/2, T) + E_{\text{sym,th}}(n, T)(1 - 2Y_p)^2, & n > n_2 \end{cases} \tag{9.23}$$

where the relativistic component,

$$E_{\text{rel}}(n, T) = \frac{4\sigma}{c} \frac{f_s}{n} T^4, \tag{9.24}$$

and the ideal component,

$$E_{\text{ideal}}(T) = \frac{3}{2} k_B T \tag{9.25}$$

are given as in eqs. (9.2) and (9.3). Here, $E_{\text{th,deg.}}(n, Y_p = 1/2, T)$ is the degenerate thermal energy of symmetric matter, which we introduce below. We note that, because the ideal-fluid and relativistic terms do not depend on the proton fraction, the symmetry-energy correction is only relevant in the degenerate regime. Finally, we define the first transition density, n_1, as the density at which the relativistic and ideal-fluid energies are equal. The second transition density, n_2, is the density at which the ideal-fluid energy is equal to the degenerate thermal energy, for a given temperature and proton fraction.

This piecewise expression of the thermal energy is convenient for later calculations of the thermal pressure and the sound speed. However, the discontinuities at the transition densities are artificial and will create problems in numerical simulations, potentially leading to undesired reflections of matter waves at density boundaries. Thus, whenever we actually implement the thermal energy or pressure, we use a smoothed version instead. This smoothed version is of the form

$$E_{\text{th}}(n, Y_p, T) \approx E_{\text{rel}}(n, T) + \left[E_{\text{ideal}}(T)^{-1} + E_{\text{th,deg.}}(n, Y_p, T)^{-1} \right]^{-1} \tag{9.26}$$

where we have added the latter two terms inversely to ensure that the ideal term dominates at intermediate densities and the degenerate term dominates at the highest densities. The smoothed approximation is also more computationally efficient than the piecewise version, as it does not require the calculation of transition densities, which will vary with the temperature and proton fraction.

In order to calculate the thermal energy in the degenerate regime, we consider the nucleons as a free Fermi gas. In that limit, the leading-order thermal energy of degenerate matter is given by

$$\begin{aligned} E_{\text{th, q}}^{\text{deg}}(n, Y_q, T) &= a(Y_q n, M^*) \left(\frac{N_q}{N_p + N_n} \right) T^2, \\ &= a(Y_q n, M^*) Y_q T^2 \end{aligned} \tag{9.27}$$

for a single-species system of particle q. For simplicity, we have introduced the level-density parameter a, which is defined as

$$a(n_q, M^*) \equiv \frac{\pi^2 k_B^2}{2} \frac{\sqrt{\left(3\pi^2 n_q\right)^{2/3} (\hbar c)^2 + M^*(n_q)^2}}{\left(3\pi^2 n_q\right)^{2/3} (\hbar c)^2}, \tag{9.28}$$

where $M^*(n_q)$ is the Dirac effective mass of the relevant species at a specific density. (For a complete derivation at next-to-leading order in temperature, see Constantinou et al., 2015).

As an example, the thermal nuclear energy for symmetric matter would be

$$\begin{aligned} E_{\text{th, nucl}}^{\text{deg}}(n, T) &= \left[\frac{a(n_p, M^*_{\text{p,SM}}) N_p + a(n_n, M^*_{\text{n,SM}}) N_n}{N_p + N_n} \right] T^2 \\ &= a(0.5n, 0.5 M^*_{\text{SM}}) T^2, \end{aligned} \tag{9.29}$$

where the subscript SM stands for symmetric matter and, in the second line, we have used the fact that $n_n = n_p = 0.5n$ in symmetric matter. We have further made the approximation that the effective masses of neutrons and protons are comparable in symmetric matter and that the average of these two effective masses gives the overall effective mass of symmetric matter, i.e., $M^*_{\text{n,SM}} \approx M^*_{\text{p,SM}} \approx {}^{1}\!/_{2} M^*_{\text{SM}}$.

By likewise defining the thermal energy per baryon for pure neutron matter

(PNM), we can calculate the thermal contribution to the symmetry energy, as

$$E_{\rm sym,th}(n,T) = \begin{cases} 0, & n < n_2 \\ \left[a(n, M^*_{\rm PNM}) - a(0.5n, 0.5M^*_{\rm SM})\right] T^2, & n > n_2, \end{cases} \tag{9.30}$$

where the low-density limit of $E_{\rm sym,th}$ arises from the fact that both pure neutron matter and symmetric matter behave identically as ideal or relativistic fluids at $n < n_2$.

In principle, this symmetry energy term extrapolates the thermal energy of symmetric nuclear matter to arbitrary proton fraction. However, we find that including this term has a negligible effect on the results. In particular, making the approximation $E_{\rm th,\ nucl}(n, Y_p, T) \approx E_{\rm th,\ nucl}(n, Y_p = {}^1\!/\!_2, T)$ introduces an average error of $\lesssim 1\%$ in the total pressure across the density range of interest. We thus neglect the thermal correction to the symmetry energy for the remainder of the chapter.

For leptons, the degenerate thermal pressure is even simpler. The effective mass of electrons is approximately constant, due to their small cross-sections of interaction. Hence, $M^*_e \approx m_e$. This allows us to write eq. (9.27) simply as

$$E^{\rm deg}_{\rm th,\ e^-}(n, Y_p, T) = a(Y_p n, m_e) Y_p T^2, \tag{9.31}$$

where we have required that the electron fraction balance the proton fraction in order to satisfy the requirement of charge neutrality and we have used eq. (9.6) to substitute Y_p. We note that in the presence of a significant population of positrons, the proton fraction in eq. (9.31) should be replaced by the net lepton fraction.

With expressions for the degenerate and ideal fluid thermal terms in hand, we can now write a complete version of eq. (9.12c) for $E_{\rm th}$ as follows:

$$E_{\rm th}(n, Y_p, T) = \begin{cases} 4\sigma f_s T^4/(cn), & n < n_1 \\ (3/2) k_B T, & n_1 < n < n_2 \\ \left[a(0.5n, 0.5M^*_{\rm SM}) + a(Y_p n, m_e) Y_p\right] T^2, & n > n_2 \end{cases} \tag{9.32}$$

where we have neglected the thermal contribution to the symmetry energy, as discussed above.

We thus have a complete expression for the thermal energy of matter as a function only of the density, temperature, proton fraction, and the effective mass of the nucleons in symmetric matter.

9.5.1 M^*-approximation

A full calculation of $E_{\rm th}$ using eq. (9.32) requires knowledge of the Dirac effective masses in symmetric matter, and hence the scalar meson interactions and particle potentials of a particular EOS. We instead choose to express the Dirac effective mass with a physically-motivated yet computationally-simple approximation. At low densities, the effective mass must approach the dominant nucleon mass, while at higher densities, M^* must decrease as particle interactions become important. We represent this behavior by introducing a power-law expression,

$$M^*(n_q) = \left\{ (mc^2)^{-b} + \left[mc^2 \left(\frac{n_q}{n_0} \right)^{-\alpha} \right]^{-b} \right\}^{-1/b}, \tag{9.33}$$

where m is the nucleon mass (which we take to be the neutron mass, $mc^2 =$ 939.57 MeV)[6] and n_0 is the transition density above which M^* starts to decrease. The exponent b determines the sharpness of the transition and α specifies the power-law slope at high densities. We find that $b = 2$ works well to represent the curvature connecting the low- and high-density regimes, and thus fix it to this value in the following analysis, leaving just two free parameters to describe the effective mass, $M^* = M^*(n_0, \alpha)$.

We fit the effective masses together at $k_B T = 1, 10,$ and 47.9 MeV for nine of the EOS in our sample, using a standard least-squares method across the entire density range provided. We exclude the models LS and SLY4-RG here because the effective masses for these EOS are not currently published (but see §9.5.3 for a separate comparison with these models). The results of these fits are given in Table 9.2 for symmetric matter. For completeness, we also include in Table 9.2 the fits for pure neutron matter, which can be used to calculate $E_{\mathrm{sym,th}}(n, T)$ in eq. (9.30).

---

[6] The EOS in our sample vary in their low-density limit of M^* from 938−939.57 MeV. This parameter can easily be adjusted to any low-density value for M^*. For simplicity, however, we take it to simply be the neutron mass. We find that this simplification has a negligible effect on our results.

We show the performance of the fit for NL3 in Fig. 9.4. In this fit, we use the NL3 tables calculated at $k_B T = 1, 10$, and 47.9 MeV (shown in purple, orange, and blue, respectively) with a proton fraction of Y_p=0.01, to emulate pure neutron matter. We show our approximation for M^* as the black solid line. We find that the M^*-approximation accurately captures the behavior predicted by the full EOS, with fit parameters $n_0 = 0.10$ fm^{-3} and $\alpha = 0.90$. Figure 9.5 shows the M^* predictions and our approximation thereof for $Y_p = 0.5$. The M^*-approximation is similarly able to capture the behavior of symmetric matter, with slightly adjusted parameters $n_0 = 0.11$ fm^{-3} and $\alpha = 1.08$.

As a brief aside, we note a discontinuity in the first derivative of M^* at approximately half the nuclear saturation density for large Y_p and low temperatures (seen most clearly in the purple stars in Fig. 9.5, at $n_{\mathrm{sat}}/2 \approx 0.08$ fm^{-3}). This discontinuity is an artifact of the treatment of the first-order phase transition to uniform nuclear matter at these densities in the original EOS calculations.

There is an easily understood origin of this artifact. Lattimer and Swesty (1991), Shen et al. (1998), and Hempel and Schaffner-Bielich (2010) all use a Maxwell construction to calculate the phase transition at approximately half the nuclear saturation density. At low proton fractions, where matter is approximately made up of a single species, the Maxwell construction works well to represent the phase transition. However, the Maxwell construction is invalid for multi-component species: When a system has more than one significant component, the Gibbs construction must instead be used (Glendenning, 1992, 2000). Because all EOS that are included in this section use the Maxwell construction, they all suffer from artifacts due to this choice at roughly half the saturation density, where the transition to uniform nuclear matter occurs.

Correcting these artifacts would require re-calculating all EOS with a different formalism and is beyond the scope of this chapter. However, we note that at high

Table 9.2. Parameters characterizing M^*, fit together at $k_BT = 1, 10$, and 47.9 Mev, for either pure neutron matter (PNM) or symmetric matter (SM).

	PNM ($Y_p = 0.01$)		SM (Y_p= 0.5)	
EOS	n_0 (fm^{-3})	α	n_0 (fm^{-3})	α
TM1	0.11	0.73	0.12	0.86
TMA	0.11	0.65	0.13	0.77
NL3	0.10	0.90	0.11	1.08
FSUGold	0.10	0.61	0.11	0.72
IUFSU	0.11	0.72	0.12	0.85
DD2	0.08	0.68	0.10	0.84
STOS	0.11	0.76	0.12	0.90
SFHo	0.21	0.82	0.22	0.89
SFHx	0.16	0.77	0.17	0.88
Range	0.08-0.21	0.61-0.90	0.10-0.22	0.72-1.08
Mean	0.12	0.74	0.13	0.87

Note. — We fix $b = 2$ and $m = m_n$ in all fits.

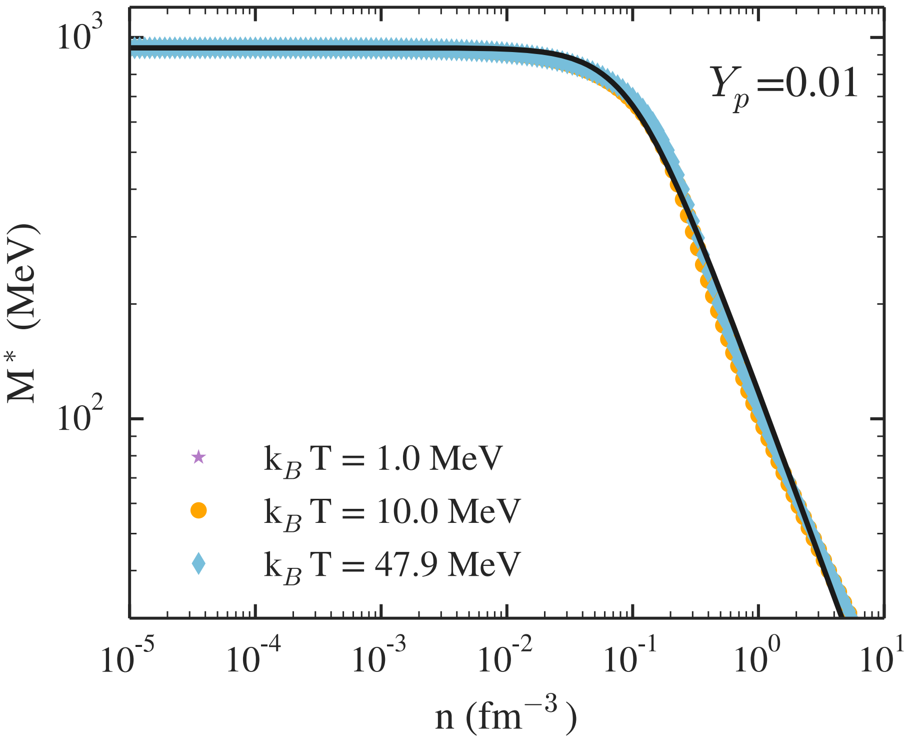

Figure 9.4 Dirac effective mass as a function of the number density, for NL3 at Y_p=0.01 (pure neutron matter) and $k_BT = 1, 10$ and 47.9 MeV (in purple, orange, and blue, respectively). The symbols represent the effective mass predictions for the full version of NL3. The solid black line shows our approximation using eq. (9.33). We find that, with fit parameters $n_0 = 0.10$ fm^{-3} and $\alpha = 0.90$, the M^*-approximation accurately reproduces the values predicted by the full EOS.

temperatures ($k_BT \gtrsim$15 MeV), the non-uniform phase of matter disappears (see discussion around Fig. 5 in Shen et al. 1998). Thus, we can avoid the issue altogether by performing our fit to M^* at only the highest temperatures, when Y_p is large. In practice, we find that whether we fit only the $k_BT = 47.9$ MeV curve for M^* or we fit the curves for all the temperatures together, the difference in the resulting parameters is small. We, therefore, choose to perform the fits to three temperatures ($k_BT = 1, 10$ and 47.9 MeV) together and use the same method for both low and high proton fractions.

Returning to our discussion of the M^* model, we note that the errors introduced by using our M^*-approximation are comparable to those shown in Figs. 9.4 and

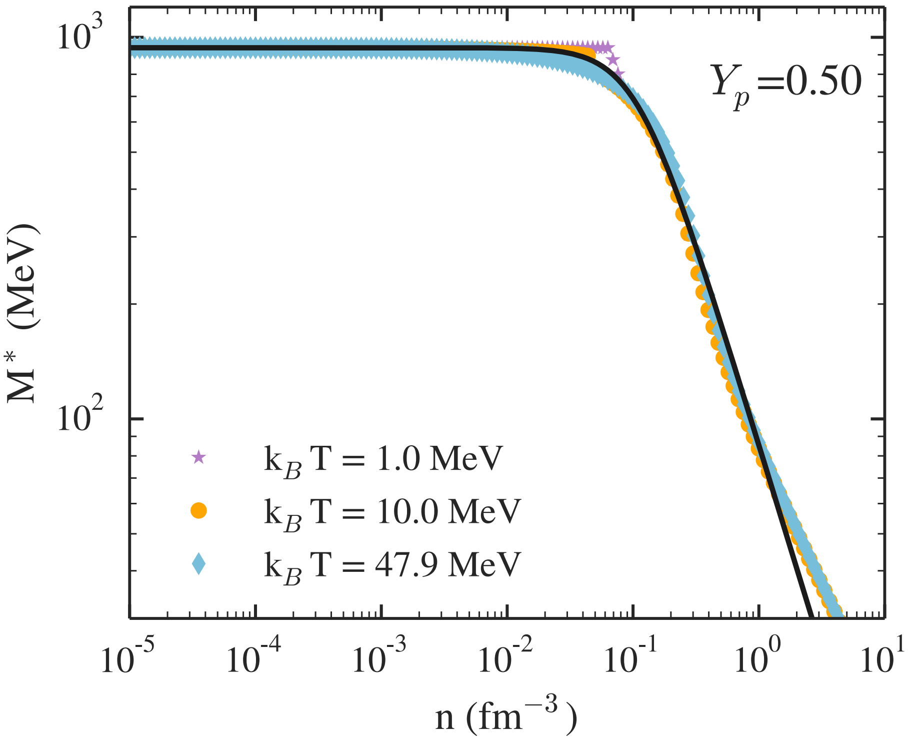

Figure 9.5 Same as Fig. 9.4, but for $Y_p = 0.5$ (symmetric matter). We find that, with fit parameters $n_0 = 0.11$ fm^{-3} and $\alpha = 1.08$, the M^*-approximation again reproduces the values predicted by NL3 reasonably well, up to $\sim 10\ n_{\rm sat}$. At low temperatures, the discontinuity in the effective mass stems from the Maxwell construction used in the original EOS calculation to represent the phase transition to uniform nuclear matter. At high temperatures, this artifact disappears.

9.5 for the full set of nine EOS in this section. We thus conclude that our M^*-approximation reasonably captures the density-dependence of the Dirac effective mass, while greatly simplifying subsequent calculations.

Moreover, we find that the range of inferred fit parameters is relatively narrow. In particular, for a wide range of temperatures and EOS, we find that the transition density lies in the range $n_0 \in (0.08, 0.22)$ fm^{-3}, with an average value of $\sim$0.13 fm^{-3} for both pure neutron matter and symmetric matter. The power-law index characterizing the decay of M^* is similarly well constrained, with $\alpha \in (0.61 - 0.90)$, with an average value of 0.74 for pure neutron matter; and $\alpha \in (0.72 - 1.08)$, with a slightly higher average value of 0.87 for symmetric matter. We find only a weak dependence of n_0 and α on the temperature, thus suggesting that these parameters could be treated as constants for use in numerical simulations.

9.5.2 Performance of the M^*-approximation of thermal effects at fixed Y_p

We now turn to a comparison between the M^*-approximation of the thermal effects and the nine EOS listed in Table 9.2. As in §9.4, we make the comparison in terms of the pressure, rather than the energy, and use eq. (9.13) to convert between the two. The expressions for $P_{\rm th}(n, Y_p, T)$ are given in Box II in §9.6. In particular, all results shown here use the smoothed approximation of the thermal pressure, as defined in eq. (9.39).

In order to focus specifically on the thermal pressure, we calculate the thermal contribution to the pressure from each realistic EOS in our sample by subtracting the cold component at the same Y_p.

In general, we find excellent agreement between the M^*-approximation and the thermal pressures calculated from the full EOS. We show an example in Fig. 9.6 for NL3. We find that our approximation of $P_{\rm th}$ closely recreates the full calculation for NL3 for nearly all densities and temperatures explored here. For comparison, we also include in Fig. 9.6 the hybrid approximation with $\Gamma_{\rm th} = 1.67$ as dashed lines.[7] The full thermal pressure agrees with the hybrid approximation only at intermediate densities. At the lowest densities, this value of $\Gamma_{\rm th}$ overestimates the contribution from relativistic species. At higher densities that are relevant for forming and merging neutron stars, particle interactions become important and the ideal-fluid approximation grossly overestimates the thermal pressure, remaining several orders of magnitude above the true thermal pressure.

In order to gain an intuitive understanding of the behavior of $P_{\rm th}$, we also ex-

---

[7] We choose the relatively low value of $\Gamma_{\rm th} = 1.67$ in order to minimize the residuals of the hybrid model. This value of $\Gamma_{\rm th}$ ensures the hybrid EOS matches an ideal fluid at intermediate densities. Larger values, as are more commonly used in numerical simulations, would cause the hybrid $P_{\rm th}$ to overestimate even the ideal regime.

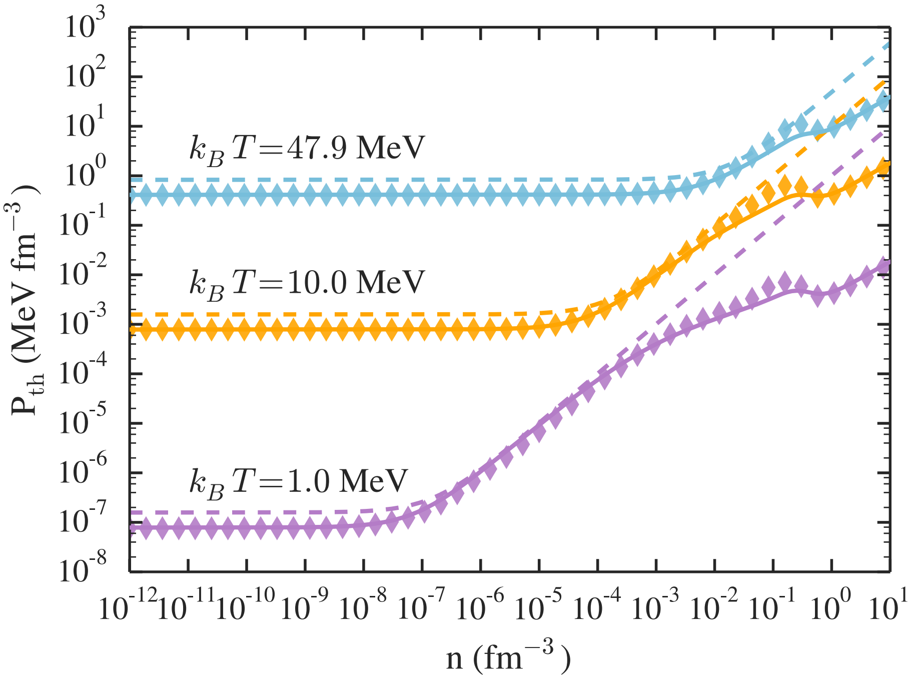

Figure 9.6 Smoothed thermal pressure as a function of density for the EOS NL3 with $Y_p = 0.1$. The various colors are calculated at k_BT=1 MeV (purple), k_BT=10 MeV (orange), and k_BT=47.9 MeV (blue). The thermal pressure of the full EOS is shown as the symbols, while the solid lines represent the M^*-approximation of $P_{\rm th}$, using the fit parameters for NL3 from Table 9.2 ($n_0 = 0.11$ fm$^{-3}, \alpha = 1.08$). The dashed lines show the $\Gamma_{\rm th} = 1.67$ hybrid approximation at each temperature. We find excellent agreement between the M^*-approximation and the full thermal pressure and find that the M^*-approximation offers a significant improvement over the hybrid EOS.

plore an extreme range of the M^* parameters. Specifically, in Fig. 9.7, we zoom in on $P_{\rm th}$ at $k_BT = 10$ MeV and $Y_p = 0.5$ and show the effect of varying the parameters n_0 and α for symmetric matter. We intentionally take extreme values for the parameters, well beyond the ranges found in Table 9.2, in order to emphasize that the variations between more realistic parameter choices will be small. Even for these unreasonable choices of values for n_0 and α, we find that $P_{\rm th}$ approximates the full thermal pressure reasonably well and, in all cases, better than the ideal fluid approximation. Analyzing the specific dependences more closely, we see in Fig. 9.7 that the parameter n_0 controls the density at which the rise in the thermal pres-

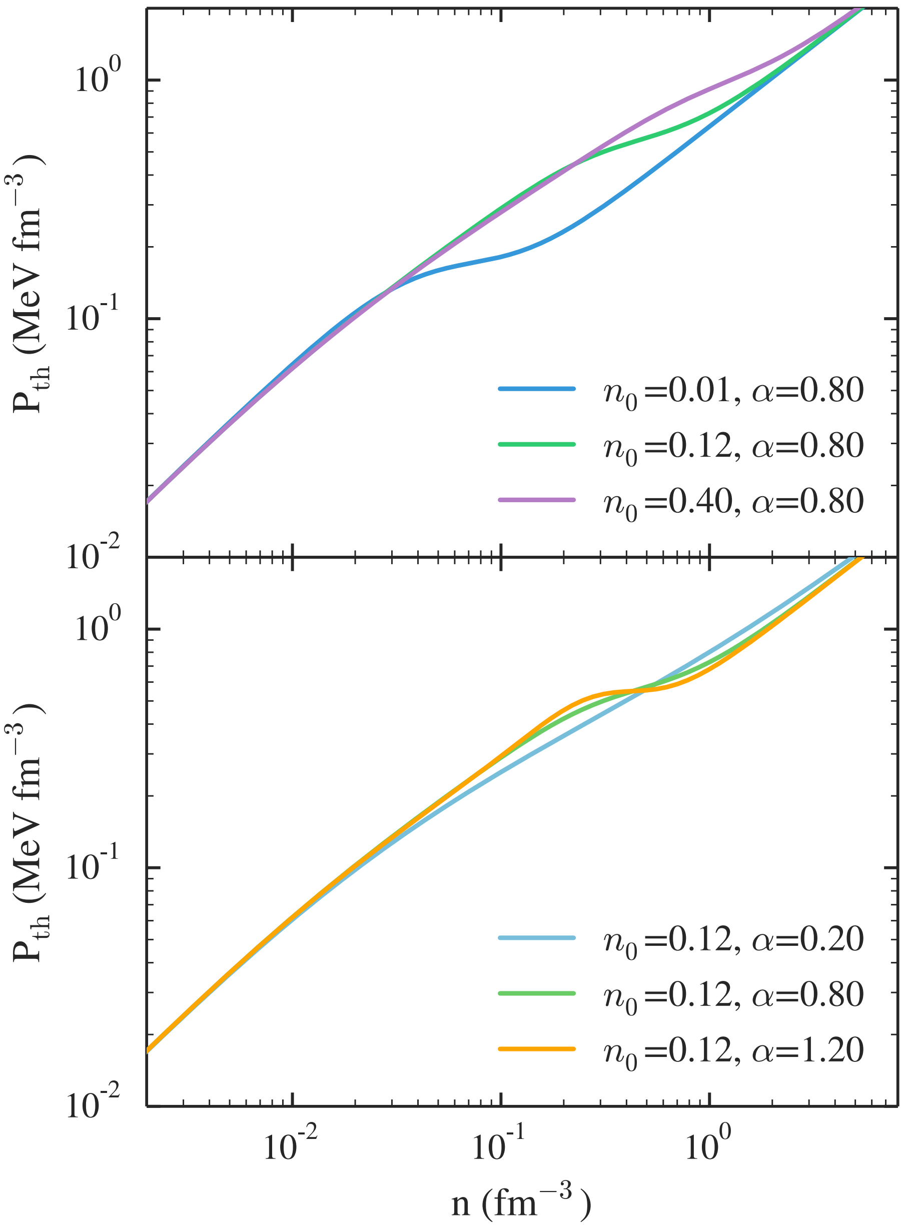

Figure 9.7 The M^*-approximation of the thermal pressure at $k_BT = 10$ MeV and $Y_p = 0.5$, with intentionally extreme choices of the parameter values. The top panel shows the effect of varying n_0 for a fixed value of $\alpha = 0.8$; the bottom panel shows the effect of varying α for fixed n_0=0.12 fm^{-3}.

sure starts to slow. This corresponds to the density at which particle interactions become significant and degenerate thermal effects can no longer be ignored. The parameter α, which controls the power-law slope of M^*, directly controls the height

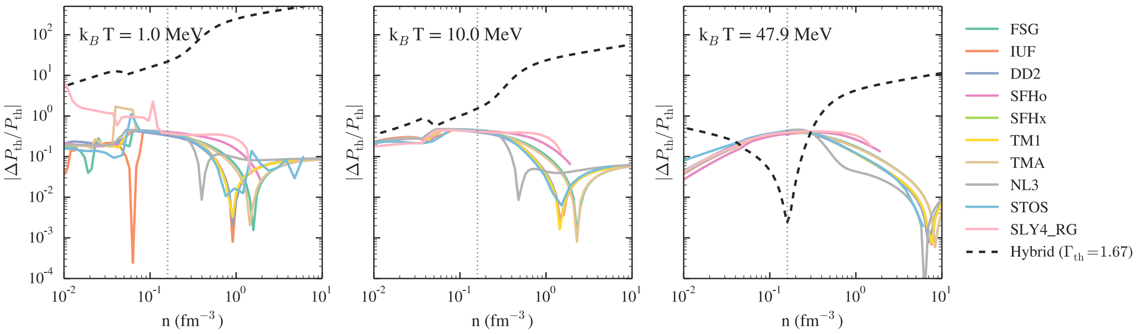

Figure 9.8 Residuals between the smoothed M^*-approximation of the thermal pressure and the full results calculated for each EOS listed in Table 9.2. From left to right, the panels are at $k_BT = 1, 10$ and 47.9 MeV; all three panels are for $Y_p = 0.1$. The various colors represent the different EOS. For comparison, we also include the residuals between the full EOS NL3 and the ideal-fluid approximation ($\Gamma_{\rm th} = 1.67$) as the black dashed line. The vertical dotted line marks $n_{\rm sat}$. Our M*-approximation of $P_{\rm th}$ produces residuals that are up to three orders of magnitude smaller than the ideal-fluid approximation.

of the dip in $P_{\rm th}$. This makes intuitive sense: if particle interactions are stronger, M^* decreases more rapidly, α will be larger, and the thermal pressure will deviate even more drastically from the ideal-fluid approximation as part of the free energy is taken up by those interactions.

Finally, we compare the M^*-approximation of the thermal pressure against the full sample of EOS listed in Table 9.2. We show the corresponding residuals at three temperatures in Fig. 9.8 and find that the residuals are typically $\lesssim 30\%$ at densities above 0.5 $n_{\rm sat}$. For comparison, Fig. 9.8 also shows a sample set of residuals between the full thermal pressure from NL3 and the hybrid approximation ($\Gamma_{\rm th} = 1.67$) as the black dashed line. We find that the M^*-approximation produces residuals that are up to three orders of magnitude smaller than the ideal-fluid approximation used in hybrid EOS, with only two additional parameters that are easy to specify.

9.5.3 M^*-approximation for non-RMF models

We have so far only calculated the thermal pressures using the sub-sample of EOS for which there exist published tables of the effective masses. While this allowed us to directly test the performance of the M^*-approximation, this set of EOS happens to also be calculated exclusively with RMF models. In this section, we compare the M^*-approximation to the LS and SLY4-RG models, which are calculated using non-relativistic Skyrme energy functionals (see § 9.2). We also include here the two-loop exchange model of Zhang and Prakash (2016), which is an extension of mean field theory. We note that the pressures of the Zhang and Prakash (2016) EOS are reported only at $Y_p = 0$ and 0.5, which is why this EOS is not included in our full sample. As a result of these and other limitations in the publicly-available values for this EOS, all comparisons in this section are made at $Y_p = 0.5$ and $T = 20$ MeV. We also fix n_0 and α to the mean values for symmetric matter from Table 9.2 for all three EOS.

Figure 9.9 shows the residuals between the M^*-approximation of the thermal pressure and the true EOS for these three models. For comparison, this figure also shows the corresponding residuals between the hybrid approximation and the true EOS (dashed lines). In general, we find that the M^*-approximation of the thermal pressure results in larger residuals for these EOS compared to the RMF models, but that it still offers a significant improvement over the hybrid approximation at densities above $\sim n_{\text{sat}}$.

We also compared the residuals at $T = 50$ MeV and found that the M^*-approximation performed comparably to the hybrid approximation at this temperature. In fact, for densities between n_{sat} and 0.7 fm^{-3}, the hybrid approximation produces slightly smaller residuals in the thermal pressure for these non-RMF models. In this regime, the hybrid approximation tends to over-estimate the thermal pressure for these models, while the M^*-approximation tends to under-estimate P_{th} by a similar degree. However, even in this case, the M^*-approximation still offers an appreciable improvement over the hybrid approximation at the highest densities, above ~ 0.7 fm^{-3}.

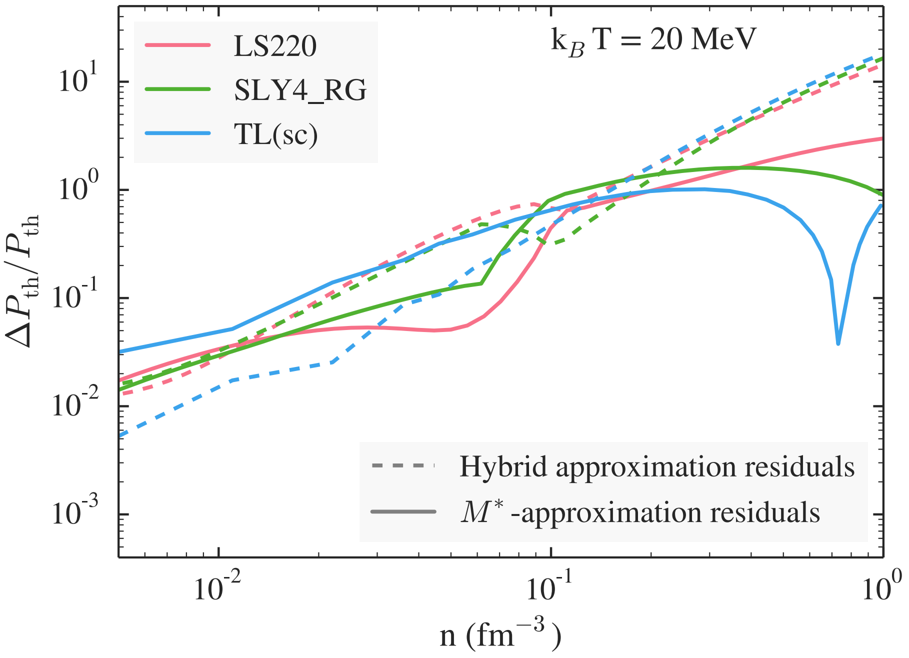

Figure 9.9 Residuals between the smoothed M^*-approximation of the thermal pressure and the true EOS at Y_p=0.5 and $T = 20$ MeV for three non-RMF models. For n_0 and α, we use the mean fit values for symmetric matter from Table 9.2. The dashed lines show the corresponding residuals between the true EOS and the hybrid approximation using $\Gamma_{\rm th}$=1.67, at the same proton fraction and temperature. The three EOS shown are LS (pink), SLY4-RG (green), and the two-loop model of Zhang and Prakash (2016) (“TL(sc)”, blue). We find that, while the M^*-approximation produces slightly larger residuals for these EOS than for the RMF models, it nevertheless offers a significant improvement over the hybrid approximation at high densities.

9.6 Putting it all together

We now summarize the equations and approximations that we have developed so far to represent the total energy per particle in Box I.

Box I: Total Energy Expressions for Finite-Temperature Dense Gas.

The energy per particle of *n*-*p*-*e* matter is given by

$$E(n, Y_p, T) = \big(\text{Cold EOS in } \beta\text{-equilibrium}\big) + 3K\left(Y_p^{4/3} - Y_{p,\beta}^{4/3}\right) n^{1/3}$$
$$+ E_{\rm sym}(n, T=0)\left[(1-2Y_p)^2 - (1-2Y_{p,\beta})^2\right]$$
$$+ \begin{cases} 4\sigma f_s T^4/(cn), & n < n_1 \\ (3/2)k_B T, & n_1 < n < n_2 \\ \left[a(0.5n, 0.5M^*_{\rm SM}) + a(Y_p n, m_e)Y_p\right]T^2, & n > n_2, \end{cases}$$

where the symmetry energy is approximated as

$$E_{\rm sym}(n, T=0) = \eta E^{\rm kin}_{\rm sym}(n) + \left[S_0 - \eta E^{\rm kin}_{\rm sym}(n_{\rm sat})\right]\left(\frac{n}{n_{\rm sat}}\right)^{\gamma},$$

$$E^{\rm kin}_{\rm sym}(n) = \frac{3}{5}\left(1 - 2^{1/3}\right)E_f(n),$$

$$\eta = \frac{5}{9}\left[\frac{L - 3S_0\gamma}{\left(1-2^{1/3}\right)(2/3-\gamma)\,E_f(n_{\rm sat})}\right],$$

and the terms of the M^*-approximation are given by

$$a(n_q, M_q^*) \equiv \frac{\pi^2 k_B^2}{2}\frac{\sqrt{M_q^*(n_q)^2 + (3\pi^2 n_q)^{2/3}(\hbar c)^2}}{(3\pi^2 n_q)^{2/3}(\hbar c)^2}$$

and

$$M^*(n_q) = \left\{(mc^2)^{-b} + \left[mc^2\left(\frac{n_q}{n_0}\right)^{-\alpha}\right]^{-b}\right\}^{-1/b}.$$

The parameters S_0, L, and $\gamma \in (0.2 - 1.2)$ are freely specified; this will uniquely specify $Y_{p,\beta}$. Alternatively, S_0, L, and $Y_{p,\beta}$ may be specified and the proton fraction may be fit for γ. We provide fits to γ for eleven EOS in Table 9.1. We find that for $M^*_{\rm SM}$, $n_0 \sim 0.13$ fm^{-3} and $\alpha \sim 0.9$ provide reasonable fits to most EOS.

Using the expressions for the energy from Box I., we can derive the pressure via the standard thermodynamic relations of eq. (9.13), where the derivatives are evaluated at constant Y_p, $Y_{p,\beta}$, and S. The total entropy of the relativistic, ideal-fluid, and degenerate terms is given by

$$S(n, N_p, N_n, N_e, T) = \begin{cases} S_{\rm rel}, & n < n_1 \\ S_{\rm ideal}, & n_1 < n < n_2 \\ S_{\rm deg}, & n > n_2, \end{cases} \tag{9.34}$$

where n_1 and n_2 are the thermal energy transition densities, as defined in §9.5.

The entropy of a gas of relativistic leptons and photons is given by

$$S_{\rm rel} = \frac{16\sigma f_s}{3c} \left(\frac{N_p + N_n}{n} \right) T^3. \tag{9.35}$$

The entropy of a monatomic ideal fluid is given by the Sackur-Tetrode equation,

$$S_{\rm ideal} = \left(N_p + N_n + N_e\right) k_B \times \left\{ \ln \left[\left(\frac{N_p + N_n}{N_p + N_n + N_e} \right) n^{-1} \left(\frac{m k_B T}{2\pi \hbar^2} \right)^{3/2} \right] + \frac{5}{2} \right\}. \tag{9.36}$$

Finally, the entropy of a degenerate Fermi gas in our framework is given by

$$S_q = 2 a_q N_q T \tag{9.37}$$

for a particle q, so that the total entropy for the degenerate terms is

$$S_{\rm deg} = 2\left\{ a(0.5n, 0.5M^*_{\rm SM})[N_n + N_p] + a(Y_p n, m_e) N_e \right\} T. \tag{9.38}$$

We summarize the resulting pressure equations in Box II.

Box II: Pressure Expressions for Finite-Temperature Dense Gas.

The pressure of n-p-e matter is given by

$$\begin{aligned} P(n, Y_p, T) = &\big(\text{Cold EOS in } \beta\text{-equilibrium}\big) + K\left(Y_p^{4/3} - Y_{p,\beta}^{4/3}\right) n^{4/3} \\ &+ P_{\rm sym}(n, T=0)\left[(1-2Y_p)^2 - (1-2Y_{p,\beta})^2\right] \\ &+ \begin{cases} 4\sigma f_s T^4/(3c), & n < n_1 \\ n k_B T, & n_1 < n < n_2 \\ -\left[\frac{\partial a(0.5n, 0.5M^*_{\rm SM})}{\partial n} + \frac{\partial a(Y_p n, m_e)}{\partial n} Y_p\right] n^2 T^2, & n > n_2, \end{cases} \end{aligned}$$

where n_1 and n_2 are the thermal energy transition densities for a particular temperature and proton fraction. The symmetry pressure, corresponding to our model of the symmetry energy, is

$$P_{\rm sym}(n, T=0) = \frac{2\eta}{3} n E^{\rm kin}_{\rm sym}(n) + \left[S_0 - \eta E^{\rm kin}_{\rm sym}(n_{\rm sat})\right]\left(\frac{n}{n_{\rm sat}}\right)^{\gamma} \gamma n.$$

The full analytic expression for $Y_{p,\beta}$ is given in eq. (9.20) and derived in Appendix B. The M^*-approximation derivatives are given by

$$\left.\frac{\partial a(n_q, M^*)}{\partial n}\right|_{Y_q} = -\left(\frac{2a(n_q, M^*)}{3n}\right) \times$$
$$\left\{1 - \frac{1}{2}\left[\frac{M^*(n_q)^2}{M^*(n_q)^2 + (3\pi^2 n_q)^{2/3}(\hbar c)^2}\right]\left(\frac{(3\pi^2 n_q)^{2/3}(\hbar c)^2}{M^*(n_q)^2} + 3\left.\frac{\partial \ln[M^*(n_q)]}{\partial \ln n}\right|_{Y_q}\right)\right\},$$

and

$$\left.\frac{\partial \ln[M^*(n_q)]}{\partial \ln n}\right|_{Y_q} = -\alpha\left[1 - \left(\frac{M^*(n_q)}{Y_q m c^2}\right)^2\right],$$

where, for symmetric matter, we replace $M^*(n_q) \rightarrow 0.5M^*_{\rm SM}(0.5n)$ and for the electrons, $M^*(n_q) \rightarrow m_e$.

As in Box I., there are five free parameters: $S_0, L, \gamma, n_0, \alpha$. A user may freely specify S_0, L, and $Y_{p,\beta}$ and fit for γ. Alternatively, a user may specify S_0, L, and γ, which will uniquely specify $Y_{p,\beta}$. We provide fits for γ, n_0, and α for the EOS in our sample in Tables 9.1 and 9.2.

The piecewise definitions of the thermal energy and pressure are mathematically convenient, but the sharp transitions are themselves unphysical, as discussed in §9.5. We, therefore, instead implement the thermal pressure using a smoothed approximation of the form

$$P_{\rm th}(n, Y_p, T) \approx P_{\rm rel} + \left(P_{\rm ideal}^{-1} + P_{\rm deg}^{-1}\right)^{-1}. \tag{9.39}$$

This smoothed approximation of the thermal pressure is used for the figures throughout this chapter. We note that we use this separate smoothing for both the thermal pressure and the thermal energy (as in eq. 9.26) in order to keep the problem tractable. However, this is not mathematically exact since, formally, the energy is the proper thermodynamic function and the pressure should, ideally, be derived from the smoothed energy. Nevertheless, the errors introduced by the separate smoothing approximations will be limited to the regions close to the transition points. Physically, the mismatch between the approximate thermal energy and pressure will correspond to a small error in the sound speed in these regions, which we neglect for the present purposes.

Finally, we note that our model allows significant freedom in creating a new finite-temperature EOS. We have provided a set of parameters that correspond to physically-motivated EOS, but if one wishes to vary these parameters significantly, it will be useful to check that the resulting EOS is still physical. One requirement of a realistic EOS is that the sound speed remain sub-luminal at all densities and temperatures of interest. For this reason, we include in Appendix C a calculation of the sound speed for astrophysical merger scenarios.

9.7 Complete model: Comparison of realistic EOS at arbitrary Y_p and T

In §9.4, we found that our model is able to extrapolate from β-equilibrium to an arbitrary proton fraction with resulting errors of $\lesssim 10\%$ at densities above 0.5 $n_{\rm sat}$. Similarly, in §9.5.2, we showed that the M^*-approximation is able to reproduce the

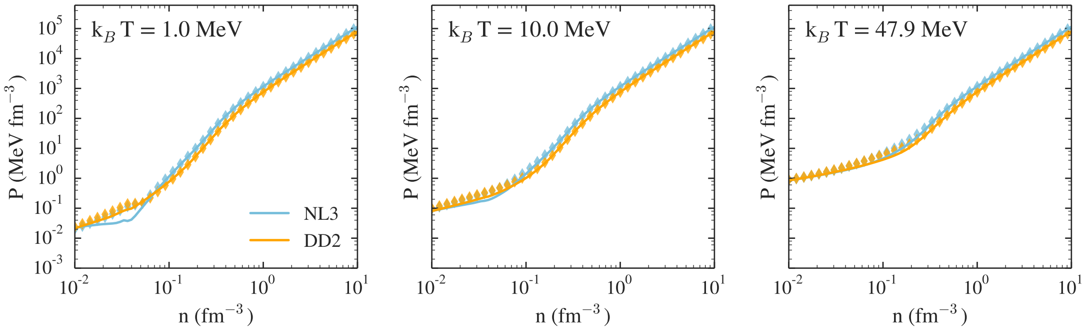

Figure 9.10 Our approximation of P and the EOS pressures predicted by NL3 and DD2 (in blue and orange, respectively). The EOS predictions are shown as the diamonds, while our model is shown as the solid lines. The three panels are at $Y_p = 0.1$ and $k_B T = 1, 10$, or 47.9 MeV (from left to right). We find that our approximation is able to closely recreate the pressures predicted by NL3 and DD2 at densities above n_{sat} for all temperatures.

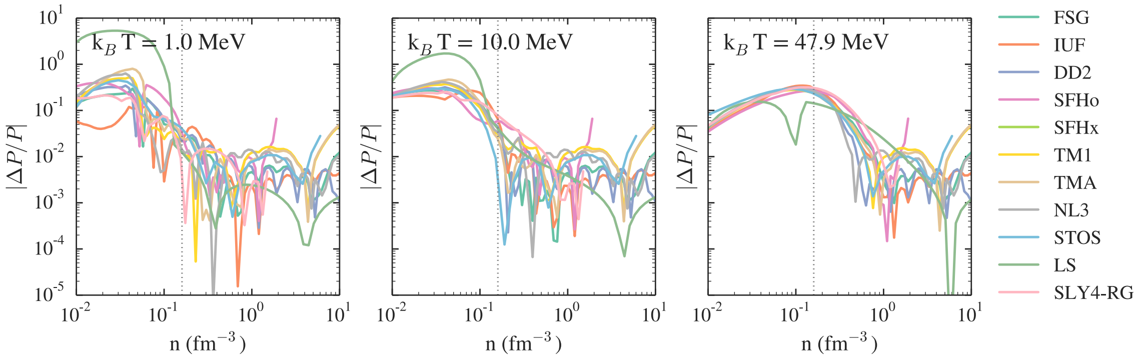

Figure 9.11 Residuals between our approximation of P and the EOS pressures predicted by the eleven EOS in our sample. The three panels are at $Y_p = 0.1$ and $k_B T = 1, 10$, or 47.9 MeV (from left to right). The vertical dotted line marks n_{sat}.

thermal pressure of realistic EOS, at fixed Y_p, to within $\sim 30\%$ for a variety of EOS based on RMF theory. In this section, we quantify the performance of our complete model: starting with a cold EOS in β-equilibrium, and extrapolating to arbitrary temperature and proton fraction.

Figure 9.10 shows an example of a complete model for NL3 and DD2 at three different temperatures. For our approximation, we start with the relevant cold EOS in β-equilibrium and add the corrections outlined in Box II, to extrapolate the pressure to $Y_p = 0.1$ and the three indicated temperatures. We take the values for n_0, α, and γ listed in Tables 9.1 and 9.2 for each EOS. We show the results as the solid lines in Fig. 9.10, while the predictions of the full EOS are shown as the diamonds. We find close agreement between our approximation and the full pressures predicted by NL3 and DD2, especially at densities above $\sim 0.5\ n_{\rm sat}$.

Figure 9.11 shows the corresponding residuals between our approximation and the full EOS for NL3 and DD2, as well as the rest of our sample of EOS. For each EOS in this figure, we use the values for n_0, α and γ listed in Tables 9.1 and 9.2, where possible. For LS and SLY4-RG, for which we do not have fit values for n_0 and α, we use the average parameter values for symmetric matter in Table 9.2. We find that our approximation works comparably well to recreate any of the EOS in our sample. Moreover, we find that for $n \gtrsim n_{\rm sat}$, the residuals are $\lesssim 20\%$ at all three temperatures.

For all the EOS in our sample, the error introduced by our model increases in the vicinity of $\sim 0.5 n_{\rm sat}$. This is a result of the break-down in the $E_{\rm sym}$ approximation at low densities. Our derivation of $E_{\rm sym}$ in §9.4 assumed uniform n-p-e matter, but at densities below $\sim 0.5\ n_{\rm sat}$, the matter becomes inhomogeneous. Nevertheless, with the exception of LS, the errors at these densities are still typically $\lesssim 50\%$.

We have thus verified that our model is able to recreate realistic EOS at relevant densities, with a simple set of parameters. The implications of this result are two-fold. First, this approximation can be used in lieu of more complicated calculations, to analytically represent the EOS that are commonly used in the literature with reasonable accuracy. Second, it implies that our approximation can be reliably used to create new finite-temperature EOS for n-p-e matter that probe different physics through the choice of n_0, α, γ, S_0, and L. Our model allows further freedom in creating a new finite-temperature EOS through the choice of the cold, β-equilibrium EOS. We thus find that this model can span a broad range of possible physics, with parameters that are directly tied to the underlying physics and that can be integrated with minimal computational cost to a large array of numerical calculations.

9.8 Conclusions

In this chapter, we have developed a general framework for calculating the pressure of neutron-star matter at arbitrary proton fraction and finite temperature. Our model is designed so that the corrections we have developed here can be added to any cold n-p-e EOS in neutrinoless β-equilibrium. The model is based on a set of five physically-motivated parameters: S_0, L, γ, n_0, and α. The first three, S_0, L, and γ characterize the symmetry energy and can be chosen to match a particular EOS or set of priors from laboratory experiments. The parameters n_0 and α are introduced through our M^*-approximation, where n_0 represents the density at which particle interactions become important and α characterizes the strength of those interactions. We find that the effective masses of nine realistic EOS can be well characterized by our M^*-approximation with a relatively narrow range of these parameters, with average values of $n_0 \sim 0.13$ fm^{-3} and $\alpha \sim 0.9$.

The complete model is able to extrapolate from cold matter in β-equilibrium to arbitrary proton fraction and temperature. We find that our model is able to recreate a sample of eleven realistic EOS with resulting errors of $\lesssim 20\%$ at a variety of temperatures and proton fractions, above $n_{\rm sat}$. In particular, by including the effects of degenerate matter, our M^*-approximation reproduces the thermal pressure of realistic EOS with residuals that are several orders of magnitude smaller than the hybrid EOS that are commonly used in the literature.

In addition to providing a $1-3$ orders-of-magnitude improvement over the ideal-fluid approximation of the thermal pressure, this model also includes the effects of changing the proton fraction, which is particularly relevant in simulating the formation and cooling of proto-neutron stars.

The complete model can thus be used to accurately recreate the realistic EOS that are currently in use in the literature with a set of simple, analytic functions. Furthermore, the model can be used to calculate new finite-temperature EOS that span a wide range of underlying physics, following one of two possible paths. One possibility is to choose a physically-motivated cold EOS, which will provide predictions for the β-equilibrium proton fraction and symmetry energy parameters. These can then be used to fit for the free parameter γ, and then used to extrapolate to an arbitrary proton fraction. Alternatively, one can use a cold, parametric EOS that does not specify the microphysics. In this case, there is freedom to choose the symmetry energy parameters to probe entirely new physics. In either case, one can freely choose the interaction parameters to control the relative importance of thermal effects. All together, these possibilities will allow a new and wide range of physics to be robustly probed in studies of dynamical neutron star phenomena.

CHAPTER 10

Future Prospects

This is an exciting time for studying the neutron star EOS. With the new gravitational wave events that are expected to be observed over the coming years and the ever-growing sample of electromagnetic observations of neutron stars, the community is poised to gain unprecedented insight into the neutron star interior. Given the wealth and diversity of these new data, it is becoming more important than ever to have a robust framework for combining and interpreting neutron star observables.

In this dissertation, I attacked this problem from many angles. I developed a Bayesian scheme to robustly infer the pressures of an optimally parametrized EOS from a diverse set of astrophysical observations. I also derived a series of new, model-independent mappings between global neutron star properties, including between the moment of inertia and the stellar radius, $\widetilde{\Lambda}$ and the radius, and $\widetilde{\Lambda}$ and the nuclear symmetry energy. Combined with the statistical framework that I developed for robustly comparing measurements made in different domains, these mappings can be used to place independent constraints on the same quantities. Using this framework, I derived new constraints on the neutron star radius of $10.2 < R < 11.7$ km from GW170817 (68% confidence; for a flat prior in R), which is already competitive, though consistent with the results from X-ray spectroscopic measurements. I also calculated new constraints on the slope of the nuclear symmetry energy and found modest tension with the results from laboratory-based nuclear physics experiments. Additionally, using the observed distribution of neutron star and black hole masses, I confronted the predictions of recent stellar evolution models and neutrino-driven supernova simulations, and found new evidence in favor of these models. I further used these simulations to uncover the progenitors of the low-mass population of neutron stars. Finally, I introduced a new framework to robustly calculate the dense-matter EOS at arbitrary temperatures and compositions, for use in future simulations of core-collapse supernova and neutron star mergers. In this final chapter of my dissertation, I turn to the prospects for deriving new EOS constraints, given upcoming new facilities and anticipated advances in numerical simulations in the coming years.

10.1 Upcoming new data

Over the next two decades, new observations of neutron stars – both from existing and from proposed next-generation facilities – will enable new EOS constraints. In some cases, these new observations will provide more stringent constraints on existing measurements (e.g., the neutron star radius), in which case the framework that I have developed throughout this dissertation can be used to immediately derive tighter constraints on the EOS. However, in other cases, the new observatories being planned may offer entirely new insight into the neutron star interior (e.g., with the anticipated detection of post-merger gravitational waves). In this section, I will present an overview of some upcoming observational developments that will further advance neutron star science.

10.1.1 X-ray observations

I will start at high energies. As discussed in Chapter 7, the NICER collaboration recently released its first X-ray dataset for four millisecond pulsars (Bogdanov et al., 2019), along with two, independent analyses of the radius of PSR J0030+0451 (Miller et al. 2019; Riley et al. 2019). Radius constraints for the other three sources are expected to follow soon (Bogdanov et al., 2019). Because the NICER data are fully public, independent research groups will have the opportunity to re-analyze these data and calculate their own constraints on R using different sets of assumptions, which may provide increasingly robust constraints as the theoretical pulse-profile models are improved.

While NICER is the current, state-of-the-art X-ray instrument for neutron star science, there are several proposals for new X-ray facilities now under consideration that would allow further advances. For example, the Spectroscopic Time-Resolving Observatory for Broadband Energy X-rays (STROBE-X) is a proposed NASA probe-class mission, with spectral and timing sensitivity that would enable precision radius measurements for nearly two dozen new pulsars (Ray et al., 2019). Additionally, the proposed soft X-ray observatory, Lynx, is one of the four NASA Strategic Mission concepts under consideration by the 2020 Decadal Survey. While Lynx will have the sensitivity and spectral resolution to measure high-quality radii from spectra of quiescent and bursting LMXB sources, its biggest contribution to neutron star science is likely to come through new 3D maps of dozens of supernova remnants. By measuring remnant morphologies, kinematics, and chemical abundances, these maps will provide provide new constraints on the supernova explosion mechanism (The Lynx Team, 2019). Finally, on the European front, the Advanced Telescope for High-ENergy Astrophysics (Athena) has been selected as ESA's new flagship X-ray observatory and is expected to launch in the early 2030s. The sensitivity, high spectral resolution, and high count rate of Athena will allow additional spectroscopic radius measurements from neutron stars in quiescent LMXBs or during a photospheric radius expansion (Motch et al., 2013; Nandra et al., 2013). As the sample of high-quality radius measurements grows – especially if the neutron stars span a wide range of masses – the Bayesian inference scheme developed in Chapter 3 can be used to place increasingly stringent constraints on the EOS.

10.1.2 Radio pulsar observations

At longer wavelengths, further advances are anticipated with the upcoming Square Kilometer Array (SKA), a next-generation radio telescope array with an effective collecting area of 1 km^2, spread across Australia and South Africa. The first phase of the SKA is set to begin construction in 2021, with initial science results expected by the mid-2020s (SKA, 2020). Phase 2 of the SKA is particularly exciting, as it will potentially discover all radio pulsars in the Galaxy that are currently beamed in our direction (approximately 10,000 puslars; Keane et al. 2015), although it may take more than a decade to develop the necessary technology (SKA, 2020). In addition to increasing the population of known pulsars – some of which may reside in exotic systems, such as a black hole-pulsar binary – the SKA will also provide excellent precision for pulsar timing experiments.

As was discussed in Chapter 1, one of the most reliable methods for determining the mass of a pulsar is through the measurement of at least one post-Keplerian parameter from a carefully-tracked sequence of pulse arrival times. For many pulsar-white dwarf binaries, the only measurable post-Keplerian parameters are those that are related to the Shapiro delay, which is caused by the increase in light-travel time as the pulsar's emission travels through the gravitational well of its binary companion. The delay is strongest for edge-on systems (which provide a more direct line-of-sight path through the gravitational well of the companion) or for systems with more massive companions (which have deeper gravitational wells). The high timing precision of the SKA will make it possible to measure the Shapiro delay for up to 5× as many systems as is currently possible, including for pulsars with companions as small as 0.1 $M_\odot$ and inclination angles down to 40° (Tauris et al., 2015; Watts et al., 2015). Not only will this provide a more complete sample of the neutron star mass distribution, but it may also help constrain $M_{\max}$, through the detection, or non-detection, of new massive pulsars.

The SKA is also expected to provide improved constraints on the moment of inertia. The prediction of a 10%-accurate measurement of the moment of inertia for PSR J0737-3039A (Kramer and Wex, 2009) assumed the availability of 5 μs timing precision. With anticipated precision of up to 50 ns, the SKA will be able to more narrowly constrain I_A for this system. Additionally, the first phase of the SKA is expected to discover roughly 100 new double neutron star systems by the mid-2020s, of which some may have suitable geometry to measure additional moments of inertia (Watts et al., 2015). With the mapping developed in Chapter 4, any such measurements can be translated directly into constraints on the neutron star radius that are fully independent from the growing sample of X-ray radii.

Given other recently launched new radio facilities – such as the Chinese Five-hundred meter Aperature Radio Telescope (FAST) and the Canadian HI Intensity

Mapping Experiment (CHIME) – precision tracking of pulsars can be expected to improve even over the next few years. FAST, which is now the largest single-dish radio telescope in the world, observed first light in 2016 and already has a timing accuracy of 120 ns, with a design sensitivity goal of 30 ns (Nan et al., 2011, 2017). Overall, the sensitivty of FAST will be comparable to that of the SKA, though the SKA will be able to survey a much larger portion of the sky and may have better survey sensitivity depending on the particular configuration of the array (Smits et al., 2009). Meanwhile, CHIME, which was originally designed to measure baryon accoustic oscillations and fast radio bursts, is turning out to be an excellent pulsar telescope as well. With the effective area of a 100-m class radio telescope and a much wider field of view of 250 square-degrees, CHIME is able to time 10 pulsars simultaneously at all times, while still meeting is primary science goals (Ng, 2018).

10.1.3 Gravitational waves

Perhaps most promisingly, the LIGO-Virgo Collaboration is continuing to observe new neutron star merger systems. At the time of writing this dissertation, the LIGO-Virgo network – consisting of the Advanced LIGO (aLIGO) and Advanced Virgo (AdV) detectors – has just finished its third observing run, O3. To date, two binary neutron star mergers have been confirmed (GW170817 and GW190425) and there are an additional 10 publicly-announced triggers that are categorized as either likely neutron star-neutron star systems or neutron star-black hole systems.[1]

Based on the results from O1, O2, and the first 50 days of O3, The LIGO Scientific Collaboration et al. (2020) recently reported new merger rates for binary neutron star systems. In the first estimate, the authors treat GW170817 and GW190425 as two counts detected from the same underlying population of uniform-in-component-mass binary neutron star systems ($M_{1,2} \in 0.8\text{-}2.3\ M_\odot$) and infer a neutron star merger rate of $\mathcal{R} = 980^{+1490}_{-730}$ Gpc^{-3} yr^{-1}. In a second calculation, the authors assume that the two events represent separate counts from individual populations (as in Kim et al. 2003) – i.e., the authors treat GW170817 as a single detection from a population of binaries with mass and spin parameters consistent with that event, while GW190425 is treated as a detection from a separate population of GW190425-like binaries. By combining these independent rates and integrating over the population parameters, the resulting merger rate is slightly higher, $\mathcal{R} = 1090^{+1720}_{-800}$ Gpc^{-3} yr^{-1} (The LIGO Scientific Collaboration et al., 2020).

---

[1] This includes all systems with greater 50% likelihood of being in either category, according to the April 2020 version of the GraceDB Public Alerts database: https://gracedb.ligo.org/superevents/public/O3/.

In order to estimate the number of expected detections from these astrophysical rates, one needs to know the search volume, VT, where V is the orientation-averaged co-moving volume surveyed by the detectors and T is the total observing time, after accounting for the detector duty cycles. The accessible volume, in turn, is defined with respect to a detector range R, which is the distance at which a binary neutron star inspiral can be detected with a SNR of at least 8. Thus, by extending the range of a single detector by a factor of 2, the number of expected counts increases by a factor of $\sim$8. With a network of X detectors, the sensitivity further increases by a factor of up to $\sqrt{X}$.

The binary neutron star ranges for existing and upcoming detectors are summarized in Table 10.1. Over the next decade, there are significant upgrades planned to the existing aLIGO and AdV detectors, which will increase their detector ranges by a factor of ~ 3 by 2025. Additionally, the O4 observing run is expected to bring KAGRA, the Japanese gravitational wave observatory, fully online; while, LIGO-India is expected to join the network in the second half of O5 (Abbott et al., 2018). On slightly longer timescales, LIGO Voyager is a proposed upgrade that would push the detector ranges to the limit possible within the constraints of the existing vacuum chambers. Expected to be operational by the mid-to-late 2020s, Voyager would provide a further factor of 3 increase in the binary neutron star detection range (to 1100 Mpc) and would extend sensitivity down to a lower frequency cutoff of 10 Hz, enabling longer-term tracking of the early inspiral (The LIGO Scientific Collaboration, 2017).

To push the limits of ground-based gravitational wave astronomy further, we

Table 10.1. Binary neutron star detection ranges for existing and upcoming detectors.

Observing period:	O3 2019-2020	O4 2021-2020	O5 2024-2025
LIGO	110-130 Mpc	160-190 Mpc	330 Mpc
Virgo	50 Mpc	90-120 Mpc	150-260 Mpc
KAGRA	–	25-130 Mpc	130+ Mpc
LIGO-India	–	–	330 Mpc

Note. — Detector ranges summarized from Abbott et al. (2018).

will need to construct new facilities. LIGO is currently proposing a next-generation detector, LIGO Cosmic Explorer, which would take advantage of Voyager technology and apply it to much longer interferometric arms (40 km; i.e., a factor of 10 longer than in the existing experiment). With a goal to increase the binary neutron star detection range to 3-4 Gpc and to push the low-frequency sensitivity limit down to 5 Hz, the LIGO team is proposing for Cosmic Explorer to begin initial observations in the 2030s and reach full sensitivity by the 2040s (Reitze et al., 2019). A similar European proposal is being proposed, called the Einstein Telescope, which would be built with 10 km arms and have a design sensitivity down to 1 Hz. Einstein Telescope would reach binary neutron star mergers out to a horizon of 1 Gpc (Sathyaprakash et al., 2012).

While these next-generation proposals have broad science goals and the exact design specifications are still being debated, neutron star science will most benefit from increased sensitivity at low frequencies (1-10 Hz), which will enable long-term tracking of the early inspiral and will thus improve the SNR, as well as from increased sensitivity in the kHz range. The high-frequency regime, in particular, may provide new insight into the neutron star EOS, through the possible detection of post-merger gravitational waves (e.g., Bauswein and Janka, 2012; Read et al., 2013; Clark et al., 2014; East et al., 2016; Rezzolla and Takami, 2016). While no post-merger signal was detected from GW170817 (Abbott et al., 2017e), at design sensitivity, the aLIGO+AdV network could detect such emission with a SNR of at least 5 at distances of 20-40 Mpc (Takami et al., 2014; Clark et al., 2016). While the likelihood of observing a GW170817-like (or closer) event soon is small, that likelihood grows with time. Moreover, the detection range would increase dramatically with proposed upgrades or the construction of next-generation facilities. For example, with LIGO-Voyager, the detection range for post-merger signals would extend to 141^{+181}_{-112} Mpc, while for Cosmic Explorer and Einstein Telescope, the detection ranges are 415^{+535}_{-330} Mpc and 267^{+343}_{-208} Mpc, respectively (Clark et al., 2016). Additionally, it has recently been shown that through coherent mode stacking of data from multiple weak events, post-merger oscillations could still be detected to high significance, potentially sufficient to constrain the neutron star radius to within $\lesssim 1\%$ with just one year of observations with Cosmic Explorer (Yang et al., 2018).

Finally, by observing a merger at lower frequencies – i.e., very early in the inspiral – Cosmic Explorer and Einstein Telescope will be able to provide advanced warning for electromagnetic follow-up. This early warning is crucial, as it gives the electromagnetic community more time to scan the 90% credibility region of the sky (as inferred from the gravitational waves) and to localize a counterpart before it fades. It is expected that Einstein Telescope will be able to give an early warning alert up to 1-20 hours before merger, for any binary neutron star merger out to distances of 40 Mpc. For events at a distance of 400 Mpc, a network of Einstein Telescope and the Cosmic Explorer will be able to provide an alert 3 hours before the merger for 98% of systems (Chan et al., 2018). The counterpart to GW170817 is still the only observed kilonova to date and was the closest– and thus best studied– GRB ever detected. With more electromagnetic data on future counterparts, we will be able to answer outstanding questions regarding the nature of jet emission in GRBs and the abundance patterns of heavy elements produced during r-process nucleosynthesis. We will also be able to better characterize the properties of the merger ejecta, including its mass, velocities, and composition, which may allow us to further probe the EOS.

10.2 New simulations of binary neutron star mergers

In order to connect these late-stage observables from a neutron star merger – including both the post-merger gravitational waves and the electromagnetic counterpart – back to the EOS, detailed numerical simulations are necessary. In the case of the post-merger gravitational waves, actually measuring such a signal requires the construction of a waveform template, which in turn needs to be calibrated using the results of merger simulations in full 3+1 numerical relativity that model the dynamically changing spacetime for various EOS. To connect the electromagnetic counterpart back to the EOS, further simulations are needed to develop a mapping between properties of the merger ejecta and specific features of the resulting light curves. For recent reviews on the progress being made on these problems, see, e.g., Fernández and Metzger (2016); Baiotti and Rezzolla (2017); Paschalidis and Stergioulas (2017); Baiotti (2019); Shibata and Hotokezaka (2019); Bernuzzi (2020); Radice et al. (2020).

However, it is important to point out that compared to the EOS constraints discussed throughout the rest of this dissertation, these late-stage observables probe a fundamentally different region of parameter space: the finite-temperature EOS with non-equilibrium compositions. There are currently only a few theoretical models that can describe dense matter at non-zero temperatures and non-equilibrium compositions and these EOS span a very limited range of the physical possibilities that can arise in neutron star interiors, which greatly limits the generality of many existing merger simulations. To probe a wider range of possible physics, other simulations resort to unphysical approximations of the thermal pressure, while simultaneously neglecting the changing composition. The microphysical framework that I developed in Chapter 9, which includes the effects of degenerate matter on the thermal pressure and accounts for changes in the composition of the matter, will allow for more realistic simulations of neutron star mergers in the coming years. I have already started a new study using this framework in a suite of merger simulations in full 3+1 numerical relativity. These simulations use the Illinois code, which consists of the `Cactus` infrastructure for spacetime evolution,[2] the `Carpet` driver to implement Berger-Oliger type adaptive mesh refinement,[3] and the IL-GRMHD code to solve the equations of general relativistic (ideal) magnetohydrodynamics (Etienne et al., 2015). Using these simulations, we intend to systematically determine the role of thermal and compositional effects on the properties of the merger ejecta, the lifetime of the remnant, and the post-merger gravitational wave spectrum. Such studies will help us prepare to interpret the new gravitational wave events that are expected to be observed over the next few years and as we anticipate next-generation gravitational wave detectors.

10.3 Conclusions

Upcoming new facilities for both electromagnetic and gravitational wave astronomy will provide a wealth of insight into the neutron star interior over the coming years. When it comes to the detection of new late-stage merger observables, however, there remain outstanding theoretical questions regarding the uncertain nature of the thermal and compositional physics that will need to be addressed. The framework that I developed in this dissertation to calculate the EOS at arbitrary temperatures and compositions will help us start to answer these questions, by allowing us to systematically and robustly study EOS effects in new simulations of neutron star mergers. As we await the detection of late-stage observables from future mergers, the methods that I developed for mapping the tidal deformability to constraints on the stellar radius and nuclear symmetry energy can be applied to the many neutron star inspirals that will be observed over the next few years. Additionally, as upcoming X-ray and radio facilities provide new measurements of neutron star radii, moments of inertia, and more massive pulsars, the framework that I developed throughout this dissertation can be used to calculate increasingly stringent constraints on the EOS. Looking forward to the next decade, as these data come in and new simulations are realized, the prospects for further constraining the neutron star EOS are bright.

---

[2] http://www.cactuscode.org/

[3] http://www.carpetcode.org/

CHAPTER 11

Appendices

APPENDIX

A Linear parametrization of the EOS

For completeness in our search for an optimally parametrized EOS (see Chapter 2), we also explored a parametrization that uses linear segments between a number of density points to represent the EOS. As in the case of our polytropic parametrization, we started this parameterization at $\rho_{\rm sat}$ and spaced the segments evenly in the logarithm of the density. The EOS along each linear segment is given by

$$P = m_i \rho + b_i \qquad (\rho_{i-1} \leq \rho \leq \rho_i), \tag{A1}$$

where continuity at the endpoints implies

$$m_i = \frac{P_i - P_{i-1}}{\rho_i - \rho_{i-1}} \tag{A2}$$

and

$$b_i = P_{i-1} - \left(\frac{P_i - P_{i-1}}{\rho_i - \rho_{i-1}} \right) \rho_{i-1}. \tag{A3}$$

Using this linear relationship for pressure to integrate the differential equation (2.4), we find that the energy density in this case is given by

$$\epsilon(\rho) = (1 + a)\rho c^2 + m\rho \log \rho - b, \tag{A4}$$

where a is an integration constant. By requiring continuity in the energy density at the endpoints of each segment, we can solve for the integration constant such that

$$\epsilon(\rho) = \left(\frac{\epsilon_{i-1} + b_i}{\rho_{i-1}} - m_i \log \rho_{i-1} \right) \rho + m_i \rho \log \rho - b_i, \quad (\rho_{i-1} \leq \rho \leq \rho_i). \tag{A5}$$

We used equation (A5) to relate the linear EOS to the energy density and then used that energy density to integrate the TOV equations and solve for the total mass, radius, and moment of inertia of the neutron star.

We applied a five-segment parametrization to the ∼53,000 mock EOS shown in Figure 2.4 and calculated the errors in radius at 1.4, 1.6, and 1.8 $M_\odot$ as well as the errors in the maximum mass. In this way, we can directly compare these results with those from the five-polytrope optimal parametrization in Figure A1. We find that the polytropic parametrization performs modestly better. However, the linear parametrization is still able to recreate the radii of the full EOS to within $\lesssim 0.5$ km for ∼80% of the extreme, mock EOS.

Even though our mock EOS are composed of polytropic segments, there are multiple mock EOS segments per parametrization segment. Moreover, the mock EOS segments are offset from the parametrization segments. We therefore do not expect that the mock EOS should significantly bias the performance of a polytropic parametrization over a linear parametrization.

In order to see how well the linear parametrization performs for more physically motivated EOS, we also applied it to the sample of 42 proposed EOS from § 2.5. We compare these results to those of the polytropic parametrization in Figure A2. We find again that the polytropic parametrization performs better than the linear parametrization, although the differences between the two parametrizations are most significant at radius and maximum mass errors that are well below observational uncertainties.

It is likely that the same levels of errors could be achieved by the linear parametrization if more than five segments were included; however, for five segments, the polytropic parametrization performs modestly better in most cases. A polytropic parametrization is also the more natural choice for the neutron star EOS. We, therefore, recommend a five-segment polytropic parametrization over a linear one.

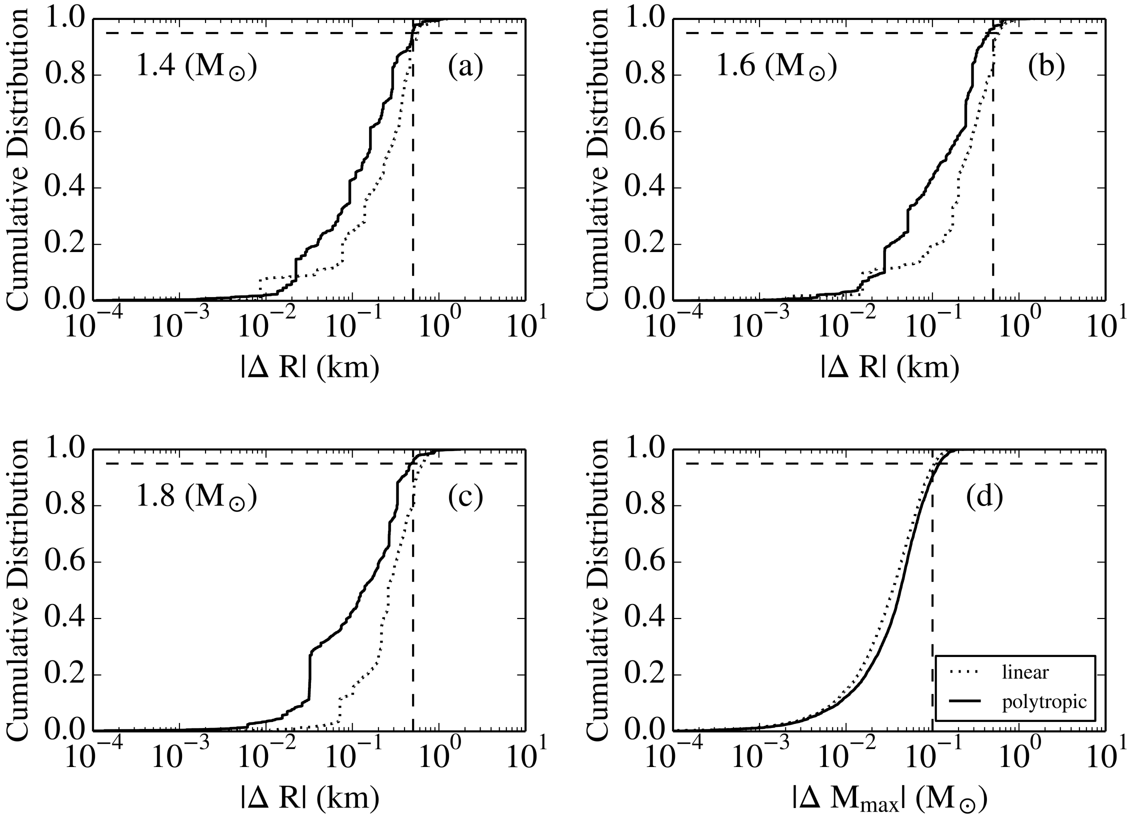

Figure A1 *(a)-(c):* Cumulative distributions of the differences in radii between a polytropic parametrization and the full EOS (solid line) and the differences between a linear parametrization and the full EOS (dashed line). These differences were calculated for all mock EOS shown in Figure 2.4. Both parametrizations contain five fiducial densities (i.e., five segments). The radius residuals are measured at 1.4, 1.6, and 1.8 $M_\odot$, respectively. The vertical dashed lines mark a residual of 0.5 km; the horizontal dashed lines mark the 95% level of the cumulative distribution. We find that a polytropic parametrization results in smaller errors, but that the linear parametrization still achieves the desired radius residual of 0.5 km for ∼80% of our extreme, mock EOS. *(d):* Cumulative distribution of the difference in maximum mass between each parametrization and the full EOS. The lines and linestyles are as for the other three panels, but here the vertical dashed line is shown at 0.1 $M_\odot$, corresponding to our desired maximum residual. We find that the linear and polytropic parametrizations perform comparably well in recreating the neutron star maximum mass.

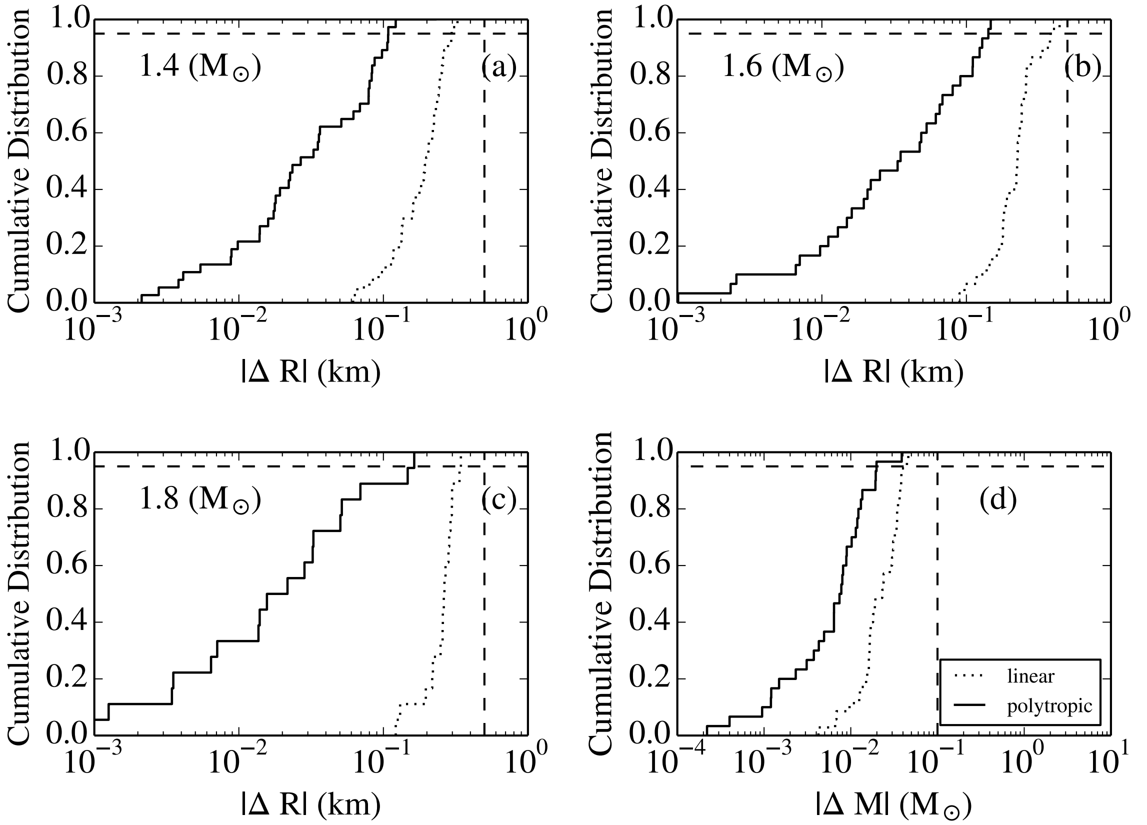

Figure A2 Same as Figure A1 but for 42 proposed, physically-motivated EOS. We find that a polytropic parametrization results in smaller errors, but that both parametrizations are able to recreate the radii and maximum masses of the full EOS to well below the expected observational uncertainties of 0.5 km and 0.1 $M_\odot$, respectively.

B Relationship between the β-equilibrium proton fraction and the symmetry energy for n-p-e matter

In this appendix, we derive the relationship shown in eq. (9.20), which asserts that the cold β-equilibrium proton fraction is uniquely specified by the symmetry energy.

At zero-temperature for n-p-e matter, the total energy per baryon is given by

$$E_{\rm tot}(n, Y_p) = E_n(n, Y_n) + E_p(n, Y_p) + E_e(n, Y_e), \tag{B1}$$

where E_n is the energy per baryon of neutrons, E_p is the energy per baryon of protons, and E_e the energy per baryon of electrons. Here, we also introduce the neutron fraction, $Y_n \equiv (1 - Y_p)$, and the electron fraction, $Y_e = Y_p$, where the latter equality holds in a charge-neutral system.

In order to find the minimum of the total energy, we differentiate with respect to Y_p and get

$$\frac{\partial E_{\rm tot}(n, Y_p)}{\partial Y_p} = \frac{\partial E_n}{\partial Y_n}\frac{\partial Y_n}{\partial Y_p} + \frac{\partial E_p}{\partial Y_p} + \frac{\partial E_e}{\partial Y_e}\frac{\partial Y_e}{\partial Y_p}, \tag{B2}$$

where all the partial derivatives here and throughout this appendix are evaluated at constant entropy and baryon density and we have suppressed the notation for clarity. By substituting in the chemical potential of a species i, given by $\mu_i \equiv \partial E_i/\partial Y_i|_{S,n}$, eq. (B2) simplifies to

$$\frac{\partial E_{\rm tot}(n, Y_p)}{\partial Y_p} = -\mu_n + \mu_p + \mu_e, \tag{B3}$$

which is zero in β-equilibrium. Alternatively, we can write the total energy as an expansion about nuclear symmetric matter with electrons added, i.e.,

$$E_{\rm tot}(n, Y_p) = E_{\rm nucl}(n, 1/2) + E_{\rm sym}(n)(1 - 2Y_p)^2 + E_e(n, Y_e). \tag{B4}$$

This results in

$$\frac{\partial E_{\rm tot}(n, Y_p)}{\partial Y_p} = -4(1 - 2Y_p)E_{\rm sym}(n) + \frac{\partial E_e}{\partial Y_e}\frac{\partial Y_e}{\partial Y_p}. \tag{B5}$$

By charge neutrality and the definition of the chemical potential, the second term is simply μ_e. Combining eqs. (B3) and (B5) in β-equilibrium gives

$$\mu_e = 4(1 - 2Y_{p,\beta})E_{\rm sym}(n). \tag{B6}$$

For relativistic electrons,

$$\mu_e = \sqrt{p_f^2 c^2 + m_e^2 c^4} \approx p_f c, \tag{B7}$$

where $p_f c = (3\pi^2 Y_e n)^{1/3}\hbar c$ is the Fermi momentum of the electrons. Combining this expression for μ with eq. (B6) yields

$$(3\pi^2 Y_{p,\beta} n)^{1/3}\hbar c = 4(1 - 2Y_{p,\beta})E_{\rm sym}(n), \tag{B8}$$

or, rearranged to match eq. (9.20),

$$\frac{Y_{p,\beta}}{(1 - 2Y_{p,\beta})^3} = \frac{64 E_{\rm sym}(n)^3}{3\pi^2 n (\hbar c)^3}. \tag{B9}$$

Solved for $Y_{p,\beta}$, this gives

$$Y_{p,\beta} = \frac{1}{2} + \frac{(2\pi^2)^{1/3}}{32}\frac{n}{\xi}\left\{(2\pi^2)^{1/3} - \frac{\xi^2}{n}\left[\frac{\hbar c}{E_{\rm sym}(n, T=0)}\right]^3\right\}, \tag{B10}$$

as in eq. (9.21), and where ξ is defined as

$$\xi \equiv \left[\frac{E_{\rm sym}(n, T=0)}{\hbar c}\right]^2 \left\{24n\left[1 + \sqrt{1 + \frac{\pi^2 n}{288}\left(\frac{\hbar c}{E_{\rm sym}(n, T=0)}\right)^3}\right]\right\}^{1/3}, \tag{B11}$$

as in eq. (9.22).

Thus, if the form of $E_{\rm sym}(n)$ is known, this will uniquely specify $Y_{p,\beta}$. Alternatively, if the β-equilibrium proton fraction is known from the cold EOS, it can be used to fit for the parameters of the particular model of $E_{\rm sym}$. In the context of this paper, specifying $Y_{p,\beta}$, S_0, and L can be used to fit for the parameter γ; or, specifying S_0, L, and γ can be used to calculate $Y_{p,\beta}$. The latter option is particularly useful as it allows our framework to be applied to parametric EOS that may not calculate $Y_{p,\beta}$ directly.

Finally, we provide the derivative of $Y_{p,\beta}$, which is required to calculate the sound speed in Appendix B. The derivative at constant entropy is given by

$$\left.\frac{\partial Y_{p,\beta}}{\partial n}\right|_S = \frac{1}{16}\left(\frac{\pi}{2}\right)^{2/3}\left\{(2\pi^2)^{1/3}\left(\frac{1-n\phi}{\xi}\right) + \xi\left[\frac{\hbar c}{E_{\rm sym}(n, T=0)}\right]^3 (3x - \phi)\right\} \tag{B12}$$

where for simplicity we have introduced the quantities

$$\phi = \frac{1}{2n}(3xn + 1) + \frac{1}{6n}\left\{1 + \frac{\pi^2 n}{288}\left[\frac{\hbar c}{E_{\rm sym}(n, T=0)}\right]^3\right\}^{-1/2}(3xn - 1) \tag{B13}$$

and

$$x = \frac{1}{n^2}\frac{P_{\rm sym}(n, T=0)}{E_{\rm sym}(n, T=0)}. \tag{B14}$$

C Calculation of the sound speed

In Chapter 9, we provided the complete set of expressions necessary to extend any cold EOS to non-equilibrium conditions and arbitrary temperature. These expressions can be used to create a new finite-temperature EOS, by varying either the cold, underlying EOS or any of the five parameters of our model. In creating a new EOS, it is useful to always to check that the choice of parameters results in a model that is causal at all densities and temperatures of interest. To that end, we here provide a sample calculation of the adiabatic sound speed for our model.

The sound speed will need to be calculated differently depending on the relevant timescales for the astrophysical system at hand. If the sound-crossing timescale is longer than the time for weak interactions, then matter will remain in β-equilibrium as the system evolves and the proton fraction will change accordingly. This scenario may correspond to the early phases of a neutron star merger or the cooling of proto-neutron stars. Alternatively, if the dynamical timescale is shorter than the timescale required to maintain β-equilibrium, as in the late stages of a merger, the proton fraction will remain approximately constant.

In this appendix, we will calculate the sound speed for the latter case: of a system with a constant proton fraction. For such a system, the adiabatic sound speed, c_s, is defined as

$$\left(\frac{c_s}{c}\right)^2 \equiv \left.\frac{\partial P(n,T)}{\partial \epsilon}\right|_{S,Y_p} \tag{C1}$$

where $\epsilon \equiv E(n,T)n + mc^2 n$ is the relativistic energy density, consisting of the classical internal energy density and the rest mass density. Here, we have suppressed the proton-fraction dependence of the pressure and energy models because we are considering a system that maintains its initial proton fraction, $Y_{p,\beta}(n)$. We can expand this derivative as follows

$$\begin{aligned}\left(\frac{c_s}{c}\right)^2 &= \left.\frac{\partial P(n,T)}{\partial n}\right|_{S,Y_p}\left(\left.\frac{\partial \epsilon}{\partial n}\right|_{S,Y_p}\right)^{-1} \\ &= \left.\frac{\partial P(n,T)}{\partial n}\right|_{S,Y_p}\left[\frac{n}{E(n,T)n + P(n,T) + mc^2 n}\right],\end{aligned} \tag{C2}$$

For each term in the pressure expressions of Box II., we calculate and provide the derivatives at constant entropy below.

For a tabular, cold EOS in β-equilibrium, the cold pressure derivative must be calculated numerically. For a polytropic cold EOS, however, the derivative is simply

$$\left.\frac{\partial P_{\mathrm{cold}}(n,T=0)}{\partial n}\right|_{S,Y_p} = \frac{\Gamma}{n}P_{\mathrm{cold}}(n,T=0), \tag{C3}$$

where Γ is the polytropic index. In the following expression for the complete derivative, we assume the cold EOS can be represented as a polytrope. However, if this is not the case, the first term should simply be replaced by the numerical derivative of the cold EOS. The total derivative for the case of a constant proton fraction is then

$$\left.\frac{\partial P(n,T)}{\partial n}\right|_{S,Y_p} = \frac{\Gamma}{n}P_{\mathrm{cold}}(n,T=0) + \begin{cases} 16f_s\sigma T^4/(9cn), & n < n_1 \\ 5T/3 & n_1 < n < n_2 \\ \left.\frac{\partial P_{\mathrm{th,deg}}(n,T)}{\partial n}\right|_{S,Y_p} & n > n_2. \end{cases} \tag{C4}$$

The degenerate thermal pressure of nucleons and electrons, $P_{\mathrm{th,deg}}$, is given for symmetric matter by

$$P_{\mathrm{th,deg}}(n,T) = -\left[a_{\mathrm{SM}}{}' + a_e{}' Y_{p,\beta}\right] n^2T^2, \tag{C5}$$

as in Box II. We assume that this is approximately equal to the β-equilibrium expression because the thermal symmetry-energy correction is small, as discussed in §9.5. This assumption will likely introduce a small error into the final sound speed, which we neglect for the present purposes.

In this appendix, for brevity, we will use the following notation: $a_{\mathrm{SM}} \equiv a(0.5n, 0.5M^*_{\mathrm{SM}})$ and $a_{\mathrm{e}} \equiv a(Y_{p,\beta}n, m_e)$. Additionally,

$$a_{\mathrm{SM}}{}' \equiv \left.\frac{\partial a(0.5n,0.5M^*_{\mathrm{SM}})}{\partial n}\right|_{Y_q} = -\frac{2a_{\mathrm{SM}}}{3n}\left\{1-\frac{B}{2}\left(C+3A\right)\right\}, \tag{C6a}$$

$$a_{\mathrm{e}}{}' \equiv \left.\frac{\partial a(Y_{p,\beta}n,m_e)}{\partial n}\right|_{Y_q} = -\frac{2a_{\mathrm{e}}}{3n}\left\{1-\frac{BC}{2}\right\}, \tag{C6b}$$

where we have introduced

$$A \equiv A(n_q, M^*) = \left.\frac{\partial \ln M^*(n_q)}{\partial \ln n}\right|_{Y_q} = -\alpha \left[1 - \left(\frac{M^*(n_q)}{mc^2}\right)^2\right] \tag{C7a}$$

$$B \equiv B(n_q, M^*) = \frac{M^*(n_q)^2}{M^*(n_q)^2 + (3\pi^2 n_q)^{2/3}(\hbar c)^2} \tag{C7b}$$

$$C \equiv C(n_q, M^*) = \frac{(3\pi^2 n_q)^{2/3}(\hbar c)^2}{M^*(n_q)^2}. \tag{C7c}$$

For the symmetric nuclear terms, $n_q \to 0.5n$ and $M^*(n_q) \to 0.5M^*_{\rm SM}(0.5n)$. For the lepton term, $n_q \to Y_{p,\beta}n$ and the effective mass is simply the electron mass.

Using the entropy expressions of §9.6, we can then write the derivative of the degenerate thermal pressure as

$$\begin{aligned}\left.\frac{\partial P_{\rm th,deg}(n,T)}{\partial n}\right|_{S,Y_p} = &-\left[\left.\frac{\partial (a_{\rm SM}\prime)}{\partial n}\right|_{S,Y_p} + \left.\frac{\partial (a_{\rm e}\prime)}{\partial n}\right|_{S,Y_p} Y_{p,\beta}\right] n^2 T^2 \\ &+2P_{\rm th,deg}(n,T)\left[\frac{1}{n} - \frac{a_{\rm SM}\prime + a_{\rm e}\prime \cdot Y_{p,\beta}}{a_{\rm SM} + a_{\rm e}Y_{p,\beta}}\right]\end{aligned} \tag{C8}$$

The second derivative of $a_{\rm SM}$ is given by

$$\left.\frac{\partial (a_{\rm SM}\prime)}{\partial n}\right|_{S,Y_p} = a_{\rm SM}\prime\left(\frac{a_{\rm SM}\prime}{a_{\rm SM}} - \frac{1}{n}\right) + \frac{2a_{\rm SM}}{3n^2}B\left[3A^2 - \frac{1}{3}B(3A+C)^2 + \frac{1}{3}C + \frac{3n}{2}\frac{\partial A}{\partial n}\right] \tag{C9}$$

The second derivative of the electron term, for which $A \to 0$ due to its constant effective mass, is simply

$$\left.\frac{\partial (a_{\rm e}\prime)}{\partial n}\right|_{S,Y_p} = a_{\rm e}\prime\left(\frac{a_{\rm e}\prime}{a_{\rm e}} - \frac{1}{n}\right) + \frac{2a_{\rm e}}{9n^2}BC(1-BC) \tag{C10}$$

Finally, the second-derivative of the M^* term is given by

$$\frac{\partial A}{\partial n} = \frac{\partial}{\partial n}\left[\frac{\partial \ln M^*(n_q)}{\partial n}\right] = \frac{2\alpha}{n}\left[\frac{M^*(n_q)}{Y_q mc^2}\right]^2\left[\frac{\partial \ln M^*(n_q)}{\partial n}\right], \tag{C11}$$

where we have assumed that M^* is defined here for symmetric matter, so that $M^*(n_q) \to 0.5M^*_{\rm SM}(0.5n)$.

REFERENCES

Abbott, B. P., R. Abbott, T. D. Abbott, M. R. Abernathy, F. Acernese, K. Ackley, C. Adams, T. Adams, P. Addesso, R. X. Adhikari, and et al. (2016a). Astrophysical Implications of the Binary Black-hole Merger GW150914. *ApJL*, **818**, L22. doi:10.3847/2041-8205/818/2/L22.

Abbott, B. P., R. Abbott, T. D. Abbott, M. R. Abernathy, F. Acernese, K. Ackley, C. Adams, T. Adams, P. Addesso, R. X. Adhikari, and et al. (2016b). Binary Black Hole Mergers in the First Advanced LIGO Observing Run. *Physical Review X*, **6**(4), 041015. doi:10.1103/PhysRevX.6.041015.

Abbott, B. P., R. Abbott, T. D. Abbott, M. R. Abernathy, F. Acernese, K. Ackley, C. Adams, T. Adams, P. Addesso, R. X. Adhikari, and et al. (2016c). GW151226: Observation of Gravitational Waves from a 22-Solar-Mass Binary Black Hole Coalescence. *Physical Review Letters*, **116**(24), 241103. doi:10.1103/PhysRevLett.116.241103.

Abbott, B. P., R. Abbott, T. D. Abbott, M. R. Abernathy, F. Acernese, K. Ackley, C. Adams, T. Adams, P. Addesso, R. X. Adhikari, and et al. (2016d). Observation of Gravitational Waves from a Binary Black Hole Merger. *Physical Review Letters*, **116**(6), 061102. doi:10.1103/PhysRevLett.116.061102.

Abbott, B. P., R. Abbott, T. D. Abbott, M. R. Abernathy, F. Acernese, K. Ackley, C. Adams, T. Adams, P. Addesso, R. X. Adhikari, and et al. (2018). Prospects for observing and localizing gravitational-wave transients with Advanced LIGO, Advanced Virgo and KAGRA. *Living Reviews in Relativity*, **21**(1), 3. doi:10.1007/s41114-018-0012-9.

Abbott, B. P., R. Abbott, T. D. Abbott, F. Acernese, K. Ackley, C. Adams, T. Adams, P. Addesso, R. X. Adhikari, V. B. Adya, and et al. (2017a). Gravitational Waves and Gamma-Rays from a Binary Neutron Star Merger: GW170817 and GRB 170817A. *Astrophys. J. Letters*, **848**, L13. doi:10.3847/2041-8213/aa920c.

Abbott, B. P., R. Abbott, T. D. Abbott, F. Acernese, K. Ackley, C. Adams, T. Adams, P. Addesso, R. X. Adhikari, V. B. Adya, and et al. (2017b). GW170104: Observation of a 50-Solar-Mass Binary Black Hole Coalescence at Redshift 0.2. *Physical Review Letters*, **118**(22), 221101. doi:10.1103/PhysRevLett.118.221101.

Abbott, B. P., R. Abbott, T. D. Abbott, F. Acernese, K. Ackley, C. Adams, T. Adams, P. Addesso, R. X. Adhikari, V. B. Adya, and et al. (2017c). GW170817:

Observation of Gravitational Waves from a Binary Neutron Star Inspiral. *Physical Review Letters*, **119**(16), 161101. doi:10.1103/PhysRevLett.119.161101.

Abbott, B. P., R. Abbott, T. D. Abbott, F. Acernese, K. Ackley, C. Adams, T. Adams, P. Addesso, R. X. Adhikari, V. B. Adya, and et al. (2017d). Multi-messenger Observations of a Binary Neutron Star Merger. *Astrophys. J. Letters*, **848**, L12. doi:10.3847/2041-8213/aa91c9.

Abbott, B. P., R. Abbott, T. D. Abbott, F. Acernese, K. Ackley, C. Adams, T. Adams, P. Addesso, R. X. Adhikari, V. B. Adya, and et al. (2017e). Search for Post-merger Gravitational Waves from the Remnant of the Binary Neutron Star Merger GW170817. *ApJ*, **851**, L16. doi:10.3847/2041-8213/aa9a35.

Abbott, B. P., R. Abbott, T. D. Abbott, F. Acernese, K. Ackley, C. Adams, T. Adams, P. Addesso, R. X. Adhikari, V. B. Adya, and et al. (2018). GW170817: Measurements of Neutron Star Radii and Equation of State. *Phys. Rev. Lett.*, **121**, p. 161101. doi:10.1103/PhysRevLett.121.161101.

Abbott, B. P., R. Abbott, T. D. Abbott, F. Acernese, K. Ackley, C. Adams, T. Adams, P. Addesso, R. X. Adhikari, V. B. Adya, and et al. (2019). Properties of the Binary Neutron Star Merger GW170817. *Physical Review X*, **9**(1), 011001. doi:10.1103/PhysRevX.9.011001.

Agathos, M., J. Meidam, W. Del Pozzo, T. G. F. Li, M. Tompitak, J. Veitch, S. Vitale, and C. Van Den Broeck (2015). Constraining the neutron star equation of state with gravitational wave signals from coalescing binary neutron stars. *PhRvD*, **92**(2), 023012. doi:10.1103/PhysRevD.92.023012.

Akmal, A., V. R. Pandharipande, and D. G. Ravenhall (1998). Equation of state of nucleon matter and neutron star structure. *Phys. Rev. C*, **58**, pp. 1804–1828. doi:10.1103/PhysRevC.58.1804.

Al-Mamun, M., A. W. Steiner, J. Nättilä, J. Lange, R. O'Shaugnessy, I. Tews, S. Gandolfi, C. Heinke, and S. Han (2020). Combining Electromagnetic and Gravitational-Wave Constraints on Neutron-Star Masses and Radii. *arXiv e-prints*, arXiv:2008.12817.

Alam, N., B. K. Agrawal, M. Fortin, H. Pais, C. Providência, A. R. Raduta, and A. Sulaksono (2016). Strong correlations of neutron star radii with the slopes of nuclear matter incompressibility and symmetry energy at saturation. *PhRvC*, **94**(5), 052801. doi:10.1103/PhysRevC.94.052801.

Alvarez-Castillo, D., A. Ayriyan, S. Benic, D. Blaschke, H. Grigorian, and S. Typel (2016). New class of hybrid EoS and Bayesian M - R data analysis. *European Physical Journal A*, **52**, 69. doi:10.1140/epja/i2016-16069-2.

Annala, E., T. Gorda, A. Kurkela, and A. Vuorinen (2018). Gravitational-Wave Constraints on the Neutron-Star-Matter Equation of State. *Phys. Rev. Lett.*, **120**, p. 172703. doi:10.1103/PhysRevLett.120.172703.

Antoniadis, J., P. C. C. Freire, N. Wex, T. M. Tauris, R. S. Lynch, M. H. van Kerkwijk, M. Kramer, C. Bassa, V. S. Dhillon, T. Driebe, J. W. T. Hessels, V. M. Kaspi, V. I. Kondratiev, N. Langer, T. R. Marsh, M. A. McLaughlin, T. T. Pennucci, S. M. Ransom, I. H. Stairs, J. van Leeuwen, J. P. W. Verbiest, and D. G. Whelan (2013). A Massive Pulsar in a Compact Relativistic Binary. *Science*, **340**, p. 448. doi:10.1126/science.1233232.

Antoniadis, J., T. M. Tauris, F. Ozel, E. Barr, D. J. Champion, and P. C. C. Freire (2016). The millisecond pulsar mass distribution: Evidence for bimodality and constraints on the maximum neutron star mass. *ArXiv e-prints*.

Arnett, W. D., J. N. Bahcall, R. P. Kirshner, and S. E. Woosley (1989). Supernova 1987A. *ARA&A*, **27**, pp. 629–700. doi:10.1146/annurev.aa.27.090189.003213.

Arun, K. G., A. Buonanno, G. Faye, and E. Ochsner (2011). Erratum: Higher-order spin effects in the amplitude and phase of gravitational waveforms emitted by inspiraling compact binaries: Ready-to-use gravitational waveforms [Phys. Rev. D 79, 104023 (2009)]. *PhRvD*, **84**(4), 049901. doi:10.1103/PhysRevD.84.049901.

Askar, A., M. Szkudlarek, D. Gondek-Rosińska, M. Giersz, and T. Bulik (2017). MOCCA-SURVEY Database - I. Coalescing binary black holes originating from globular clusters. *MNRAS*, **464**, pp. L36–L40. doi:10.1093/mnrasl/slw177.

Baiotti, L. (2019). Gravitational waves from neutron star mergers and their relation to the nuclear equation of state. *Progress in Particle and Nuclear Physics*, **109**, 103714. doi:10.1016/j.ppnp.2019.103714.

Baiotti, L. and L. Rezzolla (2017). Binary neutron star mergers: a review of Einstein's richest laboratory. *Reports on Progress in Physics*, **80**(9), 096901. doi: 10.1088/1361-6633/aa67bb.

Balberg, S. and A. Gal (1997). An effective equation of state for dense matter with strangeness. *Nuclear Physics A*, **625**, pp. 435–472. doi:10.1016/S0375-9474(97)81465-0.

Banik, S., M. Hempel, and D. Bandyopadhyay (2014). New Hyperon Equations of State for Supernovae and Neutron Stars in Density-dependent Hadron Field Theory. *ApJS*, **214**, 22. doi:10.1088/0067-0049/214/2/22.

Bauswein, A. and H.-T. Janka (2012). Measuring Neutron-Star Properties via Gravitational Waves from Neutron-Star Mergers. *Physical Review Letters*, **108**(1), 011101. doi:10.1103/PhysRevLett.108.011101.

Bauswein, A., H.-T. Janka, and R. Oechslin (2010). Testing approximations of thermal effects in neutron star merger simulations. *PhRvD*, **82**(8), 084043. doi:10.1103/PhysRevD.82.084043.

Baym, G., C. Pethick, and P. Sutherland (1971). The Ground State of Matter at High Densities: Equation of State and Stellar Models. *ApJ*, **170**, p. 299. doi:10.1086/151216.

Bednarek, I., P. Haensel, J. L. Zdunik, M. Bejger, and R. Mańka (2012). Hyperons in neutron-star cores and a 2 M pulsar. *A&A*, **543**, A157. doi:10.1051/0004-6361/201118560.

Bejger, M., T. Bulik, and P. Haensel (2005). Constraints on the dense matter equation of state from the measurements of PSR J0737-3039A moment of inertia and PSR J0751+1807 mass. *Monthly Notices of the Royal Astronomical Society*, **364**, pp. 635–639. doi:10.1111/j.1365-2966.2005.09575.x.

Belczynski, K., D. E. Holz, T. Bulik, and R. O'Shaughnessy (2016). The first gravitational-wave source from the isolated evolution of two stars in the 40-100 solar mass range. *Nature*, **534**, pp. 512–515. doi:10.1038/nature18322.

Berger, E. (2014). Short-Duration Gamma-Ray Bursts. *ARA&A*, **52**, pp. 43–105. doi:10.1146/annurev-astro-081913-035926.

Bernuzzi, S. (2020). Neutron Stars Merger Remnants. *arXiv e-prints*, arXiv:2004.06419.

Binnington, T. and E. Poisson (2009). Relativistic theory of tidal Love numbers. *PhRvD*, **80**(8), 084018. doi:10.1103/PhysRevD.80.084018.

Blaschke, D., D. E. Alvarez-Castillo, and T. Klahn (2016). Universal symmetry energy contribution to the neutron star equation of state. *ArXiv e-prints*.

Blaschke, D., A. Ayriyan, D. Alvarez-Castillo, and H. Grigorian (2020). Was GW170817 a canonical neutron star merger? Bayesian analysis with a third family of compact stars. *arXiv e-prints*, arXiv:2005.02759.

Bogdanov, S., S. Guillot, P. S. Ray, M. T. Wolff, D. Chakrabarty, W. C. G. Ho, M. Kerr, F. K. Lamb, A. Lommen, R. M. Ludlam, R. Milburn, S. Montano, M. C. Miller, M. Bauböck, F. Özel, D. Psaltis, R. A. Remillard, T. E. Riley, J. F. Steiner, T. E. Strohmayer, A. L. Watts, K. S. Wood, J. Zeldes, T. Enoto, T. Okajima, J. W. Kellogg, C. Baker, C. B. Markwardt, Z. Arzoumanian, and K. C. Gendreau (2019). Constraining the Neutron Star MassRadius Relation and Dense Matter Equation of State with NICER. I. The Millisecond Pulsar X-Ray Data Set. *ApJL*, **887**(1), L25. doi:10.3847/2041-8213/ab53eb.

Bogdanov, S., C. O. Heinke, F. Özel, and T. Güver (2016). Neutron Star Mass-Radius Constraints of the Quiescent Low-mass X-Ray Binaries X7 and X5 in the Globular Cluster 47 Tuc. *ApJ*, **831**, 184. doi:10.3847/0004-637X/831/2/184.

Bohé, A., G. Faye, S. Marsat, and E. K. Porter (2015). Quadratic-in-spin effects in the orbital dynamics and gravitational-wave energy flux of compact binaries at the 3PN order. *Classical and Quantum Gravity*, **32**(19), 195010. doi:10.1088/0264-9381/32/19/195010.

Bohé, A., S. Marsat, and L. Blanchet (2013). Next-to-next-to-leading order spin-orbit effects in the gravitational wave flux and orbital phasing of compact binaries. *Classical and Quantum Gravity*, **30**(13), 135009. doi:10.1088/0264-9381/30/13/135009.

Box, G. E. P. and G. C. Tiao (1992). *Bayesian inference in statistical analysis*. New York : Wiley.

Burrows, A., J. Hayes, and B. A. Fryxell (1995). On the Nature of Core-Collapse Supernova Explosions. *ApJ*, **450**, p. 830. doi:10.1086/176188.

Camelio, G., A. Lovato, L. Gualtieri, O. Benhar, J. A. Pons, and V. Ferrari (2017). Evolution of a proto-neutron star with a nuclear many-body equation of state: Neutrino luminosity and gravitational wave frequencies. *PhRvD*, **96**(4), 043015. doi:10.1103/PhysRevD.96.043015.

Capano, C. D., I. Tews, S. M. Brown, B. Margalit, S. De, S. Kumar, D. A. Brown, B. Krishnan, and S. Reddy (2020). Stringent constraints on neutron-star radii from multimessenger observations and nuclear theory. *Nature Astronomy*. doi:10.1038/s41550-020-1014-6.

Carbone, A., A. Polls, and A. Rios (2012). High-momentum components in the nuclear symmetry energy. *EPL (Europhysics Letters)*, **97**, p. 22001. doi:10.1209/0295-5075/97/22001.

Carney, M. F., L. E. Wade, and B. S. Irwin (2018). Comparing two models for measuring the neutron star equation of state from gravitational-wave signals. *Phys. Rev. D*, **98**, p. 063004. doi:10.1103/PhysRevD.98.063004.

Carson, Z., A. W. Steiner, and K. Yagi (2019). Constraining nuclear matter parameters with GW170817. *PhRvD*, **99**(4), 043010. doi:10.1103/PhysRevD.99.043010.

Centelles, M., X. Roca-Maza, X. Viñas, and M. Warda (2009). Nuclear Symmetry Energy Probed by Neutron Skin Thickness of Nuclei. *Physical Review Letters*, **102**(12), 122502. doi:10.1103/PhysRevLett.102.122502.

Chan, M. L., C. Messenger, I. S. Heng, and M. Hendry (2018). Binary neutron star mergers and third generation detectors: Localization and early warning. *PhRvD*, **97**(12), 123014. doi:10.1103/PhysRevD.97.123014.

Chieffi, A. and M. Limongi (2013). Pre-supernova Evolution of Rotating Solar Metallicity Stars in the Mass Range 13-120 M and their Explosive Yields. *ApJ*, **764**, 21. doi:10.1088/0004-637X/764/1/21.

Christian, J.-E. and J. Schaffner-Bielich (2020). Twin Stars and the Stiffness of the Nuclear Equation of State: Ruling Out Strong Phase Transitions below 1.7 n_0 with the New NICER Radius Measurements. *ApJL*, **894**(1), L8. doi:10.3847/2041-8213/ab8af4.

Clark, J., A. Bauswein, L. Cadonati, H. T. Janka, C. Pankow, and N. Stergioulas (2014). Prospects for high frequency burst searches following binary neutron star coalescence with advanced gravitational wave detectors. *PhRvD*, **90**(6), 062004. doi:10.1103/PhysRevD.90.062004.

Clark, J. A., A. Bauswein, N. Stergioulas, and D. Shoemaker (2016). Observing gravitational waves from the post-merger phase of binary neutron star coalescence. *Classical and Quantum Gravity*, **33**(8), 085003. doi:10.1088/0264-9381/33/8/085003.

Clausen, D., A. L. Piro, and C. D. Ott (2015). The Black Hole Formation Probability. *ApJ*, **799**, 190. doi:10.1088/0004-637X/799/2/190.

Collins, J. C. and M. J. Perry (1975). Superdense matter: Neutrons or asymptotically free quarks? *Physical Review Letters*, **34**, pp. 1353–1356. doi:10.1103/PhysRevLett.34.1353.

Constantinou, C., S. Lalit, and M. Prakash (2017). Thermal effects in dense matter beyond mean field theory. *International Journal of Modern Physics E*, **26**, 1740005. doi:10.1142/S0218301317400055.

Constantinou, C., B. Muccioli, M. Prakash, and J. M. Lattimer (2014). Thermal properties of supernova matter: The bulk homogeneous phase. *PhRvC*, **89**(6), 065802. doi:10.1103/PhysRevC.89.065802.

Constantinou, C., B. Muccioli, M. Prakash, and J. M. Lattimer (2015). Degenerate limit thermodynamics beyond leading order for models of dense matter. *Annals of Physics*, **363**, pp. 533–555. doi:10.1016/j.aop.2015.10.003.

Cook, G. B., S. L. Shapiro, and S. A. Teukolsky (1994). Rapidly rotating neutron stars in general relativity: Realistic equations of state. *ApJ*, **424**, pp. 823–845. doi:10.1086/173934.

Coughlin, E. R., E. Quataert, R. Fernández, and D. Kasen (2017). A physical model of mass ejection in failed supernovae. *ArXiv e-prints*.

Coughlin, M. W., T. Dietrich, B. Margalit, and B. D. Metzger (2019). Multimessenger Bayesian parameter inference of a binary neutron star merger. *MNRAS*, **489**(1), pp. L91–L96. doi:10.1093/mnrasl/slz133.

Coulter, D. A., R. J. Foley, C. D. Kilpatrick, M. R. Drout, A. L. Piro, B. J. Shappee, M. R. Siebert, J. D. Simon, N. Ulloa, D. Kasen, B. F. Madore, A. Murguia-Berthier, Y.-C. Pan, J. X. Prochaska, E. Ramirez-Ruiz, A. Rest, and C. Rojas-Bravo (2017). Swope Supernova Survey 2017a (SSS17a), the optical counterpart to a gravitational wave source. *Science*, **358**, pp. 1556–1558. doi:10.1126/science.aap9811.

Cromartie, H. T., E. Fonseca, S. M. Ransom, P. B. Demorest, Z. Arzoumanian, H. Blumer, P. R. Brook, M. E. DeCesar, T. Dolch, J. A. Ellis, R. D. Ferdman, E. C. Ferrara, N. Garver-Daniels, P. A. Gentile, M. L. Jones, M. T. Lam, D. R. Lorimer, R. S. Lynch, M. A. McLaughlin, C. Ng, D. J. Nice, T. T. Pennucci, R. Spiewak, I. H. Stairs, K. Stovall, J. K. Swiggum, and W. W. Zhu (2020). Relativistic Shapiro delay measurements of an extremely massive millisecond pulsar. *Nature Astronomy*, **4**, pp. 72–76. doi:10.1038/s41550-019-0880-2.

Damour, T. and A. Nagar (2009). Relativistic tidal properties of neutron stars. *PhRvD*, **80**(8), 084035. doi:10.1103/PhysRevD.80.084035.

Damour, T. and G. Schafer (1988). Higher-order relativistic periastron advances and binary pulsars. *Nuovo Cimento B Series*, **101**, pp. 127–176. doi:10.1007/BF02828697.

Damour, T. and J. H. Taylor (1992). Strong-field tests of relativistic gravity and binary pulsars. *PhRvD*, **45**(6), pp. 1840–1868. doi:10.1103/PhysRevD.45.1840.

Danielewicz, P. (2003). Surface symmetry energy. *Nuclear Physics A*, **727**, pp. 233–268. doi:10.1016/j.nuclphysa.2003.08.001.

De, S., D. Finstad, J. M. Lattimer, D. A. Brown, E. Berger, and C. M. Biwer (2018). Tidal Deformabilities and Radii of Neutron Stars from the Observation of GW170817. *Physical Review Letters*, **121**(9), 091102. doi:10.1103/PhysRevLett.121.091102.

de Mink, S. E. and I. Mandel (2016). The chemically homogeneous evolutionary channel for binary black hole mergers: rates and properties of gravitational-wave events detectable by advanced LIGO. *MNRAS*, **460**, pp. 3545–3553. doi:10.1093/mnras/stw1219.

Del Pozzo, W., T. G. F. Li, M. Agathos, C. Van Den Broeck, and S. Vitale (2013). Demonstrating the Feasibility of Probing the Neutron-Star Equation of State with Second-Generation Gravitational-Wave Detectors. *Physical Review Letters*, **111**(7), 071101. doi:10.1103/PhysRevLett.111.071101.

Demorest, P. B., T. Pennucci, S. M. Ransom, M. S. E. Roberts, and J. W. T. Hessels (2010). A two-solar-mass neutron star measured using Shapiro delay. *Nature*, **467**, pp. 1081–1083. doi:10.1038/nature09466.

Dessart, L., D. J. Hillier, C. Li, and S. Woosley (2012). On the nature of supernovae Ib and Ic. *MNRAS*, **424**, pp. 2139–2159. doi:10.1111/j.1365-2966.2012.21374.x.

Dessart, L., D. J. Hillier, S. Woosley, E. Livne, R. Waldman, S.-C. Yoon, and N. Langer (2015). Radiative-transfer models for supernovae IIb/Ib/Ic from binary-star progenitors. *MNRAS*, **453**, pp. 2189–2213. doi:10.1093/mnras/stv1747.

Dexheimer, V. (2017). Tabulated Neutron Star Equations of State Modelled within the Chiral Mean Field Model. *PASA*, **34**, e066. doi:10.1017/pasa.2017.61.

Dietrich, T., M. W. Coughlin, P. T. H. Pang, M. Bulla, J. Heinzel, L. Issa, I. Tews, and S. Antier (2020). New Constraints on the Supranuclear Equation of State and the Hubble Constant from Nuclear Physics – Multi-Messenger Astronomy. *arXiv e-prints*, arXiv:2002.11355.

Douchin, F. and P. Haensel (2001). A unified equation of state of dense matter and neutron star structure. *Astronomy & Astrophysics*, **380**, pp. 151–167. doi:10.1051/0004-6361:20011402.

East, W. E., V. Paschalidis, and F. Pretorius (2016). Equation of state effects and one-arm spiral instability in hypermassive neutron stars formed in eccentric neutron star mergers. *Classical and Quantum Gravity*, **33**(24), 244004. doi:10.1088/0264-9381/33/24/244004.

Eichler, D., M. Livio, T. Piran, and D. N. Schramm (1989). Nucleosynthesis, neutrino bursts and gamma-rays from coalescing neutron stars. *Nature*, **340**, pp. 126–128. doi:10.1038/340126a0.

Eldridge, J. J. and E. R. Stanway (2016). BPASS predictions for binary black hole mergers. *MNRAS*, **462**, pp. 3302–3313. doi:10.1093/mnras/stw1772.

Ertl, T., H.-T. Janka, S. E. Woosley, T. Sukhbold, and M. Ugliano (2016). A Two-parameter Criterion for Classifying the Explodability of Massive Stars by the Neutrino-driven Mechanism. *ApJ*, **818**, 124. doi:10.3847/0004-637X/818/2/124.

Etienne, Z. B., J. A. Faber, Y. T. Liu, S. L. Shapiro, K. Taniguchi, and T. W. Baumgarte (2008). Fully general relativistic simulations of black hole-neutron star mergers. *PhRvD*, **77**(8), 084002. doi:10.1103/PhysRevD.77.084002.

Etienne, Z. B., V. Paschalidis, R. Haas, P. Mösta, and S. L. Shapiro (2015). IllinoisGRMHD: an open-source, user-friendly GRMHD code for dynamical spacetimes. *Classical and Quantum Gravity*, **32**(17), 175009. doi:10.1088/0264-9381/32/17/175009.

Faber, J. A. and F. A. Rasio (2012). Binary Neutron Star Mergers. *Living Reviews in Relativity*, **15**, 8. doi:10.12942/lrr-2012-8.

Farr, W. M., N. Sravan, A. Cantrell, L. Kreidberg, C. D. Bailyn, I. Mandel, and V. Kalogera (2011). The Mass Distribution of Stellar-mass Black Holes. *ApJ*, **741**, 103. doi:10.1088/0004-637X/741/2/103.

Fattoyev, F. J., J. Carvajal, W. G. Newton, and B.-A. Li (2013). Constraining the high-density behavior of the nuclear symmetry energy with the tidal polarizability of neutron stars. *PhRvC*, **87**(1), 015806. doi:10.1103/PhysRevC.87.015806.

Fattoyev, F. J., C. J. Horowitz, J. Piekarewicz, and B. Reed (2020). GW190814: Impact of a 2.6 solar mass neutron star on nucleonic equations of state. *arXiv e-prints*, arXiv:2007.03799.

Fattoyev, F. J., C. J. Horowitz, J. Piekarewicz, and G. Shen (2010). Relativistic effective interaction for nuclei, giant resonances, and neutron stars. *PhRvC*, **82**(5), 055803. doi:10.1103/PhysRevC.82.055803.

Favata, M. (2014). Systematic Parameter Errors in Inspiraling Neutron Star Binaries. *Physical Review Letters*, **112**(10), 101101. doi:10.1103/PhysRevLett.112.101101.

Fernández, R. and B. D. Metzger (2016). Electromagnetic Signatures of Neutron Star Mergers in the Advanced LIGO Era. *Annual Review of Nuclear and Particle Science*, **66**(1), pp. 23–45. doi:10.1146/annurev-nucl-102115-044819.

Fernández, R., E. Quataert, K. Kashiyama, and E. R. Coughlin (2017). Mass Ejection in Failed Supernovae: Variation with Stellar Progenitor. *ArXiv e-prints*.

Fischer, T., M. Hempel, I. Sagert, Y. Suwa, and J. Schaffner-Bielich (2014). Symmetry energy impact in simulations of core-collapse supernovae. *European Physical Journal A*, **50**, 46. doi:10.1140/epja/i2014-14046-5.

Flanagan, É. É. and T. Hinderer (2008). Constraining neutron-star tidal Love numbers with gravitational-wave detectors. *Physical Review D*, **77**(2), 021502. doi:10.1103/PhysRevD.77.021502.

Fonseca, E., T. T. Pennucci, J. A. Ellis, I. H. Stairs, D. J. Nice, S. M. Ransom, P. B. Demorest, Z. Arzoumanian, K. Crowter, T. Dolch, R. D. Ferdman, M. E. Gonzalez, G. Jones, M. L. Jones, M. T. Lam, L. Levin, M. A. McLaughlin, K. Stovall, J. K. Swiggum, and W. Zhu (2016). The NANOGrav Nine-year Data Set: Mass and Geometric Measurements of Binary Millisecond Pulsars. *ApJ*, **832**, 167. doi:10.3847/0004-637X/832/2/167.

Fraga, E. S., A. Kurkela, and A. Vuorinen (2014). Interacting Quark Matter Equation of State for Compact Stars. *ApJL*, **781**, L25. doi:10.1088/2041-8205/781/2/L25.

Friedman, B. and V. R. Pandharipande (1981). Hot and cold, nuclear and neutron matter. *Nuclear Physics A*, **361**, pp. 502–520. doi:10.1016/0375-9474(81)90649-7.

Gandolfi, S., J. Carlson, and S. Reddy (2012). Maximum mass and radius of neutron stars, and the nuclear symmetry energy. *PhRvC*, **85**(3), 032801. doi:10.1103/PhysRevC.85.032801.

Gandolfi, S., J. Carlson, S. Reddy, A. W. Steiner, and R. B. Wiringa (2014). The equation of state of neutron matter, symmetry energy and neutron star structure. *European Physical Journal A*, **50**, 10. doi:10.1140/epja/i2014-14010-5.

Gendreau, K. C., Z. Arzoumanian, and T. Okajima (2012). The Neutron star Interior Composition ExploreR (NICER): an Explorer mission of opportunity for soft x-ray timing spectroscopy. In *Space Telescopes and Instrumentation 2012: Ultraviolet to Gamma Ray*, volume 8443 of *Proc. SPIE*, p. 844313. doi:10.1117/12.926396.

Glendenning, N. (1996). *Compact Stars. Nuclear Physics, Particle Physics and General Relativity.*

Glendenning, N. K. (1992). First-order phase transitions with more than one conserved charge: Consequences for neutron stars. *PhRvD*, **46**, pp. 1274–1287. doi:10.1103/PhysRevD.46.1274.

Glendenning, N. K. (2000). *Compact stars : nuclear physics, particle physics, and general relativity.*

Glendenning, N. K. and C. Kettner (2000). Possible third family of compact stars more dense than neutron stars. *A&A*, **353**, pp. L9–L12.

Grefenstette, B. W., F. A. Harrison, S. E. Boggs, S. P. Reynolds, C. L. Fryer, K. K. Madsen, D. R. Wik, A. Zoglauer, C. I. Ellinger, and et al. (2014). Asymmetries in core-collapse supernovae from maps of radioactive ^{44}Ti in CassiopeiaA. *Nature*, **506**(7488), pp. 339–342. doi:10.1038/nature12997.

Guillot, S. and R. E. Rutledge (2014). Rejecting Proposed Dense Matter Equations of State with Quiescent Low-mass X-Ray Binaries. *ApJL*, **796**, L3. doi:10.1088/2041-8205/796/1/L3.

Guillot, S., M. Servillat, N. A. Webb, and R. E. Rutledge (2013). Measurement of the Radius of Neutron Stars with High Signal-to-noise Quiescent Low-mass X-Ray Binaries in Globular Clusters. *ApJ*, **772**, 7. doi:10.1088/0004-637X/772/1/7.

Gulminelli, F. and A. R. Raduta (2015). Unified treatment of subsaturation stellar matter at zero and finite temperature. *Phys. Rev. C*, **92**, p. 055803. doi:10.1103/PhysRevC.92.055803.

Güver, T. and F. Özel (2013). The Mass and the Radius of the Neutron Star in the Transient Low-mass X-Ray Binary SAX J1748.9-2021. *ApJL*, **765**, L1. doi:10.1088/2041-8205/765/1/L1.

Güver, T., F. Özel, A. Cabrera-Lavers, and P. Wroblewski (2010). The Distance, Mass, and Radius of the Neutron Star in 4U 1608-52. *ApJ*, **712**, pp. 964–973. doi:10.1088/0004-637X/712/2/964.

Hammer, N. J., H. T. Janka, and E. Müller (2010). Three-dimensional Simulations of Mixing Instabilities in Supernova Explosions. *ApJ*, **714**(2), pp. 1371–1385. doi:10.1088/0004-637X/714/2/1371.

Hebeler, K., J. M. Lattimer, C. J. Pethick, and A. Schwenk (2010). Constraints on Neutron Star Radii Based on Chiral Effective Field Theory Interactions. *Physical Review Letters*, **105**(16), 161102. doi:10.1103/PhysRevLett.105.161102.

Hebeler, K., J. M. Lattimer, C. J. Pethick, and A. Schwenk (2013). Equation of State and Neutron Star Properties Constrained by Nuclear Physics and Observation. *ApJ*, **773**(1), 11. doi:10.1088/0004-637X/773/1/11.

Heger, A., S. E. Woosley, and H. C. Spruit (2005). Presupernova Evolution of Differentially Rotating Massive Stars Including Magnetic Fields. *ApJ*, **626**, pp. 350–363. doi:10.1086/429868.

Heida, M., P. G. Jonker, M. A. P. Torres, and A. Chiavassa (2017). The Mass Function of GX 339-4 from Spectroscopic Observations of Its Donor Star. *ApJ*, **846**(2), 132. doi:10.3847/1538-4357/aa85df.

Heinke, C. O., H. N. Cohn, P. M. Lugger, N. A. Webb, W. C. G. Ho, J. Anderson, S. Campana, S. Bogdanov, D. Haggard, A. M. Cool, and J. E. Grindlay (2014). Improved mass and radius constraints for quiescent neutron stars in ω Cen and NGC 6397. *MNRAS*, **444**, pp. 443–456. doi:10.1093/mnras/stu1449.

Hempel, M. and J. Schaffner-Bielich (2010). A statistical model for a complete supernova equation of state. *Nuclear Physics A*, **837**, pp. 210–254. doi:10.1016/j.nuclphysa.2010.02.010.

Hen, O., B.-A. Li, W.-J. Guo, L. B. Weinstein, and E. Piasetzky (2015). Symmetry energy of nucleonic matter with tensor correlations. *PhRvC*, **91**(2), 025803. doi:10.1103/PhysRevC.91.025803.

Hillebrandt, W. and P. Hoflich (1989). REVIEW: The supernova 1987A in the Large Magellanic Cloud. *Reports on Progress in Physics*, **52**(11), pp. 1421–1473. doi:10.1088/0034-4885/52/11/002.

Hinderer, T. (2008). Tidal Love Numbers of Neutron Stars. *ApJ*, **677**, 1216-1220. doi:10.1086/533487.

Hinderer, T., B. D. Lackey, R. N. Lang, and J. S. Read (2010). Tidal deformability of neutron stars with realistic equations of state and their gravitational wave signatures in binary inspiral. *PhRvD*, **81**(12), 123016. doi:10.1103/PhysRevD.81.123016.

Hobbs, G., D. R. Lorimer, A. G. Lyne, and M. Kramer (2005). A statistical study of 233 pulsar proper motions. *MNRAS*, **360**(3), pp. 974–992. doi:10.1111/j.1365-2966.2005.09087.x.

Horowitz, C. J., E. F. Brown, Y. Kim, W. G. Lynch, R. Michaels, A. Ono, J. Piekarewicz, M. B. Tsang, and H. H. Wolter (2014). A way forward in the study of the symmetry energy: experiment, theory, and observation. *Journal of Physics G Nuclear Physics*, **41**(9), 093001. doi:10.1088/0954-3899/41/9/093001.

Ivanova, N., S. Justham, X. Chen, O. De Marco, C. L. Fryer, E. Gaburov, H. Ge, E. Glebbeek, Z. Han, X.-D. Li, G. Lu, T. Marsh, P. Podsiadlowski, A. Potter, N. Soker, R. Taam, T. M. Tauris, E. P. J. van den Heuvel, and R. F. Webbink (2013). Common envelope evolution: where we stand and how we can move forward. *A&A Rv*, **21**, 59. doi:10.1007/s00159-013-0059-2.

Janka, H.-T., T. Melson, and A. Summa (2016). Physics of Core-Collapse Supernovae in Three Dimensions: A Sneak Preview. *Annual Review of Nuclear and Particle Science*, **66**, pp. 341–375. doi:10.1146/annurev-nucl-102115-044747.

Janka, H.-T. and E. Mueller (1996). Neutrino heating, convection, and the mechanism of Type-II supernova explosions. *A&A*, **306**, p. 167.

Janka, H.-T., T. Zwerger, and R. Moenchmeyer (1993). Does artificial viscosity destroy prompt type-II supernova explosions? *A&A*, **268**, pp. 360–368.

Jeffreys, H. (1946). An Invariant Form for the Prior Probability in Estimation Problems. *Proceedings of the Royal Society of London Series A*, **186**(1007), pp. 453–461. doi:10.1098/rspa.1946.0056.

Jiang, J.-L., S.-P. Tang, Y.-Z. Wang, Y.-Z. Fan, and D.-M. Wei (2020). PSR J0030+0451, GW170817, and the Nuclear Data: Joint Constraints on Equation of State and Bulk Properties of Neutron Stars. *ApJ*, **892**(1), 55. doi: 10.3847/1538-4357/ab77cf.

Kaplan, D. B. and A. E. Nelson (1986). Strange goings on in dense nucleonic matter. *Physics Letters B*, **175**, pp. 57–63. doi:10.1016/0370-2693(86)90331-X.

Keane, E., B. Bhattacharyya, M. Kramer, B. Stappers, E. F. Keane, B. Bhattacharyya, M. Kramer, B. W. Stappers, S. D. Bates, M. Burgay, S. Chatterjee, D. J. Champion, R. P. Eatough, J. W. T. Hessels, G. Janssen, K. J. Lee, J. van Leeuwen, J. Margueron, M. Oertel, A. Possenti, S. Ransom, G. Theureau, and P. Torne (2015). A Cosmic Census of Radio Pulsars with the SKA. In *Advancing Astrophysics with the Square Kilometre Array (AASKA14)*, p. 40.

Khanmohamadi, S., H. R. Moshfegh, and S. A. Tehrani (2020). Structure and tidal deformability of a hybrid star within the framework of the field correlator method. *PhRvD*, **101**(12), 123001. doi:10.1103/PhysRevD.101.123001.

Kifonidis, K., T. Plewa, H.-T. Janka, and E. Müller (2003). Non-spherical core collapse supernovae. I. Neutrino-driven convection, Rayleigh-Taylor instabilities, and the formation and propagation of metal clumps. *A&A*, **408**, pp. 621–649. doi:10.1051/0004-6361:20030863.

Kim, C., V. Kalogera, and D. R. Lorimer (2003). The Probability Distribution of Binary Pulsar Coalescence Rates. I. Double Neutron Star Systems in the Galactic Field. *ApJ*, **584**(2), pp. 985–995. doi:10.1086/345740.

Kiziltan, B., A. Kottas, M. De Yoreo, and S. E. Thorsett (2013). The Neutron Star Mass Distribution. *ApJ*, **778**, 66. doi:10.1088/0004-637X/778/1/66.

Kochanek, C. S. (2014). Failed Supernovae Explain the Compact Remnant Mass Function. *ApJ*, **785**, 28. doi:10.1088/0004-637X/785/1/28.

Kramer, M. and N. Wex (2009). TOPICAL REVIEW: The double pulsar system: a unique laboratory for gravity. *Classical and Quantum Gravity*, **26**(7), 073001. doi:10.1088/0264-9381/26/7/073001.

Krastev, P. G. and B.-A. Li (2019). Imprints of the nuclear symmetry energy on the tidal deformability of neutron stars. *Journal of Physics G Nuclear Physics*, **46**(7), p. 074001. doi:10.1088/1361-6471/ab1a7a.

Kruckow, M. U., T. M. Tauris, N. Langer, D. Szécsi, P. Marchant, and P. Podsiadlowski (2016). Common-envelope ejection in massive binary stars. Implications for the progenitors of GW150914 and GW151226. *A&A*, **596**, A58. doi:10.1051/0004-6361/201629420.

Krüger, T., I. Tews, K. Hebeler, and A. Schwenk (2013). Neutron matter from chiral effective field theory interactions. *PhRvC*, **88**(2), 025802. doi:10.1103/PhysRevC.88.025802.

Lackey, B. D., M. Nayyar, and B. J. Owen (2006). Observational constraints on hyperons in neutron stars. *PhRvD*, **73**(2), 024021. doi:10.1103/PhysRevD.73.024021.

Lackey, B. D. and L. Wade (2015). Reconstructing the neutron-star equation of state with gravitational-wave detectors from a realistic population of inspiralling binary neutron stars. *PhRvD*, **91**(4), 043002. doi:10.1103/PhysRevD.91.043002.

Lai, D., D. F. Chernoff, and J. M. Cordes (2001). Pulsar Jets: Implications for Neutron Star Kicks and Initial Spins. *ApJ*, **549**(2), pp. 1111–1118. doi:10.1086/319455.

Lalazissis, G. A., J. König, and P. Ring (1997). New parametrization for the Lagrangian density of relativistic mean field theory. *PhRvC*, **55**, pp. 540–543. doi:10.1103/PhysRevC.55.540.

Lalazissis, G. A., S. Raman, and P. Ring (1999). Ground-State Properties of Even-Even Nuclei in the Relativistic Mean-Field Theory. *Atomic Data and Nuclear Data Tables*, **71**, p. 1. doi:10.1006/adnd.1998.0795.

Landry, P. and R. Essick (2019). Nonparametric inference of the neutron star equation of state from gravitational wave observations. *PhRvD*, **99**(8), 084049. doi:10.1103/PhysRevD.99.084049.

Landry, P., R. Essick, and K. Chatziioannou (2020). Nonparametric constraints on neutron star matter with existing and upcoming gravitational wave and pulsar observations. *arXiv e-prints*, arXiv:2003.04880.

Lattimer, J. M. (2012). The Nuclear Equation of State and Neutron Star Masses. *Annual Review of Nuclear and Particle Science*, **62**, pp. 485–515. doi:10.1146/annurev-nucl-102711-095018.

Lattimer, J. M. and Y. Lim (2013). Constraining the Symmetry Parameters of the Nuclear Interaction. *ApJ*, **771**, 51. doi:10.1088/0004-637X/771/1/51.

Lattimer, J. M. and M. Prakash (2001). Neutron Star Structure and the Equation of State. *ApJ*, **550**, pp. 426–442. doi:10.1086/319702.

Lattimer, J. M. and M. Prakash (2016). The equation of state of hot, dense matter and neutron stars. *PhR*, **621**, pp. 127–164. doi:10.1016/j.physrep.2015.12.005.

Lattimer, J. M. and B. F. Schutz (2005). Constraining the Equation of State with Moment of Inertia Measurements. *ApJ*, **629**, pp. 979–984. doi:10.1086/431543.

Lattimer, J. M. and A. W. Steiner (2014). Constraints on the symmetry energy using the mass-radius relation of neutron stars. *European Physical Journal A*, **50**, 40. doi:10.1140/epja/i2014-14040-y.

Lattimer, J. M. and D. F. Swesty (1991). A generalized equation of state for hot, dense matter. *Nuclear Physics A*, **535**, pp. 331–376. doi:10.1016/0375-9474(91)90452-C.

Li, B.-A., W.-J. Guo, and Z. Shi (2015). Effects of the kinetic symmetry energy reduced by short-range correlations in heavy-ion collisions at intermediate energies. *PhRvC*, **91**(4), 044601. doi:10.1103/PhysRevC.91.044601.

Li, B.-A. and X. Han (2013). Constraining the neutron-proton effective mass splitting using empirical constraints on the density dependence of nuclear symmetry energy around normal density. *Physics Letters B*, **727**(1-3), pp. 276–281. doi:10.1016/j.physletb.2013.10.006.

Li, L.-X. and B. Paczyński (1998). Transient Events from Neutron Star Mergers. *ApJL*, **507**, pp. L59–L62. doi:10.1086/311680.

Lim, Y. and J. W. Holt (2019). Bayesian modeling of the nuclear equation of state for neutron star tidal deformabilities and GW170817. *European Physical Journal A*, **55**(11), 209. doi:10.1140/epja/i2019-12917-9.

Lindblom, L. (1984). Limits on the gravitational redshift form neutron stars. *ApJ*, **278**, pp. 364–368. doi:10.1086/161800.

Lindblom, L. (1992). Determining the nuclear equation of state from neutron-star masses and radii. *ApJ*, **398**, pp. 569–573. doi:10.1086/171882.

Lindblom, L. (2010). Spectral representations of neutron-star equations of state. *Physical Review D*, **82**(10), 103011. doi:10.1103/PhysRevD.82.103011.

Lindblom, L. and N. M. Indik (2012). Spectral approach to the relativistic inverse stellar structure problem. *PhRvD*, **86**(8), 084003. doi:10.1103/PhysRevD.86.084003.

Lindblom, L. and N. M. Indik (2014). Spectral approach to the relativistic inverse stellar structure problem II. *PhRvD*, **89**(6), 064003. doi:10.1103/PhysRevD.89.064003.

Lovato, A., O. Benhar, S. Fantoni, A. Y. Illarionov, and K. E. Schmidt (2011). Density-dependent nucleon-nucleon interaction from three-nucleon forces. *PhRvC*, **83**(5), 054003. doi:10.1103/PhysRevC.83.054003.

Lovegrove, E. and S. E. Woosley (2013). Very Low Energy Supernovae from Neutrino Mass Loss. *ApJ*, **769**, 109. doi:10.1088/0004-637X/769/2/109.

Lyne, A. G., M. Burgay, M. Kramer, A. Possenti, R. N. Manchester, F. Camilo, M. A. McLaughlin, D. R. Lorimer, N. D'Amico, B. C. Joshi, et al. (2004). A Double-Pulsar System: A Rare Laboratory for Relativistic Gravity and Plasma Physics. *Science*, **303**, pp. 1153–1157. doi:10.1126/science.1094645.

Maeda, K., K. Kawabata, P. A. Mazzali, M. Tanaka, S. Valenti, K. Nomoto, T. Hattori, J. Deng, E. Pian, S. Taubenberger, M. Iye, T. Matheson, A. V. Filippenko, K. Aoki, G. Kosugi, Y. Ohyama, T. Sasaki, and T. Takata (2008). Asphericity in Supernova Explosions from Late-Time Spectroscopy. *Science*, **319**(5867), p. 1220. doi:10.1126/science.1149437.

Malik, T., N. Alam, M. Fortin, C. Providência, B. K. Agrawal, T. K. Jha, B. Kumar, and S. K. Patra (2018). GW170817: Constraining the nuclear matter equation of state from the neutron star tidal deformability. *PhRvC*, **98**(3), 035804. doi:10.1103/PhysRevC.98.035804.

Mandel, I. and S. E. de Mink (2016). Merging binary black holes formed through chemically homogeneous evolution in short-period stellar binaries. *MNRAS*, **458**, pp. 2634–2647. doi:10.1093/mnras/stw379.

Mapelli, M. (2016). Massive black hole binaries from runaway collisions: the impact of metallicity. *MNRAS*, **459**, pp. 3432–3446. doi:10.1093/mnras/stw869.

Marchant, P., N. Langer, P. Podsiadlowski, T. M. Tauris, and T. J. Moriya (2016). A new route towards merging massive black holes. *A&A*, **588**, A50. doi:10.1051/0004-6361/201628133.

Marczenko, M., D. Blaschke, K. Redlich, and C. Sasaki (2020). Towards a unified equation of state for multi-messenger astronomy. *arXiv e-prints*, arXiv:2004.09566.

Margalit, B. and B. D. Metzger (2017). Constraining the Maximum Mass of Neutron Stars from Multi-messenger Observations of GW170817. *ApJL*, **850**, L19. doi:10.3847/2041-8213/aa991c.

Margueron, J., R. Hoffmann Casali, and F. Gulminelli (2018a). Equation of state for dense nucleonic matter from metamodeling. I. Foundational aspects. *PhRvC*, **97**(2), 025805. doi:10.1103/PhysRevC.97.025805.

Margueron, J., R. Hoffmann Casali, and F. Gulminelli (2018b). Equation of state for dense nucleonic matter from metamodeling. II. Predictions for neutron star properties. *PhRvC*, **97**(2), 025806. doi:10.1103/PhysRevC.97.025806.

Metzger, B. D., G. Martínez-Pinedo, S. Darbha, E. Quataert, A. Arcones, D. Kasen, R. Thomas, P. Nugent, I. V. Panov, and N. T. Zinner (2010). Electromagnetic counterparts of compact object mergers powered by the radioactive decay of r-process nuclei. *MNRAS*, **406**, pp. 2650–2662. doi:10.1111/j.1365-2966.2010.16864.x.

Mikóczi, B., M. Vasúth, and L. Á. Gergely (2005). Self-interaction spin effects in inspiralling compact binaries. *PhRvD*, **71**(12), 124043. doi:10.1103/PhysRevD.71.124043.

Milisavljevic, D. and R. A. Fesen (2015). The bubble-like interior of the core-collapse supernova remnant Cassiopeia A. *Science*, **347**(6221), pp. 526–530. doi:10.1126/science.1261949.

Miller, M. C., F. K. Lamb, A. J. Dittmann, S. Bogdanov, Z. Arzoumanian, K. C. Gendreau, S. Guillot, A. K. Harding, W. C. G. Ho, J. M. Lattimer, R. M. Ludlam, S. Mahmoodifar, S. M. Morsink, P. S. Ray, T. E. Strohmayer, K. S. Wood, T. Enoto, R. Foster, T. Okajima, G. Prigozhin, and Y. Soong (2019). PSR J0030+0451 Mass and Radius from NICER Data and Implications for the Properties of Neutron Star Matter. *ApJL*, **887**(1), L24. doi:10.3847/2041-8213/ab50c5.

Mishra, C. K., A. Kela, K. G. Arun, and G. Faye (2016). Ready-to-use post-Newtonian gravitational waveforms for binary black holes with nonprecessing spins: An update. *PhRvD*, **93**(8), 084054. doi:10.1103/PhysRevD.93.084054.

Mondal, C., B. K. Agrawal, J. N. De, S. K. Samaddar, M. Centelles, and X. Viñas (2017). Interdependence of different symmetry energy elements. *PhRvC*, **96**(2), 021302. doi:10.1103/PhysRevC.96.021302.

Morales, J., V. R. Pandharipande, and D. G. Ravenhall (2002). Improved variational calculations of nucleon matter. *PhRvC*, **66**(5), 054308. doi:10.1103/PhysRevC.66.054308.

Morfouace, P., C. Y. Tsang, Y. Zhang, W. G. Lynch, M. B. Tsang, D. D. S. Coupland, M. Youngs, Z. Chajecki, M. A. Famiano, T. K. Ghosh, G. Jhang, J. Lee, H. Liu, A. Sanetullaev, R. Showalter, and J. Winkelbauer (2019). Constraining the symmetry energy with heavy-ion collisions and Bayesian analyses. *Physics Letters B*, **799**, 135045. doi:10.1016/j.physletb.2019.135045.

Morrison, I. A., T. W. Baumgarte, S. L. Shapiro, and V. R. Pandharipande (2004). The Moment of Inertia of the Binary Pulsar J0737-3039A: Constraining the Nuclear Equation of State. *The Astrophysical Journal Letters*, **617**, pp. L135–L138. doi:10.1086/427235.

Most, E. R., L. R. Weih, L. Rezzolla, and J. Schaffner-Bielich (2018). New Constraints on Radii and Tidal Deformabilities of Neutron Stars from GW170817. *Phys. Rev. Lett.*, **120**, p. 261103. doi:10.1103/PhysRevLett.120.261103.

Motch, C., J. Wilms, D. Barret, W. Becker, S. Bogdanov, L. Boirin, S. Corbel, E. Cackett, S. Campana, D. de Martino, F. Haberl, J. in't Zand, M. Méndez, R. Mignani, J. Miller, M. Orio, D. Psaltis, N. Rea, J. Rodriguez, A. Rozanska, A. Schwope, A. Steiner, N. Webb, L. Zampieri, and S. Zane (2013). The Hot and Energetic Universe: End points of stellar evolution. *arXiv e-prints*, arXiv:1306.2334.

Müller, B., A. Heger, D. Liptai, and J. B. Cameron (2016). A simple approach to the supernova progenitor-explosion connection. *MNRAS*, **460**, pp. 742–764. doi:10.1093/mnras/stw1083.

Müller, H. and B. D. Serot (1996). Relativistic mean-field theory and the high-density nuclear equation of state. *Nuclear Physics A*, **606**, pp. 508–537. doi:10.1016/0375-9474(96)00187-X.

Murphy, J. W. and J. C. Dolence (2017). An Integral Condition for Core-collapse Supernova Explosions. *ApJ*, **834**, 183. doi:10.3847/1538-4357/834/2/183.

Nadezhin, D. K. (1980). Some secondary indications of gravitational collapse. *Ap&SS*, **69**, pp. 115–125. doi:10.1007/BF00638971.

Nan, R., D. Li, C. Jin, Q. Wang, L. Zhu, W. Zhu, H. Zhang, Y. Yue, and L. Qian (2011). The Five-Hundred Aperture Spherical Radio Telescope (fast) Project. *International Journal of Modern Physics D*, **20**(6), pp. 989–1024. doi:10.1142/S0218271811019335.

Nan, R.-d., H.-y. Zhang, Y. Zhang, L. Yang, W.-j. Cai, N. Liu, J.-t. Xie, and S.-x. Zhang (2017). Construction Progress of the FAST Project. *ChA&A*, **41**(3), pp. 293–301. doi:10.1016/j.chinastron.2017.08.001.

Nandra, K., D. Barret, X. Barcons, A. Fabian, J.-W. den Herder, L. Piro, M. Watson, and et al. (2013). The Hot and Energetic Universe: A White Paper presenting the science theme motivating the Athena+ mission. *arXiv e-prints*, arXiv:1306.2307.

Narayan, R., B. Paczynski, and T. Piran (1992). Gamma-ray bursts as the death throes of massive binary stars. *ApJL*, **395**, pp. L83–L86. doi:10.1086/186493.

Nättilä, J., A. W. Steiner, J. J. E. Kajava, V. F. Suleimanov, and J. Poutanen (2016). Equation of state constraints for the cold dense matter inside neutron stars using the cooling tail method. *A&A*, **591**, A25. doi:10.1051/0004-6361/201527416.

Ng, C. (2018). Pulsar science with the CHIME telescope. In Weltevrede, P., B. B. P. Perera, L. L. Preston, and S. Sanidas (eds.) *Pulsar Astrophysics the Next Fifty Years*, volume 337 of *IAU Symposium*, pp. 179–182. doi:10.1017/S1743921317010638.

Nieuwenhuijzen, H. and C. de Jager (1990). Parametrization of stellar rates of mass loss as functions of the fundamental stellar parameters M, L, and R. *A&A*, **231**, pp. 134–136.

Nikolov, N., N. Schunck, W. Nazarewicz, M. Bender, and J. Pei (2011). Surface symmetry energy of nuclear energy density functionals. *Phys. Rev. C*, **83**, p. 034305. doi:10.1103/PhysRevC.83.034305.

Nomoto, K., C. Kobayashi, and N. Tominaga (2013). Nucleosynthesis in Stars and the Chemical Enrichment of Galaxies. *ARA&A*, **51**, pp. 457–509. doi:10.1146/annurev-astro-082812-140956.

O'Connor, E. and C. D. Ott (2011). Black Hole Formation in Failing Core-Collapse Supernovae. *ApJ*, **730**, 70. doi:10.1088/0004-637X/730/2/70.

Oechslin, R., H.-T. Janka, and A. Marek (2007). Relativistic neutron star merger simulations with non-zero temperature equations of state. I. Variation of binary parameters and equation of state. *A&A*, **467**, pp. 395–409. doi:10.1051/0004-6361:20066682.

Oertel, M., M. Hempel, T. Klähn, and S. Typel (2017). Equations of state for supernovae and compact stars. *Reviews of Modern Physics*, **89**(1), 015007. doi:10.1103/RevModPhys.89.015007.

O'Leary, R. M., Y. Meiron, and B. Kocsis (2016). Dynamical Formation Signatures of Black Hole Binaries in the First Detected Mergers by LIGO. *ApJL*, **824**, L12. doi:10.3847/2041-8205/824/1/L12.

Oppenheimer, J. R. and G. M. Volkoff (1939). On Massive Neutron Cores. *Physical Review*, **55**, pp. 374–381. doi:10.1103/PhysRev.55.374.

Özel, F., G. Baym, and T. Güver (2010a). Astrophysical measurement of the equation of state of neutron star matter. *PhRvD*, **82**(10), 101301. doi:10.1103/PhysRevD.82.101301.

Özel, F. and P. Freire (2016). Masses, Radii, and the Equation of State of Neutron Stars. *Ann. Rev. Astron. Astrophys.*, **54**, pp. 401–440. doi:10.1146/annurev-astro-081915-023322.

Özel, F., T. Güver, and D. Psaltis (2009). The Mass and Radius of the Neutron Star in EXO 1745-248. *ApJ*, **693**, pp. 1775–1779. doi:10.1088/0004-637X/693/2/1775.

Özel, F. and D. Psaltis (2009). Reconstructing the neutron-star equation of state from astrophysical measurements. *PhRvD*, **80**(10), 103003. doi:10.1103/PhysRevD.80.103003.

Özel, F., D. Psaltis, T. Güver, G. Baym, C. Heinke, and S. Guillot (2016). The Dense Matter Equation of State from Neutron Star Radius and Mass Measurements. *ApJ*, **820**, 28. doi:10.3847/0004-637X/820/1/28.

Özel, F., D. Psaltis, R. Narayan, and J. E. McClintock (2010b). The Black Hole Mass Distribution in the Galaxy. *ApJ*, **725**, pp. 1918–1927. doi:10.1088/0004-637X/725/2/1918.

Özel, F., D. Psaltis, R. Narayan, and A. Santos Villarreal (2012). On the Mass Distribution and Birth Masses of Neutron Stars. *ApJ*, **757**, 55. doi:10.1088/0004-637X/757/1/55.

Özel, F., D. Psaltis, S. Ransom, P. Demorest, and M. Alford (2010c). The Massive Pulsar PSR J1614-2230: Linking Quantum Chromodynamics, Gamma-ray Bursts, and Gravitational Wave Astronomy. *Astrophys. J. Letters*, **724**, pp. L199–L202. doi:10.1088/2041-8205/724/2/L199.

Pandharipande, V. R. and R. A. Smith (1975). A model neutron solid with π^0 condensate. *Nuclear Physics A*, **237**, pp. 507–532. doi:10.1016/0375-9474(75)90415-7.

Park, D., C. Kim, H. M. Lee, Y.-B. Bae, and K. Belczynski (2017). Black hole binaries dynamically formed in globular clusters. *MNRAS*, **469**, pp. 4665–4674. doi:10.1093/mnras/stx1015.

Paschalidis, V. and N. Stergioulas (2017). Rotating stars in relativity. *Living Reviews in Relativity*, **20**, 7. doi:10.1007/s41114-017-0008-x.

Pechenick, K. R., C. Ftaclas, and J. M. Cohen (1983). Hot spots on neutron stars - The near-field gravitational lens. *ApJ*, **274**, pp. 846–857. doi:10.1086/161498.

Pejcha, O. and T. A. Thompson (2015). The Landscape of the Neutrino Mechanism of Core-collapse Supernovae: Neutron Star and Black Hole Mass Functions, Explosion Energies, and Nickel Yields. *ApJ*, **801**, 90. doi:10.1088/0004-637X/801/2/90.

Pejcha, O., T. A. Thompson, and C. S. Kochanek (2012). The observed neutron star mass distribution as a probe of the supernova explosion mechanism. *MNRAS*, **424**, pp. 1570–1583. doi:10.1111/j.1365-2966.2012.21369.x.

Petit, V., Z. Keszthelyi, R. MacInnis, D. H. Cohen, R. H. D. Townsend, G. A. Wade, S. L. Thomas, S. P. Owocki, J. Puls, and A. ud-Doula (2017). Magnetic massive stars as progenitors of 'heavy' stellar-mass black holes. *MNRAS*, **466**, pp. 1052–1060. doi:10.1093/mnras/stw3126.

Piekarewicz, J. (2004). Unmasking the nuclear matter equation of state. *PhRvC*, **69**(4), 041301. doi:10.1103/PhysRevC.69.041301.

Postnikov, S., M. Prakash, and J. M. Lattimer (2010). Tidal Love numbers of neutron and self-bound quark stars. *PhRvD*, **82**(2), 024016. doi:10.1103/PhysRevD.82.024016.

Psaltis, D., F. Özel, and S. DeDeo (2000). Photon Propagation around Compact Objects and the Inferred Properties of Thermally Emitting Neutron Stars. *ApJ*, **544**(1), pp. 390–396. doi:10.1086/317208.

Radice, D., S. Bernuzzi, and A. Perego (2020). The Dynamics of Binary Neutron Star Mergers and of GW170817. *arXiv e-prints*, arXiv:2002.03863.

Radice, D. and L. Dai (2019). Multimessenger parameter estimation of GW170817. *European Physical Journal A*, **55**(4), 50. doi:10.1140/epja/i2019-12716-4.

Raduta, A. R. and F. Gulminelli (2018). Nuclear Statistical Equilibrium Equation of State for Core Collapse. *arXiv e-prints*.

Raithel, C. A. (2019). Constraints on the neutron star equation of state from GW170817. *European Physical Journal A*, **55**(5), 80. doi:10.1140/epja/i2019-12759-5.

Raithel, C. A. and F. Özel (2019). Measurement of the Nuclear Symmetry Energy Parameters from Gravitational-wave Events. *ApJ*, **885**(2), 121. doi:10.3847/1538-4357/ab48e6.

Raithel, C. A., F. Özel, and D. Psaltis (2016). From Neutron Star Observables to the Equation of State. I. An Optimal Parametrization. *ApJ*, **831**, 44. doi:10.3847/0004-637X/831/1/44.

Raithel, C. A., F. Özel, and D. Psaltis (2018). Tidal Deformability from GW170817 as a Direct Probe of the Neutron Star Radius. *ApJL*, **857**(2), L23. doi:10.3847/2041-8213/aabcbf.

Rawls, M. L., J. A. Orosz, J. E. McClintock, M. A. P. Torres, C. D. Bailyn, and M. M. Buxton (2011). Refined Neutron Star Mass Determinations for Six Eclipsing X-Ray Pulsar Binaries. *ApJ*, **730**, 25. doi:10.1088/0004-637X/730/1/25.

Ray, P. S., Z. Arzoumanian, D. Ballantyne, E. Bozzo, S. Brandt, L. Brenneman, D. Chakrabarty, M. Christophersen, A. DeRosa, and et al. (2019). STROBE-X: X-ray Timing and Spectroscopy on Dynamical Timescales from Microseconds to Years. *arXiv e-prints*, arXiv:1903.03035.

Read, J. S., L. Baiotti, J. D. E. Creighton, J. L. Friedman, B. Giacomazzo, K. Kyutoku, C. Markakis, L. Rezzolla, M. Shibata, and K. Taniguchi (2013). Matter effects on binary neutron star waveforms. *PhRvD*, **88**(4), 044042. doi: 10.1103/PhysRevD.88.044042.

Read, J. S., B. D. Lackey, B. J. Owen, and J. L. Friedman (2009a). Constraints on a phenomenologically parametrized neutron-star equation of state. *PhRvD*, **79**(12), 124032. doi:10.1103/PhysRevD.79.124032.

Read, J. S., C. Markakis, M. Shibata, K. Uryū, J. D. E. Creighton, and J. L. Friedman (2009b). Measuring the neutron star equation of state with gravitational wave observations. *PhRvD*, **79**(12), 124033. doi:10.1103/PhysRevD.79.124033.

Reitze, D., R. X. Adhikari, S. Ballmer, B. Barish, L. Barsotti, G. Billingsley, D. A. Brown, Y. Chen, D. Coyne, R. Eisenstein, M. Evans, P. Fritschel, E. D. Hall, A. Lazzarini, G. Lovelace, J. Read, B. S. Sathyaprakash, D. Shoemaker, J. Smith, C. Torrie, S. Vitale, R. Weiss, C. Wipf, and M. Zucker (2019). Cosmic Explorer: The U.S. Contribution to Gravitational-Wave Astronomy beyond LIGO. In *BAAS*, volume 51, p. 35.

Renzo, M., C. D. Ott, S. N. Shore, and S. E. de Mink (2017). Systematic survey of the effects of wind mass loss algorithms on the evolution of single massive stars. *A&A*, **603**, A118. doi:10.1051/0004-6361/201730698.

Rezzolla, L., E. R. Most, and L. R. Weih (2017). Using gravitational-wave observations and quasi-universal relations to constrain the maximum mass of neutron stars. *ArXiv e-prints*.

Rezzolla, L. and K. Takami (2016). Gravitational-wave signal from binary neutron stars: A systematic analysis of the spectral properties. *PhRvD*, **93**(12), 124051. doi:10.1103/PhysRevD.93.124051.

Riley, T. E., G. Raaijmakers, and A. L. Watts (2018). On parametrized cold dense matter equation-of-state inference. *MNRAS*, **478**, pp. 1093–1131. doi:10.1093/mnras/sty1051.

Riley, T. E., A. L. Watts, S. Bogdanov, P. S. Ray, R. M. Ludlam, S. Guillot, Z. Arzoumanian, C. L. Baker, A. V. Bilous, D. Chakrabarty, K. C. Gendreau, A. K. Harding, W. C. G. Ho, J. M. Lattimer, S. M. Morsink, and T. E. Strohmayer (2019). A NICER View of PSR J0030+0451: Millisecond Pulsar Parameter Estimation. *ApJL*, **887**(1), L21. doi:10.3847/2041-8213/ab481c.

Rios, A., A. Polls, and W. H. Dickhoff (2014). Density and isospin-asymmetry dependence of high-momentum components. *PhRvC*, **89**(4), 044303. doi:10.1103/PhysRevC.89.044303.

Roca-Maza, X., M. Brenna, B. K. Agrawal, P. F. Bortignon, G. Colò, L.-G. Cao, N. Paar, and D. Vretenar (2013). Giant quadrupole resonances in ^{208}Pb, the nuclear symmetry energy, and the neutron skin thickness. *PhRvC*, **87**(3), 034301. doi:10.1103/PhysRevC.87.034301.

Rodriguez, C. L., C.-J. Haster, S. Chatterjee, V. Kalogera, and F. A. Rasio (2016). Dynamical Formation of the GW150914 Binary Black Hole. *ApJL*, **824**, L8. doi:10.3847/2041-8205/824/1/L8.

Sabbadini, A. G. and J. B. Hartle (1973). Upper Bound on the Mass of Non-Rotating Neutron Stars. *Astrophysics and Space Science*, **25**, pp. 117–131. doi:10.1007/BF00648231.

Sabbadini, A. G. and J. B. Hartle (1977). Bounds on the moment of inertia of nonrotating neutron stars. *Annals of Physics*, **104**, pp. 95–133. doi:10.1016/0003-4916(77)90047-1.

Salpeter, E. E. (1955). The Luminosity Function and Stellar Evolution. *ApJ*, **121**, p. 161. doi:10.1086/145971.

Sathyaprakash, B., M. Abernathy, F. Acernese, P. Ajith, B. Allen, P. Amaro-Seoane, N. Andersson, S. Aoudia, K. Arun, P. Astone, and et al. (2012). Scientific objectives of Einstein Telescope. *Classical and Quantum Gravity*, **29**(12), 124013. doi:10.1088/0264-9381/29/12/124013.

Sathyaprakash, B. S. and S. V. Dhurandhar (1991). Choice of filters for the detection of gravitational waves from coalescing binaries. *PhRvD*, **44**, pp. 3819–3834. doi:10.1103/PhysRevD.44.3819.

Sekiguchi, Y., K. Kiuchi, K. Kyutoku, and M. Shibata (2011). Gravitational Waves and Neutrino Emission from the Merger of Binary Neutron Stars. *Physical Review Letters*, **107**(5), 051102. doi:10.1103/PhysRevLett.107.051102.

Shen, G., C. J. Horowitz, and E. O'Connor (2011a). Second relativistic mean field and virial equation of state for astrophysical simulations. *Phys. Rev. C*, **83**, p. 065808. doi:10.1103/PhysRevC.83.065808.

Shen, G., C. J. Horowitz, and S. Teige (2011b). New equation of state for astrophysical simulations. *Phys. Rev. C*, **83**, p. 035802. doi:10.1103/PhysRevC.83.035802.

Shen, H., H. Toki, K. Oyamatsu, and K. Sumiyoshi (1998). Relativistic equation of state of nuclear matter for supernova and neutron star. *Nuclear Physics A*, **637**, pp. 435–450. doi:10.1016/S0375-9474(98)00236-X.

Shibata, M. and K. Hotokezaka (2019). Merger and Mass Ejection of Neutron Star Binaries. *Annual Review of Nuclear and Particle Science*, **69**, pp. 41–64. doi:10.1146/annurev-nucl-101918-023625.

Shibata, M. and K. Taniguchi (2011). Coalescence of Black Hole-Neutron Star Binaries. *Living Reviews in Relativity*, **14**, 6. doi:10.12942/lrr-2011-6.

Shlomo, S., V. M. Kolomietz, and G. Colò (2006). Deducing the nuclear-matter incompressibility coefficient from data on isoscalar compression modes. *European Physical Journal A*, **30**(1), pp. 23–30. doi:10.1140/epja/i2006-10100-3.

SKA (2020). Frequently Asked Questions. https://www.skatelescope.org/frequently-asked-questions/.

Smith, N. (2014). Mass Loss: Its Effect on the Evolution and Fate of High-Mass Stars. *ARA&A*, **52**, pp. 487–528. doi:10.1146/annurev-astro-081913-040025.

Smits, R., D. R. Lorimer, M. Kramer, R. Manchester, B. Stappers, C. J. Jin, R. D. Nan, and D. Li (2009). Pulsar science with the Five hundred metre Aperture Spherical Telescope. *A&A*, **505**(2), pp. 919–926. doi:10.1051/0004-6361/200911939.

Steiner, A. W. and S. Gandolfi (2012). Connecting Neutron Star Observations to Three-Body Forces in Neutron Matter and to the Nuclear Symmetry Energy. *Physical Review Letters*, **108**(8), 081102. doi:10.1103/PhysRevLett.108.081102.

Steiner, A. W., C. O. Heinke, S. Bogdanov, C. Li, W. C. G. Ho, A. Bahramian, and S. Han (2017). Constraining the Mass and Radius of Neutron Stars in Globular Clusters. *ArXiv e-prints*.

Steiner, A. W., J. M. Lattimer, and E. F. Brown (2010). The Equation of State from Observed Masses and Radii of Neutron Stars. *ApJ*, **722**, pp. 33–54. doi:10.1088/0004-637X/722/1/33.

Steiner, A. W., J. M. Lattimer, and E. F. Brown (2013). The Neutron Star Mass-Radius Relation and the Equation of State of Dense Matter. *ApJL*, **765**, L5. doi:10.1088/2041-8205/765/1/L5.

Steiner, A. W., J. M. Lattimer, and E. F. Brown (2016). Neutron star radii, universal relations, and the role of prior distributions. *European Physical Journal A*, **52**, 18. doi:10.1140/epja/i2016-16018-1.

Stevenson, S., A. Vigna-Gómez, I. Mandel, J. W. Barrett, C. J. Neijssel, D. Perkins, and S. E. de Mink (2017). Formation of the first three gravitational-wave observations through isolated binary evolution. *Nature Communications*, **8**, 14906. doi:10.1038/ncomms14906.

Stone, J. R., N. J. Stone, and S. A. Moszkowski (2014). Incompressibility in finite nuclei and nuclear matter. *PhRvC*, **89**(4), 044316. doi:10.1103/PhysRevC.89.044316.

Sugahara, Y. and H. Toki (1994). Relativistic mean-field theory for unstable nuclei with non-linear σ and ω terms. *Nuclear Physics A*, **579**, pp. 557–572. doi:10.1016/0375-9474(94)90923-7.

Sukhbold, T., T. Ertl, S. E. Woosley, J. M. Brown, and H.-T. Janka (2016). Core-collapse Supernovae from 9 to 120 Solar Masses Based on Neutrino-powered Explosions. *ApJ*, **821**, 38. doi:10.3847/0004-637X/821/1/38.

Sukhbold, T., S. Woosley, and A. Heger (2017). High Resolution Study of Presupernova Compactness. *ArXiv e-prints*.

Sukhbold, T. and S. E. Woosley (2014). The Compactness of Presupernova Stellar Cores. *ApJ*, **783**, 10. doi:10.1088/0004-637X/783/1/10.

Suwa, Y., T. Yoshida, M. Shibata, H. Umeda, and K. Takahashi (2018). On the minimum mass of neutron stars. *MNRAS*, **481**(3), pp. 3305–3312. doi:10.1093/mnras/sty2460.

Takami, K., L. Rezzolla, and L. Baiotti (2014). Constraining the Equation of State of Neutron Stars from Binary Mergers. *Physical Review Letters*, **113**(9), 091104. doi:10.1103/PhysRevLett.113.091104.

Tamii, A., I. Poltoratska, P. von Neumann-Cosel, Y. Fujita, T. Adachi, C. A. Bertulani, J. Carter, M. Dozono, H. Fujita, K. Fujita, et al. (2011). Complete Electric Dipole Response and the Neutron Skin in Pb208. *Physical Review Letters*, **107**(6), 062502. doi:10.1103/PhysRevLett.107.062502.

Tauris, T. M., V. M. Kaspi, R. P. Breton, A. T. Deller, E. F. Keane, M. Kramer, D. R. Lorimer, M. A. McLaughlin, A. Possenti, P. S. Ray, B. W. Stappers, and P. Weltevrede (2015). Understanding the Neutron Star Population with the SKA. In *Advancing Astrophysics with the Square Kilometre Array (AASKA14)*, p. 39.

Taylor, J. H. and J. M. Weisberg (1982). A new test of general relativity - Gravitational radiation and the binary pulsar PSR 1913+16. *ApJ*, **253**, pp. 908–920. doi:10.1086/159690.

Taylor, J. H. and J. M. Weisberg (1989). Further Experimental Tests of Relativistic Gravity Using the Binary Pulsar PSR 1913+16. *ApJ*, **345**, p. 434. doi:10.1086/167917.

Tews, I., J. M. Lattimer, A. Ohnishi, and E. E. Kolomeitsev (2017). Symmetry Parameter Constraints from a Lower Bound on Neutron-matter Energy. *ApJ*, **848**(2), 105. doi:10.3847/1538-4357/aa8db9.

The LIGO Scientific Collaboration (2017). Instrument Science White Paper: LIGO-T1700231 v2. https://dcc.ligo.org/public/0142/T1700231/003/T1700231-v3.pdf.

The LIGO Scientific Collaboration, the Virgo Collaboration, B. P. Abbott, R. Abbott, T. D. Abbott, S. Abraham, F. Acernese, K. Ackley, C. Adams, R. X. Adhikari, and et al. (2020). GW190425: Observation of a Compact Binary Coalescence with Total Mass $\sim 3.4 M_{\odot}$. *arXiv e-prints*, arXiv:2001.01761.

The LIGO Scientific Collaboration, the Virgo Collaboration, B. P. Abbott, R. Abbott, T. D. Abbott, F. Acernese, K. Ackley, C. Adams, T. Adams, P. Addesso, and et al. (2017a). GW170608: Observation of a 19-solar-mass Binary Black Hole Coalescence. *ArXiv e-prints*.

The LIGO Scientific Collaboration, the Virgo Collaboration, B. P. Abbott, R. Abbott, T. D. Abbott, F. Acernese, K. Ackley, C. Adams, T. Adams, P. Addesso, and et al. (2017b). GW170814: A Three-Detector Observation of Gravitational Waves from a Binary Black Hole Coalescence. *ArXiv e-prints*.

The Lynx Team (2019). Lynx X-ray Observatory: Concept Study Report. https://wwwastro.msfc.nasa.gov/lynx/docs/LynxConceptStudy.pdf.

Thorsett, S. E. and D. Chakrabarty (1999). Neutron Star Mass Measurements. I. Radio Pulsars. *ApJ*, **512**, pp. 288–299. doi:10.1086/306742.

Todd-Rutel, B. G. and J. Piekarewicz (2005). Neutron-Rich Nuclei and Neutron Stars: A New Accurately Calibrated Interaction for the Study of Neutron-Rich Matter. *Physical Review Letters*, **95**(12), 122501. doi:10.1103/PhysRevLett.95.122501.

Togashi, H., K. Nakazato, Y. Takehara, S. Yamamuro, H. Suzuki, and M. Takano (2017). Nuclear equation of state for core-collapse supernova simulations with realistic nuclear forces. *Nuclear Physics A*, **961**, pp. 78–105. doi:10.1016/j.nuclphysa.2017.02.010.

Toki, H., D. Hirata, Y. Sugahara, K. Sumiyoshi, and I. Tanihata (1995). Relativistic many body approach for unstable nuclei and supernova. *Nuclear Physics A*, **588**, pp. 357–363. doi:10.1016/0375-9474(95)00161-S.

Tolman, R. C. (1939). Static Solutions of Einstein's Field Equations for Spheres of Fluid. *Physical Review*, **55**, pp. 364–373. doi:10.1103/PhysRev.55.364.

Trippa, L., G. Colò, and E. Vigezzi (2008). Giant dipole resonance as a quantitative constraint on the symmetry energy. *PhRvC*, **77**(6), 061304. doi: 10.1103/PhysRevC.77.061304.

Tsang, M. B., T. X. Liu, L. Shi, P. Danielewicz, C. K. Gelbke, X. D. Liu, W. G. Lynch, W. P. Tan, G. Verde, A. Wagner, H. S. Xu, W. A. Friedman, L. Beaulieu, B. Davin, R. T. de Souza, Y. Larochelle, T. Lefort, R. Yanez, V. E. Viola, R. J. Charity, and L. G. Sobotka (2004). Isospin Diffusion and the Nuclear Symmetry Energy in Heavy Ion Reactions. *PhRvL*, **92**(6), 062701. doi:10.1103/PhysRevLett.92.062701.

Tsang, M. B., J. R. Stone, F. Camera, P. Danielewicz, S. Gandolfi, K. Hebeler, C. J. Horowitz, J. Lee, W. G. Lynch, Z. Kohley, R. Lemmon, P. Möller, T. Murakami, S. Riordan, X. Roca-Maza, F. Sammarruca, A. W. Steiner, I. Vidaña, and S. J. Yennello (2012). Constraints on the symmetry energy and neutron skins from experiments and theory. *PhRvC*, **86**(1), 015803. doi:10.1103/PhysRevC.86.015803.

Tsang, M. B., Y. Zhang, P. Danielewicz, M. Famiano, Z. Li, W. G. Lynch, and A. W. Steiner (2009). Constraints on the Density Dependence of the Symmetry Energy. *Physical Review Letters*, **102**(12), 122701. doi:10.1103/PhysRevLett.102.122701.

Typel, S. (2018). Equations of state for astrophysical simulations from generalized relativistic density functionals. *Journal of Physics G Nuclear Physics*, **45**(11), p. 114001. doi:10.1088/1361-6471/aadea5.

Typel, S., G. Röpke, T. Klähn, D. Blaschke, and H. H. Wolter (2010). Composition and thermodynamics of nuclear matter with light clusters. *PhRvC*, **81**(1), 015803. doi:10.1103/PhysRevC.81.015803.

Ugliano, M., H.-T. Janka, A. Marek, and A. Arcones (2012). Progenitor-explosion Connection and Remnant Birth Masses for Neutrino-driven Supernovae of Iron-core Progenitors. *ApJ*, **757**, 69. doi:10.1088/0004-637X/757/1/69.

van Paradijs, J. (1978). Average properties of X-ray burst sources. *Nature*, **274**, pp. 650–653. doi:10.1038/274650a0.

van Paradijs, J. (1979). Possible observational constraints on the mass-radius relation of neutron stars. *ApJ*, **234**, pp. 609–611. doi:10.1086/157535.

Vidaña, I., A. Polls, and C. Providência (2011). Nuclear symmetry energy and the role of the tensor force. *PhRvC*, **84**(6), 062801. doi:10.1103/PhysRevC.84.062801.

Vines, J., É. É. Flanagan, and T. Hinderer (2011). Post-1-Newtonian tidal effects in the gravitational waveform from binary inspirals. *PhRvD*, **83**(8), 084051. doi:10.1103/PhysRevD.83.084051.

Voss, R. and T. M. Tauris (2003). Galactic distribution of merging neutron stars and black holes - prospects for short gamma-ray burst progenitors and LIGO/VIRGO. *MNRAS*, **342**, pp. 1169–1184. doi:10.1046/j.1365-8711.2003.06616.x.

Wade, L., J. D. E. Creighton, E. Ochsner, B. D. Lackey, B. F. Farr, T. B. Littenberg, and V. Raymond (2014). Systematic and statistical errors in a Bayesian approach to the estimation of the neutron-star equation of state using advanced gravitational wave detectors. *PhRvD*, **89**(10), 103012. doi:10.1103/PhysRevD.89.103012.

Watts, A., C. M. Espinoza, R. Xu, N. Andersson, J. Antoniadis, D. Antonopoulou, S. Buchner, S. Datta, P. Demorest, P. Freire, J. Hessels, J. Margueron, M. Oertel, A. Patruno, A. Possenti, S. Ransom, I. Stairs, and B. Stappers (2015). Probing the neutron star interior and the Equation of State of cold dense matter with the SKA. In *Advancing Astrophysics with the Square Kilometre Array (AASKA14)*, p. 43.

Weaver, T. A., G. B. Zimmerman, and S. E. Woosley (1978). Presupernova evolution of massive stars. *ApJ*, **225**, pp. 1021–1029. doi:10.1086/156569.

Weisberg, J. M. and Y. Huang (2016). Relativistic Measurements from Timing the Binary Pulsar PSR B1913+16. *ApJ*, **829**(1), 55. doi:10.3847/0004-637X/829/1/55.

Weisberg, J. M. and J. H. Taylor (1981). Gravitational radiation from an orbiting pulsar. *General Relativity and Gravitation*, **13**(1), pp. 1–6. doi:10.1007/BF00766292.

Wellstein, S. and N. Langer (1999). Implications of massive close binaries for black hole formation and supernovae. *A&A*, **350**, pp. 148–162.

Wiktorowicz, G., K. Belczynski, and T. Maccarone (2014). Black hole X-ray transients: The formation puzzle. In *Binary Systems, their Evolution and Environments*, p. 37.

Wiringa, R. B., V. G. J. Stoks, and R. Schiavilla (1995). Accurate nucleon-nucleon potential with charge-independence breaking. *PhRvC*, **51**, pp. 38–51. doi:10.1103/PhysRevC.51.38.

Woosley, S. E. (2016). The Progenitor of GW150914. *ApJL*, **824**, L10. doi:10.3847/2041-8205/824/1/L10.

Woosley, S. E. (2017). Pulsational Pair-instability Supernovae. *ApJ*, **836**, 244. doi:10.3847/1538-4357/836/2/244.

Woosley, S. E. and A. Heger (2007). Nucleosynthesis and remnants in massive stars of solar metallicity. *PhR*, **442**, pp. 269–283. doi:10.1016/j.physrep.2007.02.009.

Woosley, S. E. and A. Heger (2015). The Remarkable Deaths of 9-11 Solar Mass Stars. *ApJ*, **810**, 34. doi:10.1088/0004-637X/810/1/34.

Woosley, S. E., A. Heger, and T. A. Weaver (2002). The evolution and explosion of massive stars. *Reviews of Modern Physics*, **74**, pp. 1015–1071. doi:10.1103/RevModPhys.74.1015.

Xu, C. and B.-A. Li (2011). Tensor force induced isospin-dependence of short-range nucleon-nucleon correlation and high-density behavior of nuclear symmetry energy. *ArXiv e-prints*.

Yagi, K. and N. Yunes (2013). I-Love-Q relations in neutron stars and their applications to astrophysics, gravitational waves, and fundamental physics. *PhRvD*, **88**(2), 023009. doi:10.1103/PhysRevD.88.023009.

Yagi, K. and N. Yunes (2017). Approximate universal relations for neutron stars and quark stars. *PhR*, **681**, pp. 1–72. doi:10.1016/j.physrep.2017.03.002.

Yang, H., V. Paschalidis, K. Yagi, L. Lehner, F. Pretorius, and N. Yunes (2018). Gravitational wave spectroscopy of binary neutron star merger remnants with mode stacking. *PhRvD*, **97**(2), 024049. doi:10.1103/PhysRevD.97.024049.

Zhang, N.-B., B.-J. Cai, B.-A. Li, W. G. Newton, and J. Xu (2017). How tightly is nuclear symmetry energy constrained by unitary Fermi gas? *arXiv e-prints*, arXiv:1704.02687.

Zhang, N.-B. and B.-A. Li (2019). Delineating effects of nuclear symmetry energy on the radii and tidal polarizabilities of neutron stars. *Journal of Physics G Nuclear Physics*, **46**(1), p. 014002. doi:10.1088/1361-6471/aaef54.

Zhang, X. and M. Prakash (2016). Hot and dense matter beyond relativistic mean field theory. *PhRvC*, **93**(5), 055805. doi:10.1103/PhysRevC.93.055805.

Zhu, Z.-Y., E.-P. Zhou, and A. Li (2018). Neutron Star Equation of State from the Quark Level in Light of GW170817. *ApJ*, **862**(2), 98. doi:10.3847/1538-4357/aacc28.

Zimmerman, J., Z. Carson, K. Schumacher, A. W. Steiner, and K. Yagi (2020). Measuring Nuclear Matter Parameters with NICER and LIGO/Virgo. *arXiv e-prints*, arXiv:2002.03210.